AFRL-AFOSR-VA-TR-2016-0064

PREDICTIVE MODELING OF STRUCTURAL SENSING FOR AEROSPACE APPLICATIONS

VICTOR GIURGIUTIU
SOUTH CAROLINA RESEARCH FOUNDATION

08/03/2015
Final Report

DISTRIBUTION A: Distribution approved for public release.

Air Force Research Laboratory
AF Office Of Scientific Research (AFOSR)/ RTA1
Arlington, Virginia 22203
Air Force Materiel Command

REPORT DOCUMENTATION PAGE

Form Approved
OMB No. 0704-0188

The public reporting burden for this collection of information is estimated to average 1 hour per response, including the time for reviewing instructions, searching existing data sources, gathering and maintaining the data needed, and completing and reviewing the collection of information. Send comments regarding this burden estimate or any other aspect of this collection of information, including suggestions for reducing the burden, to the Department of Defense, Executive Service Directorate (0704-0188). Respondents should be aware that notwithstanding any other provision of law, no person shall be subject to any penalty for failing to comply with a collection of information if it does not display a currently valid OMB control number.

PLEASE DO NOT RETURN YOUR FORM TO THE ABOVE ORGANIZATION.

1. REPORT DATE *(DD-MM-YYYY)*	2. REPORT TYPE	3. DATES COVERED *(From - To)*
30-06-2014	FINAL	01-07-2011 to 30-06-2015

4. TITLE AND SUBTITLE
PREDICTIVE MODELING OF STRUCTURAL SENSING FOR AEROSPACE APPLICATIONS

5a. CONTRACT NUMBER

5b. GRANT NUMBER
FA9550-11-1-0133

5c. PROGRAM ELEMENT NUMBER

6. AUTHOR(S)
VICTOR GIURGIUTIU

5d. PROJECT NUMBER

5e. TASK NUMBER

5f. WORK UNIT NUMBER

7. PERFORMING ORGANIZATION NAME(S) AND ADDRESS(ES)
UNIVERSITY OF SOUTH CAROLINA RESEARCH FOUNDATION
901 SUMTER ST. SUITE 501
COLUMBIA, SC 29208

8. PERFORMING ORGANIZATION REPORT NUMBER

9. SPONSORING/MONITORING AGENCY NAME(S) AND ADDRESS(ES)
AIR FORCE OFFICE OF SCIENTIFIC RESEARCH
875 N. RANDOLPH ST ROOM 3112
ARLINGTON, VA 22203

10. SPONSOR/MONITOR'S ACRONYM(S)
AFOSR

11. SPONSOR/MONITOR'S REPORT NUMBER(S)

12. DISTRIBUTION/AVAILABILITY STATEMENT
DISTRIBUTION STATEMENT A: FUNDAMENTAL RESEARCH APPROVED FOR PUBLIC RELEASE, DISTRIBUTION UNLIMITED

13. SUPPLEMENTARY NOTES

14. ABSTRACT
A methodology for multi-scale multi-domain predictive simulation of structural sensing in metallic aerospace structures was developed. The methodology is able to predict the signal response of structural sensors as a function of the structural state and/or the presence of structural flaws or damage, in linear and nonlinear regimes. The approach has been to combine analytical solutions with numerical analysis (e.g., finite element method, FEM) into a hybrid global-local (HGL) analysis. This novel approach allows one to keep the computational effort at a manageable level while preserving the fidelity needed to capture the local interaction between ultrasonic guided waves and structural damage.
This fundamental research project has high relevance to USAF because it has produced a methodological framework for coupling global and local models to achieve the concurrent analysis of the structure in interaction with coupled-field phenomena and efficient treatment of nonlinearities. The results of this project can be used to generate virtual data sets for testing data-driven models and filling data gaps will allow the autonomous model updating of the "digital-twins" models to predict future performance for new mission profiles.

15. SUBJECT TERMS
Structural health monitoring, SHM; nondestructive evaluation, NDE; hybrid global-local approach, HGL; piezoelectric wafer active sensors, PWAS; damage detection; damage quantification; coupled field multi-domain analysis; nonlinear interaction with damage.

16. SECURITY CLASSIFICATION OF:			17. LIMITATION OF ABSTRACT	18. NUMBER OF PAGES	19a. NAME OF RESPONSIBLE PERSON
a. REPORT	b. ABSTRACT	c. THIS PAGE			VICTOR GIURGIUTIU
U	U	U	NONE		19b. TELEPHONE NUMBER *(Include area code)* 803 777 8018

Reset

INSTRUCTIONS FOR COMPLETING SF 298

1. REPORT DATE. Full publication date, including day, month, if available. Must cite at least the year and be Year 2000 compliant, e.g. 30-06-1998; xx-06-1998; xx-xx-1998.

2. REPORT TYPE. State the type of report, such as final, technical, interim, memorandum, master's thesis, progress, quarterly, research, special, group study, etc.

3. DATES COVERED. Indicate the time during which the work was performed and the report was written, e.g., Jun 1997 - Jun 1998; 1-10 Jun 1996; May - Nov 1998; Nov 1998.

4. TITLE. Enter title and subtitle with volume number and part number, if applicable. On classified documents, enter the title classification in parentheses.

5a. CONTRACT NUMBER. Enter all contract numbers as they appear in the report, e.g. F33615-86-C-5169.

5b. GRANT NUMBER. Enter all grant numbers as they appear in the report, e.g. AFOSR-82-1234.

5c. PROGRAM ELEMENT NUMBER. Enter all program element numbers as they appear in the report, e.g. 61101A.

5d. PROJECT NUMBER. Enter all project numbers as they appear in the report, e.g. 1F665702D1257; ILIR.

5e. TASK NUMBER. Enter all task numbers as they appear in the report, e.g. 05; RF0330201; T4112.

5f. WORK UNIT NUMBER. Enter all work unit numbers as they appear in the report, e.g. 001; AFAPL30480105.

6. AUTHOR(S). Enter name(s) of person(s) responsible for writing the report, performing the research, or credited with the content of the report. The form of entry is the last name, first name, middle initial, and additional qualifiers separated by commas, e.g. Smith, Richard, J, Jr.

7. PERFORMING ORGANIZATION NAME(S) AND ADDRESS(ES). Self-explanatory.

8. PERFORMING ORGANIZATION REPORT NUMBER. Enter all unique alphanumeric report numbers assigned by the performing organization, e.g. BRL-1234; AFWL-TR-85-4017-Vol-21-PT-2.

9. SPONSORING/MONITORING AGENCY NAME(S) AND ADDRESS(ES). Enter the name and address of the organization(s) financially responsible for and monitoring the work.

10. SPONSOR/MONITOR'S ACRONYM(S). Enter, if available, e.g. BRL, ARDEC, NADC.

11. SPONSOR/MONITOR'S REPORT NUMBER(S). Enter report number as assigned by the sponsoring/ monitoring agency, if available, e.g. BRL-TR-829; -215.

12. DISTRIBUTION/AVAILABILITY STATEMENT. Use agency-mandated availability statements to indicate the public availability or distribution limitations of the report. If additional limitations/ restrictions or special markings are indicated, follow agency authorization procedures, e.g. RD/FRD, PROPIN, ITAR, etc. Include copyright information.

13. SUPPLEMENTARY NOTES. Enter information not included elsewhere such as: prepared in cooperation with; translation of; report supersedes; old edition number, etc.

14. ABSTRACT. A brief (approximately 200 words) factual summary of the most significant information.

15. SUBJECT TERMS. Key words or phrases identifying major concepts in the report.

16. SECURITY CLASSIFICATION. Enter security classification in accordance with security classification regulations, e.g. U, C, S, etc. If this form contains classified information, stamp classification level on the top and bottom of this page.

17. LIMITATION OF ABSTRACT. This block must be completed to assign a distribution limitation to the abstract. Enter UU (Unclassified Unlimited) or SAR (Same as Report). An entry in this block is necessary if the abstract is to be limited.

DISTRIBUTION STATEMENT A. Approved for public release; distribution is unlimited.

Predictive Modeling of Structural Sensing for Aerospace Applications

VICTOR GIURGIUTIU
UNIVERSITY OF SOUTH CAROLINA
phone: 803 777 8018 fax: 803 777 0106 email: victorg@sc.edu
Award Number: FA9550-11-1-0133
http://www.me.sc.edu/research/lamss/

SUMMARY

A methodology for multi-scale multi-domain predictive simulation of structural sensing in metallic aerospace structures was developed. The methodology is able to predict the signal response of structural sensors as a function of the structural state and/or the presence of structural flaws or damage, in linear and nonlinear regimes. The approach has been to combine analytical solutions with numerical analysis (e.g., finite element method, FEM) into a hybrid global-local (HGL) analysis. This novel approach allows one to keep the computational effort at a manageable level while preserving the fidelity needed to capture the local interaction between ultrasonic guided waves and structural damage.

The major achievements of this project are:

- One to two orders of magnitude increase in computational speed compared with conventional FEM modeling of wave propagation in interaction with damage
- Development of an unique analytical framework and predictive tool for simulation of multi-modal guided wave propagation and interaction with damage – WaveFormRevealer for both straight-crested (WFR-1D) and circular-crested (WFR-2D) guided Lamb waves
- Inclusion of multi-physics piezoelectric effects in both analytical and FEM models for both axial-active and shear-active piezoelectric wafer active sensors (PWAS)
- Novel combination of time-domain and frequency-domain approaches to the HGL implementation
- Development, for the first time, of nonreflective boundaries (NRB) for Lamb wave FEM modeling
- Efficient extraction of wave-damage interaction coefficients (WDIC) from small NRB FEM local models
- Modeling of nonlinear higher-harmonics wave-damage interactions in cracks and joints using nonlinear FEM

This fundamental research project has high relevance to USAF because it has produced a methodological framework for coupling global and local models to achieve the concurrent analysis of the structure in interaction with coupled-field phenomena and efficient treatment of nonlinearities.

The results of this project can be used to generate virtual data sets for testing data-driven models and filling data gaps will allow the autonomous model updating of the "digital-twins" models to predict future performance for new mission profiles.

LONG-TERM GOAL

- Predict the signal response of structural sensors as a function of the structural state and/or the presence of structural flaws or damage for aerospace applications

OBJECTIVES

- Develop a predictive methodology for multi-scale multi-domain modeling of structural sensing
- Develop linear and nonlinear finite element local model for wave-damage interaction
- Validate and verify (V&V) through experiments on geometrically tractable specimens

APPROACH

Our approach has been to combine analytical solutions with numerical analysis (e.g., finite element method, FEM) into a hybrid global-local (HGL) analysis. This is a novel approach, which allows one to keep the computational effort at a manageable level while preserving fidelity. The performed work consisted of three tasks covering a 4-year period:

Project tasks scheduled over 4 years

Tasks	Year 1	Year 2	Year 3	Year 4
1. Nonlinear analytical models for localized structural sensing				
2. Hybrid global-local (HGL) predictive modeling of large-area structural sensing				
3. Verification and validation (V&V)				

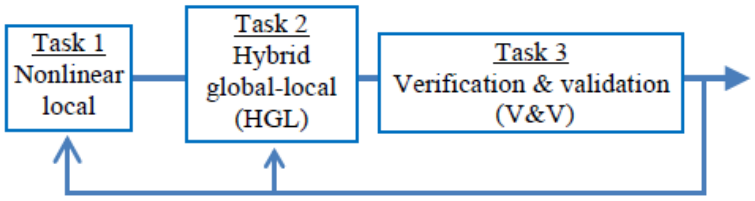

The scope of Task 1 was to develop reduced-order analytical models of structural sensing in the presence of nonlinearities in damaged material regions and/or structural joints/interfaces. The reduced order models have adjustable parameters and nonlinearity thresholds to be used as control variables. These models are able to predict higher harmonic response resulting from guided waves interacting with damage. The reduced-order nonlinear models developed in this task are incorporated in the HGL analysis to be performed in the next task.

Task 2 pursued the integration between analytical solutions in the global region and numerical solutions (e.g., FEM) in discretized local regions drawn around structural features, damage sites, sensor attachments, etc. The main difference between the prediction work done in this task and that done in Task 1 is that of scale of complexity. The present task addresses the challenges associated with the analysis of realistically sized specimens with the structural complexity representative of actual aerospace structures. This task went beyond the state of the art and achieved an HGL modeling with the following attributes: (a) 2-D guided waves travelling in thin-wall structures typical of aerospace applications; (b) local-global boundary of generic shape based on Saint- Venant's principle; (c) generalized matching condition on the global-local boundary; (d) zoom-in/zoom-out capabilities; (e) reduced-order nonlinearity treatment.

Task 3 verified that the methodology developed in the previous two tasks gives accurate and trustworthy results and will validate that this methodology can be applied to solving actual problems of interest to AFRL. The results of this V&V procedure were used as feedback to improve the approach taken in the previous Task 1 and Task 2.

WORK COMPLETED

All the work planned in this project has been completed.

- Fast analytical modeling of guided waves propagation (WFR-1D and WFR-2D algorithms)
- 1D and 2D hybrid global-local (HGL) algorithm for ultrasonic wave propagation in structures with damage and discontinuities
- Nonlinear FEM analysis of guided wave interaction with damage

RESULTS

The scientifical and technical results of this project are described in full detail in the 11 refereed archival journal articles attached to this report and will not be repeated here for the sake of brevity.

MAJOR ACHIEVEMENTS

The major achievements of this project are:

- One to two orders of magnitude increase in computational speed compared with conventional FEM modeling of wave propagation in interaction with damage
- Development of an unique analytical framework and predictive tool for simulation of multi-modal guided wave propagation and interaction with damage – WaveFormRevealer for both straight-crested (WFR-1D) and circular-crested (WFR-2D) guided Lamb waves
- Inclusion of multi-physics piezoelectric effects in both analytical and FEM models for both axial-active and shear-active piezoelectric wafer active sensors (PWAS)
- Novel combination of time-domain and frequency-domain approaches to the HGL implementation
- Development, for the first time, of nonreflective boundaries (NRB) for Lamb wave FEM modeling
- Efficient extraction of wave-damage interaction coefficients (WDIC) from small NRB FEM local models
- Modeling of nonlinear higher-harmonics wave-damage interactions in cracks and joints using nonlinear FEM

IMPACT/APPLICATIONS

The impact of this project consists in the following contributions made to the fundamental scientific understanding of this area of research:

(a) Physics-based understanding of SHM detection process
(b) Foundation for solving the inverse problem to determine structural state from sensor signals

PUBLICATIONS

This project has generated a large number of publications: **7 peer-reviewed archival journal articles** and **20 conference papers** as listed below (the J and C numbers are the journal article and conference paper number found on the LAMSS websites http://www.me.sc.edu/research/lamss/html/journals.html and http://www.me.sc.edu/research/lamss/html/conferences.html , respectively):

The list of peer-reviewed archival journal articles and conference papers follows. Copies of selected archival peer-reviewed journal articles resulting from this grant are attached at the end.

Peer-reviewed Archival Journal articles

1. J100 Shen, Y.; Giurgiutiu, V. (2015) "Effective non-reflective boundary for Lamb waves: theory, finite element implementation, and applications", *Wave Motion* (in press)
2. J95 Kamal, A.; Giurgiutiu, V. (2014) "Shear horizontal wave excitation and reception with shear horizontal piezoelectric wafer active sensor (SH-PWAS)" Smart Materials and Structures, 23 085019 doi:10.1088/0964-1726/23/8/085019
3. J94 Shen, Y.; Giurgiutiu, V. (2014) "WaveFormRevealer: An analytical framework and predictive tool for the simulation of multi-modal guided wave propagation and interaction with damage", Structural Health Monitoring – An International Journal, Vol. 13, No. 5, pp. 491-511, online May 2014, doi: 10.1177/1475921714532986
4. J93 Shen, Y.; Giurgiutiu, V. (2014) "Predictive Modeling of Nonlinear Wave Propagation for Structural Health Monitoring with Piezoelectric Wafer Active Sensors", Journal of Intelligent Material Systems and Structures, Aug. 2013, DOI 10.1177/1045389X13500572, jim.sagepub.com, Jan 2014 in print Vol. 25, No. 4, pp. 506-520
5. J92 Kamal, A.; Lin, B.; Giurgiutiu, V. (2014) "Exact Analytical Modeling of Power and Energy for Multimode Lamb Waves Excited by Piezoelectric Wafer Active Sensors", Journal of Intelligent Material Systems and Structures, first published on August 14, 2013 as doi:10.1177/1045389X13498310, Jan. 2014 in print Vol. 25, No. 4, pp. 452-471
6. J89 Gresil, M; Giurgiutiu, V (2013) "Time-Domain Global-Local Prediction of Guided Waves Interaction with Damage", Key Engineering Materials, Vol. 558 (2013), pp. 116-127
7. J88 Gresil, M; Giurgiutiu, V (2013) "Time-Domain Hybrid Global-Local Concept for Guided-Wave Propagation with Piezoelectric Wafer Active Sensor", Journal of Intelligent Material Systems and Structures, Vol. 24, No. 15, pp. 1897-1911, 2013, doi: 10.1177/1045389x13486712

Conference papers

1. C231 Kamal, A.; Giurgiutiu, V. (2014) "Analytical Study Guideline for Structural Health Monitoring of Steel Canister in Dry Cask Storage System by Using Multimodal Ultrasonic Lamb Waves" ICAPP 2014 International Congress on Advances in Nuclear Power Plants, April 6-9, 2014, Charlotte, NC
2. C228 Kamal, A. M.; Giurgiutiu, V. (2014) "Stiffness Transfer Matrix Method (STMM) for stable dispersion curves solution in anisotropic composites", SPIE Vol. 9064, paper number 9064-39
3. C227 Shen, Y.; Giurgiutiu, V. (2014) "WFR-2D: an analytical model for PWAS-generated 2D ultrasonic guided wave propagation", SPIE Vol. 9064, paper number 9064-40
4. C225 Shen, Y.; Bao, J.; Giurgiutiu, V. (2013) "Health Monitoring of Aerospace Bolted Lap Joints Using Nonlinear Ultrasonic Spectroscopy: Theory and Experiments", 9th International Workshop on Structural Health Monitoring, IWSHM, Sept. 10-12 2013, Stanford University, CA, pp. 2333-2340
5. C223 Kamas, T.; Giurgiutiu, V.; Lin, B. (2013) "Analytical Modeling of Proof-Mass Piezoelectric Wafer Active Sensor for Symmetric Lamb Waves Tuning", 9th International Workshop on Structural Health Monitoring, IWSHM, Sept. 10-12, 2013, Stanford University, CA, pp. 1494-1501
6. C222 Kamal, A.; Lin, B.; Giurgiutiu, V. (2013) "Optimizing Mode Tuning of Guided Waves and PWAS Electromechanical Impedance for Power Efficient SHM systems", 9th International Workshop on Structural Health Monitoring, IWSHM, Sept. 10-12 2013, Stanford University, CA, pp. 1479-1486

7. C221 Giurgiutiu, V. (2013) "Recent PWAS-SHM Developments in the Laboratory for Active Materials and Smart Structures", ASME pressure vessels and piping conference, July 14-18, 2013, Paris, France, PVP2013-97523
8. C219 Kamal, A.; Gresil, M.; Giurgiutiu, V. (2013) "Shear Horizontal Guided Waves in Laminated Composite Plates Using SH-PWAS", NDT of Composites, Seattle, WA, May 13-14, 2013
9. C218 Kamal A.; Gresil, M.; Giurgiutiu, V.; (2013) "Comparative Study of Several Methods for the Calculation of Ultrasonic Guided Waves in Composites", 54th AIAA/ASME/ASCE/AHS/ASC Structures, Structural Dynamics, and Materials Conference, April 8-11, 2013, Boston, Massachusetts, Chapter DOI: 10.2514/6.2013-1901
10. C217 Bao, J.; Shen, Y.; Giurgiutiu, V. (2013) "Linear and Nonlinear Finite Element Simulation of Wave Propagation through Bolted Lap Joint", 54th AIAA/ASME/ASCE/AHS/ASC Structures, Structural Dynamics, and Materials Conference, April 8-11, 2013, Boston, Massachusetts, Chapter DOI: 10.2514/6.2013-1902
11. C215 Bao, J.; Giurgiutiu, V. (2013) "Effects of fastener load on wave propagation through lap joint", SPIE 2013 Smart Structures and NDE, 10-14 March 2013, San Diego, CA, SPIE Vol. 8695, 8695-73
12. C214 Shen, Y.; Giurgiutiu, V. (2013) "Modeling of guided waves for detection of linear and nonlinear structural damage", SPIE 2013 Smart Structures and NDE, 10-14 March 2013, San Diego, CA, SPIE Vol. 8695, 8695-64
13. C213 Kamal, A.; Lin, B.; Giurgiutiu, V. (2013) "Predictive Modeling of PWAS-Coupled Shear Horizontal Waves", SPIE2013 Smart Structures and NDE, 10-14 March 2013, San Diego, CA, SPIE Vol. 8695, paper 8695-16
14. C211 Kamas, T.; Lin, B.; Giurgiutiu, V. (2013) "Analytical modeling of PWAS in-plane and out-of-plane electromechanical impedance spectroscopy (EMIS)", SPIE 2013 Smart Structures and NDE, 10-14 March 2013, San Diego, CA, SPIE Vol. 8692, paper 8692-74
15. C210 Gresil, M.; Giurgiutiu, V.; (2012) "Time-domain hybrid global-local prediction of guided waves", Asia-Pacific Workshop on Structural Health Monitoring, Melbourne, Australia, December 2012
16. C207 Shen, Y.; Giurgiutiu, V.; (2012) "Simulation of Interaction between Lamb Waves and Cracks for Structural Health Monitoring with Piezoelectric Wafer Active Sensors", ASME 2012 Conference on Smart Materials, Adaptive Structures, and Intelligent Systems SMASIS, Sept. 19-21, 2012, Stone Mountain, GA, paper SMASIS2012-7917
17. C201 Gresil, M.; Giurgiutiu, V.; Shen, Y.; Poddar, B (2012) "Guidelines for Using the Finite Element Method for Modeling Guided Lamb Wave Propagation in SHM Processes", 6th European Workshop on Structural Health Monitoring,3-6 July 2012, Dresden, Germany, paper # Tu.2.E.1
18. C200 Gresil, M.; Giurgiutiu, V.; Shen, Y (2012), "Predictive Simulation of Structural Sensing", 53rd AIAA Structures, Structural Dynamics, and Materials Conference, 23 April 2012, Honolulu, Hawaii, CID: 1215950
19. C196 Shen, Y.; Giurgiutiu, V. (2012) "Predictive Simulation of Nonlinear Ultrasonics", SPIE 2012 Smart Structures and NDE, 11-15 March 2012, San Diego, CA, SPIE Vol. 8348, paper 8348-86
20. C195 Giurgiutiu, V. (2011) "Structural Health Monitoring and Damage Detection with Piezoelectric Wafer Active Sensors", 14th Asia Pacific Vibration Conference (14th APVC), 5-8 Dec. 2011, Hong Kong Polytechnic University, Hong Kong

Original Article

Journal of Intelligent Material Systems and Structures

Journal of Intelligent Material Systems and Structures
24(15) 1897–1911
© The Author(s) 2013
Reprints and permissions:
sagepub.co.uk/journalsPermissions.nav
DOI: 10.1177/1045389X13486712
jim.sagepub.com
SAGE

Time-domain hybrid global–local concept for guided-wave propagation with piezoelectric wafer active sensor

Matthieu Gresil and Victor Giurgiutiu

Abstract

This article presents a combined finite element method and analytical process to predict the one-dimensional guided-wave propagation for nondestructive evaluation and structural health monitoring application. Analytical methods can perform efficient modeling of wave propagation but are limited to simple geometries. In response to today's most complex cases not covered by the simulation tools available, we aim to develop an efficient and accessible tool for structural health monitoring application. This tool will be based on a hybrid coupling between analytical solution and time-domain numerical codes. Using the principle of reciprocity, global analytical calculation is coupled with local finite element method analysis to utilize the advantages of both methods and obtain a rapid and accurate simulation method. The phenomenon of interaction between the ultrasonic wave, the defect, and the structure, leading to a complex signature, is efficiently simulated by this hybrid global–local approach and is able to predict the specific response signal actually received by sensor. The finite element mesh is used to describe the region around the defects/flaws. In contrast to other hybrid models already developed, the interaction between Lamb waves and defects is computed in the time domain using the explicit solver of the commercial finite element method software ABAQUS.

Keywords

Lamb waves, finite element modeling, global–local, structural health monitoring, piezoelectric wafer active sensors

Introduction

Guided-wave techniques for nondestructive evaluation (NDE) and structural health monitoring (SHM) applications are increasingly popular due to their ability to cover large areas with a relatively small number of sensors. Miniaturized guided-wave transducers, such as piezoelectric wafers attached directly to structural elements, have gained large popularity due to their low cost, simplicity, and versatility. These transducers can actively interrogate the structure using a variety of guided-wave methods such as pitch–catch, pulse-echo, phased arrays, and electromechanical (E/M) impedance technique. SHM is an emerging technology with multiple applications in the evaluation of critical structures. Numerous approaches have been utilized in recent years to perform SHM. One of the promising active SHM methods utilizes arrays of piezoelectric wafer active sensors (PWASs) bonded to a structure in order to achieve damage detection. The objective of this article is to present the framework for the development of a methodology for multi-scale multi-domain predictive simulation of structural sensing. Such methodology would be able to predict the signal response of structural sensors as a function of the structural state and/or the presence of structural flaws or damage in linear and nonlinear regimes.

Many authors have already investigated the interaction of Lamb modes with a single-defect-like crack, notch, or circular cavity. Some of them used analytical (Grahn, 2003) or semi-analytical resolutions (Castaings et al., 2002), whereas others chose a finite element (FE), a boundary element modeling, or spectral element method (Alleyne and Cawley, 1992; Diligent et al., 2001; Galan and Abascal, 2005; Giurgiutiu et al., 2012; Gresil et al., 2011a, 2011d; Guo and Cawley, 1993; Peng et al., 2009). Analytical or semi-analytical resolutions can be used when the geometry of the defect is regular and when the problem presents symmetries

Laboratory for Active Materials and Smart Structures (LAMSS), Department of Mechanical Engineering, University of South Carolina, Columbia, SC, USA

Corresponding author:
Matthieu Gresil, Laboratory for Active Materials and Smart Structures (LAMSS), Department of Mechanical Engineering, University of South Carolina, Columbia, SC 29208, USA.
Email: matthieu@mailbox.sc.edu

except for the distributed point source method (DPSM)-based semi-analytical technique (Banerjee and Kundu, 2008) when an internal anomaly was immersed in fluid. FE or boundary element modeling allows studying the interaction of Lamb modes with irregular defects but requires respecting spatial and temporal discretization that can cause numerical problems at high frequency–thickness product. In addition, to obtain accurate wave propagation solution at ultrasonic frequencies is computationally intensive and may become prohibitive for realistic structures.

The need for a predictive modeling methodology that could relate directly the presence of structural flaws to changes in the signal of structural sensors is apparent. Such predictive methodology would be able to simulate various structural scenarios (configuration changes, different flaws, temperature changes, etc.). A predictive modeling methodology would enable identifying the sensors' sensitivity and specificity to structural changes (intentional or accidental), determining best sensor placement layout, running parameter studies, and so on. To date, such a predictive modeling methodology does not exist, although some initial attempts have been made in simple cases by using finite element method (FEM) (Blackshire et al., 2006; Gresil et al., 2011b, 2011c, 2012; Kitts and Zagrai, 2009; Olson et al., 2006) and model updating (Zagrai et al., 2010). A major difficulty in developing a predictive modeling methodology for structural sensing is related to the multi-scale multi-domain aspects of the problem. The problem is multi-scale because it has to incorporate (a) the macroscale structural features, (b) the microscale flaw/damage, and (c) the mesoscale interfaces between structural parts and between sensor and structure. The modeling is multi-domain because the analysis is integrated over several physical domains, that is, (a) aerospace structural mechanics, (b) E/M transduction in the sensors, (c) guided-wave ultrasonics, (d) power and signal electronics, and so on (Figure 1). Our approach would be to combine them all into an integrated multi-scale multi-domain analysis.

It is apparent that simply bolting together existing software codes (multi-physics FEs, ultrasonics modeling, electronic circuit modeling) is not a credible option without an understanding of the interaction between the multi-domain variables native in each code and the multi-scale aspects of the problem. Fundamental studies are needed to clarify the multi-scale multi-domain interaction between structure, sensors, guided-wave patterns, damage progression, and signal processing and interpretation. In this way, one would achieve an understanding of the hierarchical variables interplay, designation of what variables need to be passed between physical domains/codes, and an understanding of how multiple scales are to be addressed.

A hybrid formulation is used wherein the FEM is employed to model small regions near the defect, whereas regions away from the defect are modeled using a suitable set of wave functions. Goetschel et al. (1982) developed a global–local FE formulation for modeling axisymmetric scattering of a steady, compressive, incident elastic wave in a homogeneous, isotropic host medium with an axisymmetric inclusion. In the area of SHM of aircraft components, the method has been applied to model wave interaction with defected lap–shear joints (Chang and Mal, 1995), as well as notches in plates (Mal and Chang, 2000). Many aircraft components are complex in either their geometry or their material properties. In this case, theoretical wave solutions for the global portion are either nonexistent or hard to determine. The semi-analytical finite element (SAFE) method can help handle these cases because of its ability to extract modal solutions of complex structures in a computationally efficient manner (Bartoli et al., 2005; Hayashi, 2004; Hayashi et al., 2003, 2006). Sabra et al. (2008) demonstrated the application of the SAFE-aided hybrid formulation to the detection of holes in aluminum plates. Srivastava (2009) extends the

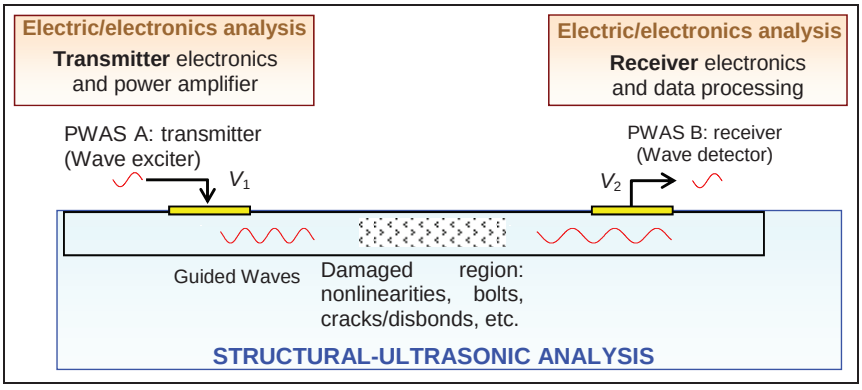

Figure 1. Conceptual schematic of a multi-scale multi-domain study: structural ultrasonics and electric/electronic parts of the analysis are indicated. Our approach would be to combine them all into an integrated multi-scale multi-domain analysis.
PWAS: piezoelectric wafer active sensor.

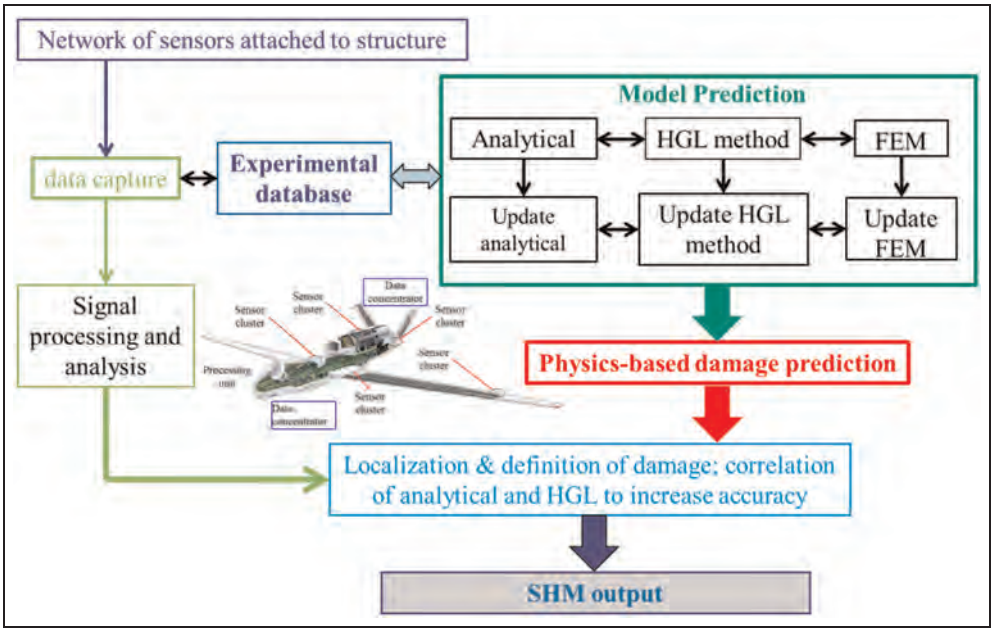

Figure 2. Structural health monitoring functional diagram shows the importance of the model prediction to obtain accurate results for the SHM output.
HGL: hybrid global–local; FEM: finite element method; SHM: structural health monitoring.

global–local approach to model notches in aluminum plates and delamination-like defects in composite panels. The SAFE approach has been previously developed for ultrasonics waveguides of complicated geometries, such as concrete reinforcing bars, tendons, track rails, one-dimensional (1D) stiffeners, and so on (Bartoli et al., 2005; Loveday, 2008; Marzani et al., 2008). In the SAFE approach, the 1D wave propagation along the waveguide is modeled analytically, whereas the waveguide modes are found numerically through FEM discretization of the cross section.

Figure 2 shows the SHM functional diagram to achieve a great accuracy of the output in order to minimize false alert on this system. This model prediction is based on the correlation between the analytical calculation, the FEM, and the hybrid global–local (HGL) results. Then, the physics-based prediction is compared and updated with the experimental database in order to obtain a damage definition with a high level of accuracy.

This article presents and discusses the challenges and opportunities related to the use of PWAS transducers in generating and sensing ultrasonic guided waves in structure and how they can be used to detect damage. This article starts with the principles of the HGL concept and then reviews the general principles of PWAS-based SHM. It discusses the analytical and FEM modeling of pitch–catch ultrasonic waves between a transmitter PWAS (T-PWAS) and a receiver PWAS (R-PWAS). Then, it compares the received signal between the analytical, the HGL, and the experimental results.

This article addresses these fundamental research gaps and strives to develop an overall methodology for multi-scale multi-domain modeling of structural sensing. The methodology will be first validated on benchmark examples that are simple to understand but sufficiently representative to convey the concept. A HGL approach is developed to keep the computational resources manageable.

HGL principles

A HGL approach will be developed to keep the computational resources manageable. The HGL approach uses local FEM discretization only in the critical regions (structural joints, discontinuities, flaws, etc.) while using global analytical solutions in the uniform outside region. Srivastava (2009) used the HGL approach to model the effect of notches and delamination in 1D waveguides. Figure 3 illustrates this concept, whereby only the local material region close to the defect needs to be FEM modeled, whereas the global waveguide to the left and right of the FEM region is modeled semi-analytically.

In contrast to other hybrid models already presented in the literature by Srivastava (2009), this article presents the Lamb waves propagation in time domain. Moreover, the SAFE method involves a FE computation in the guide section for the global part that is slower than the analytical model developed in this article. Another potential disadvantage of the SAFE method, used by Srivastava (2009), is that the necessary specialized elements are not available as standard in

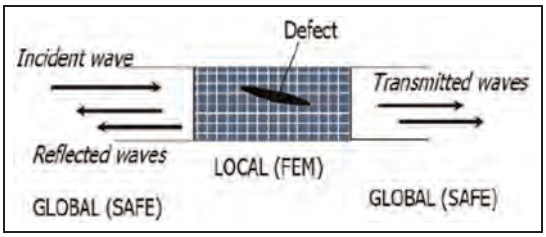

Figure 3. Waveguide scattering problem in 1D solved by the hybrid global–local (HGL) method in frequency domain (Srivastava, 2009).
FEM: finite element method; SAFE: semi-analytical finite element.

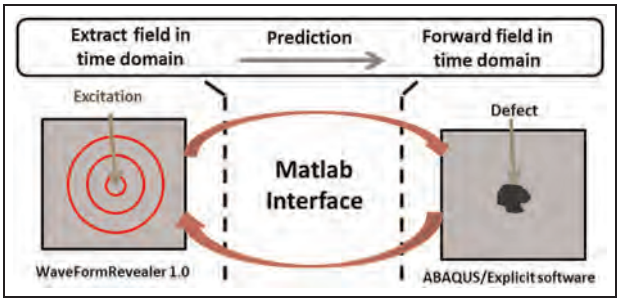

Figure 4. Illustration of our procedure to obtain time-domain model interface.

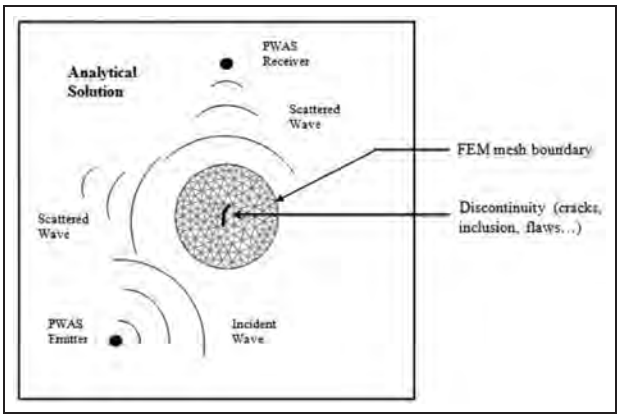

Figure 5. General 2D setup for hybrid global–local modeling of structural sensing.
FEM: finite element method; PWAS: piezoelectric wafer active sensor.

many commercial FEM packages and may need to be defined by the user. The SAFE method includes the wave propagation as a complex exponential in the element formulation, and therefore, only a two-dimensional (2D) mesh of the cross section of the waveguide is required.

As shown in Figure 4, our model consists of one analytical model (not semi-analytical as compared to Srivastava (2009)), that is, WaveFormRevealer (WFR; Gresil et al., 2011b), and FEM domain, and connected by a hybrid interface. This interface is based on input stresses and displacements monitored at a rectangular "box" surrounding the source in a time domain and then used to predict the forward field quantities. Since this interface was separately coded up, it did not require the modification of the basic FEM program, thus exemplifying a generic hybrid modeling paradigm. However, for application to practical Lamb wave inspection, it was essential for the method to be extended to work in the time domain. This is achieved by the use of inverse Fourier transforms, which also help retain the power and versatility of the method. The analytical frequency interface is used to obtain predictions at a number of frequencies within a required bandwidth, and these can then be inverse transformed to obtain the time-domain signals. Thus, the original frequency-domain interface remains at the core of the new time-domain hybrid interface, and it is now simply located within an additional frequency loop. In the section "Results and discussion," we consider a simple application example that serves to demonstrate the approach, helps appreciate important features and limitations, and also seeks validation in the process.

This new approach is realized in three steps using our propriety analytical software WFR and commercial FEM software. The first step of this method consists of using the WFR software developed for this application. The second step consists of using the output from the WFR software as two inputs (one for the symmetric mode and the second for the antisymmetric mode) to the FEM model. The third step of this method consists of using again the WFR software developed for this application. The FEM output serves as input into the global region. This hybrid global–local–global received PWAS signal will be compared with our homemade analytical model and experimental results in the last section. Compared to usual FEM model, the main advantage of the hybrid method is to reduce meaningfully the length of the mesh used to investigate the interaction of Lamb modes with defects and hence the computing time.

In our future approach, the HGL method from 1D geometries will be developed into 2D geometries. This is not an easy task because the 1D interface conditions of Figure 3 are much easier to formulate than the fully 2D conditions illustrated in Figure 5. The waves originating from the T-PWAS propagate in circular wave fronts toward the local region containing the discontinuity under investigation (crack, inclusion, flaw, etc.). The incoming waves enter the circumferential boundary of the local region and interact with the FEM model generating a complicated scattering pattern due to the presence of the discontinuity inside the FEM model. The scattered waves will be picked up by the R-PWAS (as well as by the T-PWAS acting in pulse-echo mode). If the discontinuity is not present inside the FEM model, then no wave scatter should take place.

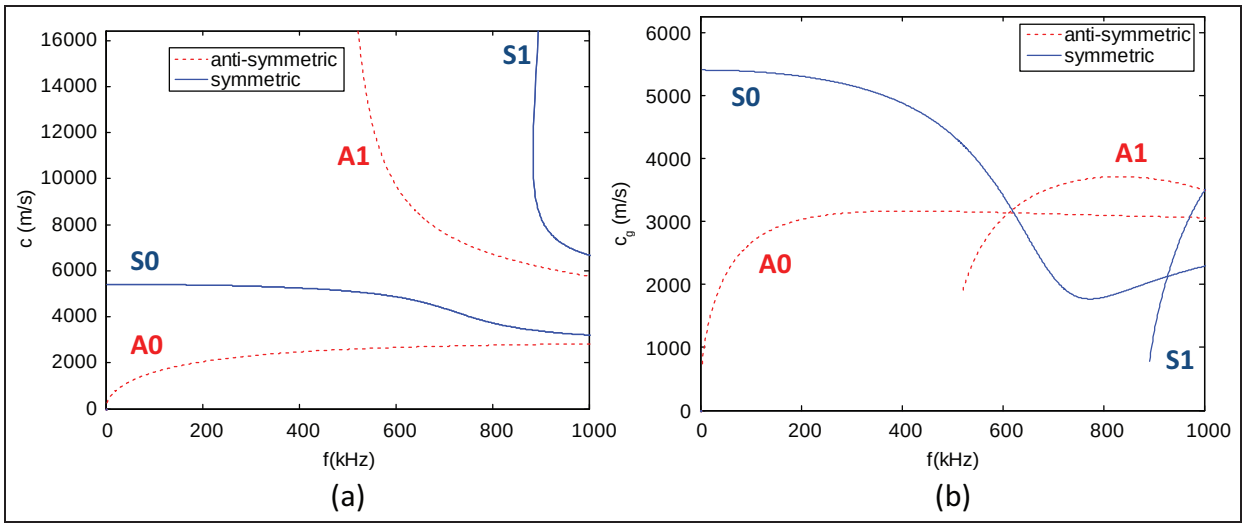

Figure 6. Dispersion curves for 3.2-mm-thick aluminum plate: (a) phase velocity curves and (b) group velocity curves.

However, it is quite possible that numerical artifacts associated with the FEM discretization will generate scatter even in a defect-free situation. The existence of such false-scatter artifacts will be an indication of deficient numerical modeling that needs to be corrected. Therefore, a possible figure of merit of the HGL modeling will be the relative smallness of the residual wave scattering in the case of a defect-free FEM region. Another possible figure of merit of our modeling would be the energy balance between incoming and outgoing wave fronts. It is expected that a major part of our effort will be concentrated on developing the proper interfacing formulation for the fully 2D analytical solution of guided-wave propagation in circular–radial geometry in interaction with the FEM model developed for the local region.

Background information

Fundamental Lamb waves

Guided waves or Lamb waves are formed by the interference of multiple reflections and mode conversions of longitudinal and shear waves at the free surfaces of a plate. These waves are typically generated and detected using conventional PWASs and are used to detect defects and measure elastic properties of thin isotropic aluminum materials. Two types of waves propagate a symmetric wave and an antisymmetric wave. Each of these wave types propagates with multiple modes.

By solving a boundary value problem for a free plate or by considering the reflection of waves at plate boundaries, the Rayleigh–Lamb frequency equations (dispersion equations) can be found (Achenbach, 1973; Auld, 1973; Rose, 1999; Viktorov, 1967). For a uniform traction-free isotropic plate, the equations for symmetric and antisymmetric modes are

$$\frac{\tan(qh)}{\tan(ph)} = -\frac{4k^2pq}{(q^2-k^2)^2}, \quad \frac{\tan(qh)}{\tan(ph)} = -\frac{(q^2-k^2)^2}{4k^2pq} \tag{1}$$

where

$$p^2 = \frac{\omega^2}{c_L^2} - k^2, \quad q^2 = \frac{\omega^2}{c_T^2} - k^2, \quad k = \frac{\omega}{c_p} \tag{2}$$

and h, k, c_L, c_T, c_p, and ω are the half-plate thickness, wave number, velocities of longitudinal and transverse modes, phase velocity, and wave circular frequency, respectively.

The phase velocity is found numerically by solving the real roots of the dispersion equation as a function of material properties, frequency, and material thickness. Group velocity dispersion curves are found from the phase velocity (Rose, 1999). Phase and group velocity dispersion curves for a 3.2-mm-thick aluminum plate are shown in Figure 6, where longitudinal and transverse velocities of the plate are equal to 6211 and 3129 m/s, respectively. These curves were generated and plotted using our homemade software "Wavescope" developed using the graphical user interface (GUI) of MATLAB. Figure 6 shows the first two symmetric and antisymmetric mode dispersion curves. At low frequencies, the wave velocity of the first symmetric mode (S0) is nearly nondispersive, while the wave velocity of the first antisymmetric mode (A0) is highly dispersive. At higher frequencies, group velocity of both zero-order modes approaches the Rayleigh wave velocity, c_R, which has a value of ~2.9 km/s for aluminum.

PWASs

Pitch–catch method is a fundamental way of detecting the structural changes that take place between a

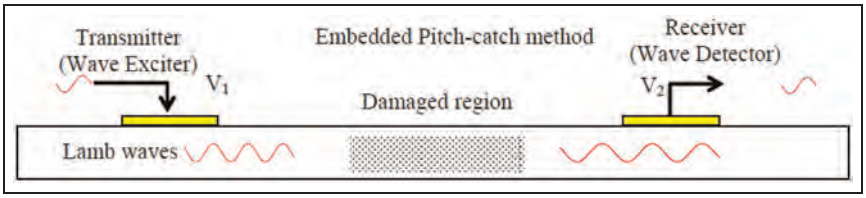

Figure 7. Pitch–catch configuration.

transmitter transducer and a receiver transducer; pitch–catch has been widely used in SHM and NDE. A diagnosis could be made by comparing the time of flight (TOF) and amplitude between the sensing signal and the pristine signal. A standard pitch–catch setup is shown in Figure 7.

One PWAS serves as the transmitter transducer, which excites the plate and generates a disturbance in the plate structure. The disturbance propagates along the plate. The second PWAS acts as the receiver, which picks up the signal at the sensing point, converting mechanical signal into electric signal.

PWASs are the enabling technology for active SHM systems. PWAS couples the electrical and mechanical effects (mechanical strain, S_{ij}, mechanical stress, T_{kl}, electrical field, E_k, and electrical displacement, D_j) through the tensorial piezoelectric constitutive equations

$$\begin{aligned} S_{ij} &= s^E_{ijkl} T_{kl} + d_{kij} E_k \\ D_j &= d_{jkl} T_{kl} + \varepsilon^T_{jk} E_k \end{aligned} \tag{3}$$

where s^E_{ijkl} is the mechanical compliance of the material measured at zero electric field ($E = 0$), ε^T_{jk} is the dielectric permittivity measured at zero mechanical stress ($T = 0$), and d_{jkl} represents the piezoelectric coupling effect. PWASs utilize the d_{31} coupling between in-plane strains, S_1 and S_2, and transverse electric field, E_3. Just like conventional ultrasonic transducers, PWASs utilize the piezoelectric effect to generate and receive ultrasonic waves. However, PWASs are different from conventional ultrasonic transducers in several aspects:

- PWASs are firmly coupled with the structure through an adhesive bonding, whereas conventional ultrasonic transducers are weakly coupled through gel, water, or air.
- PWASs are nonresonant devices that can be tuned selectively into several guided-wave modes, whereas conventional ultrasonic transducers are resonant narrow-band devices.
- PWASs are inexpensive and can be deployed in large quantities on the structure, whereas conventional ultrasonic transducers are expensive and used one at a time.

PWAS transducers can be served several purposes (Giurgiutiu, 2008): (a) high-bandwidth strain sensors, (b) high-bandwidth wave exciters and receivers, (c) resonators, and (d) embedded modal sensors with the E/M impedance spectroscopy method. By application types, PWAS transducers can be used for (a) active sensing of far-field damage using pulse-echo, pitch–catch, and phased-array methods, (b) active sensing of near field damage using high frequency electromechanical impedance spectroscopy (EMIS) and thickness gage mode, and (c) passive sensing of damage-generating events through detection of low-velocity impacts and acoustic emission at the tip of advancing cracks.

The main advantage of PWASs over conventional ultrasonic probes is in their small size, lightweight, low profile, and small cost. In spite of their small size, PWASs are able to replicate many of the functions performed by conventional ultrasonics probes.

Tuning of Lamb waves and PWAS transducers

The tuning between PWAS transducers and guided waves in isotropic metallic plates is relatively well understood and modeled (Giurgiutiu, 2008). The gift of the concept is that manipulation of PWAS size and frequency allows for selective preferential excitation of a certain guided-wave modes and the rejection of other guided-wave modes, as needed by the particular SHM application.

The tuning formula for the case of ideal bonding is defined by (Giurgiutiu, 2008)

$$\varepsilon_x(x,t) = -\frac{a\tau_0}{\mu} \left[\sin\left(\xi^S a\right) \frac{N_S\left(\xi^S\right)}{D'_S\left(\xi^S\right)} e^{i\left(\xi^S x - \omega t\right)} + \sin\left(\xi^A a\right) \frac{N_A\left(\xi^A\right)}{D'_A\left(\xi^A\right)} e^{i\left(\xi^A x - \omega t\right)} \right] \tag{4}$$

For simplicity, we have considered only the first symmetric and antisymmetric modes. N_S, N_A, D_S, and D_A are defined in the study by Giurgiutiu (2008). An example of PWAS tuning is presented in Figure 8 for a 7-mm square PWAS installed on a 3.2-mm aluminum alloy 2024-T3 plate.

Analytical model for the global domain

The analytical modeling of the pitch–catch process between two PWAS transducers separated by a distance x was carried out in frequency domain in four steps (Gresil et al., 2011a, 2011b):

- Fourier transform the time-domain excitation signal $V_e(t)$ taken into the frequency-domain spectrum, $\tilde{V}_e(\omega)$
- Calculate the frequency-domain structural transfer function at the receiver location, $G(x, \omega)$
- Multiply the structural transfer function by frequency-domain excitation signal to obtain the frequency-domain signal at the receiver, that is, $\tilde{V}_r(x, \omega) = G(x, \omega) \cdot \tilde{V}_e(\omega)$
- Perform inverse Fourier transform to obtain the time-domain receiver signal, $V_r(x, t) = IFFT\{\tilde{V}_r(x, \omega)\} = IFFT\{G(x, \omega) \cdot \tilde{V}_e(\omega)\}$.

In this article, the main interest is in symmetric fundamental mode (S0) and antisymmetric fundamental mode (A0). For Lamb waves with only two modes (A0 and S0) excited, the structure transfer function $G(\omega)$ is given by equation (99) (Giurgiutiu, 2008: 327), which gives the in-plane strain at the plate surface as

$$\varepsilon_x(x,t)\Big|_{y=d} = -i\frac{a\tau_0}{\mu}(\sin k^S a)\frac{N_S(k^S)}{D_S'(k^S)}e^{-i(k^S x-\omega t)} - i\frac{a\tau_0}{\mu}(\sin k^A a)\frac{N_A(k^A)}{D_A'(k^A)}e^{-i(k^A x-\omega t)} \quad (5)$$

$$G(\omega) = S(\omega)e^{-ik^S x} + A(\omega)e^{-ik^A x} \quad (6)$$

$$S(\omega) = -i\frac{a\tau_0}{\mu}(\sin k^S a)\frac{N_S(k^S)}{D_S'(k^S)}, \quad A(\omega) = -i\frac{a\tau_0}{\mu}(\sin k^A a)\frac{N_A(k^A)}{D_A'(k^A)} \quad (7)$$

$$D_S(\omega,d) = \left(k^2-\beta^2\right)^2\cos\alpha d\sin\beta d + 4k^2\alpha\beta\sin\alpha d\cos\beta d$$
$$D_A(\omega,d) = \left(k^2-\beta^2\right)^2\sin\alpha d\cos\beta d + 4k^2\alpha\beta\cos\alpha d\sin\beta d \quad (8)$$

$$N_S = k\beta\left(k^2-\beta^2\right)\cos(\alpha d)\sin(\beta d), \quad N_A = k\beta\left(k^2-\beta^2\right)\sin(\alpha d)\cos(\beta d) \quad (9)$$

$$\alpha^2 = \frac{\omega^2}{c_p^2} - k^2, \quad \beta^2 = \frac{\omega^2}{c_s^2} - k^2 \quad (10)$$

where a is the half length of the PWAS, d is the half thickness of the plate; τ_0 is the shear stress between PWAS and the plate; μ is Lame's constant; k^S and k^A are the wave numbers for S0 and A0, respectively; x denotes the distance between the two PWAS transducers; k represents the wave number for S0 or A0 accordingly; and c_p and c_s are the wave speed for pressure wave and shear wave, respectively. In the transfer function, it could be observed that $S(\omega)$ and $A(\omega)$ will determine the amplitude of S0 and A0 modes. In both $S(\omega)$ and $A(\omega)$ terms, there is $\sin(k^S a)$ and $\sin(k^A a)$, which represent the tuning effect.

The wave speed dispersion curve is obtained by solving Rayleigh–Lamb equations (1), which are transcendental equations that require numerical solution. The usual form of Rayleigh–Lamb equations (1) expressed as

$$D_S(\omega, d) = 0 \quad \text{and} \quad D_A(\omega, d) = 0 \quad (11)$$

After getting the wave speed dispersion curve, the wave number for each frequency component, that is, $\xi = \omega/c$, is known. Thus, all the terms involved in the plate transfer function could be solved, and the plate transfer function $G(\omega)$ is obtained. After the plate transfer function $G(\omega)$ is obtained, the excitation signal is Fourier transformed.

The software program WFR has been developed in MATLAB GUI environment to predict the waveform of the analytical modeling. The WFR software is described in detail in the study by Shen and Giurgiutiu (in press). This software allows users to get the desired analytical solution by inputting material properties, specimen geometry, excitation signal count number, excitation signal frequency, and time range. It can also show a continuous waveform change by clicking on the frequency control slider, which is just like the waveform shown on an oscilloscope when adjusting the excitation signal frequency. The time range to show a waveform could also be set by users through entering the "range" information.

FE model for the local domain

The effectiveness of conventional FE modeling of elastic waves propagating in structural components has been shown in the past. The case of Lamb waves in free plates is a classic example (Alleyne and Cawley, 1990; Moser et al., 1999). The package used in this study, ABAQUS/Explicit, uses an explicit integration based on a central difference method (ABAQUS, 2008). The stability of the numerical solution is dependent upon the temporal and the spatial resolution of the analysis. To avoid numerical instability, ABAQUS/Explicit recommends a stability limit for the integration time step (Moser et al., 1999)

$$\Delta t = \frac{1}{20 f_{\max}} \quad (12)$$

The maximum frequency of the dynamic problem, $f_{\max}$, limits both the integration time step and the element size. The size of the mesh in FE, L_e, is typically derived from the smallest wavelength to be analyzed, $\lambda_{\min}$. For a good spatial resolution, 20 nodes per wavelength are

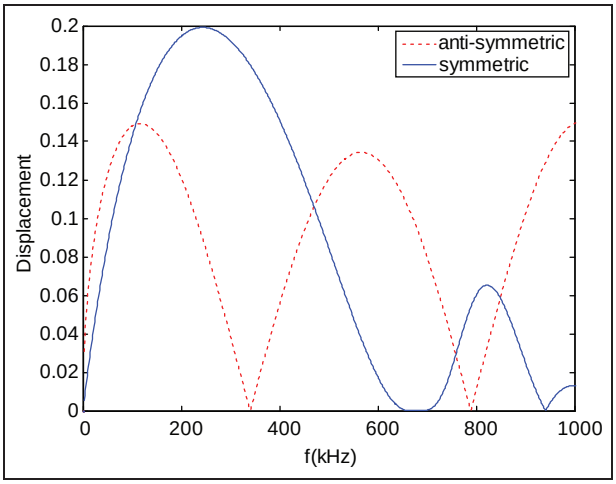

Figure 8. Tuning curves for 3.2-mm-thick aluminum plate.

required (Moser et al., 1999). This condition can be written as

$$L_e = \frac{\lambda_{\min}}{20} \tag{13}$$

To generate the appropriate pure Lamb mode (S0 or A0) in the structure, boundary conditions are imposed on the left of the plate (Figure 9). This simplification is available only for the low frequency. The plate length is defined to prevent that reflections from the edges of the mesh disturb the analysis of the calculated waveforms and is minimized to reduce the computing time.

FEM codes: most commercially available FEM codes have a multi-physics capability. In our preliminary work, we have experimented with ANSYS and ABAQUS capabilities and obtained acceptable results. We were able to simulate both pitch–catch/pulse-echo wave propagation as well as E/M impedance standing waves using direct excitation of the piezoelectric wafer bonded to the structure. During these preliminary studies, some convergence differences between two commercial codes were discovered, whereas the same geometry analyzed with the same element type did not have same convergence characteristics.

One-dimensional wave propagation FEM modeling, which discretizes the local area, is done under the z-invariant (plane-strain) assumption. Hence, only the plate cross section needs to be meshed. For wave propagation modeling, the choice of the solving technique, mesh density, and time step influences the outcomes and level of accuracy with which the phenomenon is simulated. The time-domain explicit solver of the ABAQUS software and the linear quadrilateral CPE4R element were used. We investigated (Gresil et al., 2011b) how the group velocities of the S0 and A0 waves vary with mesh density (nodes per wavelength) $N = \lambda/L$, where λ is the wavelength and L is the size of the element. Figure 10 shows the convergence study using ABAQUS/Explicit for both modes, S0 and A0. For the A0 mode, the error varies from ~4.7% for $N = 25$ to ~0% for $N = 180$. For the S0 mode, the error varies from ~2.2% for $N = 25$ to ~0% for $N = 75$. A mesh density $N = 180$ was chosen, which gives a very good accuracy.

Experimental results

Experimental setup

The test specimen is designed to develop and calibrate the damage detection methodology using a simple geometry specimen and also to validate the analytical and the HGL results. Thin aluminum plate specimens were constructed from 3.2-mm-thick 2024-alloy stock in the form of a square plate ($1118\,\text{mm} \times 1118\,\text{mm} \times 3.2\,\text{mm}$). The specimen is instrumented with arrays of 7-mm square and 7-mm circular PWAS (Figure 11). The (x, y) sensor locations are given in Table 1. The PWAS network is not used for this study particularly but will be used to detect and locate defect in the plate for future study.

An HP33120A arbitrary signal generator is used to generate a 150-kHz windowed harmonic burst excitation to active sensors with a 10-Hz repetition rate. Under harmonic burst excitation, the active sensor generates a package of elastic waves that spread out into the entire plate according to a circular wave front pattern. A Tektronix TDS210 four-channel digital oscilloscope, synchronized with the signal generator, was used to collect the response signals from the active sensors.

The results for the rectangular plate were remarkably clear and easy to interpret. Reflection wave packets could be easily avoided because the edges of the rectangular plate were far away from the source.

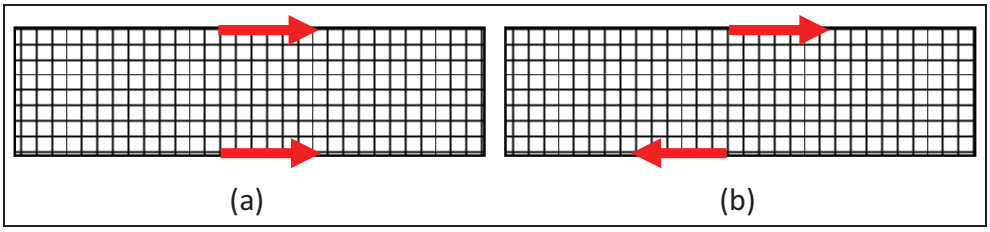

Figure 9. Lamb mode excitation for (a) S0 mode and (b) A0 mode.

Table 1. Locations of PWAS transducers on the square plate specimen.

PWAS#	1	2	3	4	5	6	7	8	9	10	11	12	13	14	15	16
x (mm)	31	31	31	31	51	51	51	51	71	71	71	71	91	91	91	91
y (mm)	31	51	71	91	91	71	51	31	31	51	71	91	91	71	51	31
Square	X	X					X	X			X	X	X	X		
Circular			X	X	X	X			X	X					X	X

PWAS: piezoelectric wafer active sensor.

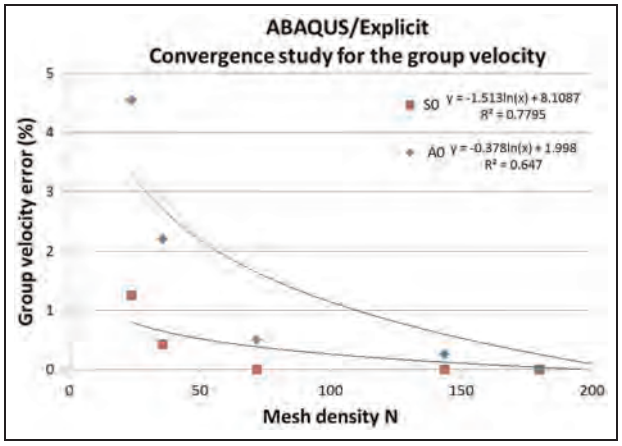

Figure 10. Convergence study of the group velocity for a 2D plane-strain problem in ABAQUS/Explicit. The excitation is modeled by two equilibrated forces.

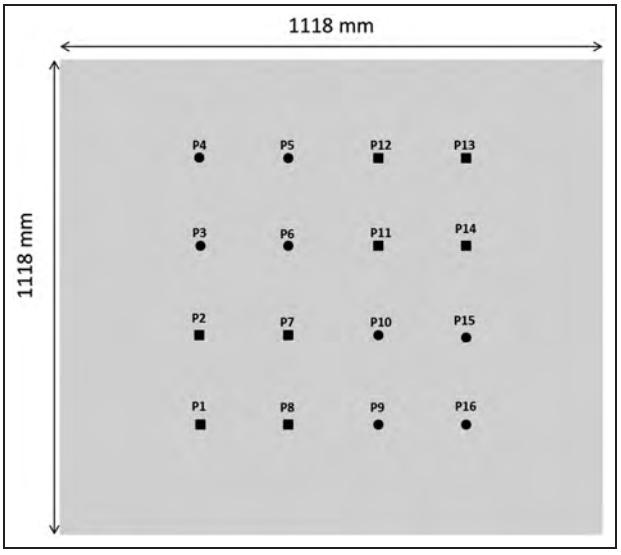

Figure 11. Arrangement of PWAS transducers bonded on the plate.

Comparison of prediction and experiments

Using the principle of reciprocity, global analytical calculation is coupling with the local FEM analysis to utilize the advantages of both methods and obtain a rapid and accurate simulation method. Figure 12 illustrates the HGL setup for this example, whereby only the local material region close to the defect needs to be FEM modeled, whereas the global waveguide to the left and right of the FEM region is modeled analytically with compatibility being ensured at the interface.

The first step of this method consists of using the WFR software developed for this application. The second step consists of using the output from the WFR software as two inputs (one for the S0 mode and the second for the A0 mode) in the FEM model. In order to avoid the reflections from the edges of the FEM domain, the FEM domain was extended outside the 100-mm local region to a total length of 250 mm. Finally, the third step consists of using the output from the FEM as input in the WFR (global 2).

Comparison between analytical, FEM, and HGL

Figure 13 shows the signal received after a travel of 250 mm; the analytical model is compared with the HGL approach and the full FEM model. A very good matching is observed between these three results, which means that the interface between the global 1 and the local do not create scatter or any reflection on the received signal. The signal from the HGL approach will be the input for the global 2 analytical region.

Figure 14 shows the signal received after a travel of 565 mm; the analytical model is compared with the HGL approach and the full FEM model. A very good matching is observed between these three results specifically between the HGL and the analytical results, that means that the two interfaces, that is, between global 1 to local and local to global 2, do not create interference or any reflection on the received signal. As shown in Figures 13 and 14, the received signal with the HGL method in time domain gives us a rapid and accurate simulation method.

The analytical resolution can be used when the geometry of the specimen is regular and when the problem presents symmetries. The analytical approach gives us the capacity to create very simple damage in comparison of the FEM advantage that gives us the capability to integrate complex and irregular defects. But as described in the introduction, to obtain accurate wave propagation solution at ultrasonic frequencies is

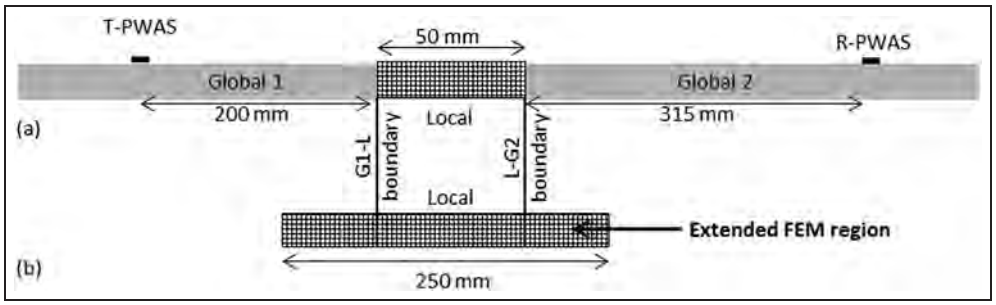

Figure 12. Waveguide problem in 1D solved by the hybrid global–local (HGL) method in time domain: (a) step 1: global 1 using the software "WaveFormRevealer"; (b) step 2: local using FEM software discretization including extended regions for reflection avoidance in time domain; (a) step 3: global 2 using the software "WaveFormRevealer."
FEM: finite element method; PWAS: piezoelectric wafer active sensor; R: receiver; T: transmitter.

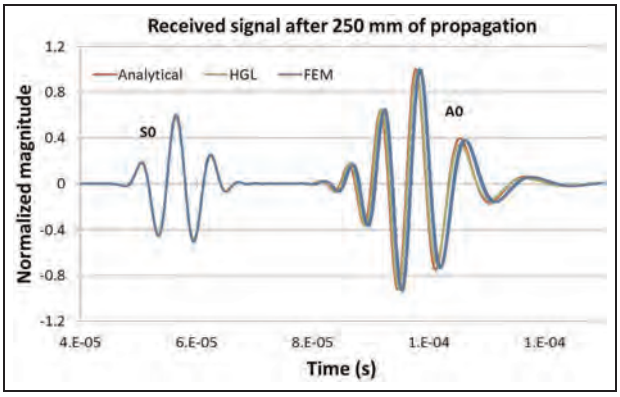

Figure 13. Comparison between the analytical, HGL, and FEM results of the received signal after a length path of 250 mm; in this case, HGL means global 1 then local.
HGL: hybrid global–local; FEM: finite element method.

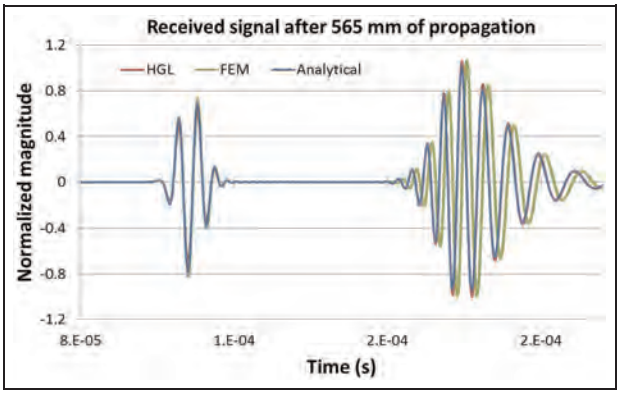

Figure 14. Comparison between the analytical, HGL, and FEM results of the received signal after a length path of 565 mm; in this case, HGL means global 1, local, and then global 2.
HGL: hybrid global–local; FEM: finite element method.

computationally intensive and may become prohibitive for realistic structures.

HGL method validation by comparison with experiments

This hybrid global–local–global R-PWAS signal is compared with the analytical model and the experimental results, after a length path of 565 mm (Figure 15). A good agreement for the S0 wave packet is observed. For the A0 mode, a good agreement is also observed but a slight time shift exists at the end of the A0 wave packet. We can conclude that this time-domain HGL approach is in good agreement with the experimental results and with our analytical model. The slight difference in the A0 packet can be explained by the fact that these models, analytical and HGL, are 1D guided waves that are not exactly representative of the experimental results, that is, 2D guided waves.

HGL advantages for inclusion of structural damage

Metal structures exhibit a wide range of corrosion types including uniform, pitting, galvanic, crevice, concentration cell, and graphite corrosion (Roberge, 2007). When the guiding structure has changes due to corrosion in the geometry, materials properties, supports, or attachments, the guided waves that propagate through will be modified accordingly. Hence, loss of material due to corrosion presents geometrical changes that will cause the guided-wave scattering and can be used for inspection of corrosion.

In this study, corrosion is simulated by a uniform notch on an aluminum plate. The depth and the width were increased gradually in order to simulate corrosion progression. This thickness loss produced a change in the waveguide impedance and thus caused (a) scattering and reflection, (b) modification of the wave speed of the Lamb waves crossing the corrosion area, and (c) conversion mode propagation. In practice, corrosion defects are geometrically complex and require multiple parameters to describe them and their scattering behaviors. Simplified shapes were used, as a uniform notch, for propagating Lamb wave paths to reduce number of parameter in order to better understand the changes caused by material loss. In the HGL model, simulated corrosion was made on 3.2-mm-thick aluminum plate.

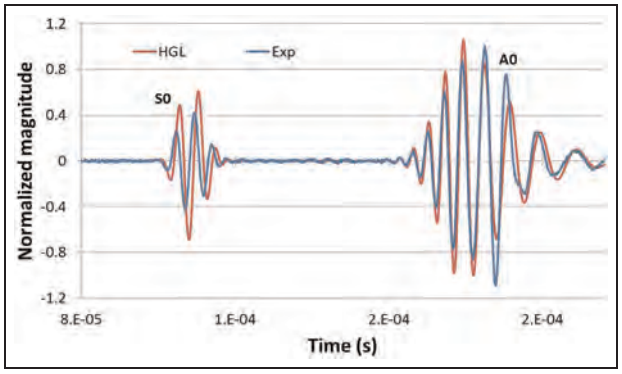

Figure 15. Comparison of the signal received after a travel of 565 mm for the analytical model, the experimental results, and the HGL three-step approach (global–local–global).
HGL: hybrid global–local.

The location of the corrosion was on the middle of the local zone as described in Figure 16.

Transient analysis of Lamb wave interaction with a surface notch in a plate is conducted using our HGL approach using our analytical software WFR and the commercial ABAQUS software.

Incident wave from the T-PWAS will propagate and then interact with the notch, undergoing mode conversion. Hence, there will be reflected waves traveling toward the left edge to be captured by T-PWAS and transmitted waves traveling toward the right edge to be captured by the R-PWAS. If the incident wave is fixed, the reflection and transmission coefficients are affected by the severity of the structural discontinuity, which, in this case, is the notch geometry. These coefficients, when measured experimentally, can be used as a quantitative measure to characterize the discontinuity. To analyze the sensitivity of the Lamb waves to the size of the notch, the reflection coefficients of A0 and S0 from the notch are computed using our HGL approach. The rectangular notches have a constant width of 1 mm and depth varying from 1 to 3 mm. The results are shown in Figure 17 for A0 input and in Figure 18 for S0 input. The reflection coefficients of A0 and S0 from a notch have been studied by Lowe et al. (2002) and Lowe and Diligent (2002) by using an in-house FEM software. The results in Figures 17(a) and 18(a) agree with their results. Experiments to verify these theoretical predictions are under way, and the results will be presented comparatively in a future publication.

The case of A0 input is first discussed based on Figure 17. The notch depth is normalized by the plate thickness, d/h. As shown in Figure 17(a), for $d/h<0.6$, the notch depth is around 1/20 the wavelength of A0 (which is 12.4 mm). Hence, the wave will transmit through the notch almost completely with negligible reflection, which agrees well with the low coefficients obtained for the reflected A0 wave components. If the notch spans over the full depth, then the A0 wave is fully reflected with no conversion. The coefficient for the reflected A0 wave component approaches 1 and that for the reflected S0 wave approaches 0. In between these two extremes, the incident A0 wave will undergo mode conversion, partially transmitted and partially reflected containing both A0 and S0 components. It is also not surprising that in Figure 17(c), the transmitted S0 coefficient first increases and then decreases with depth, with the maximum value occurring when the notch depth is close to half the thickness of the plate.

The reflection, transmission, and mode conversion coefficients for S0 input are plotted in Figure 18. A phenomenon similar to the A0 case can be observed where mode conversion is maximum when notch depth is about half-plate thickness (Figure 18(b)). Unlike A0, S0 exhibits good sensitivity even for a shallow notch. For $d/h>0.4$, the notch depth is around 1/100 wavelength of S0 (which is 35.9 mm) and the reflection can be distinctly observed. This could be due to its small value at the surface that any change becomes significant. The existence of surface crack destroys the symmetry of the wave, resulting in mode conversion. It is shown here that the mode shape also contributes significantly to the sensitivity of the detection.

Similar analysis can be performed to evaluate the dependence of the coefficients on notch width, which for concise reasons will not be discussed in detail. They

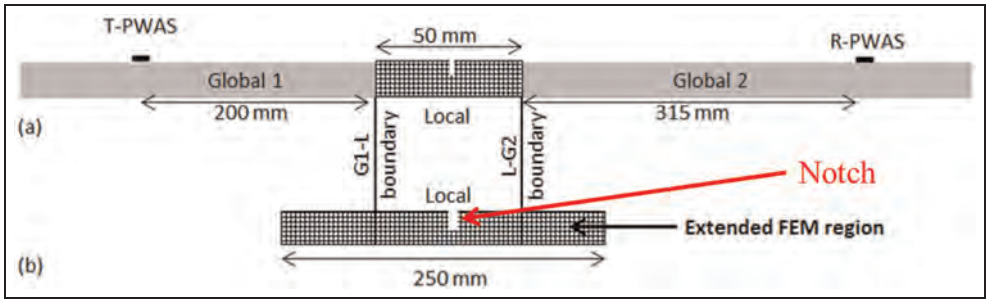

Figure 16. Waveguide problem in 1D solved by the hybrid global–local (HGL) method in time domain: (a) overall HGL setup and (b) FEM discretization including extended regions to avoid reflection and also a notch in the middle of the interest area.
FEM: finite element method; PWAS: piezoelectric wafer active sensor; R: receiver; T: transmitter.

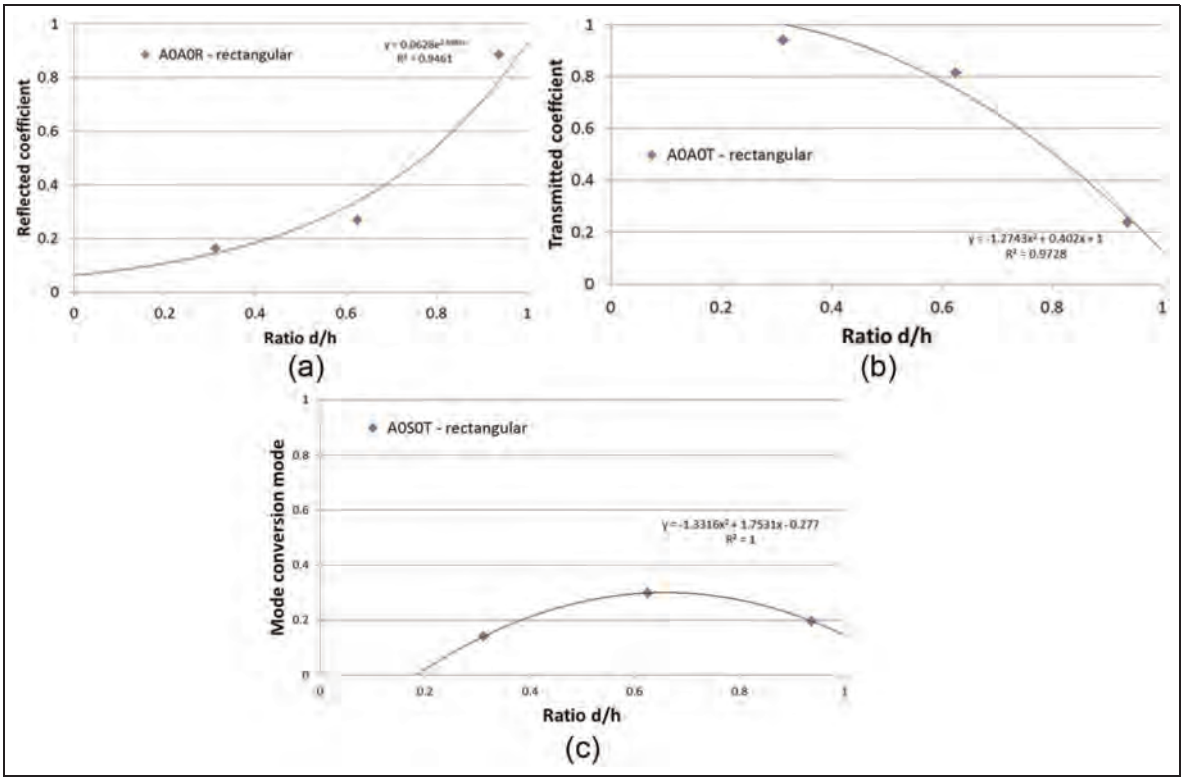

Figure 17. Coefficients versus normalized notch depth/thickness ration for A0 input: (a) reflection A0, (b) transmission A0, and (c) transmission S0 mode conversion.

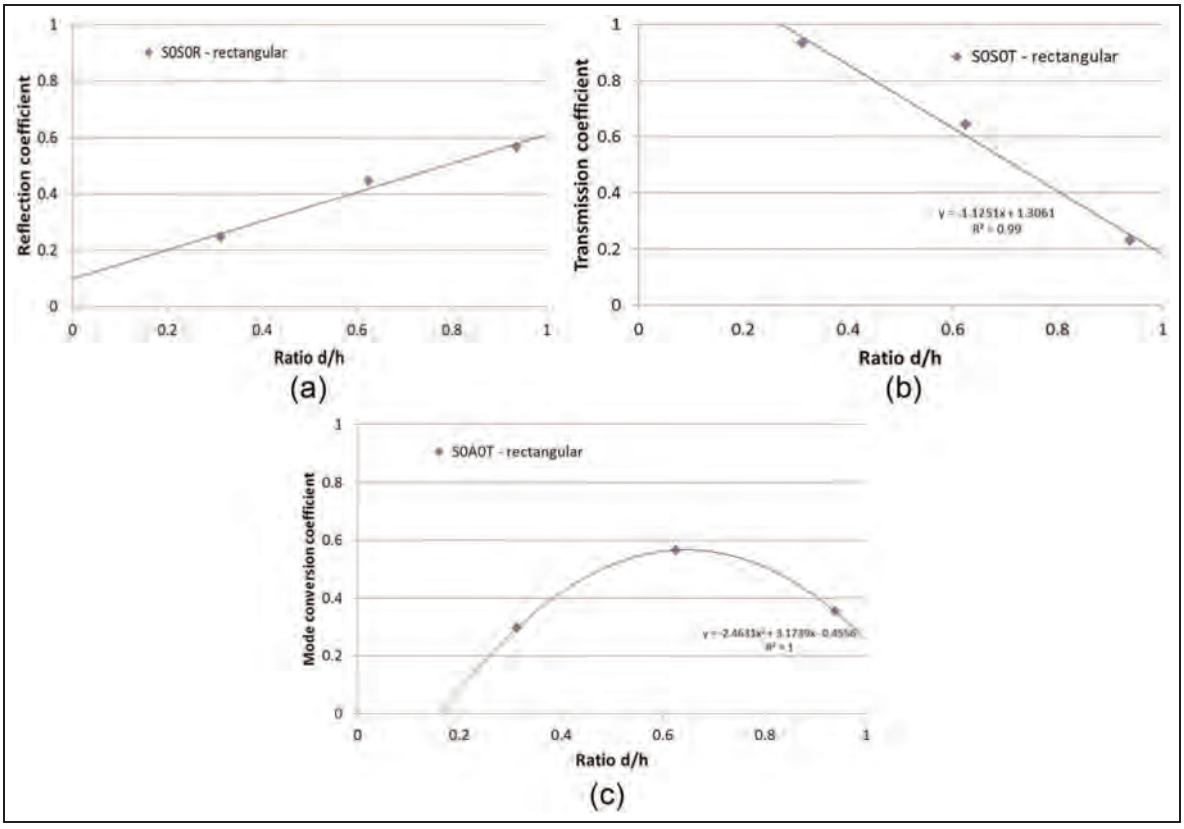

Figure 18. Coefficients versus normalized notch depth ration for S0 input: (a) reflection S0, (b) transmission S0, and (c) transmission A0 mode conversion.

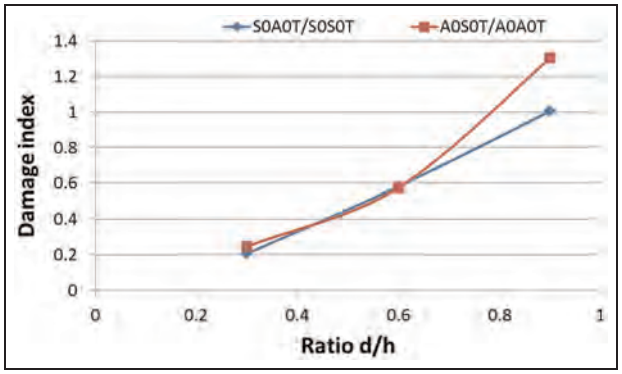

Figure 19. Damage index based on the ratio of the transmitted mode conversion and the input transmitted for S0 and A0 input.

agree well with the results presented by Lowe et al. (2002) and Lowe and Diligent (2002). The variation of the coefficients exhibited against notch width is somewhat periodic and relates to the wave numbers of the Lamb modes.

A damage index (DI) can be computed using the ratio of the amplitudes of the original and mode-converted waves as received at the R-PWAS. Figure 19 shows the DI for S0 and A0 input. For $d/h \leqslant 0.2$, the ratio based on the S0 input would be more sensitive than the A0 input mode. However, for $d/h > 0.6$, the DI is bigger for A0 mode input. So using the S0 and the A0 modes, the notch dimension is quantified.

Changes caused by the damage were also quantified with the root mean square deviation (RMSD) algorithm. The RMSD DI is a scalar quantity that results from a statistical comparison between the signal in the present state and the signal in the reference state (baseline). Such a scalar reveals the difference between pristine data and measurement caused by the presence of damage and provides an overall change of the structure between sensors. This feature would be ideal for corrosion or notch detection since it carries information of both the amplitude and the phase changes from the growth of the corrosion. The RMSD DI is defined as the relative ratio of the difference between each measurement and baseline signals as follows:

$$\text{RMSD DI} = \sqrt{\frac{\sum_{j=0}^{N-1} [s_i(j) - s_0(j)]^2}{\sum_{j=0}^{N} s_0^2(j)}} \tag{14}$$

where s_i is the ith measurement, s_0 the baseline signal and N the data length.

RMSD DI defined in equation (17) is applied on each mode (windowed parts). The plotted curves in Figure 20 show clearly that the RMSD DI of A0 mode changes significantly with the thickness loss in the plate between the two PWASs, whereas that for S0 was almost unchanged. In addition, as shown in Figure 20, the DI is the same for all the widths. In other term, the notch detection is not sensitive of the widths but only on the depths of the notch.

Alleyne and Cawley (1992) investigated the interaction of Lamb waves with notches in plates from both an FE simulation viewpoint and by experiment. Among the conclusions of this article was the fact that Lamb waves could be used to detect notches when the wavelength to notch depth ratio was of the order of 40. The wavelength of the 3.2-mm-thick plate at a center frequency of 150 kHz is

- For S0 mode: $c = 5388\text{m/s}$, so $\lambda = 35.9\text{mm}$
- For A0 mode: $c = 1853\text{m/s}$, so $\lambda = 12.4\text{mm}$

Using the conclusion of Alleyne and Cawley, the minimum of the depth notch detection is $R = \lambda/40$, so $R = 0.31\text{mm}$. In our time-domain HGL approach, and

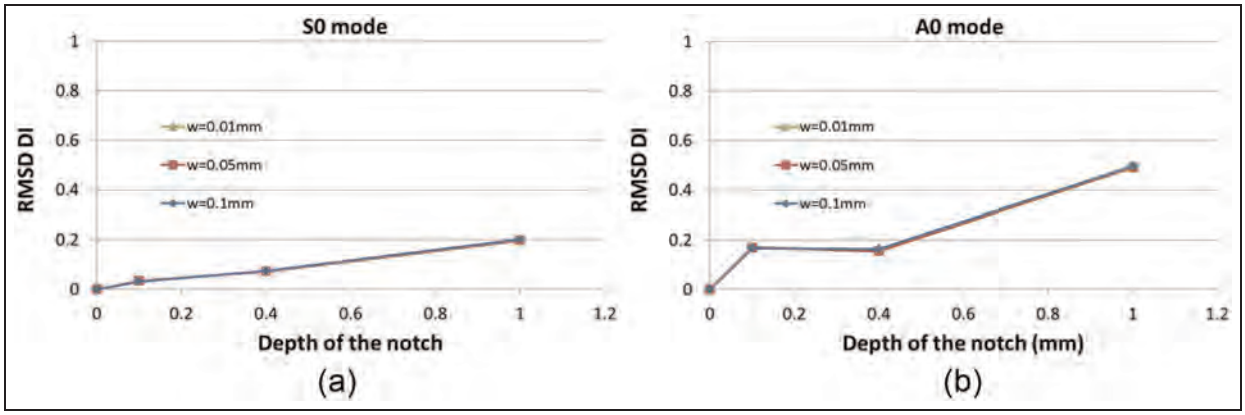

Figure 20. Root mean square deviation damage index curves versus the depths of the notch for various widths from 0.01 to 0.1 mm of (a) S0 mode and (b) A0 mode.
RMSD: root mean square deviation; DI: damage index.

using the RMSD DI, the minimum detection of the depth notch is around 0.1 mm, corresponding to the wavelength-to-notch ratio with an order of 120 in theory. From these simulations, it is found that, with 99% of confidence, the minimum detectable depth notch size is around 0.1 mm.

Conclusion

This article has presented a combined FE and analytical method to predict the 1D guided-wave propagation for NDE and SHM application. The FE mesh is used to describe the region around the defects/flaws. On the contrary to other hybrid models already developed, the interaction between Lamb waves and defects is computed in the time domain using the explicit solver of the commercial FEM software ABAQUS. Compared to usual FEM model, the main advantage of the hybrid method is to reduce meaningfully the length of the mesh used to investigate the interaction of Lamb modes with defects and hence the computing time. Theory of guided-wave propagation between two PWAS transducers was studied and analytical model was built to give the theoretical waveforms of pitch–catch signals. Analytical modeling and FE modeling have good match with experimental results and can well describe guided-wave propagation between two PWAS transducers.

A time-domain HGL approach was realized using the analytical and the FEM for the global area and the local area, respectively. Lamb wave interaction with a notch is investigated by using this method, and the results obtained are consistent with the physical consideration of Lamb mode shape and energy conservation with respect to transmission, reflection, and mode conversion. Because of the symmetric mode shape, S0 is more sensitive to the shallow notch than A0. By making use of the fact that the reflection increases with increase in notch depth and mode conversion are maximized when the notch is around half through the thickness of the plate, the reflection and conversion coefficients can be used to characterize the depth of the notch.

For the future work, the analytical model will be extended to three-dimensional (3D) circular PWAS analysis using, for example, Bessel function representation. Thus, we will realize the modeling of the guided-wave propagation between two circular PWAS transducers in an arbitrary 2D geometry. The analytical modeling is expected to include damage/flaw in the plate structure, more complex structure (plate with double stiffener), and also include the second modes A1 and S1 for higher frequency excitation. The competitive complexity would be to develop a time-domain HGL for 2D wave propagation in structures.

Acknowledgements

Support of Office of Naval Research # N00014-11-1-0271, Dr Ignacio Perez, Technical Representative, and Air Force Office of Scientific Research #FA9550-11-1-0133, Dr David Stargel, Program Manager, are thankfully acknowledged.

Funding

This study was performed under the support of the Office of Naval Research #N00014-11-1-0271, Technical Representative Dr. Ignacio Perez and the Air Force Office of Scientific Research #FA9550-11-1-0133, Program Manager Dr. David Stargel.

References

ABAQUS (2008) *Analysis User's Manual*, Version 6-9.2.

Achenbach JD (1973) Wave Propagation in Elastic Solids. Amsterdam/New York: Elsevier.

Alleyne DN and Cawley P (1990) A 2-dimensional Fourier transform method for the quantitative measurement of Lamb modes. In: *IEEE ultrasonics symposium*, 4–7 December 1990, Vol. 2, pp. 1143–1146.

Alleyne DN and Cawley P (1992) The interaction of Lamb waves with defects. *IEEE Transactions on Ultrasonics Ferroelectrics and Frequency Control* 39(3): 381–397.

Auld BA (1973) *Acoustic Fields and Waves in Solids,* pp. 357–382. New York: John Wiley and Sons.

Banerjee S and Kundu T (2008) Semi-analytical modeling of ultrasonic fields in solids with internal anomalies immersed in fluid. *Wave Motion* 45(5): 581–595.

Bartoli I, Lanza di Scalea F, Fateh M, et al. (2005) Modeling guided wave propagation with application to the long-range defect detection in railroad tracks. *NDT & E International* 38(5): 325–334.

Blackshire JL, Martin S and Cooney A (2006) Evaluation of crack and corrosion detection sensitivity using piezoelectric sensor arrays. In: *3rd European workshop on structural health monitoring*, 5–7 July 2006, Granada, Spain.

Castaings M, Le Clezio E and Hosten B (2002) Modal decomposition method for modeling the interaction of Lamb waves with cracks. *Journal of the Acoustical Society of America* 112(6): 2567–2582.

Chang Z and Mal AK (1995) A global local method for wave propagation across a lap joint. In: *Numerical Methods in Structural Mechanics*, vol. 204. ASME, pp. 1–11.

Diligent O, Lowe MJS and Cawley P (2001) Reflection and scattering of the S0 Lamb mode from circular defects in plates. *AIP Conference Proceedings* 557(1): 134–141.

Galan JM and Abascal R (2005) Boundary element solution for the bidimensional scattering of guided waves in laminated plates. *Computers & Structures* 83: 740–757.

Giurgiutiu V (2008) *Structural Health Monitoring with Piezoelectric Wafer Active Sensor*, Elsevier Academic Press, pp 747. ISBN 9780120887606.

Giurgiutiu V, Gresil M, Lin B, et al. (2012) Predictive modeling of piezoelectric wafer active sensors interaction with high-frequency structural waves and vibration. *Acta Mechanica* 223: 1681–1691.

Goetschel DB, Dong SB and Muki M (1982) A global local finite element analysis of axisymmetric scattering of elastic waves. *Journal of Applied Mechanics* 49(4): 816–820.

Grahn T (2003) Lamb wave scattering from a circular partly through-thickness hole in a plate. *Wave Motion* 37(1): 63–80.

Gresil M, Lin B, Shen Y, et al. (2011a) Predictive modeling of space structures for SHM with PWAS transducers. In: *ASME conference proceedings* (No. 54723), 18–21 September 2011, Phoenix, Arizona, USA, pp. 525–534.

Gresil M, Yu L, Giurgiutiu V, et al. (2012) Predictive modeling of electromechanical impedance spectroscopy for composite materials. *Structural Health Monitoring: An International Journal*. DOI: 10.1177/1475921712451954.

Gresil M, Shen Y and Giurgiutiu V (2011b) Benchmark problems for predictive fem simulation of 1-D and 2-D guided waves for structural health monitoring with piezoelectric wafer active sensors. *AIP Conference Proceedings* 1430(1): 1835–1842.

Gresil M, Shen Y and Giurgiutiu V (2011c) Predictive modeling of ultrasonics SHM with PWAS transducers. In: *8th international workshop on structural health monitoring*, 13–15 September 2011, Stanford, CA.

Gresil M, Yu L and Giurgiutiu V (2011d) Fatigue crack detection in thick steel structures with piezoelectric wafer active sensors. In: *Proceedings SPIE: the International Society for Optical Engineering*, 19 April 2011, San Diego, CA, 7983-101, 7983 7982Y.

Guo N and Cawley P (1993) The interaction of Lamb waves with delaminations in composite laminates. *Journal of the Acoustical Society of America* 94(4): 2240–2246.

Hayashi T (2004) Guided wave animation using semi-analytical finite element method. In: *WCNDT*, 30 August-3 September 2004, Montreal, Canada, 1328.

Hayashi T, Kawashima K, Sun Z, et al. (2003) Analysis of flexural mode focusing by a semianalytical finite element method. *Journal of the Acoustical Society of America* 113(3):1241–1248.

Hayashi T, Murase M, Song W-J, et al. (2006) Development of calculation software for guided wave propagation in a pipe. *AIP Conference Proceedings*, 31 July-5 August 2005, Brunswick, Maine (USA). 820(1): 173–180.

Kitts DJ and Zagrai AN (2009) Finite element modeling and effect of electrical/mechanical parameters on electromechanical impedance damage detection. In: *ASME conference proceedings* (No. 48975), 21–23 September 2009, Oxnard, California, USA, pp. 487–497.

Loveday PW (2008) Simulation of piezoelectric excitation of guided waves using waveguide finite elements. *IEEE Transactions on Ultrasonics Ferroelectrics and Frequency Control* 55(9): 2038–2045.

Lowe MJS and Diligent O (2002) Low-frequency reflection characteristics of the S0 Lamb wave from a rectangular notch in plate. *Journal of the Acoustical Society of America* 111(1): 64–74.

Lowe MJ and Diligent O (2002) The low frequency reflection characteristics of the fundamental antisymmetric Lamb wave A0 from a rectangular notch in a plate. *Journal of the Acoustical Society of America* 112: 2612–2622.

Mal A and Chang Z (2000) A semi-numerical method for elastic wave scattering calculations. *Geophysical Journal International* 143: 328–334.

Marzani A, Viola E, Bartoli I, et al. (2008) A semi-analytical finite element formulation for modeling stress wave propagation in axisymmetric damped waveguides. *Journal of Sound and Vibration* 318(3): 488–505.

Moser F, Jacobs LJ and Qu J (1999) Modeling elastic wave propagation in waveguides with the finite element method. *NDT & E International* 32(4): 225–234.

Olson SE, Desimio NP and Derriso MM (2006) Analytical modeling of Lamb waves for structural health monitoring. In: *3rd European workshop on structural health monitoring*, 5–7 July 2006, Granada, Spain.

Peng H, Meng G and Li F (2009) Modeling of wave propagation in plate structures using three-dimensional spectral element method for damage detection. *Journal of Sound and Vibration* 320(4–5): 942–954.

Roberge P (2007) *Corrosion Inspection and Monitoring*. New York: McGraw-Hill; John Wiley & Sons.

Rose JL (1999) *Ultrasonic Waves in Solid Media*. Cambridge, UK: Cambridge University Press.

Sabra KG, Srivastava A, di Scalea FL, et al. (2008) Structural health monitoring by extraction of coherent guided waves from diffuse fields. *Journal of the Acoustical Society of America* 123(1): EL8–EL13.

Shen Y and Giurgiutiu V (in press) WaveFormRevealer—an analytical predictive tool for the simulation of multimodal guided waves propagation and interaction with damage. *Structural Health Monitoring: An International Journal*. SHM-13-0016.

Srivastava A (2009) *Quantitative structural health monitoring using ultrasonic guided waves*. PhD Thesis, University of California, San Diego, CA.

Viktorov IA (1967) *Rayleigh and Lamb Waves—Physical Theory and Application*. New York: Plenum Press.

Zagrai A, Doyle D, Gigineishvili V, et al. (2010) Piezoelectric wafer active sensor structural health monitoring of space structures. *Journal of Intelligent Material Systems and Structures* 21(9): 921–940.

Journal of
Intelligent Material
Systems and Structures

Original Article

Journal of Intelligent Material Systems and Structures
2014, Vol. 25(4) 506–520
© The Author(s) 2013
Reprints and permissions:
sagepub.co.uk/journalsPermissions.nav
DOI: 10.1177/1045389X13500572
jim.sagepub.com
SAGE

Predictive modeling of nonlinear wave propagation for structural health monitoring with piezoelectric wafer active sensors

Yanfeng Shen and Victor Giurgiutiu

Abstract

This article presents predictive modeling of nonlinear guided wave propagation for structural health monitoring using both finite element method and analytical approach. In our study, the nonlinearity of the guided waves is generated by interaction with a nonlinear breathing crack. Two nonlinear finite element method techniques are used to simulate the breathing crack: (a) element activation/deactivation method and (b) contact analysis. Both techniques are available in ANSYS software package. The solutions obtained by these two finite element method techniques compare quite well. A parametric analytical predictive model is built to simulate guided waves interacting with linear/nonlinear structural damage. This model is coded into MATLAB, and the WaveFormRevealer graphical user interface is developed to obtain fast predictive waveform solutions for arbitrary combinations of sensor, structural properties, and damage. The predictive model is found capable of describing the nonlinear wave propagation phenomenon. This article finishes with summary and conclusions followed by recommendations for further work.

Keywords

Piezoelectric wafer active sensors, nonlinear ultrasonics, Lamb waves, damage detection, structural health monitoring, nondestructive evaluation, breathing crack, higher harmonics

Introduction

Nonlinear ultrasonic technique, which uses distinctive higher harmonics and subharmonics features, proves itself a promising approach to detect incipient changes which are precursors to structural damage (Jhang, 2009; Kruse and Zagrai, 2009). The combined use of guided Lamb waves and nonlinear methods is drawing increasing interest because the nonlinear Lamb waves are endowed with both sensitivity of nonlinear methods and large inspection ranges of guided waves.

To date, most studies on nonlinear ultrasonics have been experimental, demonstrating the capability of nonlinear Lamb waves to detect structural damage (Bermes et al., 2007; Cantrell, 2009; Dutta et al., 2009; Kumar et al., 2009; Nagy, 1998). However, few theoretical predictive studies exist especially for nonlinear Lamb waves. Generation of higher harmonics of Lamb waves has been investigated theoretically (Deng, 1999, 2003), and the existence of antisymmetric or symmetric Lamb waves at nonlinear higher harmonics has been discussed via modal analysis approach and the method of perturbation (Srivastava and di Scalea, 2009). However, these theoretical studies considered only the situations where nonlinearity are present over the whole domain of wave propagation in the material (mesoscopic nonlinearity); other cases of nonlinear wave propagation, such as wave propagation through localized breathing cracks, are also possible.

When structures are under cyclic fatigue loading, microscopic cracks will begin to form at the structure surface, as shown in Figure 1. They need to be found out before they grow to the critical size and cause catastrophic failures. In our study, we want to know what characteristics the inspection waves will have after interacting with this kind of microscopic cracks, especially when they behave as nonlinear breathing cracks under wave cycles.

Department of Mechanical Engineering, University of South Carolina, Columbia, SC, USA

Corresponding author:
Yanfeng Shen, Department of Mechanical Engineering, University of South Carolina, Columbia, SC 29208, USA.
Email: shen5@email.sc.edu

Figure 1. Microscopic cracks nucleated at structural surface (Corrosion Testing Laboratories, Inc., 2007).

When ultrasonic waves reach a microscopic crack, the crack can be closed and opened under compression and tension, with the compression part of the waves penetrating the crack, while the tension part cannot. The nonlinear phenomenon lies in the fact that the apparent local stiffness of the crack region changes under tension and compression.

The interaction of elastic waves with clapping mechanisms has been studied in the past. Researches on clapping-induced nonlinearities and higher harmonics have been carried out (Biwa et al., 2004, 2006; Richardson, 1979). However, most of these investigations aim at the nonlinearity of elastic bulk waves. Our study focuses on the modeling aspect of contact acoustic nonlinearity (CAN) of Lamb waves, which is a localized nonlinear phenomenon of dispersive guided waves and is different from the previous theoretical studies of nonlinear Lamb waves (Deng, 1999, 2003; Srivastava and di Scalea, 2009).

Generation of higher harmonics in nonlinear ultrasonics

A distinctive beneficial feature of nonlinear ultrasonics is the generation of nonlinear higher harmonics, which allows us to diagnose the presence and severity of nonlinear damage in structures. There are various mechanisms behind generation of higher harmonics in ultrasonics, for example, nonlinear mesoscopic (hysteretic) nonlinearity and CAN. The phenomena of higher harmonics generation can be illustrated in a simple way by using a general nonlinear dynamic system (Hagedorn, 1988; Lee and Choi, 2008; Naugoslnykh and Ostrovsky, 1998)

$$U = Ax\left(1 + \beta x + \gamma x^2 + \cdots\right) \tag{1}$$

where U is the output of the system, A is a scale factor, and β and γ are the second and third nonlinear coefficients. Consider a harmonic input

$$X(\omega) = \hat{x} \cdot e^{i\omega t} \tag{2}$$

By substituting equation (2) into equation (1), the output of the nonlinear system takes the form

$$\begin{aligned} U &= A\hat{x}e^{i\omega t} + A\beta(\hat{x}e^{i\omega t})^2 + A\gamma(\hat{x}e^{i\omega t})^3 + \cdots \\ &= A\hat{x}e^{i\omega t} + A\beta\hat{x}\hat{x}e^{i2\omega t} + A\gamma\hat{x}^2\hat{x}e^{i3\omega t} + \cdots \\ &= AX(\omega) + A\beta\hat{x} \cdot X(2\omega) + A\gamma\hat{x}^2 \cdot X(3\omega) + \cdots \end{aligned} \tag{3}$$

Equation (3) shows that the output of the nonlinear system contains higher harmonics $2\omega, 3\omega, \ldots$, while the input to the system contains only one frequency component ω. This distinctive feature allows us to detect material degradation, fatigue, microcracks, or state of clamping surfaces, which introduce nonlinearity to structures.

Finite element simulation of Lamb waves interacting with nonlinear breathing cracks

A pitch–catch method may be used to interrogate a plate with a breathing crack which opens and closes under tension and compression. The ultrasonic waves generated by the piezoelectric wafer active sensor (PWAS) propagate into the structure, interact with the breathing crack, acquire nonlinear features, and are picked up by the receiver PWAS. This process is shown in Figure 2.

Two methods are used to model the breathing crack: (a) element activation/deactivation method and (b) contact analysis. The solving scheme and results from both methods are discussed and compared.

Element activation/deactivation method

Element activation/deactivation technique could be described as deactivating and reactivating selected elements according to certain criteria. To deactivate elements, the stiffness matrices of the elements are

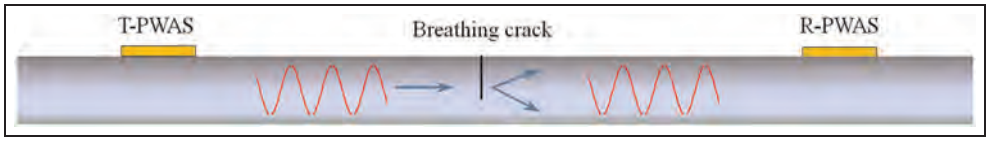

Figure 2. Pitch–catch method for the detection of breathing crack; the mode conversion at the crack is illustrated by the two arrows.

multiplied by a severe small reduction factor, η (usually 1E−6 or smaller), while mass, damping, loads, and other such effects are set to zero. Thus, upon deactivation, the element stiffness matrix, mass matrix, and associated loads will no longer contribute to the assembled global matrices. It should be noted that, through this approach, the deactivated elements are not removed from the model, but left in place in a dormant state with a greatly diminished participation. Similarly, when elements are activated, they are not added to the model. Instead, the dormant elements are simply reactivated, recovering their original stiffness, mass, damping, element loads, and so on. The assembled global equation will take the following form

Original global equation

$$\begin{pmatrix} M_{11} & \cdots & 0 \\ \vdots & +M^e & \vdots \\ 0 & \cdots & M_{nn} \end{pmatrix} \begin{Bmatrix} \ddot{u}_1 \\ \vdots \\ \ddot{u}_n \end{Bmatrix} + \begin{pmatrix} C_{11} & \cdots & 0 \\ \vdots & +C^e & \vdots \\ 0 & \cdots & C_{nn} \end{pmatrix} \begin{Bmatrix} \dot{u}_1 \\ \vdots \\ \dot{u}_n \end{Bmatrix} + \begin{pmatrix} K_{11} & \cdots & 0 \\ \vdots & +K^e & \vdots \\ 0 & \cdots & K_{nn} \end{pmatrix} \begin{Bmatrix} u_1 \\ \vdots \\ u_n \end{Bmatrix} = \begin{Bmatrix} Q_1 \\ \vdots + Q^e \\ Q_n \end{Bmatrix} \tag{4}$$

Deactivated global equation

$$\begin{pmatrix} M_{11} & \cdots & 0 \\ \vdots & +\Phi & \vdots \\ 0 & \cdots & M_{nn} \end{pmatrix} \begin{Bmatrix} \ddot{u}_1 \\ \vdots \\ \ddot{u}_n \end{Bmatrix} + \begin{pmatrix} C_{11} & \cdots & 0 \\ \vdots & +\Phi & \vdots \\ 0 & \cdots & C_{nn} \end{pmatrix} \begin{Bmatrix} \dot{u}_1 \\ \vdots \\ \dot{u}_n \end{Bmatrix} + \begin{pmatrix} K_{11} & \cdots & 0 \\ \vdots & +\eta K^e & \vdots \\ 0 & \cdots & K_{nn} \end{pmatrix} \begin{Bmatrix} u_1 \\ \vdots \\ u_n \end{Bmatrix} = \begin{Bmatrix} Q_1 \\ \vdots + \Phi \\ Q_n \end{Bmatrix}, \tag{5}$$

where M^e, C^e, K^e, and, Q^e are the elemental mass matrix, damping matrix, stiffness matrix, and external loads, respectively. The reduction factor η is very small ($\eta << 1$, typically $\eta < 1E-6$). And the symbol Φ denotes a zero matrix or vector. Comparing equation (5) with equation (4), it is apparent that the elements, after deactivation, will no longer contribute to the structure because $\eta K^e \approx [\Phi]$ with $\eta << 1$. The nonlinear effect is imparted by the periodical change of matrices M, C, and K.

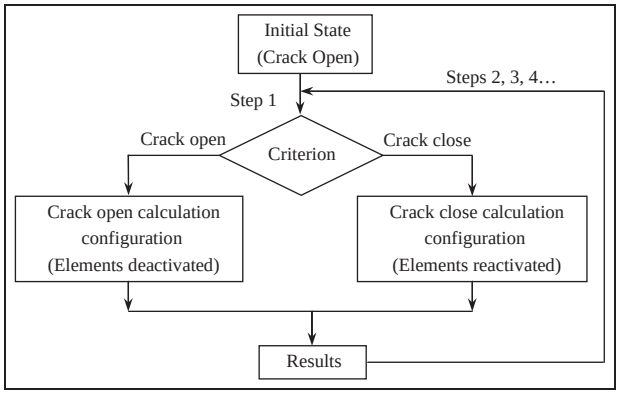

Figure 3. Solving scheme of element activation/deactivation method.

The solving scheme for this transient dynamic problem using element activation/deactivation method is shown in Figure 3. The crack opening or closing status is judged for each calculation step in the transient analysis; calculation configuration of the current step is based on the results of the previous step.

The crack open/close criterion is developed based on the tension and compression status of the thin layer of nonlinear elements simulating the breathing crack. When these elements are under tension, the crack is considered open. The criterion is shown in the following equation

$$(U2 - U1 < 0) \cap \left(\bar{\varepsilon} = \frac{\sum_1^n \varepsilon_n}{n} < 0\right) \tag{6}$$

where $U1$ and $U2$ are the displacements of the two nodes located on the two edges of the selected element in crack opening direction. $\bar{\varepsilon}$ is the average strain of the selected elements in crack opening direction. This criterion is developed based on the contact behavior of the breathing crack and through numerical experiments. Details of this criterion can be found in Shen and Giurgiutiu (2012). It should be noted that for mode shapes at high-frequency big plate thickness combination (high fd value), this criterion needs to be modified by taking into account more nodes across the crack surface to consider the more complicated contact behavior.

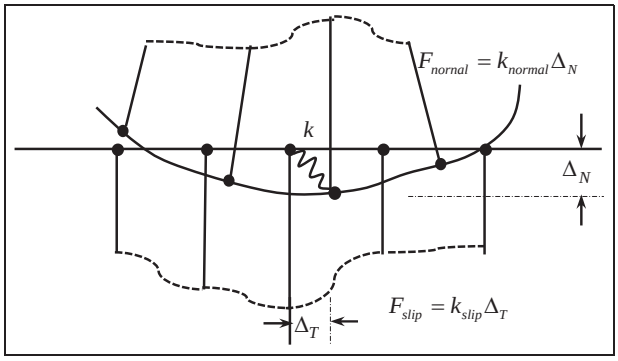

Figure 4. Penetration between contact surfaces showing contact tractions (Hughes et al., 1975).

Contact analysis with finite element methods

In the physical world, no penetration will happen between contact surfaces; however, in finite element analysis, hypothetical penetration is allowed to ensure equilibrium. The contact parameters are determined by (a) Lagrange multiplier or (b) penalty methods. In this research, the penalty method is adopted. The relationship of penetration and contact tractions is illustrated in Figure 4, where k is the contact stiffness and Δ_N and Δ_T are the normal and tangential penetrations.

The choice of contact stiffness is an important part of contact analysis, because it influences both the accuracy and convergence of the solution, and usually calls for previous experience. When analyzing contact problem, a dilemma will come to us: a small amount of penetration will render more accurate results, so we should chose large contact stiffness; however, this may lead to ill conditioning of the global stiffness matrix and to convergence difficulties. Lower stiffness values can lead to a certain amount of penetration/slip and make the solution easier to converge but give a less accurate solution. Thus, we are searching for a high enough stiffness that the penetration/slip is acceptably small and render a relatively accurate result, but a low enough stiffness that the problem will be well behaved in terms of convergence. ANSYS provides a suggested value of contact stiffness, which will modified by the penalty coefficient to achieve both convergence and accuracy. A common practice is to start from a low contact stiffness which ensures convergence, check if the penetration of the contact surfaces is reasonable, and then increase the penalty coefficient until the surface penetration is reasonably small and solutions between two sequent penalty coefficients do not change. The final contact stiffness used in this study is 7.051×10^{15} Pa.

Finite element model for pitch–catch analysis

Figure 5 shows the finite element model of pitch–catch method for detection of nonlinear breathing crack. Two 7mm × 7mm × 0.2mm PWAS are considered ideally bonded on a 2-mm-thick aluminum plate. The plate is long enough to ensure the received signals are not influenced by boundary reflections. The crack is located at 200 mm from the transmitter, such that the S0 and A0 wave packets have already separated before they arrive at the crack location; hence the S0 and A0 wave packets interact with the breathing crack individually, which allows us to see how the crack interacts with S0 and A0 waves.

The plate is made of aluminum 2024-T3 with Young's modulus of 72.4 GPa, density of 2700 kg/m^3, and Poisson's ratio of 0.33. The APC-850 material properties are assigned to the PWAS as follows

$$[C_p] = \begin{bmatrix} 97 & 49 & 49 & 0 & 0 & 0 \\ 49 & 84 & 49 & 0 & 0 & 0 \\ 49 & 49 & 97 & 0 & 0 & 0 \\ 0 & 0 & 0 & 24 & 0 & 0 \\ 0 & 0 & 0 & 0 & 22 & 0 \\ 0 & 0 & 0 & 0 & 0 & 22 \end{bmatrix} \text{GPa} \quad (7)$$

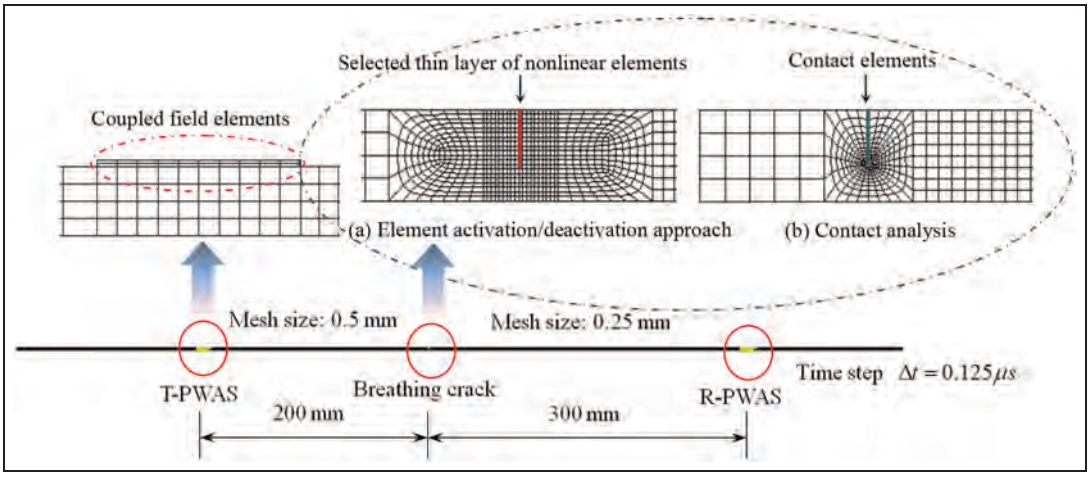

Figure 5. Nonlinear finite element model of breathing crack.

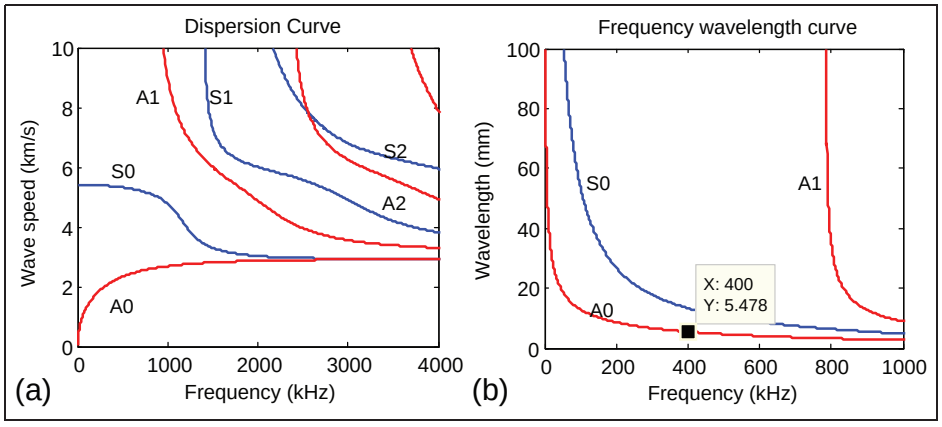

Figure 6. (a) Dispersion curve and (b) frequency wavelength curve.

$$[\varepsilon_p] = \begin{bmatrix} 947 & 0 & 0 \\ 0 & 605 & 0 \\ 0 & 0 & 947 \end{bmatrix} \times 10^{-8}\text{F/m} \tag{8}$$

$$[e_p] = \begin{bmatrix} 0 & 0 & 0 & 12.84 & 0 & 0 \\ -8.02 & 18.31 & -8.02 & 0 & 0 & 0 \\ 0 & 0 & 0 & 0 & 12.84 & 0 \end{bmatrix} \text{C/m}^2 \tag{9}$$

where $[C_p]$ is the stiffness matrix, $[\varepsilon_p]$ is the dielectric matrix, and $[e_p]$ is the piezoelectric matrix. The density of the PWAS material is assumed to be $\rho = 7600\ \text{kg/m}^3$.

The finite element model is built under the plane strain assumption. PWAS transducers are modeled with coupled field elements (PLANE13) which couple the electrical and mechanical variables (ANSYS 13.0 Multi-Physics). The plate is modeled with four-node structure element PLANE182 with "element birth and death" capability. A 20 vpp 5-count Hanning window modulated sine tone burst signal centered at 100 kHz is applied on the top electrode of the transmitter PWAS. The plate is under free boundary condition.

To solve this problem with good accuracy and high efficiency, a meshing strategy of varying density needs to be performed. The maximum acceptable element size and time step to ensure accuracy are shown in the following equations (Moser et al., 1999)

$$l_e = \frac{\lambda_{\min}}{20} \tag{10}$$

$$\Delta t = \frac{1}{20\ f_{\max}} \tag{11}$$

For the excitation centered at 100 kHz, we considered the maximum frequency of interest up to 400 kHz, containing up to the third higher harmonic. The dispersion curve is calculated by solving the Rayleigh–Lamb equation and shown in Figure 6(a). The frequency–wavelength relationship is obtained using equation (12) from the dispersion data and plotted in Figure 6(b). The minimum wavelength at 400 kHz appears in A0 mode at 5.478 mm. According to equation (10), the maximum element size should be 0.275 mm. According to equation (11), for 400 kHz, the maximum time step is 0.125 μs

$$\lambda = \frac{c}{f} \tag{12}$$

Since the mechanical response at crack zone is very complicated, the crack zone is more densely meshed. The region between the breathing crack and the receiver has a mesh size of 0.25 mm (smaller than 0.275) to accurately depict up to the third higher harmonic. A time step of 0.125 μs is adopted. In the element activation/deactivation method, a very thin layer of nonlinear elements (0.1 mm thick) at the crack zone are selected to be deactivated and reactivated. For the contact analysis, the contact pair is constructed using contact elements (CONTA172 and TARGE169).

The severity of damage is represented by the number of elements selected to be deactivated and reactivated. We define the damage severity as the index where $r = a/h$ (a and h are the crack size and plate thickness, respectively). An index of $r = 0.0$ corresponds to pristine condition, where there is no crack in the plate. In our simulation, we used 20 elements across the thickness at the crack zone. Different damage severities $r = 0.6, 0.5, 0.4, 0.3, 0.2, 0.1,$ and 0.0 are generated by selecting 12, 10, 8, 6, 4, 2, and 0 elements. ANSYS uses an average nodal solution for data postprocessing. Hence, the deactivated elements must be excluded from the average process to avoid result contamination. To highlight the effect of nonlinear wave propagation through a breathing crack, the linear wave propagation through the crack is also investigated.

Finite element method simulation results and discussions

The $r = 0.6$ case is used as a representative for demonstrating Lamb waves interacting with a breathing crack

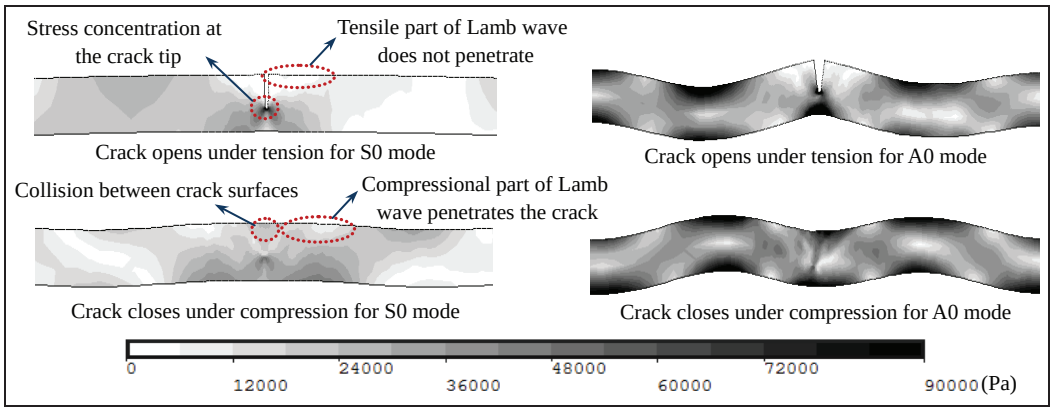

Figure 7. Finite element method simulation of Lamb waves interacting with breathing crack.

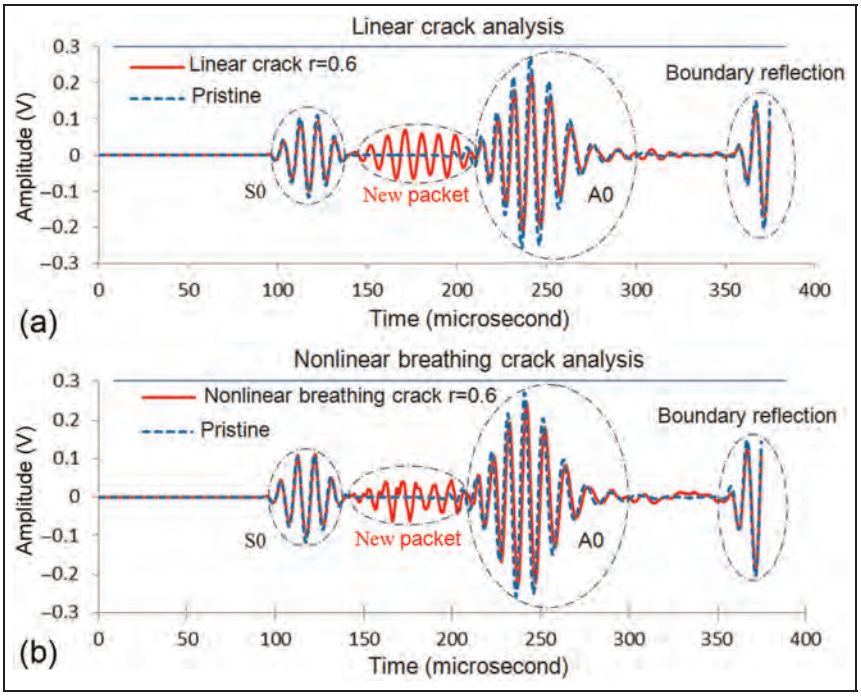

Figure 8. Superposed time-domain simulation signals at receiver piezoelectric wafer active sensor for pristine (r = 0) and cracked (r = 0.6) cases: (a) linear crack analysis and (b) nonlinear breathing crack analysis.

and is shown in Figure 7. The same crack behavior could be observed from both the element activation/deactivation method and contact analysis. It is noticed that the tension part of the Lamb waves opens the crack and do not penetrate through it. On the contrary, the compression part of the Lamb waves closes the crack with collision between crack surfaces; hence, the compression part of the Lamb wave can penetrate into the crack.

Figure 8 shows the waveforms of Lamb waves after linear interaction with the crack (Figure 8(a)) and the waveforms of Lamb waves after nonlinear interaction with a breathing crack (Figure 8(b)).

It can be observed that compared with pristine condition, the cracked plate signal has a slight amplitude drop and phase shift in both S0 and A0 packets. Another difference is that a new wave packet appears due to the presence of the crack. This new packet is introduced by mode conversion and contains both S0 packet converted A0 mode and A0 packet converted S0 mode. The linear crack signal is smooth, but the nonlinear breathing crack signal has small zigzags.

The S0, A0, and new wave packets were extracted from the whole time-history using Hanning window and then Fourier transformed. Frequency spectrums of S0, A0, and the new wave packets of $r = 0.6$ case for

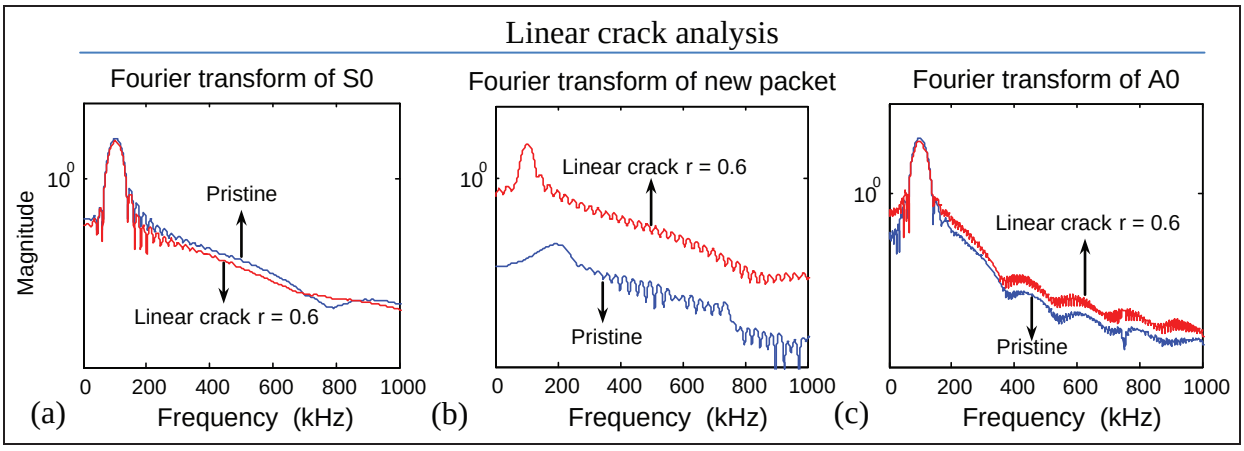

Figure 9. Frequency spectrum of the Lamb wave signals after linear interaction with a crack: (a) S0 mode, (b) new packet, and (c) A0 mode. Note the absence of higher harmonics.

linear crack signal and nonlinear breathing crack signal are carried out and plotted in Figures 9 and 10, respectively. For all the wave packets, the pristine signal does not show any higher frequency components. Figure 9 shows, for the linear crack case, all the wave packets show only the fundamental excitation frequency at 100 kHz. It should be noted that there are no higher harmonics for linear interaction between Lamb waves and the crack.

However, the signal from breathing crack plate shows distinctive nonlinear higher harmonics. Figure 10(a) shows nonlinear higher harmonics in the S0 wave packet. Since the excitation frequency is centered at 100 kHz, the 102.8-kHz peak corresponds to the excitation frequency, and the 203.1 and 300.5 kHz correspond to second and third higher harmonics, respectively. It should be noted that the higher harmonics below 400 kHz can be accurately simulated according to the discussions on the mesh size and time step. The frequency components calculated beyond 400 kHz cannot be correctly described and predicted by the finite element mesh employed. For the A0 wave packet (Figure 10(c)), the first peak corresponds to the excitation frequency, and the second higher harmonic could be clearly observed at 198.2 kHz, but the third harmonic is somehow missing. This phenomenon is due to the tuning effect of PWAS and plate structure combination (Giurgiutiu, 2005). The tuning curve shown in Figure 10(d) indicates that at around 300 kHz, where the third harmonic should appear, the A0 mode reaches its rejection point. In other words, for the given PWAS and plate structure, this frequency could not be detected due to the rejection effect at the receiver PWAS. Analysis of the observed "new packet" (Figure 10(b)) also reveals the nonlinear higher harmonics pattern. In this new packet, the feature of nonlinear higher harmonics seems to be more obvious than in the S0 and A0 packets. And the spectral amplitudes of the higher harmonics are closer to that of the excitation.

To diagnose the severity of this nonlinear damage, the results of all the damage severities are compared. The square root of spectral amplitude ratio of second harmonic to excitation frequency is adopted to show the degree of signal nonlinearity, which may serve as a damage index (DI), that is

$$\mathrm{DI} = \sqrt{\frac{A(2f_c)}{A(f_c)}} \tag{13}$$

where $A(f_c)$ and $A(2f_c)$ denote the spectral amplitude at the excitation frequency and the second higher harmonic. The variation of DI with crack damage intensity is shown for S0 and A0 packets in Figure 11(a) and for the new packet in Figure 11(b). It can be observed that the amplitude ratio DI is relatively small for both S0 and A0 packets, but it is quite big for the new wave packet even at small damage severity. The DI for S0 and A0 has a monotonically increasing relationship with the crack damage intensity. So the DI from the new packet could serve as an early indicator for the presence of a breathing crack, and the DI for the S0 and A0 packets can serve as an indicator of damage severity.

Comparison of numerical results between two nonlinear finite element methods

The numerical results from element activation/deactivation method and the contact analysis are compared. The superposed time-domain simulation signals and frequency spectrum from the two finite element methods for $r = 0.6$ case are shown in Figure 12(a) and (b). It could be observed that the solutions from these two methods agree well with each other. S0 packet has better accuracy; A0 and new packet have slight phase and

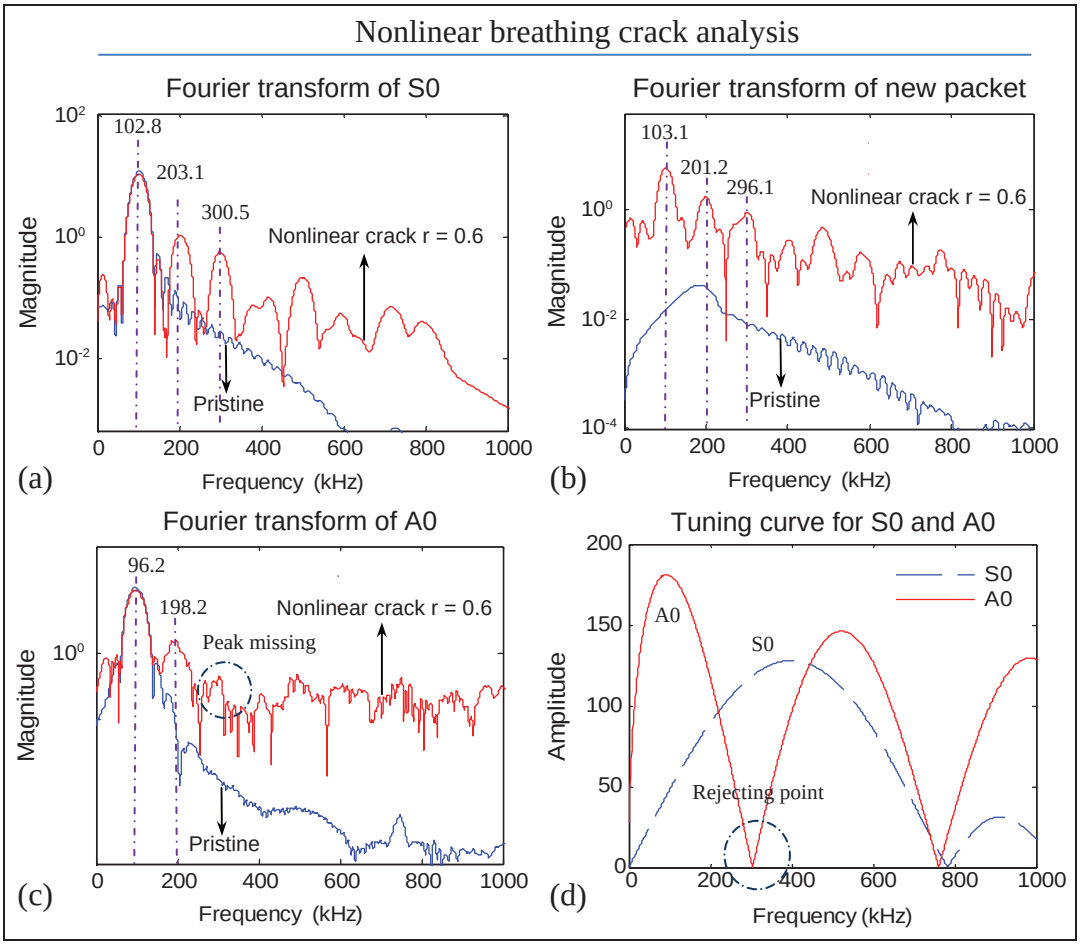

Figure 10. Frequency spectrum of the Lamb wave signals after nonlinear interaction with a crack: (a) S0 mode, (b) new packet, (c) A0 mode, and (d) tuning curves for A0 and S0 modes explaining the missing A0 peak in (c). Note the presence of distinctive nonlinear higher harmonics.

amplitude difference. In the frequency spectrum, it could be noticed that at lower frequency range (with two harmonics range) the two methods have good match, but at higher frequency they deviate from each other.

The difference between two solutions are measured and presented by the nondimensional L_2 norm

$$\|u_e - u_c\| = \sqrt{\frac{\sum_1^N (u_e - u_c)^2}{\sum_1^N u_c^2}} \tag{14}$$

where u_e and u_c are the solutions from element activation/deactivation method and contact analysis and N is the number of solution points in the time-domain signal. The L2 norm values for $r = 0.1, 0.2, 0.3, 0.4, 0.5,$ and 0.6 cases are plotted in Figure 13. It could be observed that for all the damage severity cases, both methods match stably well with each other.

Analytical modeling of Lamb waves interacting with nonlinear structural damage

Figure 14 shows the pitch–catch active sensing method for damage detection: the T-PWAS transducer generates ultrasonic-guided waves which propagate into the structure, interact with structural damage at $x = x_d$, carry the damage information with them, and are picked up by the R-PWAS transducer at $x = x_r$.

To model the damage effect on Lamb wave propagation, we consider the damage as a new wave source at $x = x_d$ and we add mode conversion and nonlinear sources at the damage location through damage interaction coefficients. The predictive analytical model for Lamb wave interaction with damage is constructed in frequency-domain in the following steps:

Step 1. Perform Fourier transform of the time-domain excitation signal $V_T(t)$ to obtain the frequency-domain excitation spectrum, $\tilde{V}_T(\omega)$.

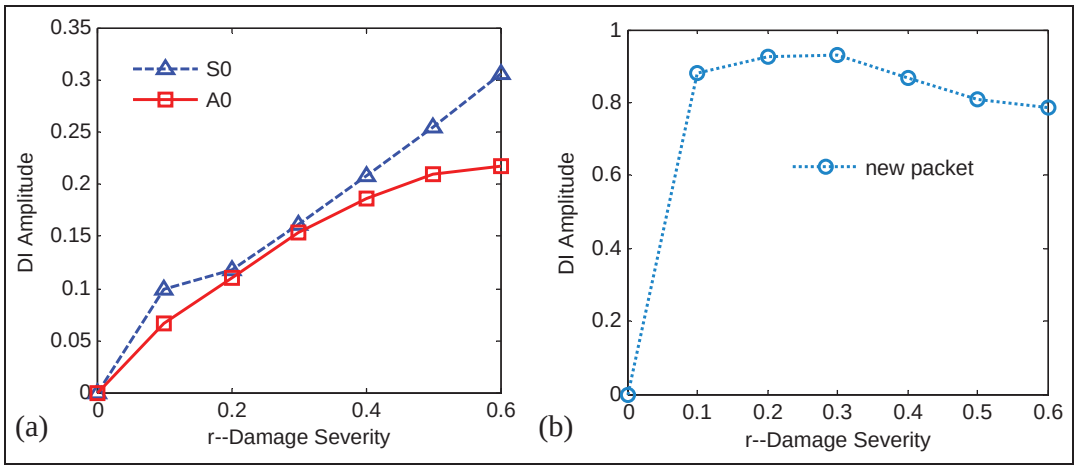

Figure 11. Damage severity index: (a) S0 and A0 packets and (b) new packet.

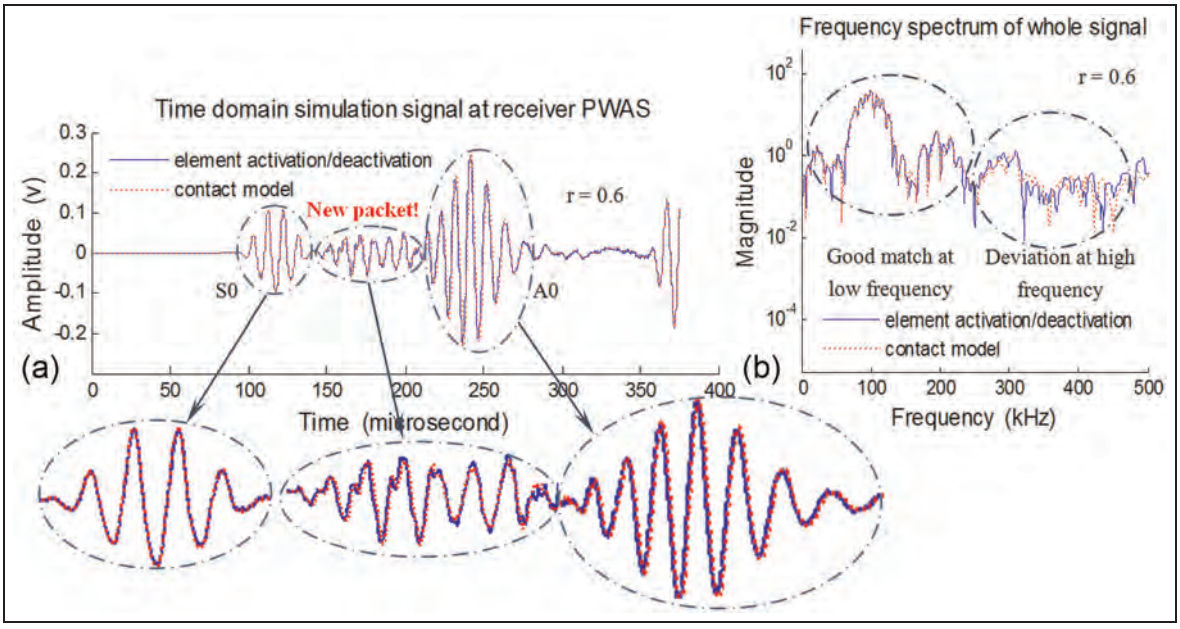

Figure 12. Comparison between signals from element activation/deactivation method and contact analysis (a) time-domain signal and (b) frequency spectrum.
PWAS: piezoelectric wafer active sensor.

Step 2. Calculate the frequency-domain structural transfer function $G(x_r, \omega)$ from T-PWAS to R-PWAS. The structure transfer function $G(x_r, \omega)$ is given by equation (99) of Giurgiutiu (2007: 327), which gives the in-plane wave strain at the plate surface as

$$\varepsilon_x(x,t) = -i\frac{a\tau_0}{\mu}\left\{\sum_{\xi^S}(\sin\xi^S a)\frac{N_S(\xi^S)}{D_S'(\xi^S)}e^{-i(\xi^S x-\omega t)} + \sum_{\xi^A}(\sin\xi^A a)\frac{N_A(\xi^A)}{D_A'(\xi^A)}e^{-i(\xi^A x-\omega t)}\right\} \quad (15)$$

where ξ is the frequency-dependent wavenumber of each Lamb wave mode and the superscripts S and A refer to symmetric and antisymmetric Lamb wave modes. If only the two fundamental modes, S0 and A0, are present, then $G(x_r, \omega)$ can be written as

$$G(x_r,\omega) = S(\omega)e^{-i\xi^S x_r} + A(\omega)e^{-i\xi^A x_r}$$

$$S(\omega) = \kappa_{\mathrm{PWAS}}\sin\xi^S a\frac{N_S(\xi^S)}{D_S'(\xi^S)},$$

$$A(\omega) = \kappa_{\mathrm{PWAS}}\sin\xi^A a\frac{N_A(\xi^A)}{D_A'(\xi^A)} \quad (16)$$

where

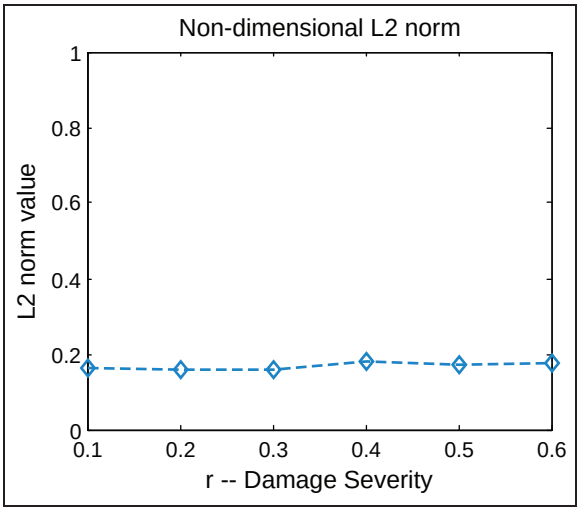

Figure 13. Difference between two solutions for various damage severities.

$$
\begin{aligned}
&N_s(\xi) = \xi\beta\left(\xi^2 + \beta^2\right)\cos\alpha d\cos\beta d;\\
&D_s = \left(\xi^2 - \beta^2\right)^2\cos\alpha d\sin\beta d + 4\xi^2\alpha\beta\sin\alpha d\cos\beta d\\
&N_A(\xi) = \xi\beta\left(\xi^2 + \beta^2\right)\sin\alpha d\sin\beta d;\\
&D_A = \left(\xi^2 - \beta^2\right)^2\sin\alpha d\cos\beta d + 4\xi^2\alpha\beta\cos\alpha d\sin\beta d\\
&\alpha^2 = \frac{\omega^2}{c_p^2} - \xi^2; \quad \beta^2 = \frac{\omega^2}{c_s^2} - \xi^2;\\
&c_p = \sqrt{\frac{\lambda + 2\mu}{\rho}}; \quad c_s = \sqrt{\frac{\mu}{\rho}}; \quad \kappa_{PWAS} = -i\frac{a\tau_0}{\mu}
\end{aligned}
\tag{17}
$$

where κ_{PWAS} is the complex transduction coefficient that converts applied voltage into guided wave strain at the T-PWAS, a half length of PWAS size, and d plate half thickness. The modal participation functions $S(\omega)$ and $A(\omega)$ determine the amplitudes of the S0 and A0 wave modes. The terms $\sin(\xi^S a)$ and $\sin(\xi^A a)$ control the tuning between the PWAS transducer and the Lamb waves. λ and μ are Lame's constants of the structural material; ρ is the material density. The wavenumber ξ of a specific mode for certain frequency ω is calculated from Rayleigh–Lamb equation

$$
\frac{\tan\beta d}{\tan\alpha d} = \left[\frac{-4\alpha\beta\xi^2}{\left(\xi^2 - \beta^2\right)^2}\right]^{\pm 1} \tag{18}
$$

where $+1$ exponent corresponds to symmetric Lamb wave modes and -1 exponent corresponds to antisymmetric Lamb wave modes.

Step 3. Multiply the structural transfer function by frequency-domain excitation signal to obtain the frequency-domain signal at the damage location, that is, $\tilde{V}_D(x_d,\omega) = G(x_d,\omega)\cdot\tilde{V}_T(\omega)$. Hence, the signal at the damage location is

$$
\tilde{V}_D(x_d,\omega) = S(\omega)\tilde{V}_T(\omega)e^{-i\xi^S x_d} + A(\omega)\tilde{V}_T(\omega)e^{-i\xi^A x_d} \tag{19}
$$

This signal could be decomposed into symmetric and antisymmetric components

$$
\tilde{V}_D^S(x_d,\omega) = S(\omega)\tilde{V}_T(\omega)e^{-i\xi^S x_d} \tag{20}
$$

$$
\tilde{V}_D^A(x_d,\omega) = A(\omega)\tilde{V}_T(\omega)e^{-i\xi^A x_d} \tag{21}
$$

Step 4. The wave signal at the damage location takes the damage information by considering transmission, reflection, mode conversion, and higher harmonics. Each of these addition phenomena is modeled as a new wave source at the damage location using damage interaction coefficients (Figure 15). We distinguish two damage interaction types: (a) linear and (b) nonlinear, as discussed next.

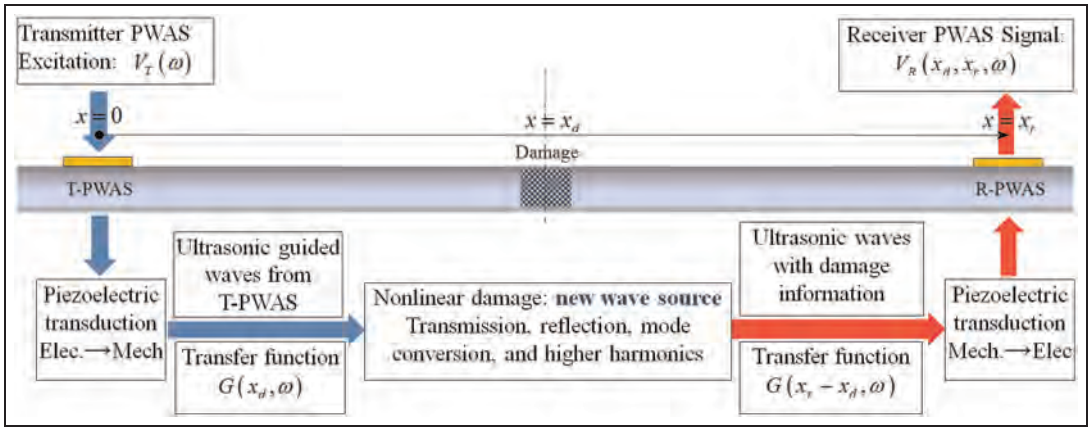

Figure 14. A pitch–catch configuration between a transmitter PWAS and a receiver PWAS.
PWAS: piezoelectric wafer active sensor.

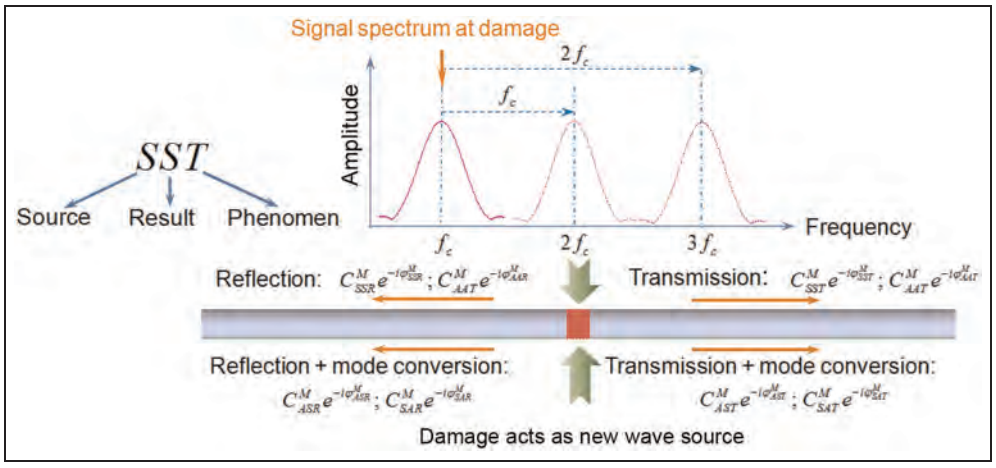

Figure 15. Modeling wave transmission, reflection, mode conversion, and higher harmonics components.

Linear damage interaction. Wave transmission, reflection, and mode conversion are realized by using complex-amplitude damage interaction coefficients. Our notations are as follows: we use three letters to describe the interaction phenomena, with the first letter denoting the incident wave type, the second letter standing for resulting wave type, and the third letter meaning propagation direction (transmission/reflection). For instance, SST (symmetric-symmetric-transmission) means the incident symmetric waves transmitted as symmetric waves, while SAT (symmetric-antisymmetric-transmission) means incident symmetric waves transmitted and mode converted to antisymmetric waves. Thus, the complex-amplitude damage interaction coefficient $C_{SST} \cdot e^{-i\varphi_{SST}}$ denotes the transmitted symmetric mode generated by incident symmetric mode with magnitude C_{SST} and phase φ_{SST}. Similarly, $C_{SAT} \cdot e^{-i\varphi_{SAT}}$ represents the transmitted antisymmetric mode generated by incident symmetric mode with magnitude C_{SAT} and phase φ_{SAT}. These coefficients are determined by the features of the damage and are to be imported into the WaveFormRevealer (WFR) model.

Nonlinear damage interaction. The center frequency of waves arriving at the damage location can be obtained from equations (20) and (21) as ω_c. The second and third higher harmonics act as wave sources with center frequencies of $2\omega_c$ and $3\omega_c$, respectively. Modeling of higher harmonics is achieved by moving the frequency-domain signal at the damage location to the right-hand side of the frequency axis by ω_c and $2\omega_c$, that is, $\tilde{V}_{2D}(x_d, \omega) = \tilde{V}_D(x_d, \omega - \omega_c)$ and $\tilde{V}_{3D}(x_d, \omega) = \tilde{V}_D(x_d, \omega - 2\omega_c)$ represent the second and third higher harmonics nonlinear wave source.

The nonlinear damage interaction coefficients are defined in the same way as the linear ones. For instance, the complex-amplitude damage interaction coefficient $C^M_{SST} \cdot e^{-i\varphi^M_{SST}}$ denotes the Mth higher harmonics transmitted symmetric mode generated by incident symmetric mode with magnitude C^M_{SST} and phase φ^M_{SST}.

Step 5. The guided waves from the new wave sources created at the damage location propagate through the rest of the structure and arrive at the R-PWAS. The received wave signal is calculated in frequency-domain as

$$\tilde{V}_R(x_d, x_r, \omega) = \sum_{M=1}^{m} \left[C^M_{SST} e^{-i\varphi^M_{SST}} \cdot \tilde{V}^S_{MD}(x_d, \omega) + C^M_{AST} e^{-i\varphi^M_{AST}} \cdot \tilde{V}^A_{MD}(x_d, \omega) \right] e^{-i\xi^S(x_r - x_d)} + \sum_{M=1}^{m} \left[C^M_{AAT} e^{-i\varphi^M_{AAT}} \cdot \tilde{V}^A_{MD}(x_d, \omega) + C^M_{SAT} e^{-i\varphi^M_{SAT}} \cdot \tilde{V}^S_{MD}(x_d, \omega) \right] e^{-i\xi^A(x_r - x_d)} \quad (22)$$

where M is the number of higher harmonics considered. For linear interaction with damage, M equals to one.

Step 6. Perform inverse Fourier transform to obtain the time-domain receiver sensing signal

$$V_R(x_d, x_r, t) = \mathrm{IFFT}\{\tilde{V}_R(x_d, x_r, \omega)\} \quad (23)$$

The analytical procedure is coded in MATLAB and resulted in the graphical user interface (GUI) called WFR as shown in Figure 16(a). Full details of this GUI and MATLAB code are available in Shen and Giurgiutiu (2012). The linear interaction between guided waves and damage is described by the transmission, reflection, and mode conversion parameters as shown in Figure 16(b). For example, SST represents the magnitude of transmitted S0 mode generated by an incoming S0 mode; whereas SAT and phi-SAT represent the magnitude and phase of the transmitted A0 mode resulting from the mode conversion of an incoming S0 mode.

For the purpose of this study, we have also introduced nonlinear parameters representing the result of the nonlinear interaction between the incoming guided

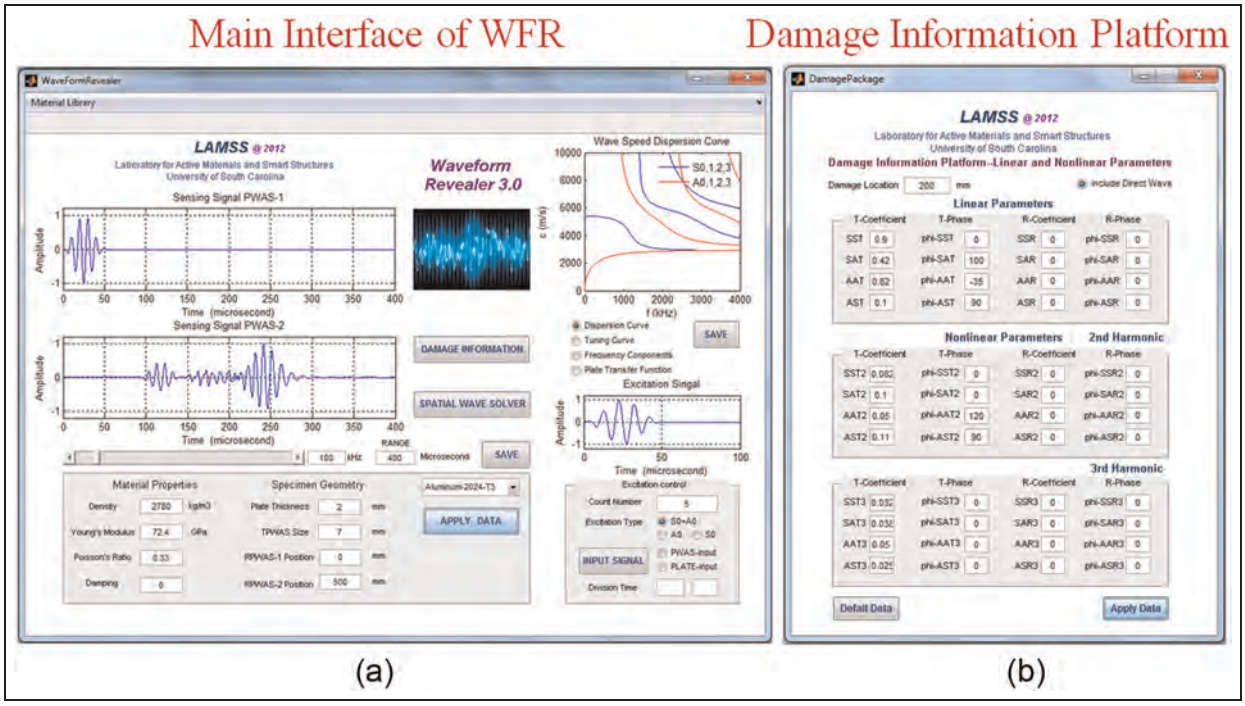

Figure 16. Graphical user interface of WFR. (a) General penal showing transmission and reception signals and (b) panel for insertion of damage interaction parameters.
WFR: WaveFormRevealer.

waves and the nonlinear damage. The nonlinear parameters are represented by the magnitude and phase of the second and third harmonic waves (transmitted, reflected, mode converted).

The values of these damage-interaction coefficients are not calculated by the WFR code. These coefficients may be determined experimentally or calculated through other methods: analytical, finite element method (FEM), boundary element method (BEM), etc. In this study, we used a trial-and-error approach to tune the WFR coefficients to the data simulated by the FEM analysis (similar tuning could be done with experimental data, and this approach may be tried in a future study). The tuning procedure is taken out via comparing the analytical solution with FEM results and adjusting the damage interaction coefficients in WFR until both results match with each other. The beneficial aspect of this analytical model is that one would not need to run the FEM model for the whole geometric domain. A local FEM mesh can provide the damage interaction coefficients. A local–global method then could be applied to find the predictive sensing signal (Gresil and Giurgiutiu, 2013a, 2013b). This will greatly enhance the computational efficiency of the target problem.

WFR allows users to conduct fast parametric studies. It may take several hours for commercial finite element software to obtain an acceptable-accuracy solution for high-frequency, long-distance propagating waves; but it takes only several seconds to obtain the same predictive solution with WFR. Besides, the WFR allows the user to play with all the parameters: PWAS size, plate material properties, sensor/damage locations, and damage type (linear/nonlinear damage with various severities).

Predictive solution of parametric analytical model for nonlinear wave propagation

The parametric analytical model is used to predict the nonlinear waveform of finite element simulations. The transmission, mode conversion coefficients, and phase information are obtained from the finite element results. In our analytical model, only the first three harmonics are considered (totally 12 variables need to be defined). The coefficients are shown in Table 1 and input into the WFR.

Figure 17 shows the comparison between finite element simulation and analytical solution from WFR. It is noticed that once the parameters for the analytical solution are given, the finite element simulation result and the analytical solution agree well with each other. The time-domain waveforms share the same nonlinear characteristics of noticeable zigzags in the new packet, and the frequency spectrums match well with each other as well. Since we only consider up to the third higher harmonic in this parametric analytical case study, the frequency-domain of analytical solution shows only the first three peaks, while the finite element

Table 1. Magnitude and phase parameters to input into analytical solution.

Magnitude coefficient	C^1_{SST}	C^1_{SAT}	C^1_{AAT}	C^1_{AST}	C^2_{SST}	C^2_{SAT}	C^2_{AAT}	C^2_{AST}	C^3_{SST}	C^3_{SAT}	C^3_{AAT}	C^3_{AST}
Value (normalized)	0.900	0.420	0.820	0.100	0.082	0.100	0.050	0.110	0.032	0.038	0.005	0.025
Phase coefficient	φ^1_{SST}	φ^1_{SAT}	φ^1_{AAT}	φ^1_{AST}	φ^2_{SST}	φ^2_{SAT}	φ^2_{AAT}	φ^2_{AST}	φ^3_{SST}	φ^3_{SAT}	φ^3_{AAT}	φ^3_{AST}
Value (°)	0	100	−35	90	0	0	120	90	0	0	0	0

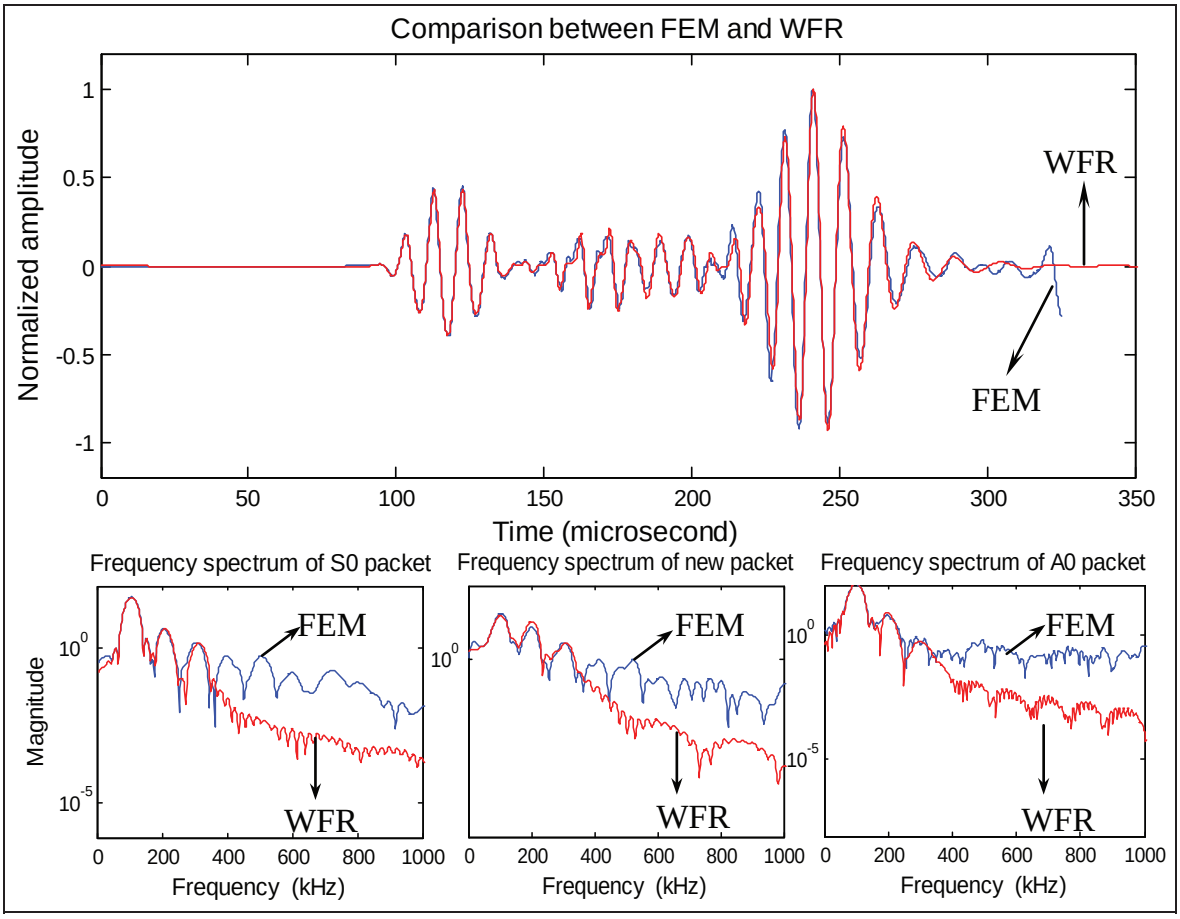

Figure 17. Comparison between FEM and analytical simulation (WFR).
FEM: finite element simulation; WFR: WaveFormRevealer.

solution have even higher harmonics. But the solution up to the third higher harmonics is accurate enough to render a decent waveform in time-domain. Given the damage-interaction parameters (DIPs), this predictive model can well describe high-frequency, long-distance, linear/nonlinear wave propagation.

Summary, conclusions, and future work

Summary

In this study, we presented predictive modeling of nonlinear guided wave propagation for structural health monitoring using both FEM and analytical approach. The nonlinearity of the guided waves was generated by interaction with a nonlinear breathing crack. Two nonlinear FEM techniques were used to simulate the breathing crack: (a) element activation/deactivation method and (b) contact analysis. The solutions obtained by these two FEM techniques compared quite well. A linear FEM analysis of this situation was also performed. A parametric analytical predictive model was built to simulate guided waves interaction with linear/nonlinear structural damage. This model was coded into MATLAB, and the WFR GUI was developed to obtain fast predictive waveform solutions for arbitrary combinations of sensor, structural properties, and damage.

Conclusions

It was found that the two FEM methods considered in this study can simulate equally well the nonlinear behavior of the breathing crack. It was found that the nonlinear interaction between guided waves and the breathing crack generates higher harmonics which were not found in the linear FEM simulation. A DI was proposed based on the amplitude ratio of the signal spectral harmonics to relate the signal nonlinearity with damage severity. This DI was applied to the S0 and A0 wave packets as well as to a new packet resulting from the interaction between the guided waves and the damage. It was found that the DI of the new packet is more sensitive to the presence of the crack, while the DIs of the S0 and A0 packets can provide monitoring information on the damage severity. It was found that the analytical predictive model WFR can predict the nonlinear effect in the signal using DIPs which were obtained by "trial and error." It was also found that computational time savings of several orders of magnitude are obtained by using the analytical model WFR instead of FEM methods.

Future work

The behavior of breathing crack under different interrogating wave amplitude should be studied, as well as the transition requirement from initially opened or closed crack into breathing crack. Experiments should be performed to verify these theoretical predictions. Rational methods of determining DIP values need to be found (not trial and error). Work should be carried out to extend the analysis to two-dimensional (2D) wave propagation (three-dimensional (3D) FEM and 2D WFR).

Funding

This work received support from Office of Naval Research # N00014-11-1-0271, Dr. Ignacio Perez, Technical Representative; Air Force Office of Scientific Research #FA9550-11-1-0133, Dr. David Stargel, Program Manager.

References

Bermes C, Kim J and Qu J (2007) Experimental characterization of material nonlinearity using Lamb waves. *Applied Physics Letters* 90: 021901.

Biwa S, Hiraiwa S and Matsumoto E (2006) Experimental and theoretical study of harmonic generation at contacting interface. *Ultrasonics* 44: e1319–e1322.

Biwa S, Nakajima S and Ohno N (2004) On the acoustic nonlinearity of solid-solid contact with pressure-dependent interface stiffness. *Journal of Applied Mechanics: Transactions of the ASME* 71: 508–515.

Cantrell JH (2009) Nondestructive evaluation of metal fatigue using nonlinear acoustics. *Review of Quantitative Nondestructive Evaluation* 1096: 19–32.

Corrosion Testing Laboratories, Inc. (2007) *Fatigue Cracking of Steam Line Expansion Bellow*. Newark, DE: Corrosion Testing Laboratories, Inc.

Deng MX (1999) Cumulative second-harmonic generation of Lamb-modes propagation in a solid plate. *Journal of Applied Physics* 85: 3051–3058.

Deng MX (2003) Analysis of second-harmonic generation of Lamb modes using a modal analysis approach. *Journal of Applied Physics* 94: 4152–4159.

Dutta D, Sohn H and Harries KA (2009) A nonlinear acoustic technique for crack detection in metallic structures. *Structural Health Monitoring* 8: 251–262.

Giurgiutiu V (2005) Tuned Lamb wave excitation and detection with piezoelectric wafer active sensors for structural health monitoring. *Journal of Intelligent Material Systems and Structures* 16: 291–306.

Giurgiutiu V (2007) *Structural Health Monitoring with Piezoelectric Wafer Active Sensors*. Burlington, MA: Academic Press.

Gresil M and Giurgiutiu V (2013a) Time-domain global-local prediction of guided waves interaction with damage. *Key Engineering Materials* 558: 116–127.

Gresil M and Giurgiutiu V (2013b) Time-domain hybrid global-local concept for guided-wave propagation with piezoelectric wafer active sensor. *Journal of Intelligent Material Systems and Structures*. Epub ahead of print 2 May. DOI: 10.1177/1045389x13486712.

Hagedorn P (1988) *Nonlinear Oscillations*. New York: Oxford University Press.

Hughes TJR, Taylor RL, Sackman JL, et al. (1975) A finite element method for a class of contact-impact problems. *Computer Methods in Applied Mechanics and Engineering* 8: 249–276.

Jhang KY (2009) Nonlinear ultrasonic techniques for nondestructive assessment of micro damage in material: a review. *International Journal of Materials* 10: 123–135.

Kruse W and Zagrai A (2009) Investigation of linear and nonlinear electromechanical impedance techniques for detection of fatigue damage in aerospace materials. In: *7th international workshop on structural health monitoring*, Stanford, CA, 9–11 September.

Kumar A, Torbert C, Jones JW, et al. (2009) Nonlinear ultrasonics for in situ damage detection during high frequency fatigue. *Journal of Applied Physics* 106: 024904-1–024904-9.

Lee TH and Choi IH (2008) The nonlinearity of guided waves in an elastic plate. *Modern Physics Letter* 22: 1135–1140.

Moser F, Jacobs LJ and Qu J (1999) Modeling elastic wave propagation in waveguides with the finite element method. *NDT & E International* 32: 225–234.

Nagy BP (1998) Fatigue damage assessment by nonlinear ultrasonic materials characterization. *Ultrasonics* 36: 375–381.

Naugoslnykh K and Ostrovsky L (1998) *Nonlinear Wave Processes in Acoustics*. Cambridge, MA: Cambridge University Press.

Richardson J (1979) Harmonic generation at an unbonded interface: I. Planar interface between semi-infinite elastic media. *International Journal of Engineering Science* 17: 73–85.

Shen Y and Giurgiutiu V (2012) Predictive simulation of nonlinear ultrasonics. In: *SPIE 2012 Smart Structures and NDE*, San Diego, CA, 11–15 March.

SHEN Y and Giurgiutiu V (2012) WaveFormRevealer 1-D – An Analytical Predictive Tool for the 1-D Simulation of Multimodal Guided Waves Propagation and Interaction with Damage: User's Guide and Theoretical Foundation. *Report # USC-ME-LAMSS-2012-101,* August 2012.

Srivastava A and di Scalea F (2009) On the existence of anti-symmetric or symmetric Lamb waves at nonlinear higher harmonics. *Journal of Sound and Vibration* 323(3–5): 932–943.

Original Article

Structural Health Monitoring
2014, Vol. 13(5) 491–511
© The Author(s) 2014
Reprints and permissions:
sagepub.co.uk/journalsPermissions.nav
DOI: 10.1177/1475921714532986
shm.sagepub.com

WaveFormRevealer: An analytical framework and predictive tool for the simulation of multi-modal guided wave propagation and interaction with damage

Yanfeng Shen and Victor Giurgiutiu

Abstract

This article presents the WaveFormRevealer—an analytical framework and predictive tool for the simulation of guided Lamb wave propagation and interaction with damage. The theory of inserting damage effects into the analytical model is addressed, including wave transmission, reflection, mode conversion, and nonlinear higher harmonics. The analytical model is coded into MATLAB, and a graphical user interface (WaveFormRevealer graphical user interface) is developed to obtain real-time predictive waveforms for various combinations of sensors, structural properties, and damage. In this article, the main functions of WaveFormRevealer are introduced. Case studies of selective Lamb mode linear and nonlinear interaction with damage are presented. Experimental verifications are carried out. The article finishes with summary and conclusions followed by recommendations for further work.

Keywords

Guided waves, structural health monitoring, damage detection, piezoelectric wafer active sensors, analytical model, nonlinear ultrasonics

Introduction

Guided waves retain a central function in the development of structural health monitoring (SHM) systems using piezoelectric wafer active sensor (PWAS) principles. The modeling of Lamb waves is challenging, because Lamb waves propagate in structures with multi-mode dispersive characteristics. At a certain value of the plate thickness-frequency product, several Lamb modes may exist simultaneously, and their phase velocities vary with frequency.[1–3] When Lamb waves interact with damage, they will be transmitted, reflected, scattered, and mode converted. Nonlinear interaction with damage may also exist, and this will introduce distinctive features like higher harmonics.[4–6] These aspects give rise to the complexity of modeling the interaction between Lamb waves and damage. To solve such complicated problems, numerical methods like finite element method (FEM) and boundary element method (BEM) are usually adopted. However, to ensure the accuracy of simulating high-frequency waves of short wavelengths, the transient analysis requires considerably small time step and very fine mesh ($T/\Delta t$, $\lambda/l_{FEM} \geq 20 \sim 30$), which is expensive both in computational time and computer resources.[7,8] Analytical model provides an alternative approach to attack the same problem with much less cost.[9]

PWAS transducers are a convenient way of transmitting and receiving guided waves in structures for SHM applications.[3] The analytical model of PWAS-generated Lamb waves and its tuning effect has been investigated, and a close-form solution for straight crested guided Lamb wave was derived by Giurgiutiu.[10] Extension of tuning concepts to 2D analytical models of Lamb waves generated by finite-dimensional piezoelectric transducers was given in Raghavan and Cesnik.[11] These analytical developments facilitate the understanding of PWAS-coupled Lamb waves for SHM applications.

Department of Mechanical Engineering, University of South Carolina, Columbia, SC, USA

Corresponding author:
Yanfeng Shen, Department of Mechanical Engineering, University of South Carolina, Columbia, SC 29208, USA.
Email: shen5@email.sc.edu

Downloaded from shm.sagepub.com by guest on August 20, 2014

However, these analytical solutions only applied to guided wave propagation in pristine structures, whereas the use of Lamb waves in SHM applications requires that their interaction with damage also be studied. After interacting with damage, Lamb waves will carry damage information resulting in waveforms with special characteristics (phase change, new wave packets generation through mode conversion, higher harmonic components, etc.), which need to be investigated for damage detection.

Several investigators have studied the interaction between guided waves and damage analytically using normal-mode expansion and boundary-condition matching.[12–18] Damage interaction coefficients were derived to quantify the guided wave transmission, reflection, mode conversion, and scatter at the damage site. Due to their mathematical complexity, these analytical solutions are restricted to simple damage geometries: notches, holes, and partially through holes. Extension to more complicated damage geometries has been attempted through series expansion of the rugged damage contour. In the generic case of arbitrary-shape damage, the numerical approaches using space discretization (FEM, BEM) are used due to their convenience, but on the expense of orders of magnitude increase in computational time and/or computer resources.

The design of a SHM system requires computationally efficient predictive tools that permit the exploration of a wide parameter space to identify the optimal combination between the transducers type, size, number, and guided wave characteristics (mode type, frequency, and wavelength) to achieve best detection and quantification of a certain damage type. Such parameter space exploration desiderate can be best achieved with analytical tools which are fast and efficient.

In this article, we describe an analytical approach based on the one-dimensional (1D) (straight crested) guided wave propagation analysis. In our study, we inserted the damage effect into the analytical model by considering wave transmission, reflection, mode conversion, and higher harmonics components described through damage interaction coefficients at the damage site. We do not attempt to derive these damage interaction coefficients here, but assume that they are available either from literature or from FEM, BEM analysis performed separately in a separate computational module. This analytical approach was coded into MATLAB and the WaveFormRevealer (WFR) graphical user interface (GUI) was developed. The WFR can generate fast predictions of waveforms resulting from Lamb wave interaction with damage for arbitrary positioning of PWAS transmitters and receivers with respect to damage and with respect to each other. The users may choose their own excitation signal, PWAS size, structural parameters, and damage description. The current version of the WFR code is limited to 1D (straight crested) guided wave propagation; extension of this approach to two-dimensional (2D) (circular crested) guided wave propagation will be attempted in the future.

PWAS Fundamentals

PWAS couple the electrical and mechanical effects (mechanical strain, S_{ij}; mechanical stress, T_{kl}; electrical field, E_k; and electrical displacement, D_j) through the tensorial piezoelectric constitutive equations

$$\begin{aligned} S_{ij} &= s^E_{ijkl} T_{kl} + d_{kij} E_k \\ D_j &= d_{jkl} T_{kl} + \varepsilon^T_{jk} E_k \end{aligned} \tag{1}$$

where s^E_{ijkl} is the mechanical compliance of the material measured at zero electric field ($E = 0$), ε^T_{jk} is the dielectric permittivity measured at zero mechanical stress ($T = 0$), and d_{jkl} represents the piezoelectric coupling effect. PWAS utilize the d_{31} coupling between in-plane strains, S_1, S_2, and transverse electric field E_3.

PWAS transducers can be used as both transmitters and receivers. Their modes of operation are shown in Figure 1. PWAS can serve several purposes[3]: (a) high-bandwidth strain sensors, (b) high-bandwidth wave exciters and receivers, (c) resonators, and (d) embedded modal sensors with the electromechanical (E/M) impedance method. By application types, PWAS transducers can be used for (a) active sensing of far-field damage using pulse-echo, pitch-catch, and phased-array methods, (b) active sensing of near-field damage using high-frequency E/M impedance method and thickness gage mode, and (c) passive sensing of damage-generating events through detection of low-velocity impacts and acoustic emission at the tip of advancing cracks (Figure 1). The main advantage of PWAS over conventional ultrasonic probes is in their small size, light-weight, low profile, and small cost. In spite of their small size, PWAS are able to replicate many of the functions performed by conventional ultrasonic probes.

Analytical modeling of Lamb waves interacting with damage

Analytical modeling of guided Lamb waves propagation in a pristine structure

One aspect of the difficulties in modeling Lamb wave propagation is due to their multi-mode feature. WFR is capable of modeling multi-mode Lamb wave propagation in structures. From Rayleigh–Lamb equation, it is found that the existence of certain Lamb mode depends on the plate thickness-frequency product. The fundamental S0 and A0 modes will always exist, but

Downloaded from shm.sagepub.com by guest on August 20, 2014

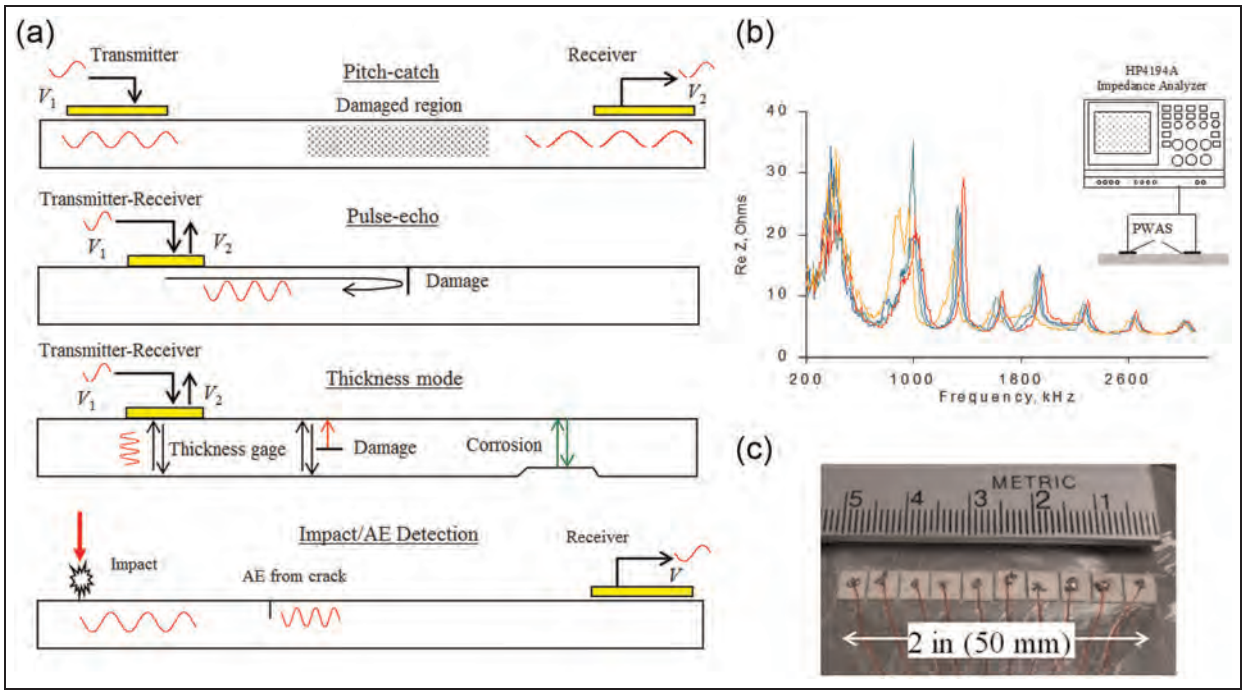

Figure 1. Schematic of PWAS application modes (from Giurgiutiu[19]): (a) propagating Lamb waves, (b) standing Lamb waves (E/M impedance), and (c) PWAS phased arrays.
E/M: electromechanical; PWAS: piezoelectric wafer active sensor; AE: acoustic emission.

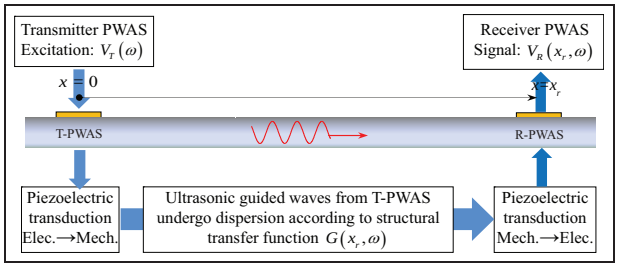

Figure 2. A pitch-catch configuration between a transmitter PWAS (T-PWAS) and a receiver PWAS.
PWAS: piezoelectric wafer active sensor.

the higher modes will only appear beyond the cutoff frequencies.[1]

This section describes how an electrical tone burst applied to a transmitter PWAS (T-PWAS) transducer propagates through a structural waveguide to the receiver PWAS (R-PWAS) transducer in pitch-catch mode (Figure 2).

The propagation takes place through ultrasonic guided Lamb waves which are generated at the T-PWAS through piezoelectric transduction and then captured and converted back into electric signal at the R-PWAS. Since several Lamb wave modes traveling with different wave speeds exist simultaneously, the electrical tone-burst applied on the T-PWAS will generate several wave packets. These wave packets will travel independently through the waveguide and will arrive at different times at the R-PWAS where they are converted back into electric signals through piezoelectric transduction. The predictive analytical model for Lamb wave propagation between the T-PWAS and R-PWAS is constructed in frequency domain in the following steps (Figure 3(a)).

Step 1. Perform Fourier transform of the time-domain excitation signal $V_T(t)$ to obtain the frequency-domain excitation spectrum, $\tilde{V}_T(\omega)$. For a tone burst, the signal $V_T(t)$ and its Fourier transform $\tilde{V}_T(\omega)$ are shown in Figure 4.

Step 2. Calculate the frequency-domain structural transfer function $G(x_r,\omega)$ from T-PWAS to R-PWAS. The structure transfer function $G(x_r,\omega)$ is given in equation (99) in the study by Giurgiutiu,[3] page 327, which gives the in-plane wave strain at the plate surface as

$$\varepsilon_x(x,t) = -i\frac{a\tau_0}{\mu}\left\{\sum_{\xi^S}(\sin\xi^S a)\frac{N_S(\xi^S)}{D'_S(\xi^S)}e^{-i(\xi^S x-\omega t)} + \sum_{\xi^A}(\sin\xi^A a)\frac{N_A(\xi^A)}{D'_A(\xi^A)}e^{-i(\xi^A x-\omega t)}\right\} \quad (2)$$

Downloaded from shm.sagepub.com by guest on August 20, 2014

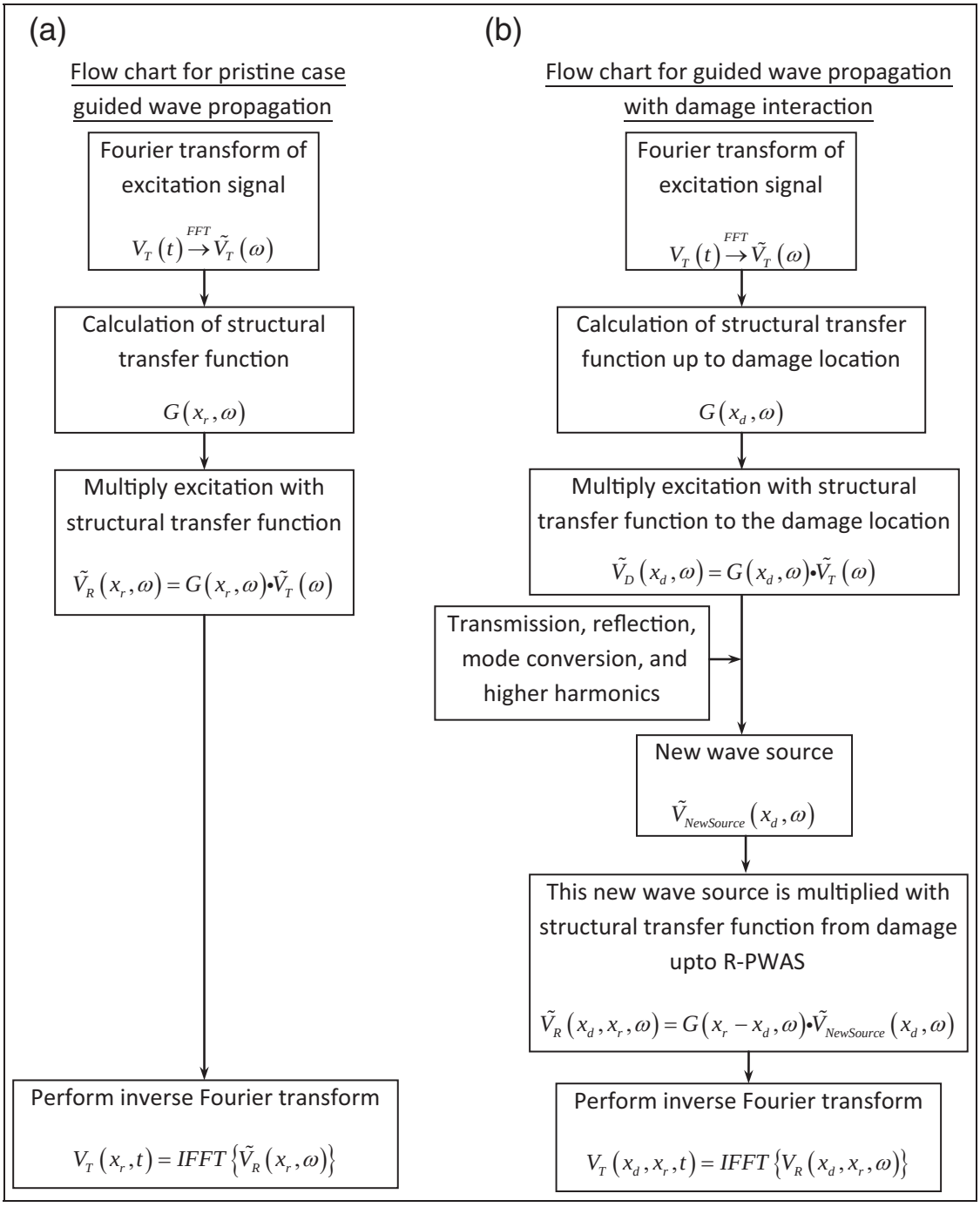

Figure 3. WaveFormRevealer flow charts: (a) propagation in a pristine structural waveguide and (b) propagation and interaction with damage at location x_d.

where ξ is the frequency-dependent wavenumber of each Lamb wave mode and the superscripts S and A refer to symmetric and antisymmetric Lamb wave modes. If only the two fundamental modes, S0 and A0, are present, then $G(x_r, \omega)$ can be written as

$$\begin{aligned} G(x_r, \omega) &= S(\omega) e^{-i\xi^S x_r} + A(\omega) e^{-i\xi^A x_r} \\ S(\omega) &= \kappa_{PWAS} \sin \xi^S a \frac{N_S(\xi^S)}{D'_S(\xi^S)}, \\ A(\omega) &= \kappa_{PWAS} \sin \xi^A a \frac{N_A(\xi^A)}{D'_A(\xi^A)} \end{aligned} \tag{3}$$

Downloaded from shm.sagepub.com by guest on August 20, 2014

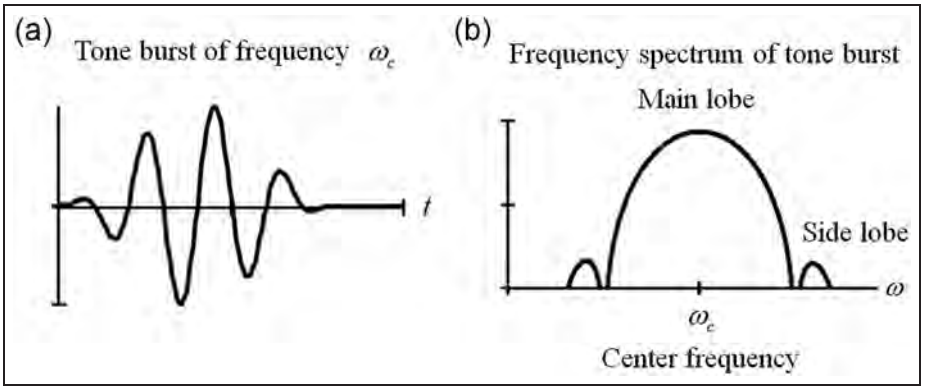

Figure 4. Tone burst signal: (a) time domain and (b) frequency domain (From Giurgiutiu,[3] p. 153).

where

$$
\begin{aligned}
N_s(\xi) &= \xi\beta\left(\xi^2+\beta^2\right)\cos\alpha d\cos\beta d;\\
D_s &= \left(\xi^2-\beta^2\right)^2\cos\alpha d\sin\beta d+4\xi^2\alpha\beta\sin\alpha d\cos\beta d\\
N_A(\xi) &= -\xi\beta\left(\xi^2+\beta^2\right)\sin\alpha d\sin\beta d;\\
D_A &= \left(\xi^2-\beta^2\right)^2\sin\alpha d\cos\beta d+4\xi^2\alpha\beta\cos\alpha d\sin\beta d\\
\alpha^2 &= \frac{\omega^2}{c_p^2}-\xi^2;\quad \beta^2=\frac{\omega^2}{c_s^2}-\xi^2;\quad c_p=\sqrt{\frac{\lambda+2\mu}{\rho}};\\
c_s &= \sqrt{\frac{\mu}{\rho}};\quad \kappa_{PWAS}=-i\frac{a\tau_0}{\mu}
\end{aligned}
\tag{4}
$$

κ_{PWAS} is the complex transduction coefficient that converts applied voltage into guided wave strain at the T-PWAS, a is half length of PWAS size, and d is plate half thickness. The modal participation functions $S(\omega)$ and $A(\omega)$ determine the amplitudes of the S0 and A0 wave modes. The terms $\sin(\xi^S a)$ and $\sin(\xi^A a)$ control the tuning between the PWAS transducer and the Lamb waves. λ and μ are Lame's constants of the structural material, and ρ is the material density. The wavenumber ξ of a specific mode for certain frequency ω is calculated from Rayleigh–Lamb equation

$$
\frac{\tan\beta d}{\tan\alpha d}=\left[\frac{-4\alpha\beta\xi^2}{\left(\xi^2-\beta^2\right)^2}\right]^{\pm 1} \tag{5}
$$

where $+1$ exponent corresponds to symmetric Lamb wave modes and -1 exponent corresponds to antisymmetric Lamb wave modes.

Step 3. Multiply the structural transfer function by frequency-domain excitation signal (Figure 4(b)) to obtain the frequency-domain signal at the R-PWAS, that is, $\tilde{V}_R(x_r,\omega)=G(x_r,\omega)\cdot\tilde{V}_T(\omega)$. Hence, the wave arriving at the R-PWAS location is

$$
\tilde{V}_R(x_r,\omega)=S(\omega)\tilde{V}_T(\omega)e^{-i\xi^S x_r}+A(\omega)\tilde{V}_T(\omega)e^{-i\xi^A x_r} \tag{6}
$$

This signal in equation (6) can be decomposed into symmetric and antisymmetric components

$$
\tilde{V}_R^S(x_r,\omega)=S(\omega)\tilde{V}_T(\omega)e^{-i\xi^S x_r} \tag{7}
$$

$$
\tilde{V}_R^A(x_r,\omega)=A(\omega)\tilde{V}_T(\omega)e^{-i\xi^A x_r} \tag{8}
$$

Step 4. Perform the inverse Fourier transform to obtain the time-domain wave signal at the R-PWAS, that is

$$
V_R(x_r,t)=IFFT\{\tilde{V}_R(x_r,\omega)\} \tag{9}
$$

Due to the multi-mode character of guided Lamb wave propagation, the received signal has at least two separate wave packets, S0 and A0 (Figure 5).

This analysis can be extended to include higher guided wave modes (S1, A1, etc.), that is

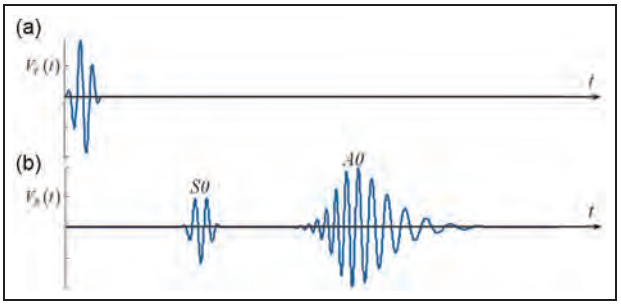

Figure 5. (a) T-PWAS signal and (b) R-PWAS signal.
T-PWAS: transmitter piezoelectric wafer active sensor; R-PWAS: receiver piezoelectric wafer active sensor.

Downloaded from shm.sagepub.com by guest on August 20, 2014

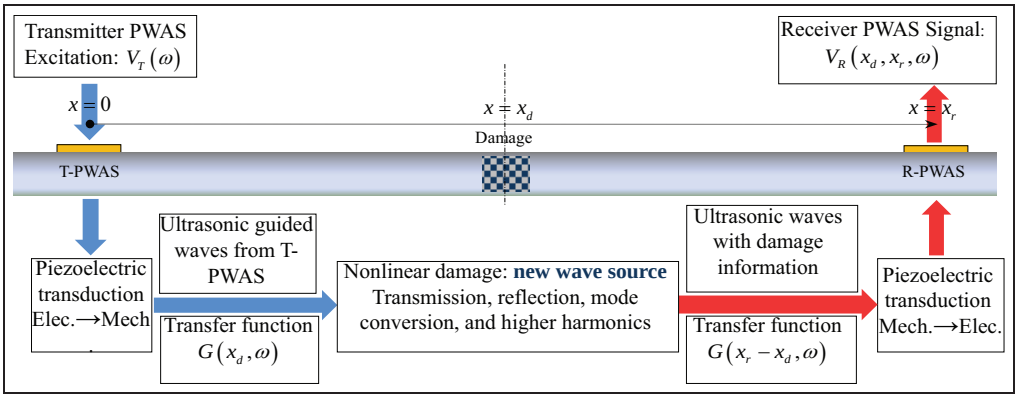

Figure 6. A pitch-catch configuration between a transmitter PWAS and a receiver PWAS.
PWAS: receiver piezoelectric wafer active sensor.

$$\tilde{V}_R(x_r,\omega) = \sum_{\xi^S} S(\omega)\tilde{V}_T(\omega)e^{-i\xi^S x_r} + \sum_{\xi^A} A(\omega)\tilde{V}_T(\omega)e^{-i\xi^A x_r} \tag{10}$$

All the wave modes propagate independently in the structure. The final waveform will be the superposition of all the propagating waves and will have the contribution from each Lamb mode.

Insertion of damage effects into the analytical model

Figure 6 shows the pitch-catch active sensing method for damage detection: the T-PWAS transducer generates ultrasonic guided waves which propagate into the structure, interact with structural damage at $x = x_d$, carry the damage information with them, and are picked up by the R-PWAS transducer at $x = x_r$.

To model the damage effect on Lamb wave propagation, we consider the damage as a new wave source at $x = x_d$, and we add mode conversion and nonlinear sources at the damage location through damage interaction coefficients. The predictive analytical model for Lamb wave interaction with damage is constructed in frequency domain in the following steps:

Step 1. This step is identical to step 1 of the pristine case. Perform Fourier transform of the time-domain excitation signal $V_T(t)$ to obtain the frequency-domain excitation spectrum, $\tilde{V}_T(\omega)$.

Step 2. Calculate the frequency-domain structural transfer function up to the damage location, $G(x_d, \omega)$. The structure transfer function $G(x_d, \omega)$ is similar to equation (3) of previous section, only that $x = x_d$, that is

$$G(x_d,\omega) = S(\omega)e^{-i\xi^S x_d} + A(\omega)e^{-i\xi^A x_d} \tag{11}$$

Step 3. Multiply the structural transfer function by frequency-domain excitation signal to obtain the frequency-domain signal at the damage location, that is, $\tilde{V}_D(x_d,\omega) = G(x_d,\omega)\cdot\tilde{V}_T(\omega)$. Hence, the signal at the damage location is

$$\tilde{V}_D(x_d,\omega) = S(\omega)\tilde{V}_T(\omega)e^{-i\xi^S x_d} + A(\omega)\tilde{V}_T(\omega)e^{-i\xi^A x_d} \tag{12}$$

This signal could be decomposed into symmetric and antisymmetric components

$$\tilde{V}_D^S(x_d,\omega) = S(\omega)\tilde{V}_T(\omega)e^{-i\xi^S x_d} \tag{13}$$

$$\tilde{V}_D^A(x_d,\omega) = A(\omega)\tilde{V}_T(\omega)e^{-i\xi^A x_d} \tag{14}$$

Step 4. The wave signal at the damage location takes the damage information by considering transmission, reflection, mode conversion, and higher harmonics. Each of these addition phenomena is modeled as a new wave source at the damage location using damage interaction coefficients (Figure 7). We distinguish two damage interaction types: (a) linear and (b) nonlinear, as discussed next.

Linear damage interaction. Wave transmission, reflection, and mode conversion are realized by using complex-amplitude damage interaction coefficients. Our notations are as follows: we use three letters to describe the interaction phenomena, with the first letter denoting the incident wave type, the second letter standing for resulting wave type, and the third letter meaning propagation direction (transmission/reflection). For instance, symmetric-symmetric-transmission (SST) means the incident symmetric waves transmitted as symmetric waves, while symmetric-antisymmetric-transmission (SAT) means incident symmetric waves transmitted and mode converted to antisymmetric waves. Thus, the complex-amplitude damage interaction coefficient $C_{SST}\cdot e^{-i\varphi_{SST}}$ denotes the transmitted symmetric mode generated by incident symmetric mode with magnitude

Downloaded from shm.sagepub.com by guest on August 20, 2014

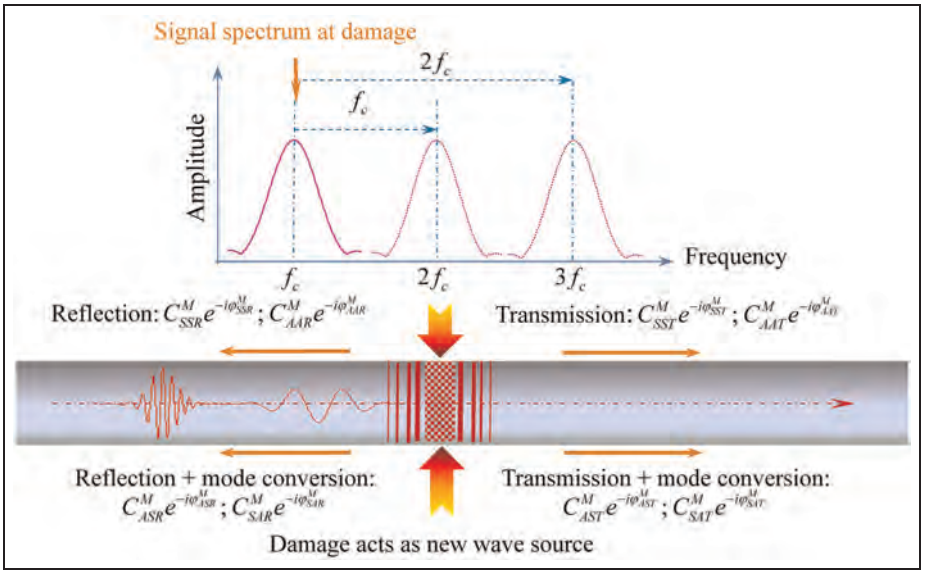

Figure 7. Modeling wave transmission, reflection, mode conversion, and higher harmonics components.

C_{SST} and phase φ_{SST}. Similarly, $C_{SAT} \cdot e^{-i\varphi_{SAT}}$ represents the transmitted antisymmetric mode generated by incident symmetric mode with magnitude C_{SAT} and phase φ_{SAT}. These coefficients are determined by the features of the damage and are to be imported into the WFR model.

Nonlinear damage interaction. The center frequency of waves arriving at the damage location can be obtained from equations (13) and (14) as ω_c. The second and third higher harmonics act as wave sources with center frequencies of $2\omega_c$ and $3\omega_c$, respectively. Modeling of higher harmonics is achieved by moving the frequency-domain signal at the damage location to the right-hand side of the frequency axis by ω_c and $2\omega_c$, that is, $\tilde{V}_{2D}(x_d, \omega) = \tilde{V}_D(x_d, \omega - \omega_c)$ and $\tilde{V}_{3D}(x_d, \omega) = \tilde{V}_D(x_d, \omega - 2\omega_c)$ represent the second and third higher harmonics nonlinear wave source.

The nonlinear damage interaction coefficients are defined in the same way as the linear ones. For instance, the complex-amplitude damage interaction coefficient $C^M_{SST} \cdot e^{-i\varphi^M_{SST}}$ denotes the Mth higher harmonics transmitted symmetric mode generated by incident symmetric mode with magnitude C^M_{SST} and phase φ^M_{SST}.

Step 5. The guided waves from the new wave sources created at the damage location propagate through the rest of the structure and arrive at the R-PWAS. The received wave signal is calculated in frequency domain as

$$\begin{aligned}\tilde{V}_R(x_d, x_r, \omega) = &\sum_{M=1}^{m}\left[C^M_{SST}e^{-i\varphi^M_{SST}} \cdot \tilde{V}^S_{MD}(x_d, \omega) + C^M_{AST}e^{-i\varphi^M_{AST}} \cdot \tilde{V}^A_{MD}(x_d, \omega)\right]e^{-i\xi^S(x_r - x_d)} \\ &+ \sum_{M=1}^{m}\left[C^M_{AAT}e^{-i\varphi^M_{AAT}} \cdot \tilde{V}^A_{MD}(x_d, \omega) + C^M_{SAT}e^{-i\varphi^M_{SAT}} \cdot \tilde{V}^S_{MD}(x_d, \omega)\right]e^{-i\xi^A(x_r - x_d)}\end{aligned} \quad (15)$$

where M is the number of higher harmonics considered. For linear interaction with damage, M equals to one.

Step 6. Perform inverse Fourier transform to obtain the time-domain receiver sensing signal

$$V_R(x_d, x_r, t) = IFFT\{\tilde{V}_R(x_d, x_r, \omega)\} \quad (16)$$

It should be noted that the above analysis only considers S0 and A0 modes. But the principle could be easily extended to higher modes (S1, A1, etc.). The difficulty with extending to higher modes will be on defining the increasing number of transmission, reflection, and mode conversion coefficients. For each excited Lamb mode, the interaction with damage may result in more mode conversion possibilities. In this study, the WFR has been designed to simulate (a) multi-mode (S0, A0, S1, A1) Lamb waves propagation in pristine plates and (b) fundamental modes (S0 and A0) Lamb wave interaction with damage.

WFR interface and main functions

The analytical representation of this process was coded in MATLAB and resulted in the GUI called WFR shown in Figure 8.

Downloaded from shm.sagepub.com by guest on August 20, 2014

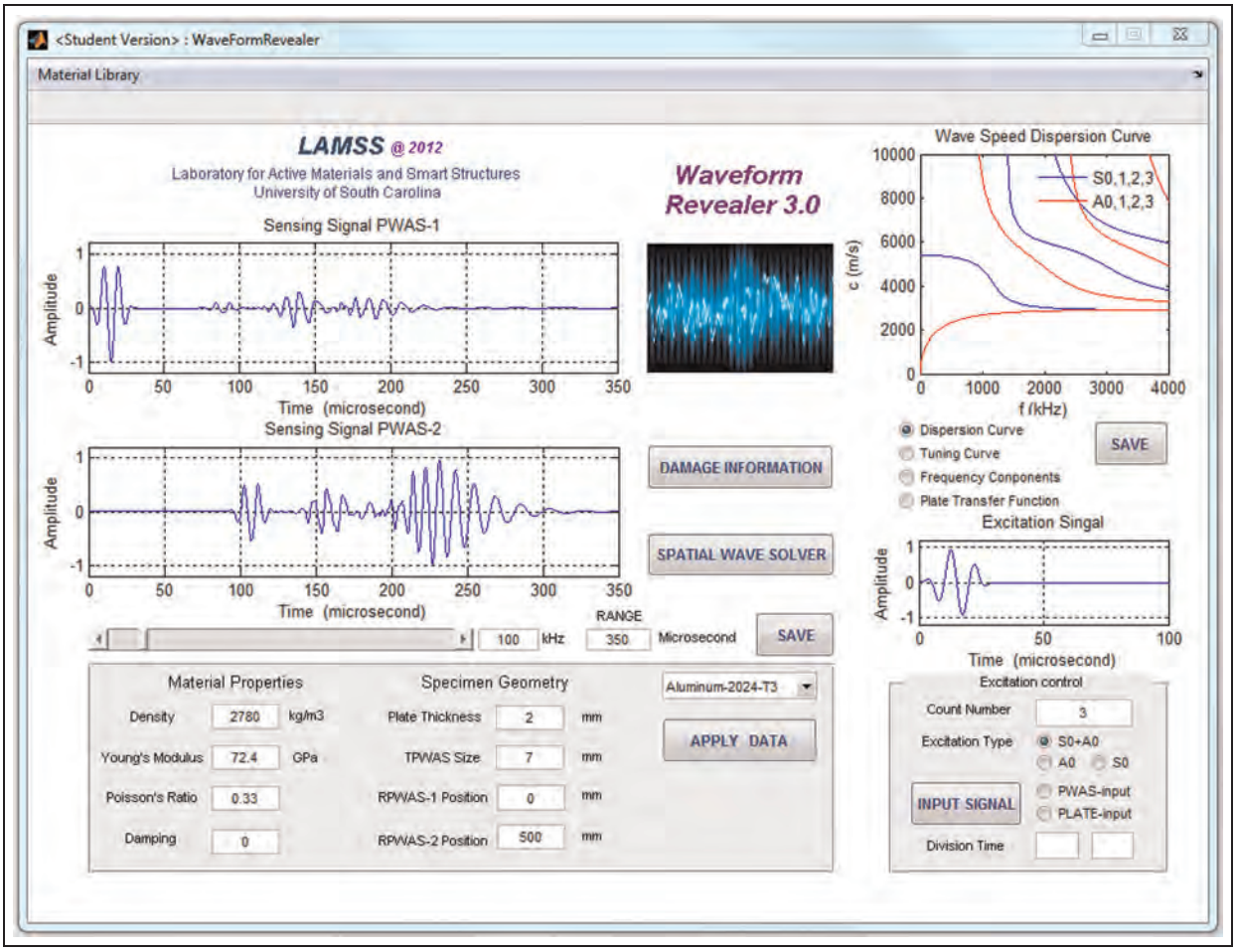

Figure 8. Main GUI of WaveFormRevealer.
GUI: graphic user interface.

WFR allows users to control several parameters: structure material properties, PWAS size, location of sensors, location of damage, damage type (linear/nonlinear damage of various severities), and excitation signal (frequencies, count numbers, signal mode excitation, arbitrary waveform type, etc.). Dual display of waveforms allows for the sensing signals to be shown at two different sensor locations. For instance, Figure 8 shows two receiver waveforms at locations $x_1 = 0$ mm and $x_2 = 500$ mm as measured from the transmitter (in this case $x_1 = 0$ mm means that R-PWAS-1 collocated with the T-PWAS). Thus, PWAS-1 shows the reflections from damage, and PWAS-2 shows the signal modified after passing through the damage. Users are able to conduct fast parametric studies with WFR. It may take several hours for commercial finite element software to obtain an acceptable-accuracy solution for high-frequency, long distance propagating waves, but it takes only several seconds to obtain the same solution with WFR. Besides analytical waveform solutions, the WFR can also provide users with wave speed dispersion curves, tuning curves, frequency components of received wave packets, structure transfer function, and so on. All the calculated results are fully available to the user, and could be saved in Excel files by clicking the "SAVE" button. Figure 9 shows a case study for Lamb wave propagation of a 100 kHz tone burst in a 1-mm-thick aluminum plate. Figure 9(a) shows the dispersion curves; Figure 9(b) shows the excitation spectrum overlap with the S0 and A0 tuning curves. Figure 9(c) shows the spectra of the S0 and A0 packets displaying frequency shifts to the right and to the left, respectively, due to the interaction between excitation spectrum and the tuning curves. Figure 9(d) shows the structure transfer function $G(x, \omega)$.

Besides the main interface, WFR has two subinterfaces shown in Figure 10: (a) damage information platform and (b) guided wave spatial propagation solver. The *damage information platform* allows users to input the damage location and damage interaction coefficients. For example, SST represents the magnitude of transmitted S0 mode generated by an incoming

Downloaded from shm.sagepub.com by guest on August 20, 2014

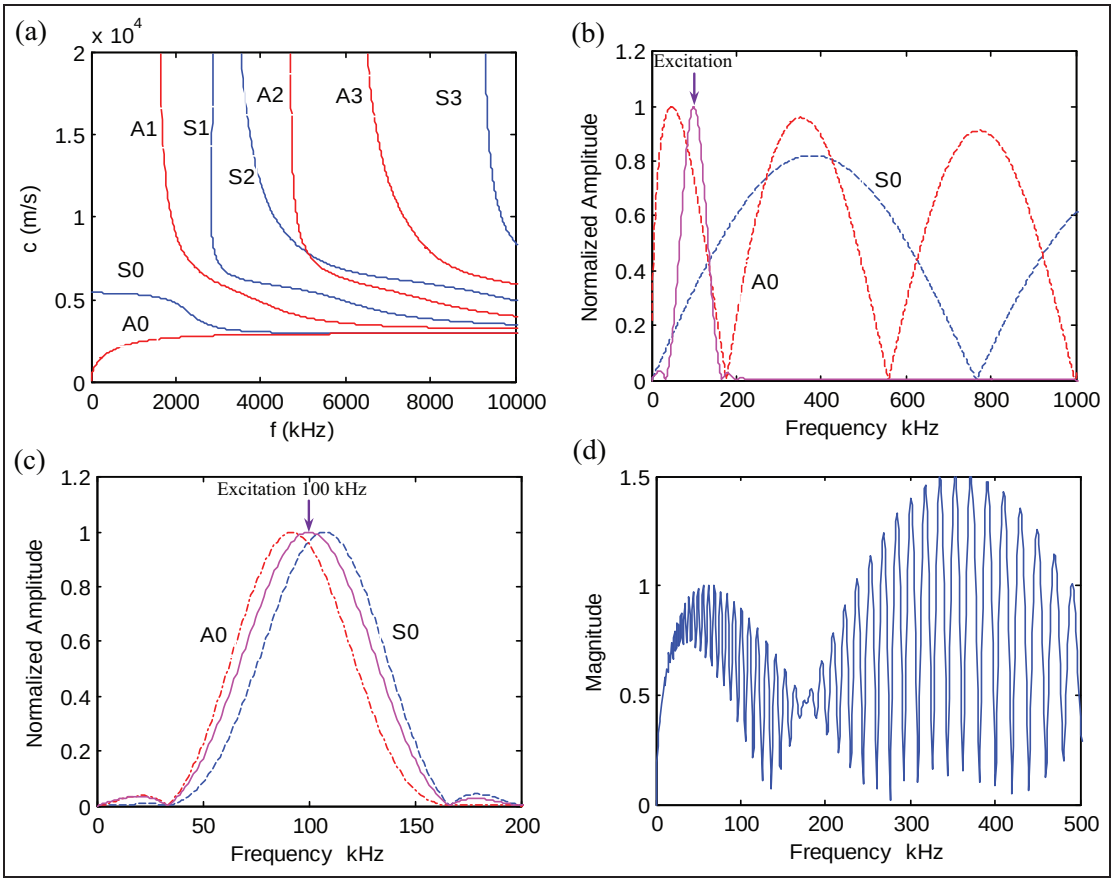

Figure 9. Calculation of various quantities in Lamb wave propagation: (a) wave speed dispersion curve, (b) tuning curve, (c) frequency contents of received wave packets, and (d) structure transfer function.

S0 mode, whereas SAT and phi-SAT represent the magnitude and phase of the transmitted A0 mode resulting from the mode conversion of an incoming S0 mode. The values of these damage interaction coefficients are not calculated by the WFR. This gives the users the freedom to define their own specific problem. For instance, a particular type of damage (plastic zone, fatigue, cracks) with certain degree of severity will have different interaction characteristics with the interrogating guided waves. These coefficients may be determined experimentally or calculated through other methods (analytical, FEM, BEM, etc.). Among all the above methods, FEM approach shows good results for obtaining the interaction coefficients of arbitrary shaped damage. Successful examples and details can be found in Velichko and Wilcox[20,21] and Moreau et al.[22] In an example presented later in this study, we used a trial-and-error approach to tune the WFR coefficients to the data obtained from experiments and finite element simulations.

The *spatial propagation solver* is like a B-scan. Using the analytical procedure, we obtain the time-domain waveform solution at various locations along the structure. Thus, the time-domain waveform solutions of a sequence of points along the wave propagation path are obtained. If we select the sequence of solution points fine enough, a time-spatial domain solution of the wave field is obtained. The spatial solution of wave field at a particular instance in time is available as shown in Figure 10(b). After the time-spatial solution of wave field is obtained, we can do the frequency–wavenumber analysis[23] to see the wave components of the signal (Figure 11). These will be illustrated in the case studies discussed later in this article.

Case studies

Linear interaction with damage of selective Lamb wave modes

WFR allows users to select single mode (S0 and A0) or multi-mode (S0 and A0) to be excited into the structure. Three test cases were conducted: (a) incident S0 wave linear interaction with damage, (b) incident A0 wave linear interaction with damage, and (c) combined S0 and A0 waves linear interaction with damage. The test case setup is shown in Figure 12. The T-PWAS and R-PWAS are placed 600 mm away from each other on a 1-mm-thick aluminum 2024-T3 plate. The damage is

Downloaded from shm.sagepub.com by guest on August 20, 2014

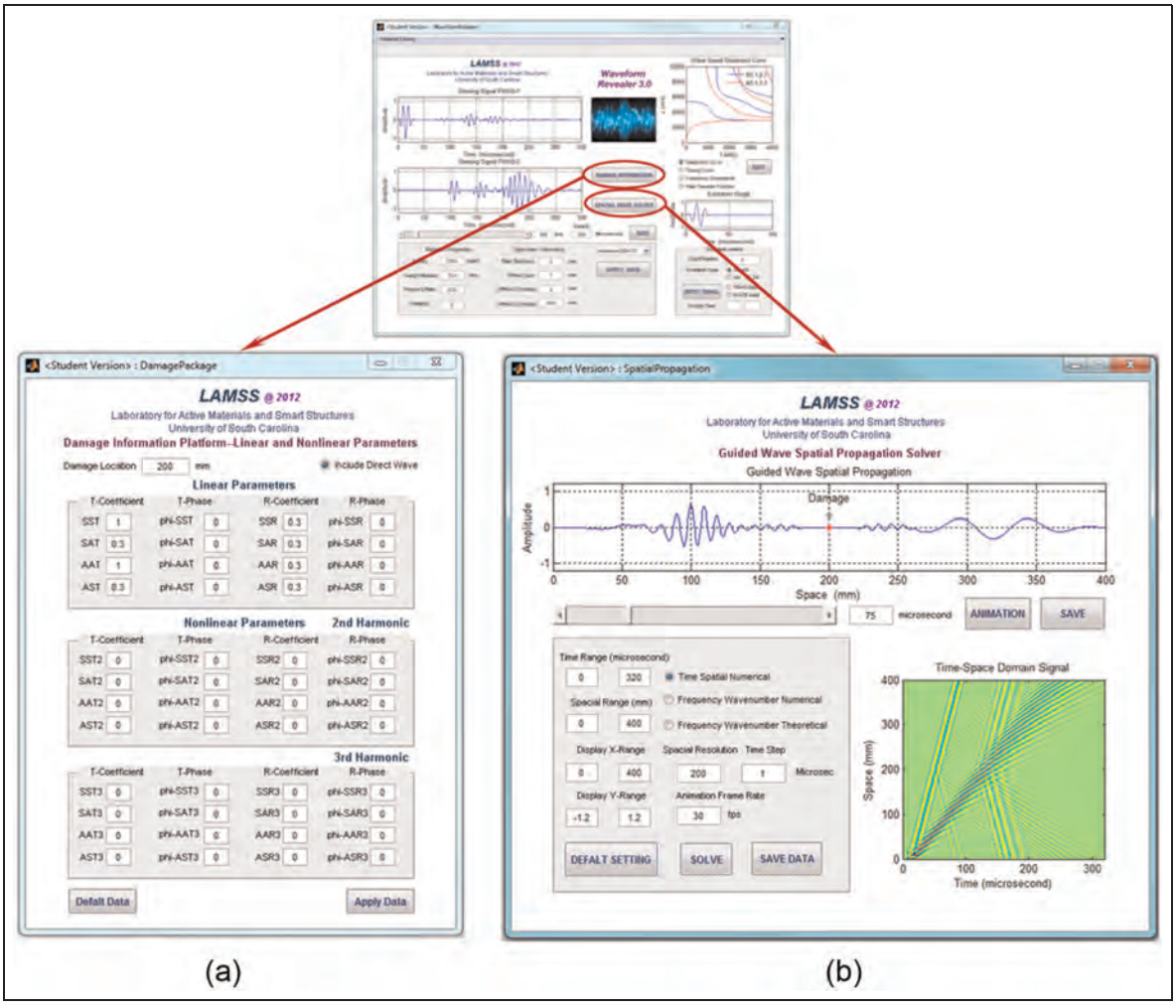

Figure 10. User interfaces: (a) damage information platform and (b) guided wave spatial propagation solver.

placed 200 mm from the T-PWAS. A 5-count Hanning window modulated tone burst centered at 100 kHz is used as the excitation. The time-domain and the time–frequency domain signals of the test cases are shown in Figure 13.

Figure 13 shows that new wave packets appear due to the interaction between interrogation Lamb waves and damage. Incident S0 wave will generate A0 wave from mode conversion at the damage, whereas incident A0 wave will generate S0 wave from mode conversion at the damage. However, from the time-frequency analysis, it could be observed that after linear interaction, the frequency spectrum of the waves still center around the excitation frequency 100 kHz.

Nonlinear interaction with damage of selective Lamb wave modes

As test cases for nonlinear interaction between Lamb waves and damage, three simulations were carried out:

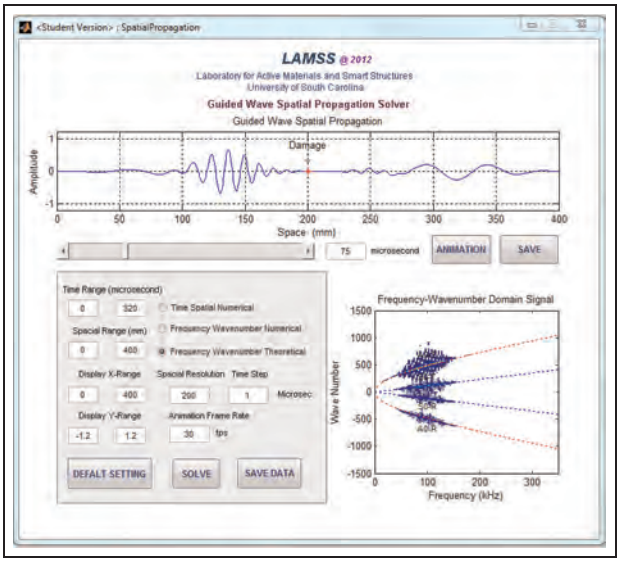

Figure 11. Frequency–wavenumber display window.

Downloaded from shm.sagepub.com by guest on August 20, 2014

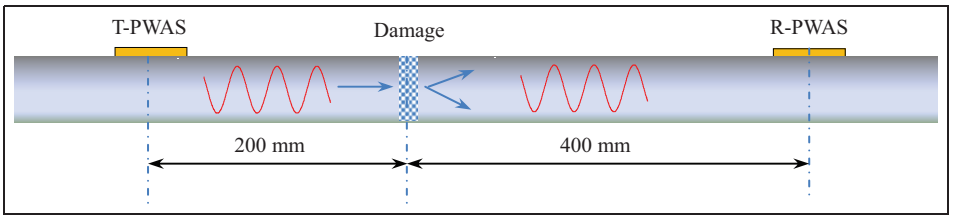

Figure 12. Test case setup for pitch-catch Lamb wave interaction with damage.
T-PWAS: transmitter piezoelectric wafer active sensor; R-PWAS: receiver piezoelectric wafer active sensor.

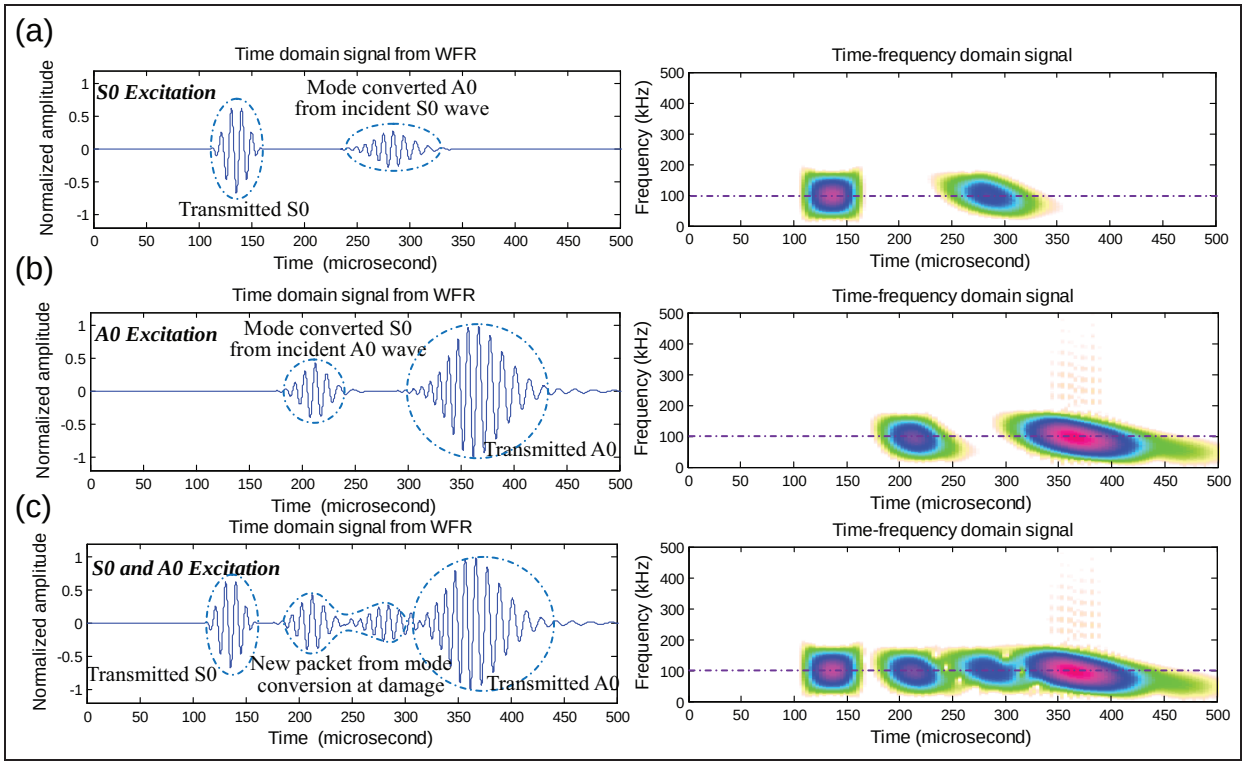

Figure 13. Simulation of linear interaction between Lamb waves and damage: (a) S0 mode excitation, (b) A0 mode excitation, and (c) S0 and A0 modes excitation. It should be noted that no higher harmonics are observed.
WFR: WaveFormRevealer.

(a) incident S0 wave nonlinear interaction with damage, (b) incident A0 wave nonlinear interaction with damage, and (c) combined S0 and A0 waves nonlinear interaction with damage. The test case setup is the same as shown in Figure 12, only the interaction with damage is nonlinear. The time signals and the time-frequency analysis of the test cases are shown in Figure 14.

It can be observed in Figure 14 that after nonlinear interaction with the damage, the waveforms become distorted and contain distinctive nonlinear higher harmonics. For S0 waves which are less dispersive at the given frequency range, the nonlinear higher harmonics stay inside the wave packet. However, for A0 waves which are dispersive at the given frequency range, the higher harmonic components travel faster, leading the way and may escape from the fundamental wave packet.

Experimental verifications

Multi-mode Lamb wave propagation in a pristine plate

In our study, two PWAS transducers were mounted on a 3.17-mm-thick aluminum 7075-T6 plate. Figure 15 shows the experiment setup. The T-PWAS sends out ultrasonic guided waves into the structure. The guided waves, that is, Lamb waves propagate in the plate,

Downloaded from shm.sagepub.com by guest on August 20, 2014

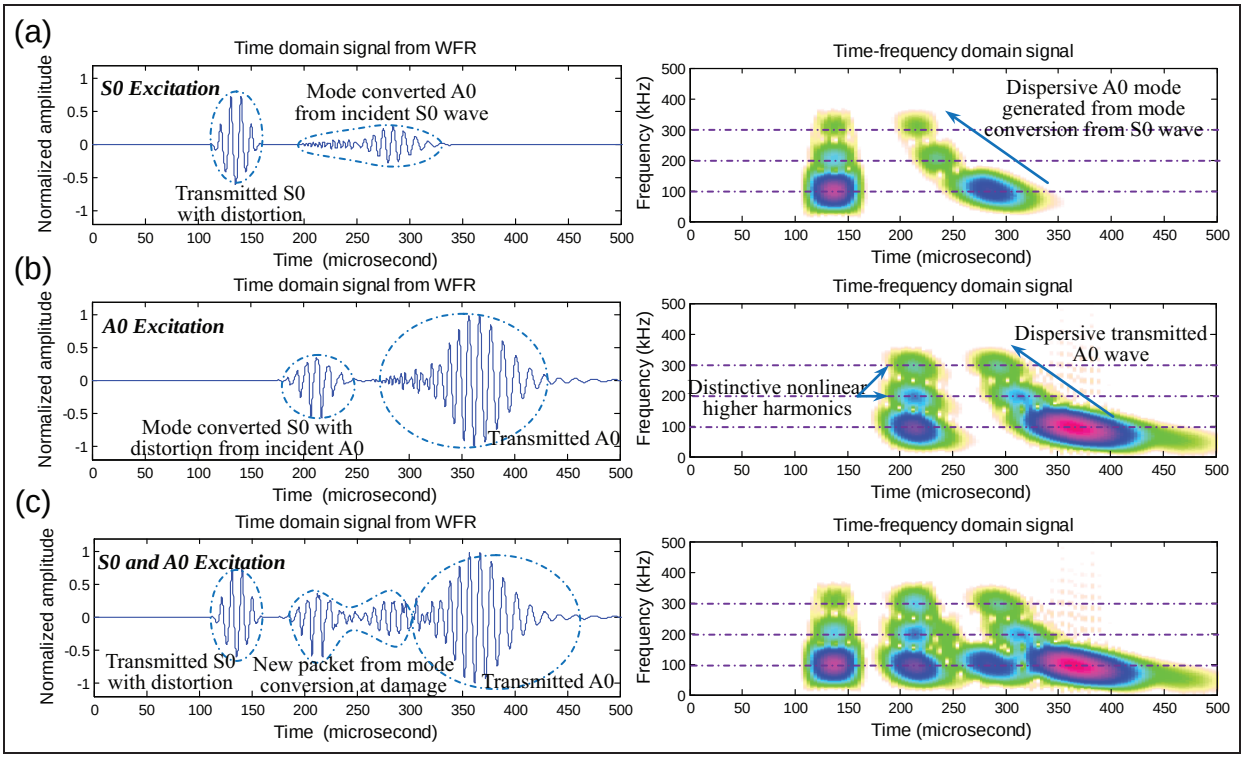

Figure 14. Simulation of nonlinear interaction between Lamb waves and damage: (a) S0 mode excitation, (b) A0 mode excitation, and (c) S0 and A0 modes excitation. It should be noted that distinctive higher harmonics are observed.
WFR: WaveFormRevealer.

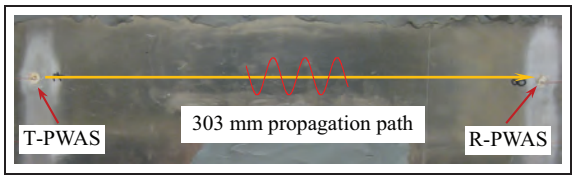

Figure 15. Experiment setup for multi-mode Lamb wave propagation.
WFR: WaveFormRevealer.

undergoing dispersion and are picked up by the R-PWAS. The Lamb waves are multi-modal, hence several wave packets appear in the received signal. Agilent 33120A Arbitrary Waveform Generator is used to generate 3-count Hanning window modulated tone burst excitations. A Tektronix Digital Oscilloscope is used to record the experimental waveforms. The excitation frequency is increased from 300 to 600 kHz.

Corresponding plate material, thickness, PWAS size, and sensing location information is input into the WFR. The analytical waveforms of various frequencies are obtained. Figure 16 shows the comparison between analytical solution from WFR and experimental data.

It can be observed that at 300 kHz, only S0 and A0 modes exist. The WFR solution matches well with experimental data. At 450 kHz, S0 mode becomes more dispersive; besides S0 and A0 modes, A1 mode starts to pick up with highly dispersive feature. At 600 kHz, S0, A0, and A1 modes exist simultaneously. The simulation results and the experimental data have slight differences due to the fact that 1D analytical formulas and pin force excitation assumptions are used in this study. To further validate WFR predictions, we also conducted 2D FEM simulation with pin force excitation (1D Lamb wave propagation simulation). Figure 17 shows the comparison between WFR and FEM simulations. It can be observed that the 300 and 450 kHz waveforms match very well between WFR and FEM. Signals of 600 kHz also have reasonably good agreement. It should be noted, even for 1D Lamb wave propagation simulation, that the 600 kHz wave computation requires considerably small element size and time marching step. The FEM simulation for such high-frequency, short-wavelength situation is becoming prohibitive due to the heavy consumption of computation time and computer resources. On the contrary, WFR only requires several seconds to obtain the same results due to its highly efficient analytical formulation.

The guided wave spatial propagation solver in WFR is used to obtain the time–space wave field (B-scan) as shown in Figure 18(a). The frequency–wavenumber analysis is conducted next, as shown in Figure 18(b).

Downloaded from shm.sagepub.com by guest on August 20, 2014

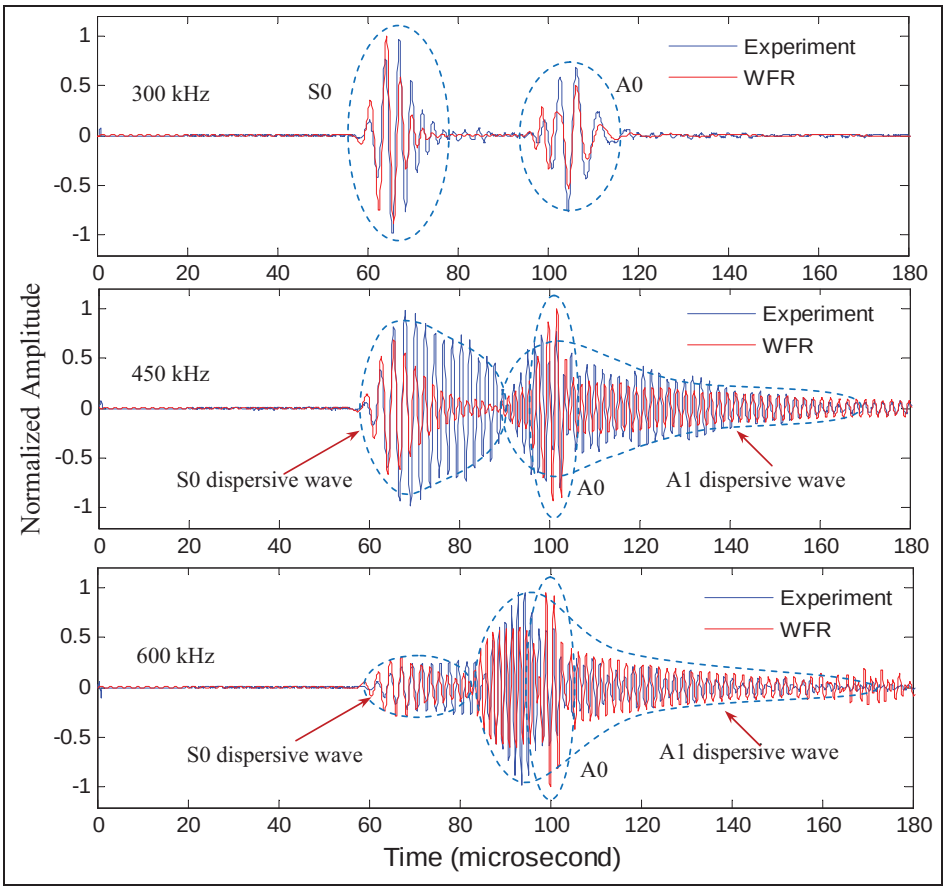

Figure 16. Comparison between WFR and experiment for multi-mode Lamb wave propagation in a pristine 3.17-mm aluminum plate.
WFR: WaveFormRevealer.

The 600 kHz case is used as an example. From the B-scan, S0, A0, and A1 wave components can be observed. Frequency–wavenumber analysis gives very clear information on the wave mode components of the wave field. Transmitted S0 wave (S0-T), A0 wave (A0-T), and A1 wave (A1-T) are clearly noticed in Figure 18(b).

Linear interaction between Lamb waves and damage

Pitch-catch mode. Figure 19 shows the experimental specimen (3.17-mm-thick Aluminum-7075-T6 plate), with PWAS #3 used as the transmitter (T-PWAS) and PWAS #4 used as the receiver (R-PWAS). A notch ($h_1 = 2.5$ mm, $d_1 = 0.25$ mm) is machined on the plate, 143.5 mm from the T-PWAS. The wave propagation path from T-PWAS to R-PWAS is 303 mm. The 3-count Hanning window modulated tone burst signals with center frequencies varying from 150 to 300 kHz are used as the excitation.

S0 and A0 waves are transmitted by the T-PWAS. At the notch, S0 waves will be transmitted as S0 waves and also will be mode converted to transmitted A0 waves. A0 waves will be transmitted as A0 waves and also will be mode converted to transmitted S0 waves. All these transmitted waves will propagate along the rest of the structure and be picked up by the R-PWAS. The damage interaction coefficients are physically determined by the size, severity, type of the damage. In this study, we used a trial-and-error approach to tune the WFR damage interaction coefficients to the data obtained from the experiments. The adjusted damage interaction coefficients which gave best match with experiments for 150 kHz excitation case are shown in Table 1.

Figure 20 shows the WFR simulation results compared with experiments. It can be noticed that the analytical waveforms agree well with experimental data. A new wave packet is generated due to mode conversion at the notch.

Pulse-echo mode. Figure 21 shows the experimental setup for pulse-echo active sensing method. The same specimen is used, with an R-PWAS bounded side by

Downloaded from shm.sagepub.com by guest on August 20, 2014

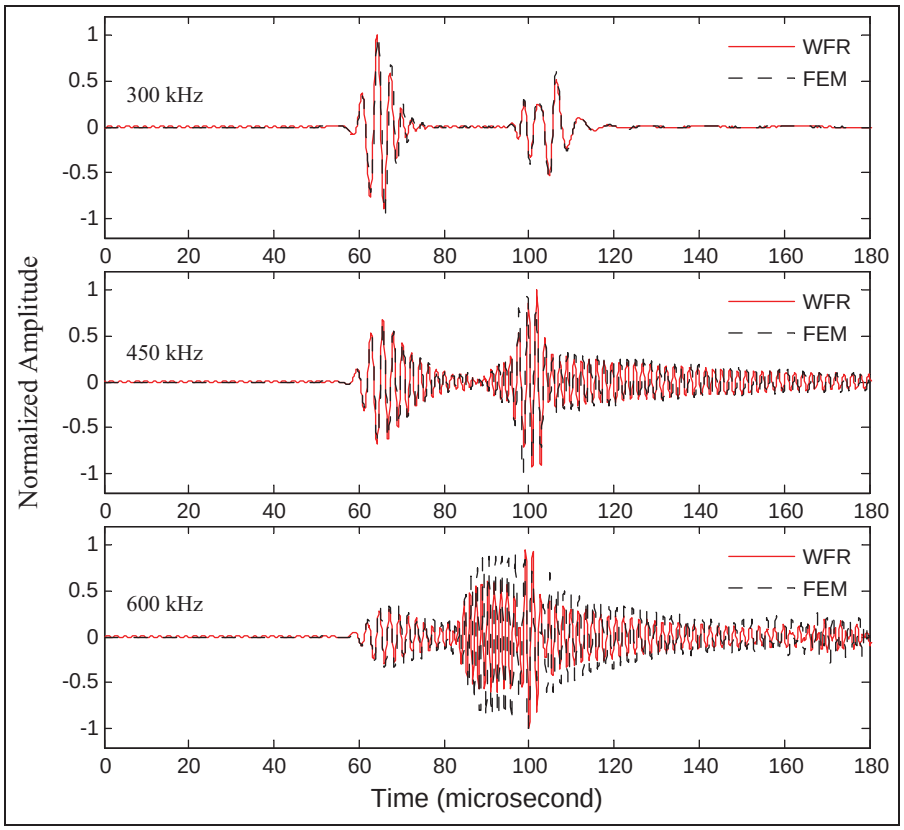

Figure 17. Comparison between WFR and FEM for multi-mode Lamb wave propagation in a pristine 3.17-mm aluminum plate.
WFR: WaveFormRevealer; FEM: finite element method.

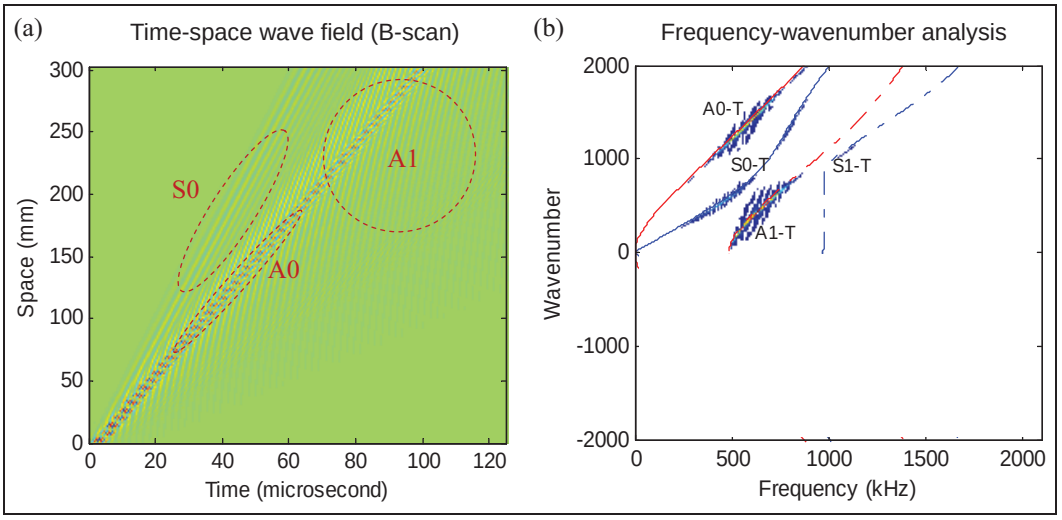

Figure 18. (a) Time–space wave field (B-scan) and (b) frequency–wavenumber analysis from WFR.
WFR: WaveFormRevealer.

side to the T-PWAS. The 3-count Hanning window modulated tone burst signals with the center frequency of 95.5 kHz is used as the excitation. Guided Lamb waves generated by the T-PWAS will propagate into the structure, reach the notch, and be reflected back as echoes. At the notch, S0 waves will be reflected as S0

Downloaded from shm.sagepub.com by guest on August 20, 2014

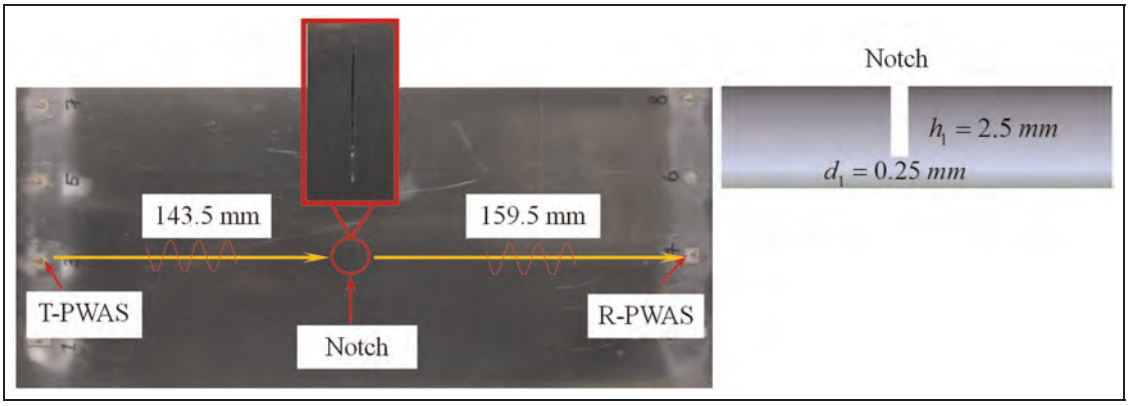

Figure 19. Experiment for Lamb wave linear interaction with a notch (pitch-catch mode).
T-PWAS: transmitter piezoelectric wafer active sensor; R-PWAS: receiver piezoelectric wafer active sensor.

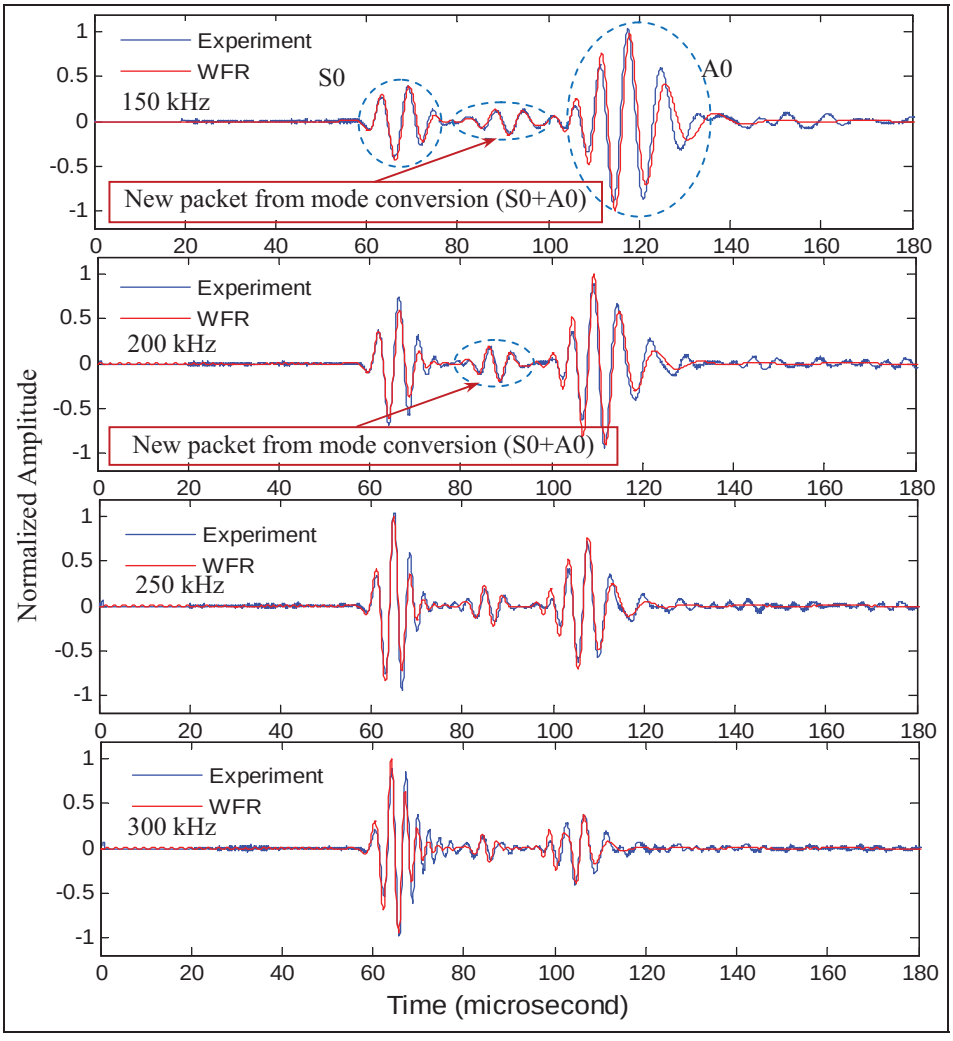

Figure 20. Comparison between WFR simulations and experiments for Lamb wave interaction with a notch in pitch-catch mode.
WFR: WaveFormRevealer.

Downloaded from shm.sagepub.com by guest on August 20, 2014

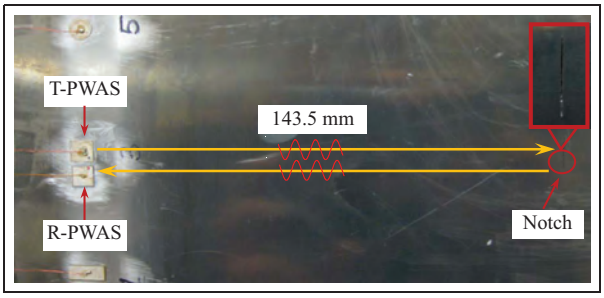

Figure 21. Experiment for Lamb wave linear interaction with a notch (pulse-echo mode).
T-PWAS: transmitter piezoelectric wafer active sensor; R-PWAS: receiver piezoelectric wafer active sensor.

waves and also will be mode converted to reflected A0 waves. A0 waves will be reflected as A0 waves and also will be mode converted to reflected S0 waves. All the echoes will reach the R-PWAS and be picked up.

The adjusted damage interaction coefficients which gave best match with the experiment are shown in Table 2.

Figure 22 shows the WFR simulation result compared with the experiment. The reflected S0 and A0 wave packets could be observed. The new waves between S0 and A0 wave packets are from mode conversion at the notch. The analytical simulation matches the experiment data. Differences are noticed: first, the direct waves have a phase shift due to the fact that the R-PWAS and T-PWAS are some distance away from each other, while in our analytical model, we consider them to be at the same location; second, the boundary reflections are present and mixed with the weak echoes from the notch in the experiment, but in our model, the boundary reflections are not considered.

Figure 23 shows the results from WFR spatial propagation solver. The wave transmission, reflection, and mode conversion can be clearly noticed in both the B-scan and frequency–wavenumber analysis. It is apparent that the wave field contains transmitted S0 and A0 modes, and reflected S0 and A0 modes.

Table 1. Damage interaction coefficients for pitch-catch mode.

Magnitude coefficient	C^I_{SST}	C^I_{SAT}	C^I_{AAT}	C^I_{AST}
Value (normalized)	0.55	0.11	0.8	0.06
Phase coefficient	φ^I_{SST}	φ^I_{SAT}	φ^I_{AAT}	φ^I_{AST}
Value (°)	−30	30	0	30

Table 2. Damage interaction coefficients for pulse-echo mode.

Magnitude coefficient	C^I_{SSR}	C^I_{SAR}	C^I_{AAR}	C^I_{ASR}
Value (normalized)	0.2	0.04	0.12	0.04
Phase coefficient	φ^I_{SSR}	φ^I_{SAR}	φ^I_{AAR}	φ^I_{ASR}
Value (°)	60	60	−60	60

Nonlinear interaction between Lamb waves and damage

A guided wave pitch-catch method may be used to interrogate a plate with a breathing crack which opens and closes under tension and compression.[6,24] The ultrasonic waves generated by the T-PWAS propagate into the structure, interact with the breathing crack, acquire nonlinear features, and are picked up by the R-PWAS. This process is shown in Figure 24. The nonlinear interaction between Lamb waves and the breathing crack will introduce nonlinear higher harmonics into the interrogation waves. A multi-physics transient finite element model was used to simulate the Lamb wave interaction with a nonlinear breathing crack. The damage interaction coefficients obtained from fitting the FEM solution (Table 3) were input into the WFR simulator.

Figure 25 shows the comparison between FEM and the WFR analytical solution. It is noticed that the FEM results and the analytical solution agree very well because the damage interaction coefficients were fitted to the FEM solution. The time-domain waveforms show nonlinear characteristics of noticeable nonlinear

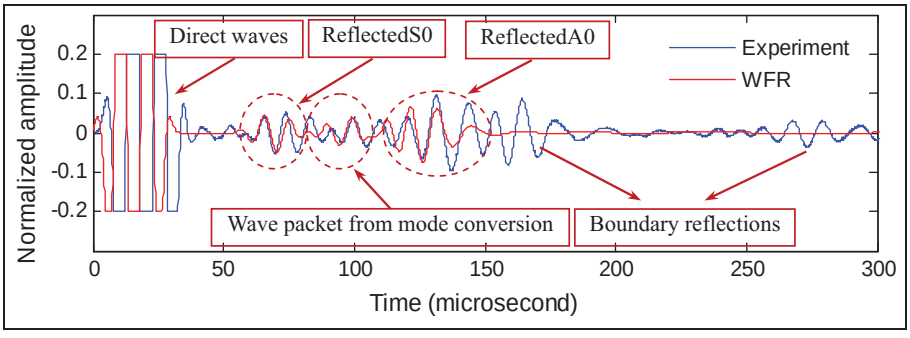

Figure 22. Comparison between WFR simulations and experiments for Lamb wave interaction with a notch in pulse-echo mode.
WFR: WaveFormRevealer.

Downloaded from shm.sagepub.com by guest on August 20, 2014

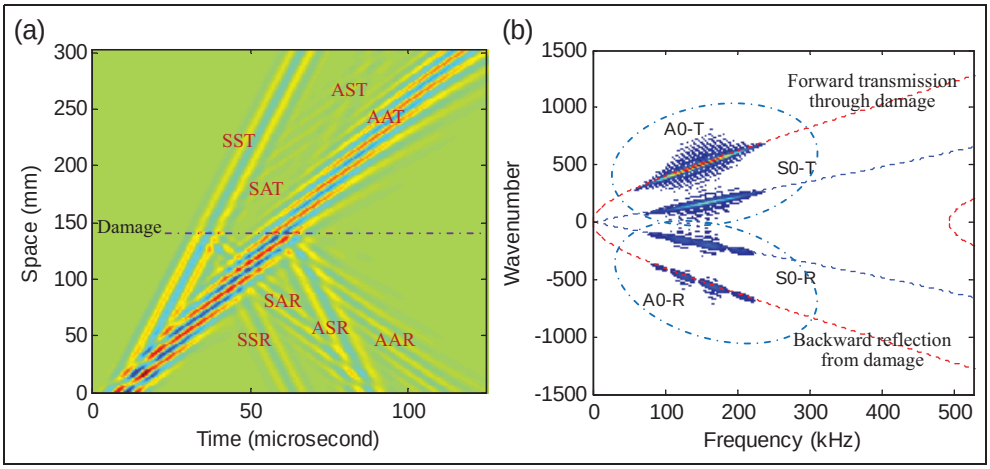

Figure 23. (a) Time–space domain solution (B-scan) and (b) frequency–wavenumber analysis from WFR with transmission, reflection, and mode conversion damage effects.
WFR: WaveFormRevealer.

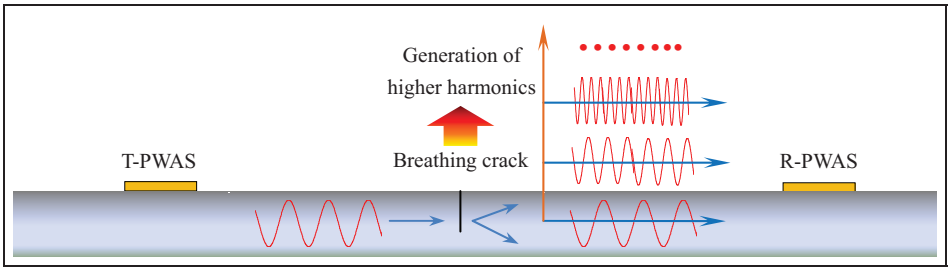

Figure 24. Pitch-catch method for the detection of breathing crack; the mode conversion at the crack is illustrated by the two arrows.
T-PWAS: transmitter piezoelectric wafer active sensor; R-PWAS: receiver piezoelectric wafer active sensor.

Table 3. Nonlinear interaction coefficients.

Magnitude coefficient	C^1_{SST}	C^1_{SAT}	C^1_{AAT}	C^1_{AST}	C^2_{SST}	C^2_{SAT}	C^2_{AAT}	C^2_{AST}	C^3_{SST}	C^3_{SAT}	C^3_{AAT}	C^3_{AST}
Value (normalized)	0.900	0.420	0.820	0.100	0.082	0.100	0.050	0.110	0.032	0.038	0.005	0.025
Phase coefficient	φ^1_{SST}	φ^1_{SAT}	φ^1_{AAT}	φ^1_{AST}	φ^2_{SST}	φ^2_{SAT}	φ^2_{AAT}	φ^2_{AST}	φ^3_{SST}	φ^3_{SAT}	φ^3_{AAT}	φ^3_{AST}
Value (°)	0	100	−35	90	0	0	120	90	0	0	0	0

distortion in S0 packet and zigzags in the new packet. The frequency spectrums show distinctive nonlinear higher harmonics (200 and 300 kHz). Since we only consider up to the third higher harmonic in this case study, the frequency domain of analytical solution shows only the first three peaks, while the finite element solution have even higher harmonics. But the solution up to the third higher harmonics is accurate enough to render an acceptable waveform in time domain.

The guided wave spatial propagation solver in WFR was used to obtain the time–space wave field. Figure 26 shows the time–space wave field and frequency–wavenumber analysis of Lamb wave interaction with nonlinear breathing crack.

Transmission, reflection, and mode conversion phenomena at the damage can be clearly noticed. The frequency–wavenumber analysis reveals the wave components during the interaction process. The wave field contains transmitted S0 and A0 waves and reflected S0 and A0 waves. Nonlinear higher harmonics can be observed at 200 kHz.

The WFR-guided wave spatial propagation solver can provide the spatial wave pattern at any instance of time. The spatial waveforms at 0, 25, 50, 75, 100, 125, 150, 175, and 200 μs are displayed in Figure 27. The spatial waveforms shows (a) Lamb waves propagating into the structure at $T = 25\,\mu s$, (b) Lamb modes separating into distinct packets at $T = 50\,\mu s$, (c) Lamb wave

Downloaded from shm.sagepub.com by guest on August 20, 2014

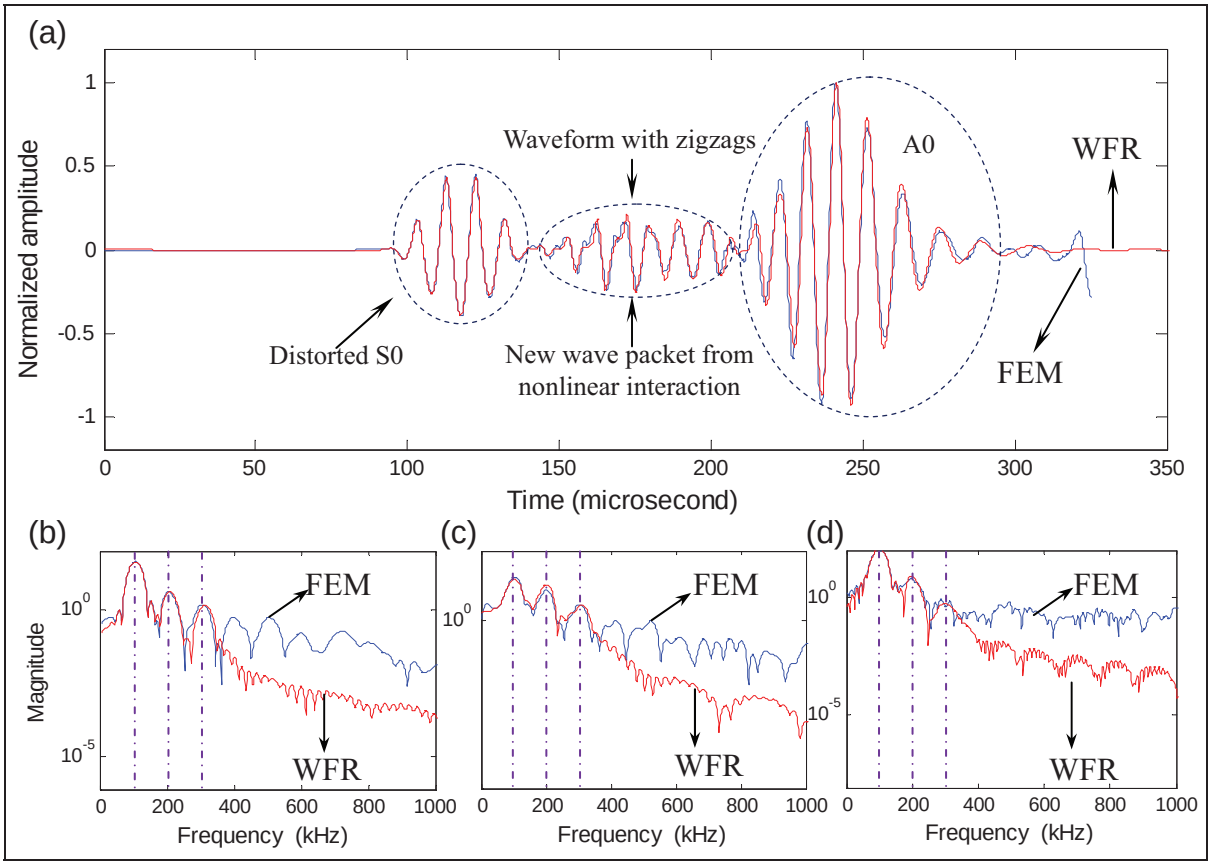

Figure 25. (a) Comparison between finite element simulation (FEM) and analytical simulation (WFR), (b) frequency spectrum of S0 packet, (c) frequency spectrum of new packet and (d) frequency spectrum of A0 packet.
WFR: WaveFormRevealer; FEM: finite element method.

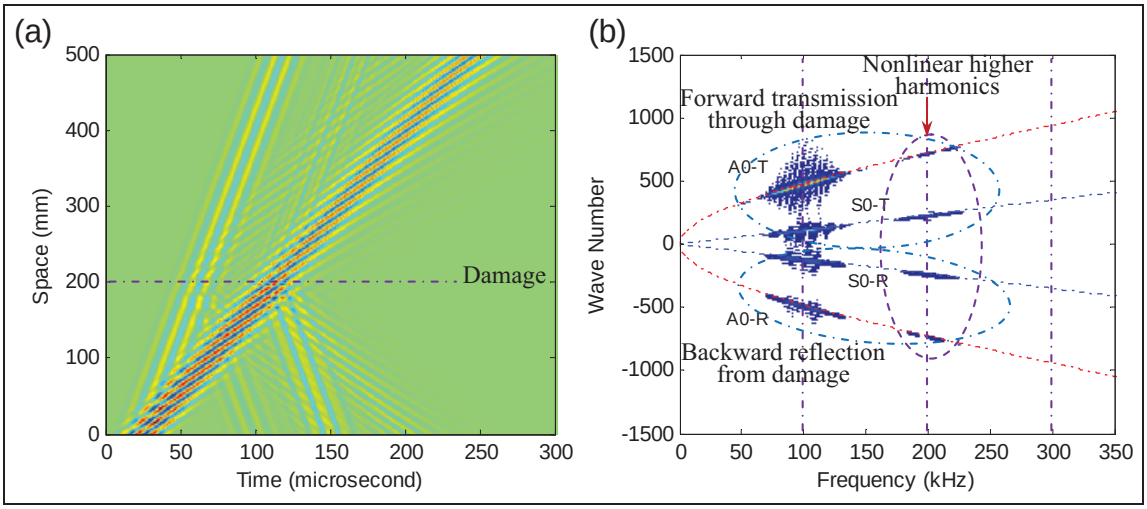

Figure 26. (a) Time–space wave field (B-scan) and (b) frequency–wavenumber analysis from WFR.
WFR: WaveFormRevealer.

Downloaded from shm.sagepub.com by guest on August 20, 2014

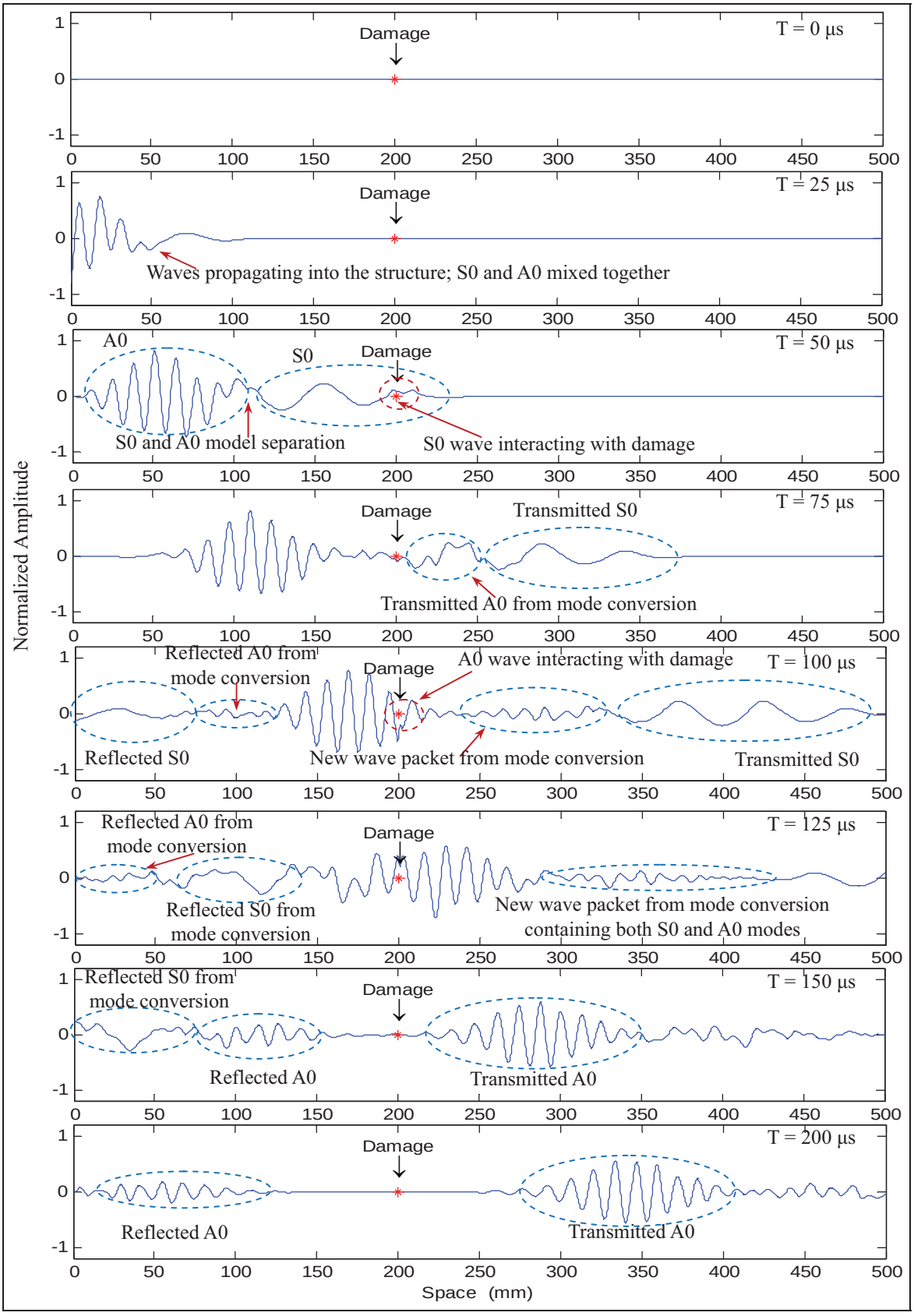

Figure 27. Spatial wave propagation of Lamb wave interaction with breathing crack (calculated using WFR).
WFR: WaveFormRevealer.

Downloaded from shm.sagepub.com by guest on August 20, 2014

packets interaction with the damage also at $T = 50\,\mu s$, and (d) wave transmission, reflection, mode conversion, and nonlinear distortion of waveforms at various instances ($T = 75$, 100, 125, 150, and $200\,\mu s$).

Summary, conclusions, and future work

Summary

In this study, we presented the WFR—an analytical framework and predictive tool for the simulation of guided Lamb wave interaction with damage. The theory of inserting damage effects into the analytical model was addressed, including wave transmission, reflection, mode conversion, and nonlinear higher harmonics components. The analytical model was coded into MATLAB, and the WFR GUI was developed to obtain fast predictive waveforms for arbitrary combinations of sensors, structural properties, and damage. Main functions of WFR were introduced, including the calculation for dispersion curves, tuning curves, frequency spectrum of sensing signal, plate transfer function, time–space domain waveforms with damage effects, frequency–wavenumber analysis, and the capability of considering arbitrary user defined excitation signals. Test cases were carried out. Experimental verifications were presented. The predictive solution from WFR agreed well with experiments and finite element simulations. WFR can be downloaded from: http://www.me.sc.edu/Research/lamss/html/software.html.

Conclusion

The WFR was capable of calculating dispersion curves, tuning curves, frequency components of wave packets, and structural transfer function. It could be used to obtain time–space domain waveforms with damage effects and frequency–wavenumber analysis. WFR could provide fast predictive solutions for multi-mode Lamb wave propagation and interaction with linear/nonlinear damage. The solutions compared well with experiments and finite element simulations. It was also found that computational time savings of several orders of magnitude are obtained by using the analytical model WFR instead of FEM methods. WFR allowed users to conduct fast parametric studies with their own designed materials, geometries, and excitations.

Future work

Rational methods for determining damage interaction coefficient values need to be found (not trial and error). Work should be carried out to extend the analysis to 2D wave propagation (three-dimensional (3D) FEM and 2D WFR). The 2D WFR with damping effect should be built to simulate wave attenuation in waveguides. Boundary reflection and damage effects in 2D wave propagation should be investigated. Attempts for simulating guided wave propagation in composite structures should be made using WFR.

Declaration of conflicting interests

The authors declare that there is no conflict of interest.

Funding

The following funding supports for this study are thankfully acknowledged: Office of Naval Research # N00014-11-1-0271, Dr. Ignacio Perez, Technical Representative; Air Force Office of Scientific Research # FA9550-11-1-0133, Dr. David Stargel, Program Manager.

References

1. Graff KF. *Wave motion in elastic solids*. New York: Dover publications, Inc., 1991.
2. Rose JL. *Ultrasonic waves in solid media*. Cambridge: Cambridge University Press, 1999.
3. Giurgiutiu V. *Structural health monitoring with piezoelectric wafer active sensors*. Oxford, UK: Elsevier Academic Press, 2007.
4. Jhang KY. Nonlinear ultrasonic techniques for nondestructive assessment of micro damage in material: a review. *Int J Precis Eng Man* 2009; 10: 123–135.
5. Dutta D, Sohn H and Harries KA. A nonlinear acoustic technique for crack detection in metallic structures. *Struct Health Monit* 2009; 8: 251–262.
6. Shen Y and Giurgiutiu V. Simulation of interaction between Lamb waves and cracks for structural health monitoring with piezoelectric wafer active sensors. In: *Proceedings of the ASME 2012 conference on smart materials, adaptive structures and intelligent systems*, Stone Mountain, GA, 19–21 September 2012. New York: ASME.
7. Moser F, Jacobs LJ and Qu J. Modeling elastic wave propagation in waveguides with the finite element method. *NDT&E Int* 1999; 32: 225–234.
8. Gresil M, Shen Y and Giurgiutiu V. Predictive modeling of ultrasonics SHM with PWAS transducers. In: *Proceedings of the 8th international workshop on structural health monitoring*, Stanford, CA, 13–15 September 2011.
9. Giurgiutiu V, Gresil M, Lin B, et al. Predictive modeling of piezoelectric wafer active sensors interaction with high-frequency structural waves and vibration. *Acta Mech* 2012; 223: 1681–1691.
10. Giurgiutiu V. Tuned Lamb wave excitation and detection with piezoelectric wafer active sensors for structural health monitoring. *J Intel Mat Syst Str* 2005; 16: 291–305.
11. Raghavan A and Cesnik CES. Finite-dimensional piezoelectric transducer modeling for guided wave based structural health monitoring. *Smart Mater Struct* 2005; 14: 1448–1461.
12. Norris AN and Vemula C. Scattering of flexual waves in thin plates. *J Sound Vib* 1995; 181: 115–125.

Downloaded from shm.sagepub.com by guest on August 20, 2014

13. Vemula C and Norris AN. Flexual wave propagation and scattering on thin plates using Mindlin theory. *Wave Motion* 1997; 26: 1–12.
14. McKeon JCP and Hinders MK. Lamb waves scattering from a through hole. *J Sound Vib* 1999; 224: 843–862.
15. Hinders MK. Lamb wave scattering from rivets. In: Thompson DO and Chimenti DE (eds) *Review of progress in quantitative nondestructive evaluation*, vol. 15A. New York: Plenum Press, 1996, pp. 209–216.
16. Grahn T. Lamb wave scattering from a circular partly through-thickness hole in a plate. *Wave Motion* 2002; 37: 63–80.
17. Moreau L, Caleap M, Velichko A, et al. Scattering of guided waves by flat-bottomed cavities with irregular shapes. *Wave Motion* 2012; 49: 375–387.
18. Moreau L, Caleap M, Velichko A, et al. Scattering of guided waves by through-thickness cavities with irregular shapes. *Wave Motion* 2011; 48: 586–602.
19. Giurgiutiu V. Structural health monitoring with piezoelectric wafer active sensors—predictive modeling and simulation. *INCAS Bull* 2010; 2: 31–44.
20. Velichko A and Wilcox P. Efficient finite element modeling of elastodynamic scattering from near surface and surface-breaking defects. *AIP Conf Proc* 2011; 1335: 59–66.
21. Velichko A and Wilcox P. Efficient finite element modeling of elastodynamic scattering with non-reflective boundary conditions. *AIP Conf Proc* 2012; 1430: 142–149.
22. Moreau L, Velichko A and Wilcox P. Accurate finite element modelling of guided wave scattering from irregular defects. *NDT&E Int* 2012; 45: 46–54.
23. Ruzzene M. Frequency-wavenumber domain filtering for improved damage visualization. *Smart Mater Struct* 2007; 16: 2116–2129.
24. Shen Y and Giurgiutiu V. Predictive simulation of nonlinear ultrasonics. In: *Proceedings of the 2012 SPIE smart structures and materials & nondestructive evaluation and health monitoring*, San Diego, CA, 11–15 March 2012. Washington, USA: SPIE.

Downloaded from shm.sagepub.com by guest on August 20, 2014

Wave Motion 58 (2015) 22–41

Contents lists available at ScienceDirect

Wave Motion

journal homepage: www.elsevier.com/locate/wavemoti

Effective non-reflective boundary for Lamb waves: Theory, finite element implementation, and applications

Yanfeng Shen [a,*], Victor Giurgiutiu [b]

[a] Department of Aerospace Engineering, University of Michigan, Ann Arbor, USA
[b] Department of Mechanical Engineering, University of South Carolina, Columbia, USA

HIGHLIGHTS

- We presented a new approach to designing non-reflective boundary for Lamb waves.
- This approach can be conveniently implemented in commercial finite element codes.
- It achieves better performance for Lamb wave absorption than existing techniques.
- This approach is effective for both time domain and frequency domain simulations.
- Important applications were demonstrated to investigate wave damage interaction.

ARTICLE INFO

Article history:
Received 14 October 2014
Received in revised form 23 May 2015
Accepted 26 May 2015
Available online 9 June 2015

Keywords:
Lamb waves
Non-reflective boundary
Absorbing boundary
Finite element simulation
Local finite element model
Structural health monitoring

ABSTRACT

This article presents a new approach to designing non-reflective boundary (NRB) for inhibiting Lamb wave reflections at structural boundaries. Our NRB approach can be effectively and conveniently implemented in commercial finite element (FE) codes. The paper starts with a review of the state of the art: (a) the absorbing layers by increasing damping (ALID) approach; and (b) the Lysmer–Kuhlemeyer absorbing boundary conditions (LK ABC) approach is briefly presented and its inadequacy for Lamb wave applications is explained. Hence, we propose a modified Lysmer–Kuhlemeyer approach to be used in the NRB design for Lamb wave problems; we call our approach MLK NRB. The implementation of this MLK NRB was realized using the spring–damper elements which are available in most commercial FE codes. Optimized implementation parameters are developed in order to achieve the best performance for Lamb wave absorption. Our MLK NRB approach is compared with the state of the art ALID and LK ABC methods. Our MLK NRB shows better performance than ALID and LK ABC for all Lamb modes in the thin-plate structures considered in our examples. Our MLK NRB approach is also advantageous at low frequencies and at cut-off frequencies, where extremely long wavelengths exist. A comprehensive study with various design parameters and plate thicknesses which illustrates the advantages and limitations of our MLK NRB approach is presented. MLK NRB applications for both transient analysis in time domain and harmonic analysis in frequency domain are illustrated. The article finishes with conclusions and suggestions for future work.

© 2015 Elsevier B.V. All rights reserved.

* Corresponding author.
E-mail address: yanfengs@umich.edu (Y. Shen).

http://dx.doi.org/10.1016/j.wavemoti.2015.05.009
0165-2125/© 2015 Elsevier B.V. All rights reserved.

1. Introduction

Finite element method (FEM) has been widely investigated as a convenient easy-to-use tool for the study of ultrasonic wave propagation and its interaction with structural flaws and damage [1]. However, FEM is computationally intensive: to ensure computational accuracy, strict rules of spatial and temporal discretization need to be adhered to, i.e., the element size must be smaller than one twentieth of the smallest wavelength and the time step must be smaller than one twentieth of the smallest period [2]. Thus, the propagation of high-frequency short-wavelength waves over long distances may become computationally prohibitive to model because of the very fine mesh and very small time step required to ensure validity of the simulated wave signals, especially in interaction with structural flaws and damage [3].

In order to make the computational burden manageable, one notices that the FEM model is mainly necessary in the study of the scattering interaction between waves and structural damage because the FEM approach allows the detailed modeling of the damage geometry that is not possible analytically. However, outside the damage area, the wave propagation can be modeled analytically and the use of large plate models has only been justified by the need to avoid boundary reflections contaminating the scatter signal. Hence, researchers have developed the concept of non-reflective boundaries (NRB), which would eliminate the unwanted boundary reflections and allow the use of a finite size FEM model to simulate infinite medium conditions. The benefit of an NRB approach is that computational resources can be focused on the region of interest without modeling the redundant outside domain merely for the purpose of avoiding boundary reflections.

Current techniques for removing boundary reflections fall into three main categories: (i) infinite element methods; (ii) non-reflective boundary conditions [4]; and (iii) absorbing layer methods [5]. The infinite element methods use only one layer of specialty elements around the boundary to absorb the incident waves. This technique is available in commercial software such as ABAQUS. But discrepancies have been reported in elastic wave scattering problems when both the pressure and shear wave modes are present [6,7]. Lysmer and Kuhlemeyer [4] introduced the absorbing boundary condition (LK ABC) which imposes matching reaction forces at the boundaries to simulate time domain wave propagation into infinite medium. This technique is only available in special commercial software package such as ANSYS LS-DYNA solver in time domain simulations. LK ABC was found to work well with bulk waves, but its application to Lamb waves experiences noticeable reflections and poor performance for antisymmetric Lamb modes. Other successful non-reflective boundary conditions have been developed by Givoli and Keller in the frequency domain [8,9]. This approach was extended by Moreau et al. [10] to solve scattered waves from irregular defects using a frequency domain small-size FEM. However, these non-reflective boundary conditions require the modification of standard FEM solving procedure and the development of specialist codes. The absorbing layer techniques can be classified into two main subcategories: (iiia) the Perfectly Matched Layers (PMLs); and (iiib) Absorbing Layers by Increasing Damping (ALID). Both techniques extend the boundary using several layers of absorbing elements with gradually varying properties. The damping mechanism contributes to the imaginary part of the wavenumbers, which results in the attenuation of the wave amplitudes along the propagation path. The PML technique optimizes the material properties to match the acoustic impedance of successive layers, so that no reflections occur between adjacent layers [5,11,12]. PML works well in both the frequency and time domain analyses but it is only available in a very limited number of commercial FE packages such as the COMSOL RF Module, which is an optional COMSOL add-on package. On the other hand, the ALID method adopts increasing damping along wave propagation to absorb incident waves, accompanied by impedance mismatches between successive layers [13–17]. The impedance-mismatch reflections may be minimized by optimizing the damping properties. It has been reported that ALID is much easier to be implemented in commercial FE software packages, because the users only need to define the increasing damping properties of the layer materials, which can be achieved with the standard techniques. A more recent contribution to ALID-type method was given by Pettit et al. [18], who develop a stiffness reduction method (SRM) to further optimizing its performance. The SRM showed improved results compared with traditional ALID.

It is apparent that the state of the art in removing boundary reflections has generally focused on bulk waves, while only a few results have so-far been reported on removing boundary reflections for Lamb waves and other guided waves [10,12,19–21]. Current solutions for Lamb wave absorption mainly stem from the absorbing-layer family of methods, while other techniques are also desired to develop more effective solutions. In this article, we propose a different and new approach which employs an absorbing mechanism that is custom-built for the suppression of Lamb wave reflections. In developing this method, we started with the conventional LK ABC method and endeavored to modify it to address the issues stemming from the multi-modal dispersive character of Lamb waves propagating in thin-plate structures. We call our method "modified LK non-reflective boundaries (MLK NRB)". We have also noticed that most of the existing studies used the time domain simulations, while frequency domain simulations are only a few and sometimes limited to specialist FE codes. Our MLK NRB approach, which is specially designed for Lamb waves, is effective for both time-domain and frequency-domain simulations and is easy to implement in commercial FE packages. In this article, we will present and discuss three aspects of our MLK NRB approach:

(1) The theoretical background for designing NRB conditions specific for Lamb wave applications: we will first briefly review the LK ABC theory and identify the reason behind its inadequacy for Lamb wave applications. Then, we will develop the theory of our MLK NRB method that underpins its suitability for Lamb wave absorption. Parametric studies are used to develop guidelines for the choice of effective MLK NRB design variables.
(2) The MLK NRB implementation in commercial FE packages and performance tests: we will demonstrate the MLK NRB implementation in both 2-D and 3-D FE models. Performance tests and comparison with conventional LK ABC and ALID

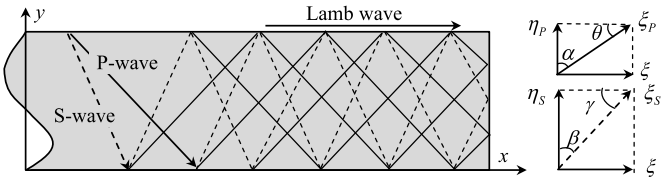

Fig. 1. Lamb wave formation: multiple reflections of P-wave and S-wave.

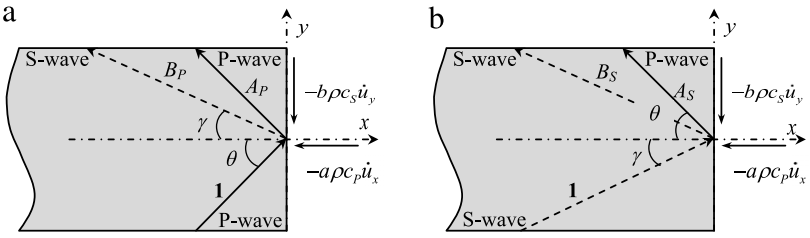

Fig. 2. Schematic of P-wave and S-wave incidence at the plate boundary: (a) incident P-wave; (b) incident S-wave.

methods will be given for multiple Lamb modes at various frequencies. The advantages and limitations of our proposed MLK NRB method will be evaluated through a parametric study to assess plate thickness and implementation length effects.

(3) The capability of the MLK NRB method in both time domain and frequency domain will be demonstrated using two application case studies: (a) time domain simulation of Lamb wave generation, propagation, and interaction with a structural feature; (b) frequency domain simulation of Lamb wave scattering from damage and determination of optimum interrogation frequency.

2. Modification of the Lysmer–Kuhlemeyer method to overcome Lamb wave related difficulties

This section discusses the difficulties encountered when trying to apply the conventional LK ABC method to Lamb wave problems and then develops our proposed MLK NRB method. Guidelines for the proper choice of MLK NRB parameters are also developed.

2.1. Theory of conventional Lysmer–Kuhlemeyer absorbing boundary condition

Lysmer and Kuhlemeyer [4] developed a dynamic model for the absorption of P-wave and S-wave reflections at the boundary of an semi-infinite half plane using two coefficients, a and b, first proportional with the P-wave speed $c_P = \sqrt{(\lambda + 2\mu)/\rho}$, the other proportional with the S-wave speed $c_S = \sqrt{\mu/\rho}$, where λ and μ are Lame's constants and ρ is the material density. They demonstrated that the proper choice of these a and b coefficients will result in the maximum energy absorption capability of a viscous boundary impinged upon by P and S waves. They also extended their method to Rayleigh wave absorption.

2.2. Inadequacy of conventional LK ABC for Lamb waves absorption

However, the Lysmer and Kuhlemeyer paper [4] did not consider the case of Lamb wave reflections at a plate boundary. To understand the intricacies of such a problem, recall that Lamb waves, by their nature, are the constructive and destructive interferences and superposition of pressure wave (P-wave) and shear vertical wave (S-wave) undergoing multiple reflections between the top and bottom plate surfaces. As illustrated in the LK theory [4], it is apparent that the absorbing capability of a conventional LK viscous boundary placed at the edge of the plate is sensitive to the incident wave angle, which makes it improper for Lamb wave absorption. Fig. 1 shows the multiple reflections of P-wave and S-wave in the formation of Lamb waves. The reflection angles of P-wave and S-wave are denoted by α and β, respectively. Their incident angle to the plate boundary are denoted by θ and γ.

Hence, when analyzing the Lamb wave reflection at a plate boundary, one should actually analyze the reflections of the P-wave and S-wave components as shown in Fig. 2.

It is apparent from Fig. 2 that the incident P and S waves interacting at a plate boundary get reflected and mode converted both at the free-end surface which is normal to the midplane and at the upper and lower free surfaces of the plate which are adjacent to the free end. If these reflected and mode-converted waves are to be suppressed by an absorbing viscous boundary, then this absorbing boundary has to extend around the complete contour at the end of the plate and not just be placed on the free-end surface as implied by the LK ABC method.

Recall the potential formulation of z-invariant Lamb waves [22]. The displacements are expressed as

$$u_x = \frac{\partial \Phi}{\partial x} + \frac{\partial \mathrm{H}_z}{\partial y}; \qquad u_y = \frac{\partial \Phi}{\partial y} - \frac{\partial \mathrm{H}_z}{\partial x} \tag{1}$$

where Φ and H_z are the displacement potentials of the P and S waves, respectively. Assuming a unit-amplitude harmonic incident P-wave, we can write the total-wave potentials as a superposition of incident and reflected waves, i.e.,

$$\begin{aligned} \Phi^P &= 1e^{i(\xi_P \cos\theta x + \xi_P \sin\theta y - \omega t)} + A_P e^{i(-\xi_P \cos\theta x + \xi_P \sin\theta y - \omega t)} \\ \mathrm{H}_z^P &= B_P e^{i(-\xi_S \cos\gamma x + \xi_S \sin\gamma y - \omega t)} \end{aligned} \tag{2}$$

where θ, ξ_P and γ, ξ_S are the reflection angles and the wavenumbers of the P-wave and S-wave, respectively, whereas ω and t are the angular frequency and time. Note that A_P and B_P are the amplitudes of the reflected P and S waves generated by a unit-amplitude incident P-wave.

Similarly, for a unit-amplitude incident S-wave case, we can express the total-wave potentials as

$$\begin{aligned} \Phi^S &= A_S e^{i(-\xi_P \cos\theta x + \xi_P \sin\theta y - \omega t)} \\ \mathrm{H}_z^S &= 1e^{i(\xi_S \cos\gamma x + \xi_S \sin\gamma y - \omega t)} + B_S e^{i(-\xi_S \cos\gamma x + \xi_S \sin\gamma y - \omega t)} \end{aligned} \tag{3}$$

where A_S and B_S are the amplitudes of the reflected P and S waves generated by a unit-amplitude incident S-wave. Note that in Eqs. (2) and (3), the superscripts on the wave potentials indicate the incident wave type, i.e., Φ^P represents the P-wave potential for a P-type incident wave, Φ^S represents the P-wave potential for an S-type incident wave, etc.

Next, we use the wave potentials to write the stress components [22,23] and impose the viscous boundary conditions as

$$\begin{aligned} \sigma_{xx} &= (\lambda + 2\mu)\left(\frac{\partial^2 \Phi}{\partial x^2} + \frac{\partial^2 \Phi}{\partial y^2}\right) - 2\mu\left(\frac{\partial^2 \Phi}{\partial y^2} - \frac{\partial^2 \mathrm{H}_z}{\partial x \partial y}\right) = -a\rho c_P\left(\frac{\partial \dot{\Phi}}{\partial x} + \frac{\partial \dot{\mathrm{H}}_z}{\partial y}\right) \\ \tau_{xy} &= \mu\left(2\frac{\partial^2 \Phi}{\partial x \partial y} - \frac{\partial^2 \mathrm{H}_z}{\partial x^2} + \frac{\partial^2 \mathrm{H}_z}{\partial y^2}\right) = -b\rho c_S\left(\frac{\partial \dot{\Phi}}{\partial y} - \frac{\partial \dot{\mathrm{H}}_z}{\partial x}\right) \end{aligned} \tag{4}$$

where a and b are the previously discussed viscous coefficients for direct stress and shear stress as introduced by Lysmer and Kuhlemeyer [4]. Impose Snell's law and recall the wave speed ratio k to write

$$\frac{\sin\theta}{\sin\gamma} = \frac{\xi_S}{\xi_P} = \frac{c_P}{c_S} = k \tag{5}$$

For incident P-wave (Fig. 2(a)), substitution of Eqs. (2) and (5) into Eq. (4) yields a set of linear algebraic equations in the reflected wave amplitudes A_P and B_P, i.e.,

$$\begin{bmatrix} 2\sin^2\theta - k^2 - ak^2\cos\theta & k^2\sin 2\gamma + ak^3\sin\gamma \\ \sin 2\theta + bk\sin\theta & k^2\cos 2\gamma + bk^2\cos\gamma \end{bmatrix} \begin{bmatrix} A_P \\ B_P \end{bmatrix} = \begin{bmatrix} k^2 - 2\sin^2\theta - ak^2\cos\theta \\ \sin 2\theta - bk\sin\theta \end{bmatrix} \tag{6}$$

Similarly, for incident S-wave (Fig. 2(b)), substitution of Eqs. (3) and (5) into Eq. (4) yields a system of linear algebraic equations in A_S and B_S, i.e.,

$$\begin{bmatrix} 2\sin^2\theta - k^2 - ak^2\cos\theta & k^2\sin 2\gamma + ak^3\sin\gamma \\ \sin 2\theta + bk\sin\theta & k^2\cos 2\gamma + bk^2\cos\gamma \end{bmatrix} \begin{bmatrix} A_S \\ B_S \end{bmatrix} = \begin{bmatrix} k^2\sin 2\gamma - ak^3\sin\gamma \\ bk^2\cos\gamma - k^2\cos 2\gamma \end{bmatrix} \tag{7}$$

Lysmer and Kuhlemeyer [4] reported that when $a = b = 1$, the viscous boundary will achieve the best energy absorption capability. This may be so for the case of bulk waves at a half plane boundary [4], but not necessarily so for Lamb waves reflecting at the end of a plate as shown in Fig. 2. In this latter case, the incident angles θ and γ also play an important role in this process besides a and b. Fig. 3 shows the reflected wave amplitudes versus the incident wave angle in an aluminum plate. It can be observed that for both incident P-wave and incident S-wave cases, the reflected wave amplitudes depend strongly on the incident wave angle. When the incident wave angle is very small, the reflected wave amplitudes approaches zero, demonstrating that the LK approach is effective in absorbing the wave energy. However, as the incident wave angle increases, the conventional LK viscous boundary begins to lose its absorbing capability.

In order to calculate the incident angles θ and γ of Fig. 2, recall the following notations used in the derivation of the Rayleigh–Lamb equation [22–24]

$$\eta_P^2 = \omega^2/c_P^2 - \xi^2; \qquad \eta_S^2 = \omega^2/c_S^2 - \xi^2 \tag{8}$$

where ξ is the wavenumber of Lamb wave, and η_P and η_S may be interpreted as the vertical wavenumbers of the P and S waves that make up the Lamb waves (see p. 315 of Ref. [23]). Thus, for the benefit of Fig. 2, the incident angles θ and γ of the P and S waves that make up the Lamb waves can be calculated as

$$\theta = \arctan\left(\frac{\eta_P}{\xi}\right); \qquad \gamma = \arctan\left(\frac{\eta_S}{\xi}\right) \tag{9}$$

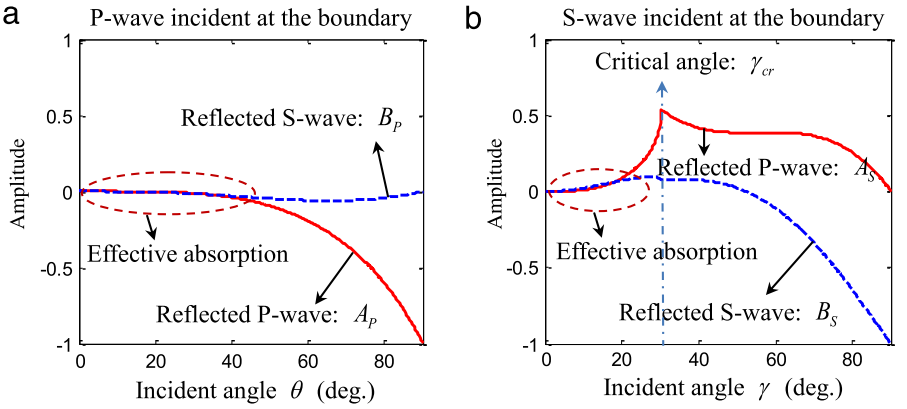

Fig. 3. Reflected wave amplitudes versus incident wave angle calculated with the conventional LK ABC method (viscous boundary $a = b = 1$) in an aluminum plate: (a) P-wave incidence; (b) S-wave incidence.

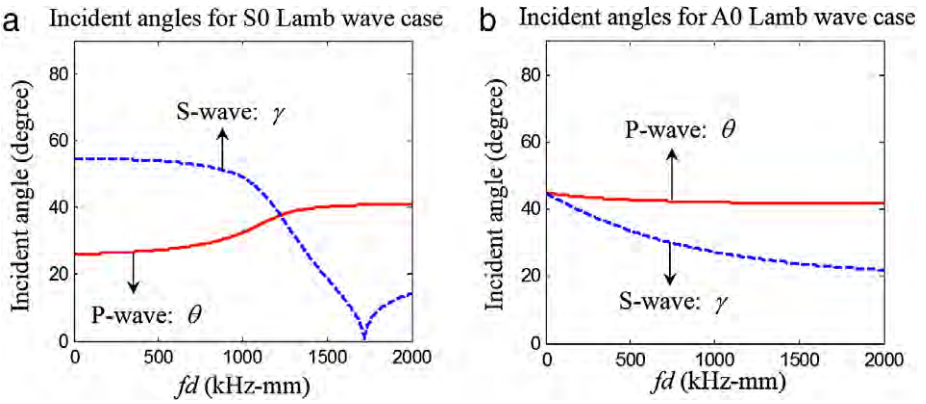

Fig. 4. Incident angles of P-wave (θ) and S-wave (γ) at the plate edge in aluminum plates: (a) S0 Lamb wave case; (b) A0 Lamb wave case.

Note: when solving Eq. (9), proper choice of real and imaginary solution should be made on η_P and η_S according to various regions the Rayleigh–Lamb equation (see p. 447 in Ref. [23]).

Fig. 4 shows the incident angles of P-wave and S-wave at the plate edge for both fundamental S0 Lamb mode and A0 Lamb mode in aluminum plates. The unit *fd* is the combination of frequency and half plate thickness. It can be noticed that both S0 and A0 Lamb waves contain bulk wave components beyond the effective absorption angles shown in Fig. 3. This illustrates the inadequacy of the conventional LK ABC approach for avoiding Lamb wave reflections at a plate boundary.

2.3. Development of the modified Lysmer–Kuhlemeyer (MLK) approach for Lamb wave NRB design

Noticing that the conventional LK ABC approach is inadequate for effective absorption of Lamb waves at a plate boundary, we developed a MLK NRB approach that would effectively absorb the Lamb waves at plate free edges. Our concept takes into account that Lamb waves result from the superposition of P and S waves that undergo multiple reflections at the top and bottom surfaces of the plate. Hence, we want to inhibit these top and bottom reflections near the plate boundary. In order to achieve this, we added viscous boundaries on the top and bottom surfaces near the plate edge and smoothed them out by adopting a gradually increasing viscosity parameter from the inner region toward the plate edge (Fig. 5). Thus, one part of our contribution is to extend the absorbing medium from the plate edge over the top and bottom surfaces of the plate in order to absorb the P and S wave reflection on these top and bottom surfaces. The other part of our contribution is to design a smooth-out law by which the top and bottom absorbing interfaces gradually participate in the absorption toward the plate edge; this second part is needed in order to prevent reflections from the Lamb waves interacting with the top and bottom viscous boundaries. Our MLK NRB design has the absorbing interface placed both at the plate edge and on its top and bottom surfaces as shown in Fig. 5.

In this MLK NRB design, the P and S wave components of the Lamb wave interact with the viscous boundary multiple times, both at the plate surfaces and at the plate edge. This design of the absorbing boundary takes advantage of the multiple reflection character of the bulk waves forming the Lamb waves; thus the effective absorption of the Lamb waves is achieved through the multiple absorptions of the bulk wave components. Since the reflection angles at the plate surfaces and the plate boundary are complementary, the effective absorbing capability are also complementary at these two locations. This will

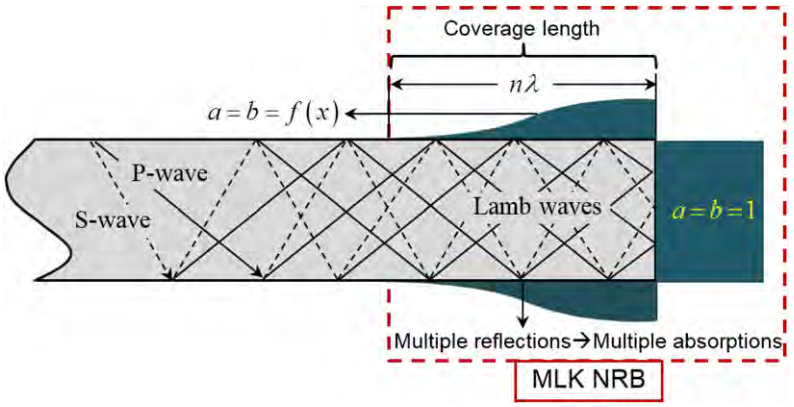

Fig. 5. Extended viscous boundary on top and bottom surfaces for effective absorption of Lamb waves. The variation of coefficients a and b is described by the filled profile.

ensure that the MLK NRB is effective for all the bulk wave angles of all the Lamb modes. Fig. 5 shows the extended viscous boundary on the top and bottom surfaces, as well as the variation of coefficients a and b around the plate edge. It should be noted that the plate edges have the full value of the absorption coefficients ($a = b = 1$) as suggested by Lysmer and Kuhlemeyer [4] for the best absorption capability at the plate vertical edge. However, at the top and bottom surfaces, the value of these a, b absorption coefficients is not constant along the plate but it is smoothed out such as to avoid Lamb wave reflections due to the impedance mismatch that would be introduced by an abrupt change in the boundary viscosity at the plate top and bottom surfaces. To achieve this smooth transition, we used a transition function $f(x)$, which introduces the viscosity gradually over a length $n\lambda$ consisting of several wavelength.

3. Guidelines for the proper choice of MLK NRB parameters

The choice of the MLK NRB parameters directly influences its performance. There are three major aspects to consider when constructing the MLK NRB, namely, the absorbing profile shape $f(x)$, the maximum damping parameter of the profile δ, and the minimum coverage length $n\lambda$ where λ is the longest wavelength under consideration.

3.1. The choice of the absorbing function $f(x)$

In our study, we considered three possible transitional profile functions $f(x)$: a linear function, a half Hanning window function, and a cubic function, i.e.,

$$f(x) = \delta \frac{x}{n\lambda}, \quad x \in (0, n\lambda) \quad \text{(Linear function)} \tag{10}$$

$$f(x) = \frac{\delta}{2}\left[1 - \cos\left(\frac{\pi x}{n\lambda}\right)\right], \quad x \in (0, n\lambda) \quad \text{(Half Hanning window function)} \tag{11}$$

$$f(x) = \delta \left(\frac{x}{n\lambda}\right)^3, \quad x \in (0, n\lambda) \quad \text{(Cubic function)} \tag{12}$$

These three function profiles have different orders of smoothness, which can be evaluated using the Taylor series expansion: the order of smoothness for the linear function Eq. (10) is one; the order of smoothness for the half Hanning window Eq. (11) is two; the order of smoothness for the cubic function Eq. (12) is three.

To test the performance of the profile functions of Eqs. (10), (11), and (12), we conducted a parametric study on an 8-mm thick aluminum plate that has the phase velocity and wavelength curves shown in Fig. 6. The parametric study was conducted with the FEM model shown in Fig. 7 using ANSYS 14.0. The coverage length L was set to 50 mm for all three profile functions. The maximum damping parameter δ was increased from zero to 0.5 with a step of 0.05. The S0 and A0 modes were selectively excited by the application of a pair of symmetric and antisymmetric point forces at the top and bottom plate surfaces. A 100 kHz 10-cycle smoothed tone burst excitation was used to generate narrow-band Lamb waves. The analysis was performed in the time domain. The excited and reflected waves were recorded at the bottom node. The amplitude reflection coefficient was used as a performance and effectiveness metric.

The results of this parametric study are shown in Fig. 8. In general, all three profile functions seemed to achieve better performance with higher δ values. However, the linear and half Hanning window profiles achieve better performance than the cubic profile. The performance also depends on the excitation mode, i.e., a clear difference can be noticed between S0 excitation (Fig. 8(a)) and A0 excitation (Fig. 8(b)).

For S0 excitation, the linear profile function has the best result quality at low δ values ($0 < \delta < 0.2$). Beyond $\delta = 0.2$, the half Hanning function seems to achieve a marginally better performance than the linear function. The cubic function is

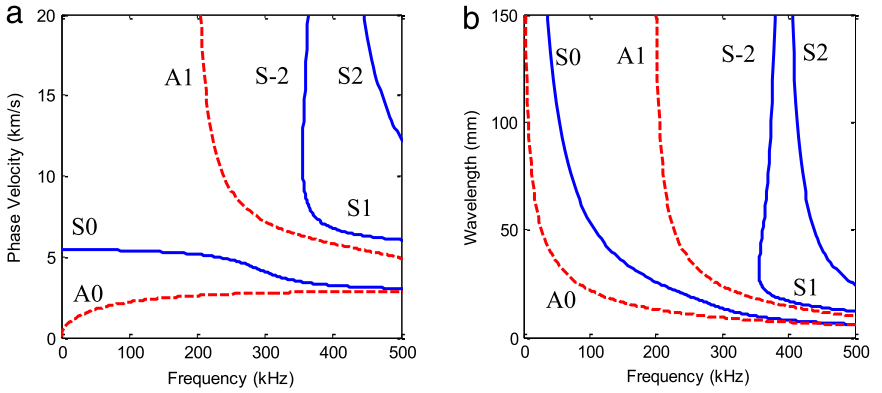

Fig. 6. Dispersion curves and wavelengths in an 8-mm thick aluminum plate: (a) phase velocity plot; (b) wavelength plot.

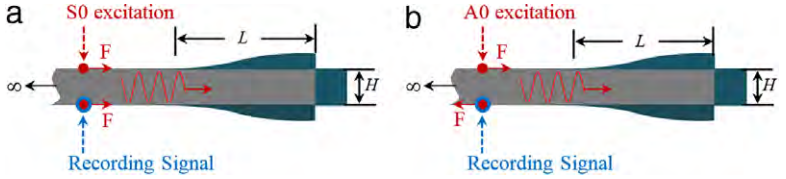

Fig. 7. Schematic of the FEM model used in the parametric study: (a) S0 mode excitation; A0 mode excitation.

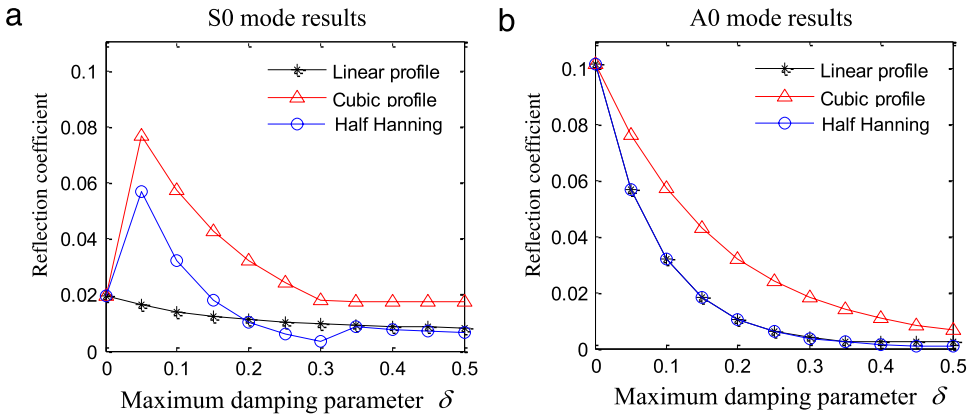

Fig. 8. Performance of various profile functions for a 100 kHz narrow-band signal: (a) S0 mode excitation; (b) A0 mode excitation.

consistently worst because its reflection coefficients stay higher than the other two functions for all tested values of δ. In addition, the cubic function plateaus out beyond $\delta = 0.3$.

For A0 excitation, the half Hanning function seems to offer the best performance although the linear function performance is almost as good except at high δ where it plateaus out while the half Hanning function continues to improve.

The case of the conventional LK ABC is recovered at $\delta = 0$; as indicated in Fig. 8, the LK ABC method achieves some effectiveness for S0 excitation (only 2% reflection) but worse results for A0 excitation (10% reflection).

It should be noted that in this case study the coverage length was $L = 50$ mm, which is approximately one wavelength of the S0 mode at 100 kHz (see Fig. 6(b)). We expect that a longer coverage length would diminish the difference between the half Hanning window function and the linear function at low values of δ.

3.2. The choice of δ value and the coverage length L

After the discussion for the proper choice of the smoothing function $f(x)$, the next important aspect to discuss is the proper choice of δ, i.e., maximum value of the damping parameter in the top and bottom plate surfaces. Recall that in the LK ABC approach, the damping was applied only to the vertical end of the plate and that its value was $a = b = 1$. In the MLK NRB approach, we apply additional damping of value $f(x)$ to the top and bottom surfaces of the plate. In our study, we took various δ values between 0 and 0.5 and studied their effect on reflection suppression. (Please note that this damping applied to the plate top and bottom surfaces does not exceed 50% of the LK ABC damping applied to the vertical end of the plate.)

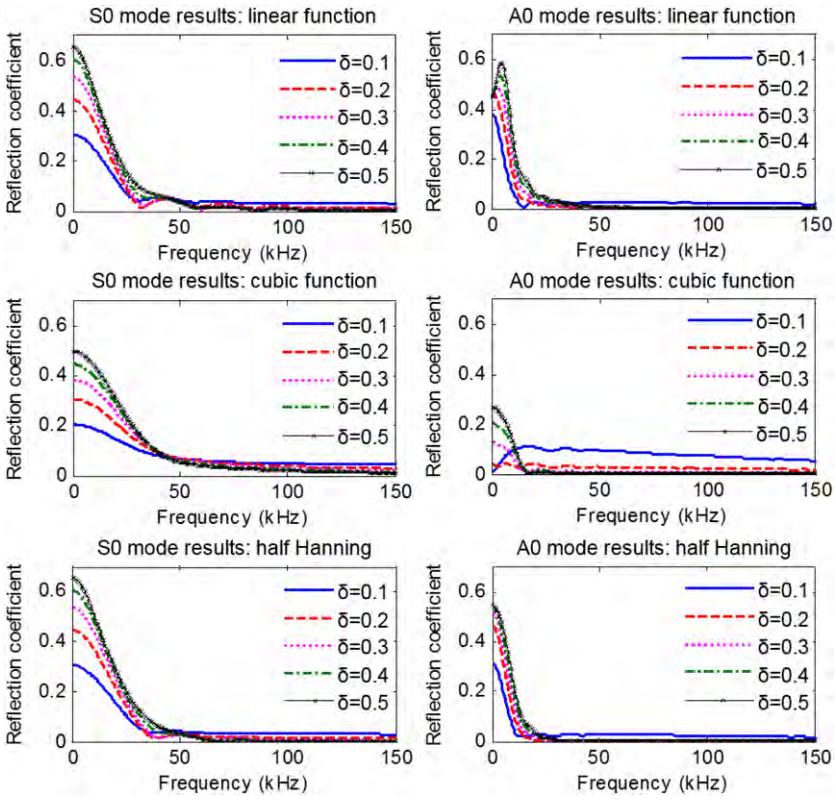

Fig. 9. High values of δ show poor performance at low-frequency range with long wavelengths.

According to Fig. 8, a higher δ leads to a better performance for a 100-kHz narrow-band wave signal. The question that was investigated next was this: What happens at lower frequencies where the wavelengths are much longer?

To study this effect, we used the same FEM model of an 8-mm thick aluminum plate but with a signal of 100 kHz 2-cycle smoothed tone burst excitation which has a much broader frequency band. The MLK NRB coverage length was taken $L = 100$ mm. After signal processing, we were able to identify the wave components belonging to various frequencies in the broad-band signal.

The results shown in Fig. 9 indicate that the absorbing effectiveness becomes worse at low frequency where long wavelength Lamb waves exist. It was also noticed that, in these low-frequency long-wavelength cases, the higher damping values (e.g., $\delta = 0.5$ in Fig. 9) gave worse results than the lower damping (e.g., $\delta = 0.1$). It was also noticed that the cubic smoothing function had better performance in these low-frequency long-wavelength cases, but worse performance otherwise.

3.3. Optimal MLK NRB design parameters

In many practical applications, multimodal Lamb waves at various frequency ranges with different wavelength contents (S0, A0, S1, A1, etc.) propagate simultaneously. The choice of optimal MLK NRB design parameters should be made taking all these factors into consideration.

Based on the results of Figs. 8 and 9 and on the authors' experience, the choice of half Hanning window profile $f(x) = \frac{\delta}{2}\left[1 - \cos\left(\frac{\pi x}{n\lambda}\right)\right]$ with δ value between 0.15 and 0.3 will, in general, ensure satisfactory results. The third important choice is a proper coverage length of the MLK NRB. The top and bottom viscous interface covers a length $L = n\lambda$, where λ is the longest wavelength of the Lamb mode under consideration. In general, an effective coverage requires $n \geq 2$.

Note that the lower δ values would apply to long wavelength components in which case a longer MLK NRB coverage length will also be necessary.

When broad band Lamb waves containing extremely long wavelength components participate in the interaction with MLK NRB, a high value of δ usually results in poor performance in the absorption of such components. This aspect will be further illustrated with parametric studies on coverage length L and plate thickness H presented later in Section 5.2.

4. MLK NRB implementation in commercial FE codes

The implementation of the MLK NRB method in commercial FE codes can be readily realized using spring–damper elements or dashpot elements, which are usually available in most commercial FE codes. (This approach does not require

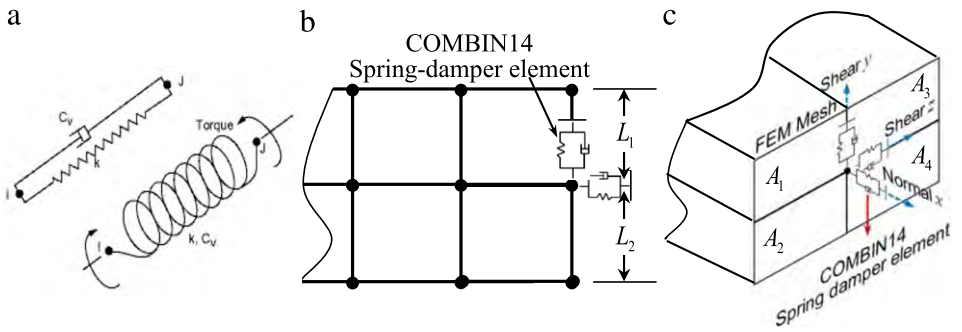

Fig. 10. Implementation of viscous boundary using COMBIN14 spring–damper element: (a) COMBIN14 element [26]; (b) 2-D FEM implementation; (c) 3-D FEM implementation.

specialized FE codes or the modification of standard solving procedure.) Lysmer and Kuhlemeyer [4] have shown the successful implementation of the conventional LK ABC in a 2-D FE model with dashpot elements. Liu et al. [25] implemented a time domain viscoelastic artificial boundary for bulk waves in a 3-D FE model. In this section, the details and guidelines of MLK NRB implementation with spring–damper elements in both 2-D and 3-D FE ANSYS models will be presented.

4.1. Selection of spring-dashpot parameters

According to Eq. (4), the viscous boundary reaction stresses should satisfy the following conditions:

$$\sigma_{xx} = -a\rho c_P \frac{\partial u_x}{\partial t}; \qquad \tau_{xy} = -b\rho c_S \frac{\partial u_y}{\partial t} \tag{13}$$

where the reaction stresses depends on the normal and tangential particle velocities at the boundary. In this study, COMBIN14 spring–damper elements in ANSYS were used to construct the MLK NRB. Similar element options such as dashpot elements can be found in ABAQUS. Fig. 10 shows the schematic of COMBIN14 element in ANSYS, the 2-D FEM implementation, and the 3-D FEM implementation. Since the viscous reaction forces must be proportional to the boundary particle velocity, we only keep the damping coefficient and set the spring coefficient to zero.

For 2-D FEM implementation, a pair of COMBIN14 elements are used, one in the normal direction, and the other in the tangential direction. One side of the elements are attached to the structural boundary node, while the degrees of freedom (DOFs) of the other side are fixed. Thus, the motion of the structural boundary node will cause reaction forces in both normal and shear directions from the spring–damper elements, which are proportional to the nodal velocities. The spring–damper coefficients K_N, K_T, C_N, C_T, which will generate reaction forces that correspond to the equivalent boundary stresses presented in Eq. (13), are as follows:

$$\begin{aligned} K_N &= 0; \qquad C_N = \frac{a}{2}(L_1 + L_2)\,\rho c_P \\ K_T &= 0; \qquad C_T = \frac{b}{2}(L_1 + L_2)\,\rho c_S \end{aligned} \tag{14}$$

where L_1 and L_2 are the element sizes in the neighborhood of the boundary node, and subscripts N and T represent normal and tangential directions. The spring coefficients are set to zero, while the damping coefficients depend on the bulk wave speeds c_P, c_S, the material density ρ, and the average element size $(L_1 + L_2)/2$. Coefficients a and b are the damping parameters; they are equal to one at the vertical boundary and follow the $f(x)$ function along the top and bottom surfaces of the plate. It should be noted that all the nodes along the defined MLK NRB should be connected to COMBIN14 element pairs; the drawing in Fig. 10(b) demonstrates the implementation for only one boundary node.

For 3-D implementation, three COMBIN14 elements should be used, with one in the normal direction, and the other two along two mutually orthogonal tangential directions. One side of the three elements are attached to the structural boundary node, and the DOFs of the other side are fixed. The corresponding spring–damper coefficients are taken as

$$\begin{aligned} K_N &= 0; \qquad C_N = \frac{a}{4}(A_1 + A_2 + A_3 + A_4)\,\rho c_P \\ K_T &= 0; \qquad C_T = \frac{b}{4}(A_1 + A_2 + A_3 + A_4)\,\rho c_S \end{aligned} \tag{15}$$

where A_1, A_2, A_3, A_4 are the neighboring element facet areas surrounding the boundary node. Again, it should be noted that all the nodes on the NRB should be restricted by COMBIN14 elements, while Fig. 10(c) only demonstrated the implementation for one of the boundary nodes.

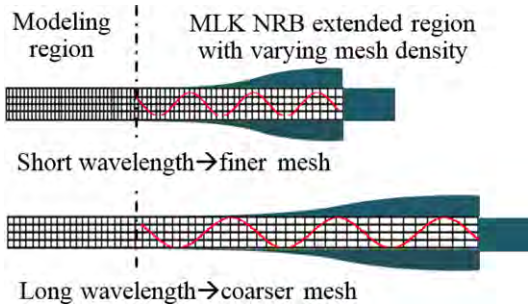

Fig. 11. Different FE meshes with the same wavelength to element size ratio. It should be noted that the total computational burden does not change.

4.2. Selection of mesh size

Fig. 6(b) has shown that large wavelengths may be encountered for the S0 mode at low frequencies and for the higher modes near the cutoff frequencies. To effectively absorb Lamb modes with large wavelength, longer MLK NRB coverage is required. However, the longer wavelengths also allows us to achieve good accuracy with a coarser mesh. Hence, the total computational burden (degrees of freedom) should not change if one keeps the ratio between the wavelength and the mesh size constant and equal to the value that ensures computational accuracy. An illustration of this concept is given in Fig. 11 which shows a finer MLK NRB mesh for shorter wavelengths and a coarser one for longer wavelengths.

Another concept depicted in Fig. 11 is that the MLK NRB region may have a much coarser mesh than the FEM region modeling the phenomenon of interest. In addition, this NRB region mesh can become even coarser as we approach the plate boundary. The rationale for this is that the function of the NRB region is only to eliminate boundary reflections and thus the accuracy of the wave phenomena inside the MLK NRB coverage region is not of interest. Hence, we can relax the accuracy criteria in the MLK NRB coverage region by increasing the mesh size gradually toward the plate edge. This leads to a varying-density mesh strategy that can further minimize the computational burden caused by the MLK NRB region.

When multiple Lamb modes exist simultaneously, the largest mesh size within the modeling region (as shown in Fig. 11) should be smaller than one twentieth of the shortest wavelength. But the mesh density in the MLK NRB extended region toward the plate end does not need to satisfy this accuracy requirement and hence may have a coarse mesh. However, the coverage length in this MLK extended region should be larger than twice the longest wavelength.

4.3. Considerations for frequency domain analysis

Mesh-size considerations discussed in the previous section may become even more important for frequency-domain analysis, where a wide frequency range needs to be explored. In our experience, it is useful to identify several separate frequency regions within the whole frequency range and, for each region, choose different mesh sizes according to the wavelength to element size ratio criteria. Thus, the problem can be solved in the most efficient way using an adaptive FE mesh: the frequency ranges containing very long wavelengths can be treated separately using a large extended region with fairly coarse mesh, while the frequency ranges containing short wavelengths will use a small extended region with a dense mesh.

5. Performance and effectiveness tests

To demonstrate the performance and effectiveness of the proposed MLK NRB, we conducted a case study comparing it with two existing methods: ALID and conventional LK ABC. We also carried out a parametric study on the coverage length and plate thickness with an asymptotic case, followed by the discussion on the advantages and limitations of the MLK NRB.

5.1. Comparison with existing techniques

Fig. 12 shows the setup for the comparative study between our MLK NRB method and the existing ALID and LK ABC methods. We used the same plate thickness, material properties, and parameters as used by Drozdz et al. [19] for the ALID method. An 8-mm thick aluminum plate was used, with 135-mm extended absorbing region. The loss factor η was determined by the cubic function shown in Fig. 12(c). Drozdz et al. [19] also suggested that, when $K = 5$, the ALID method would work well for both symmetric and antisymmetric modes. For our MLK NRB, the coverage length L was set to be the same length as the ALID extended region. For this comparative study, we chose MLK profile to be the half Hanning window function of Eq. (11) with δ equals 0.15. Similar to Fig. 7, symmetric and antisymmetric excitations were used to selectively generate symmetric and antisymmetric Lamb modes. The left side of the model extended to a very long distance to avoid reflections from the left boundary. The transmitted and reflected waves passing the same location were recorded. A large model was first used to obtain the excited wave signal. Then, the subtraction method was used to extract the waves reflected from the boundary.

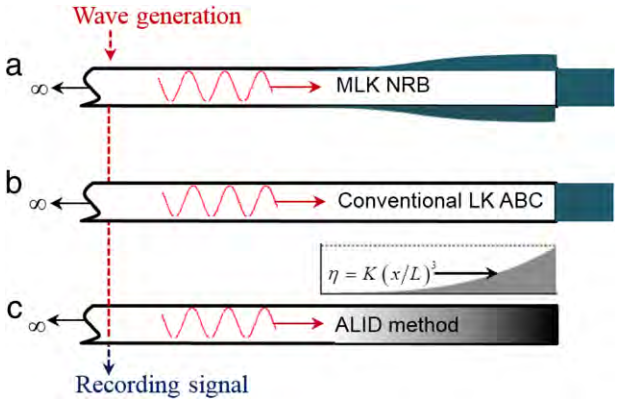

Fig. 12. Comparative case study with existing ALID method and conventional LK ABC.

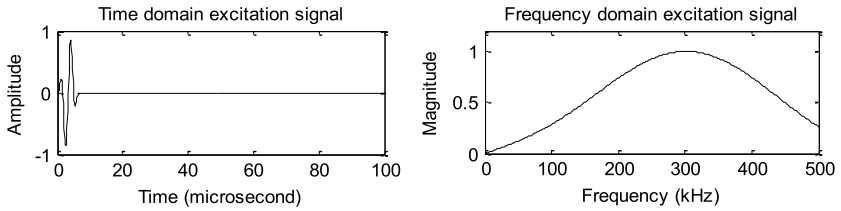

Fig. 13. Time domain excitation signal and its frequency spectrum.

A broad-band 2-cycle 300 kHz smoothed tone burst was used for Lamb wave excitation. Fig. 13 shows the time trace and frequency spectrum of the excitation signal. The dispersion curves of Fig. 6(a) indicates that such a broad-band excitation will produce higher Lamb modes. Thus, this case study allows us to examine the MLK NRB performance in the presence of multimodal Lamb waves near the cut-off frequencies.

As in previous sections, two situations were examined: (a) symmetric modes; (b) antisymmetric modes. The symmetric mode results are shown in Fig. 14 (time traces) and Fig. 15 (frequency spectra). The signal amplitudes were normalized to the full reflection condition, where no absorbing mechanism was applied. Three boundary absorption methods were compared: (i) our MLK NRB; (ii) conventional LK ABC; and (iii) ALID. Examination of the time traces presented in Fig. 14 indicates that our MLK NRB achieves much better performance than both ALID method and the conventional LK ABC, because our MLK NRB method yields almost insignificant reflections amplitudes whereas the other two method have quite significant reflection signals. Examination of the frequency spectra of Fig. 15 shows the frequency components of the reflections. It shows that the conventional LK ABC works generally well for symmetric modes at low frequency ranges, but its performance deteriorates when higher modes appear. ALID method achieves better performance than the conventional LK ABC at high frequency range and cut-off frequencies, but poor performance can be noticed for low frequency components. Compared with ALID method, the MLK NRB achieves much better performance, in general, for all the frequency components. The full-reflection energy has the maximum magnitude just after the cut-off frequencies of the S1 and S2 modes where these modes begin to participate in the wave propagation process. At these frequencies, our MLK NRB method yields very low reflection amplitudes, much smaller than both LK and ALID. It is thus clear that our MLK NRB is better than the existing methods both at low frequencies for the fundamental modes and near the cut-off frequencies for the higher order modes.

The antisymmetric mode results are shown in Fig. 16 (time traces) and Fig. 17 (frequency spectra). Examination of the time traces presented in Fig. 16 indicates that both our MLK NRB method and the existing ALID method perform much better than the LK ABC. The frequency spectra of the reflected waves are shown in Fig. 17. At low frequencies, where the fundamental A0 mode has a long wavelength, the conventional LK ABC and our MLK NRB give excellent results, much better than ALID. At the A1 cut-off frequency, where the 'newcomer' A1 mode has a very long wavelength, our MLK NRB method behaves again much better than ALID and LK ABC methods. Thus, it can be said that our MLK NRB method is better than the existing ALID and LK ABC methods at all frequencies.

This comparative study demonstrates the effectiveness of the proposed MLK method and its advantage over conventional/existing techniques for both symmetric and antisymmetric Lamb wave modes, both fundamental and higher order.

5.2. Parametric study on coverage length and plate thickness

Section 3 provided some guidelines for the proper choice of MLK NRB parameters, with the coverage length L identified as very important for good performance. In this section, we present a parametric study on the coverage length L and plate thickness H in order to substantiate these guidelines and to further demonstrate the effectiveness of our MLK NRB method.

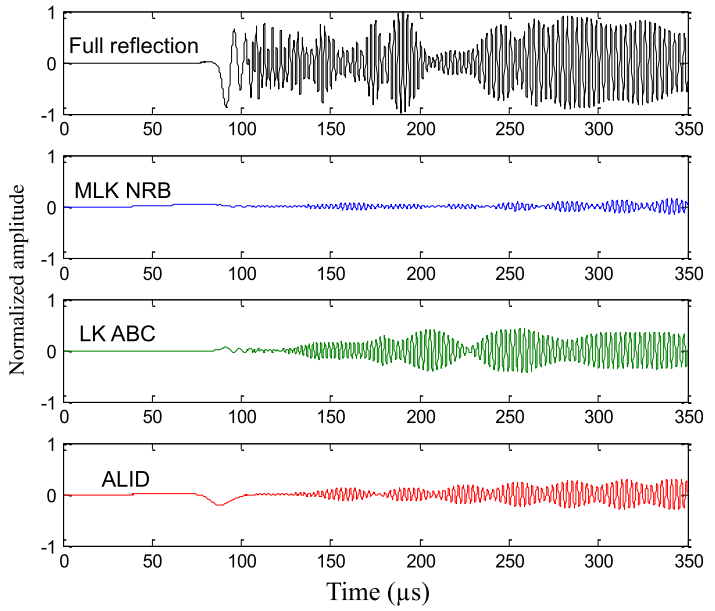

Fig. 14. Symmetric mode waves reflected from different boundary conditions.

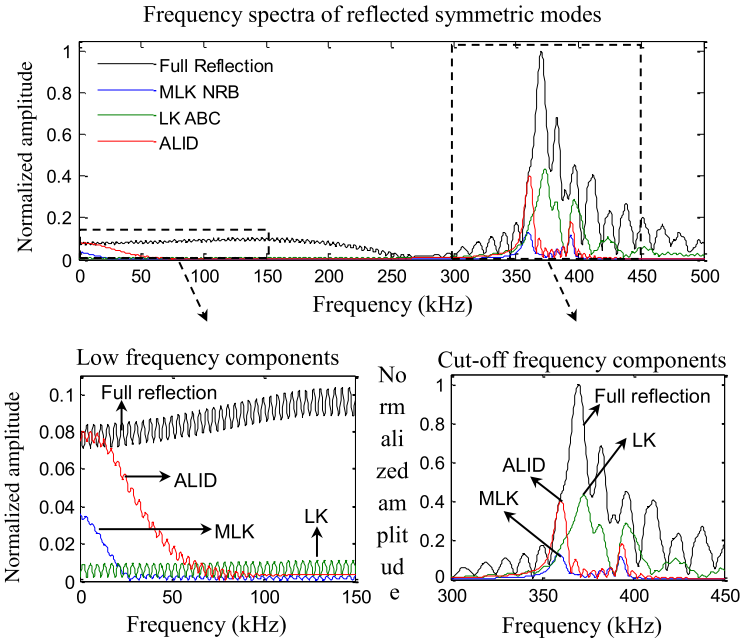

Fig. 15. Frequency spectra of the reflected symmetric waves.

We used the FE model shown in Fig. 7. The coverage length L was varied from 20 mm to 100 mm in steps of 20 mm. The plate thickness was changed from 2 mm to 10 mm in steps of 2 mm. The other parameters were consistent with those presented in Section 5.1. We used a 100 kHz 10-cycle tone burst to generate narrow-band Lamb waves in the plates. The transmitted and reflected waves were recorded and the refection coefficients were calculate to serve as the evaluating metric. Fig. 18 shows the results of this parametric study for both symmetric and antisymmetric modes: our MLK NRB is compared with the ALID method. Each bar represents a numerical case with a specific combination of the L and H parameters. The bar height and color are indicative of the reflection coefficient amplitude.

It can be noticed that when the coverage length goes beyond $L = 2\lambda$, the MLK NRB method achieves good performance for all the plate thicknesses with the reflection coefficients staying below 0.01, which implies that only 0.01% of the wave energy is reflected. This observation applies to both symmetric (S0) and antisymmetric (A0) Lamb wave modes. In contrast, the ALID method displays worse performance for S0 Lamb wave mode in thin plates (2–6 mm), although it works well for

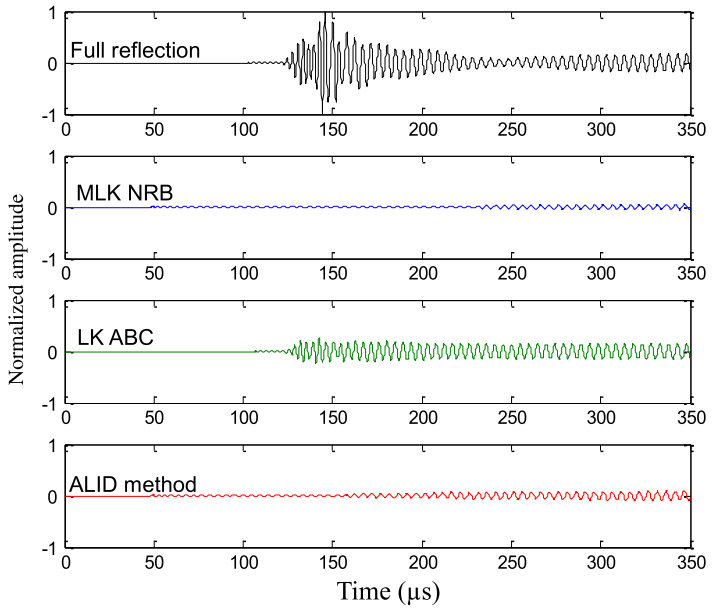

Fig. 16. Antisymmetric mode waves reflected from different boundary conditions.

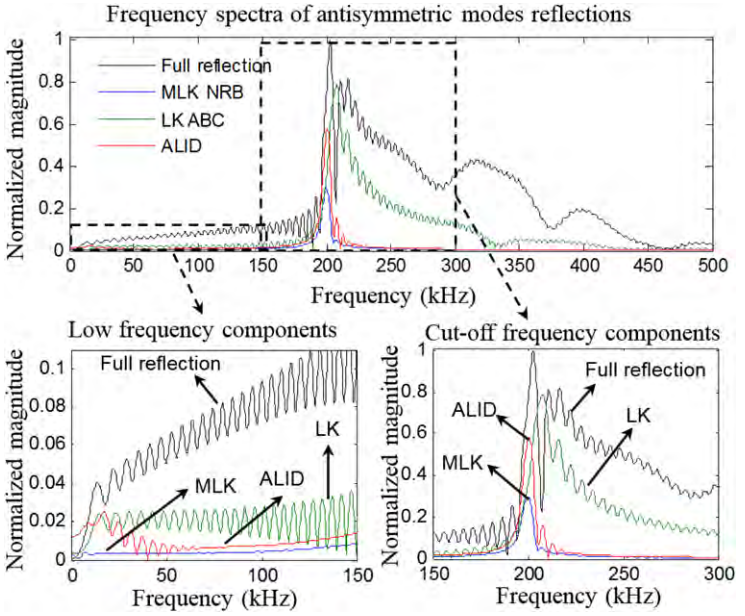

Fig. 17. Frequency spectra of the reflected antisymmetric waves.

the A0 Lamb wave mode in thick plates. Based on this parametric study, we can conclude that the MLK NRB has advantages over the ALID method in thin plates, which are extensively used in aerospace and many mechanical engineering structures. For thick plates, which are found in naval and nuclear engineering structures, ALID method remains a better choice. This parametric study also confirms the guideline of $L = 2\lambda$ coverage for the effective absorption of Lamb waves with MLK NRB. As an illustration, the 2λ curves corresponding to the S0 and A0 modes were plotted on the charts to serve as a reference for when the MLK NRB method starts to become strongly effective.

5.3. An asymptotic case with discussion on MLK NRB limitations

Although the focus of this article is on Lamb wave absorption, the case of Rayleigh waves was also considered because the Rayleigh waves can be viewed as the asymptotic behavior of Lamb waves at high-frequency in thick plates. We considered the wave propagation in a semi-infinite medium with an end boundary. In such a situation, excitations will introduce both

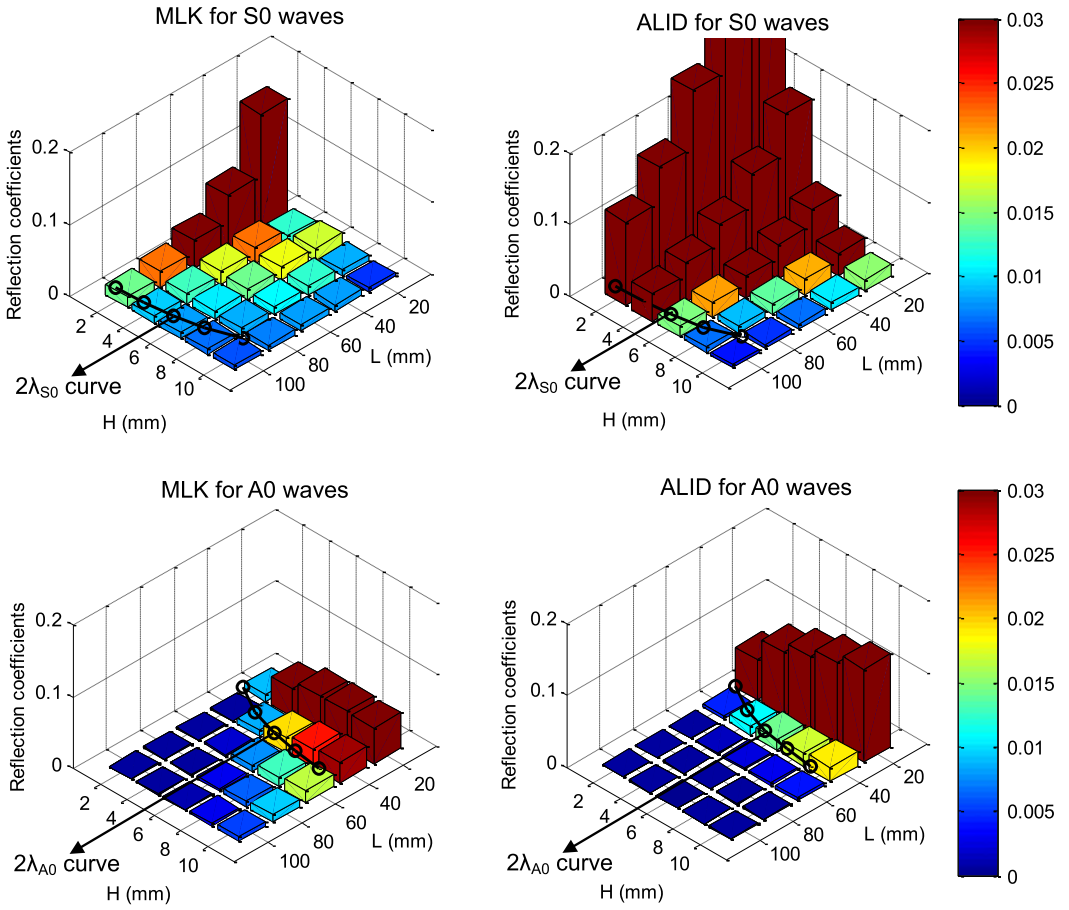

Fig. 18. Parametric study results for MLK coverage length and plate thickness. (For interpretation of the references to color in this figure legend, the reader is referred to the web version of this article.)

bulk waves and surface guided Rayleigh waves (Fig. 19). The finite element model of this situation consisted of MLK NRB absorbing layers on the right and upper free surface and ALID boundary conditions at the bottom of the model to simulate the semi-infinite extension of the medium as shown in Fig. 19. We used two excitation points: one placed on the surface (F_1) and the other placed at a certain depth (F_2). The surface excitation F_1 would produce Rayleigh waves whereas the subsurface excitation F_2 would produce mostly bulk waves. A 500-kHz 5-cycle smoothed tone burst was used. The response was recorded at three depth locations, R1, R2, and R3 (Fig. 19).

The simulation results are presented in Fig. 20 in the form of wave propagation snapshots. When surface excitation F_1 was applied, P-wave and strong Rayleigh wave were generated. The Rayleigh waves showed dominant surface motion with rapid amplitude decrease along the depth. The MLK NRB displayed good absorbing capability for the surface Rayleigh waves (Fig. 20(a)).

When sub-surface excitation F_2 was applied, three wave types (P-wave, strong S-wave, and Rayleigh wave) were generated. When Rayleigh waves entered the MLK NRB region, they were again effectively absorbed. However, it was noticed that the S-wave reflection was not completely eliminated. When the S-wave entered the MLK NRB region, it did not decay much along the coverage path due to the fact that its dominant motion was far away from the absorbing top surface. Then, the S-wave interacted with LK ABC layer at the right hand end of the domain where it was damped significantly but not completely eliminated.

Time traces of the receiver signals at three locations R1, R2, and R3 are shown in Fig. 21. When surface excitation was applied, the signal recorded close to the surface at R1 had the highest amplitude as expected from the surface-dominant motion of the Rayleigh wave. Since the Rayleigh wave decays rapidly with the depth, the signals recorded at R2 and R3 are progressively smaller. A zoom-in was applied to the signal tail to identify reflections. As shown in the top of Fig. 21, these reflections are indeed very small which indicates that the MLK NRB method has a good performance for the absorption of Rayleigh waves. When sub-surface excitation was applied (bottom of Fig. 21), the reflections were found to be much stronger. We attribute this behavior to the fact that, in this case, S-waves also exist in addition to Rayleigh waves. As already

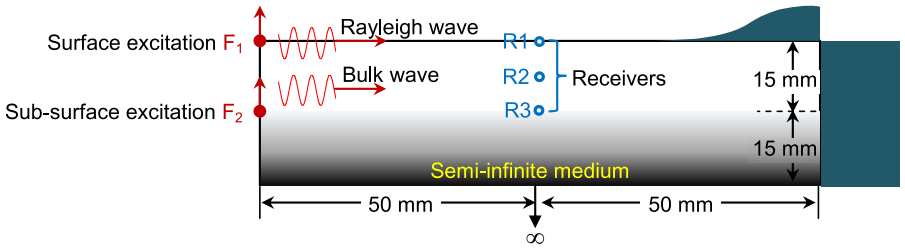

Fig. 19. Finite element model for wave absorption in a semi-infinite medium.

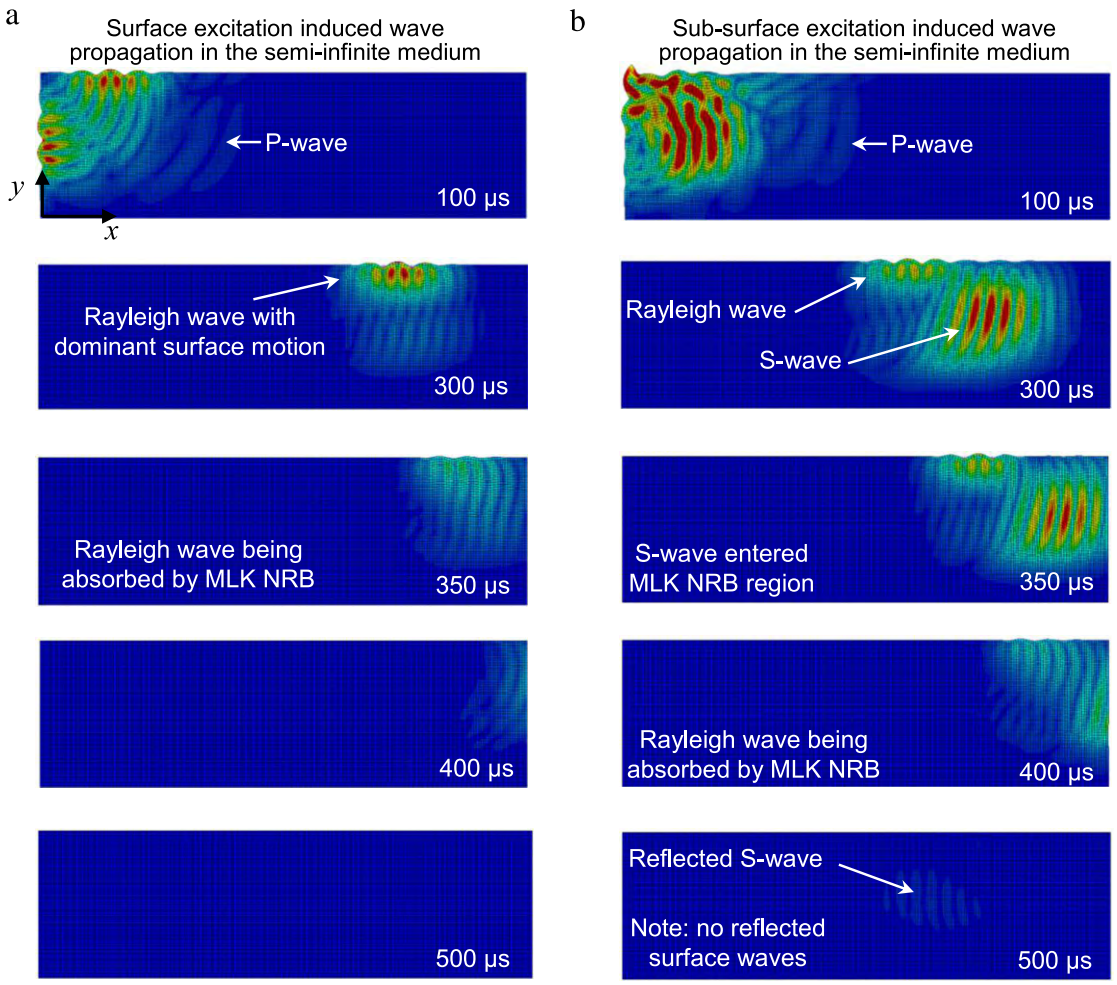

Fig. 20. MLK NRB effectiveness in a semi-infinite medium: (a) surface excitation generating predominantly Rayleigh waves; (b) sub-surface excitation simultaneously generating P-waves, S-waves, and Rayleigh waves.

shown in Fig. 20(b), these S-waves had large motion deep into the medium. This was especially clear at the R3 receiver, where strong reflected S-waves were picked up.

From this asymptotic example, we learned that our MLK NRB is also effective in absorbing surface guided waves (Rayleigh waves) in addition to absorbing plate guided waves (Lamb waves). However, its performance in absorbing bulk waves is not better than that of the conventional LK ABC method.

6. MLK NRB application to time domain and frequency domain analyses

In this section, we will demonstrate the application of our MLK NRB method to two 3-D FEM Lamb wave damage interaction examples in which its effectiveness was found particularly useful. The first example will be the time-domain

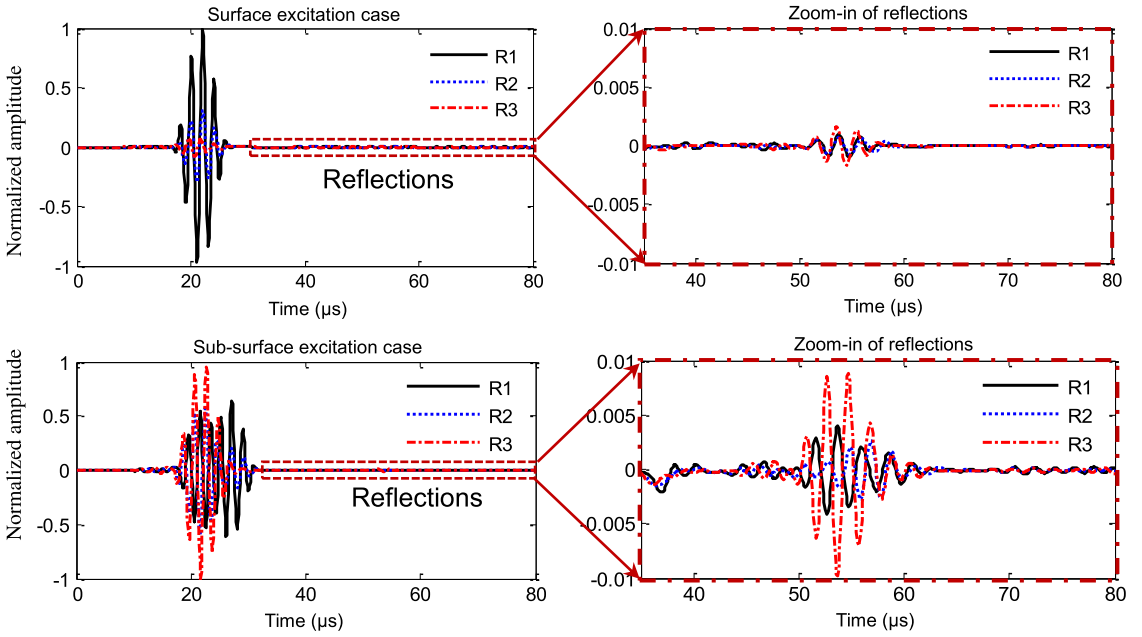

Fig. 21. Receiver signals (u_y) at three locations R1, R2, and R3 for surface excitation (top) and sub-surface excitation (bottom).

transient analysis of Lamb wave propagation and interaction with a structural feature. The second example will be the frequency-domain harmonic analysis of Lamb wave scattering from a structural damage.

6.1. Time domain transient analysis of Lamb wave interaction with a structural feature

We wanted to analyze the interaction between Lamb waves and a structural feature such as a 5-mm diameter rivet hole in a 2.032-mm thick aluminum plate. The Lamb waves were generated by a transmitter piezoelectric wafer active sensor (T-PWAS) surface-mounted at a location 100 mm away from the hole. The measured signal was picked up at a sensing location placed onto the 100-mm wave propagation path between the transmitter and the hole. The pickup point was 10 mm away from the transmitter. The Lamb waves were generated by a 200-kHz 3-cycle smoothed tone burst excitation applied on the T-PWAS, which, because of its surface mounted location, generates both S0 and A0 Lamb waves. The measured signal was the in-plane strain along the wave propagation direction. The analysis was 3D using SOLID45 ANSYS elements with a 1-mm mesh size along in-plane directions and an approximately 0.5-mm mesh size in the thickness direction.

In a conventional FEM analysis, one would have to consider a plate at least 0.5-m long and wide in order to avoid the boundary reflections from contaminating the signal scattered from the hole. This would likely lead to very large problem of approximately $3 * 10^6$ DOFs which would take considerable time and much computer resources. However, with our implementation of the MLK NRB method, we were able to use only a small model of 0.28 m by 0.18 m. Our MLK NRB boundary absorbing layer extended 40 mm inward away from the plate edges all the way around the plate.

Fig. 22 presents snapshots of the 3-D transient simulation showing Lamb wave generation, propagation, and interaction with the rivet hole. Two wave propagation cases were simulated: (a) a clean plate; (b) a plate with a rivet hole. In the clean plate (Fig. 22(a)), the absorption of each of the S0 and A0 wave modes at the boundary can be clearly noticed; no boundary reflections are present. In the plate with a rivet hole (Fig. 22(b)), the interaction between the incoming Lamb waves and the rivet hole resulted in scattered S0, SH0, and A0 waves. These waves are clearly identifiable in Fig. 22(b). Again, no reflections from the boundaries were present, hence the scattered waves are easy to pick up. A time-trace of the signal picked up at the sensing location is given in Fig. 23; the reflected S0 and A0 wave packets are clearly shown. The SH0 reflection is not shown in this signal because the scattered SH0 wave reaches its minimum amplitude along the sensing direction (as shown in Fig. 22(b)). This example has demonstrated that important wave interaction phenomena can be efficiently modeled with a small FEM model by using the MLK NRB method to avoid boundary reflection contaminations to the scatter signal.

6.2. Frequency-domain harmonic analysis of Lamb wave scattering from a structural damage

Another important use of our MLK NRB method can be found in the frequency domain wave scatter analysis. Such frequency domain analysis would be used to compute the damage scatter coefficients to be used in a normal modes expansion (NME) representation of the wave-damage interaction phenomenon.

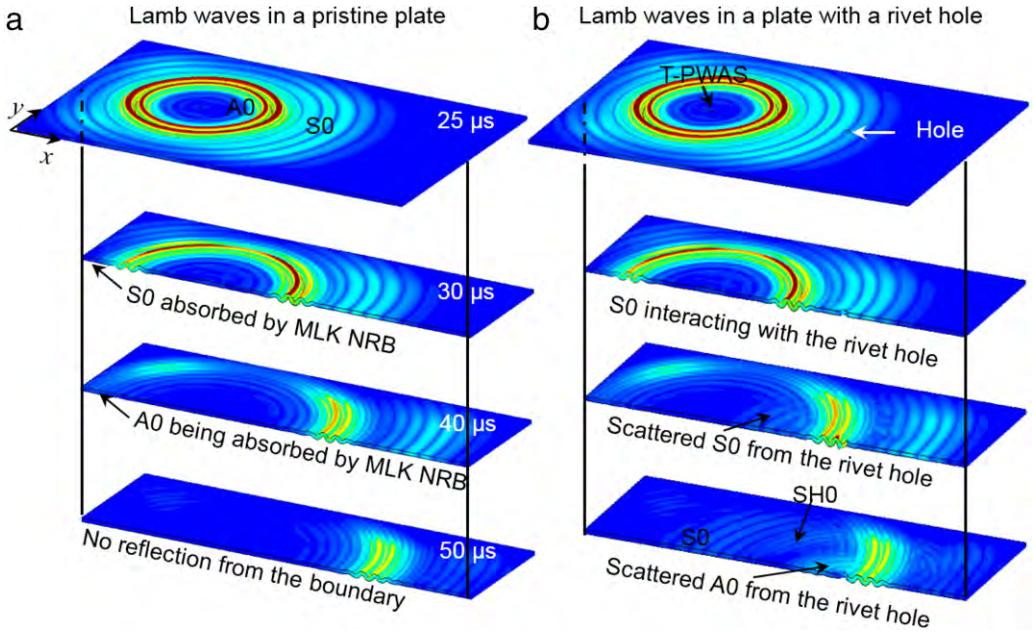

Fig. 22. Transient analysis of the interaction between Lamb waves and a rivet hold in a 3D FEM model using the MLK NRB method: (a) wave propagation in a pristine plate; (b) wave propagation in a plate with a rivet hole.

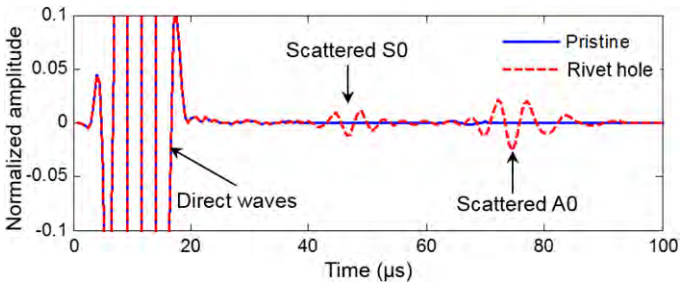

Fig. 23. Distinctive scatter effect identified by comparing with baseline pristine signal.

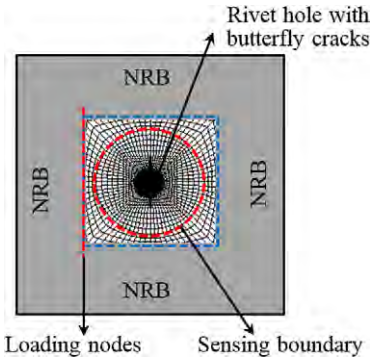

Fig. 24. Schematic of the small-size local FEM for a 1.6 mm thick aluminum plate and the rivet hole with butterfly cracks.

For example, consider the interaction of Lamb waves with the butterfly cracks emanating from a rivet hole as shown in Figs. 24 and 25. The difficulty of the problem resides in the fact that the rivet hole, even if pristine, is a scatterer. Hence, when crack damage occurs around the hole, the nature of this scatterer will change, but not very much. The challenge of the problem is to separate from the scattered field the effect of the crack from the effect of the pristine hole.

For this problem, the analysis is conducted in the frequency domain. Using our MLK NRB technique, we constructed a small-size local FEM using the frequency domain harmonic analysis module of a commercial FE software. The schematic

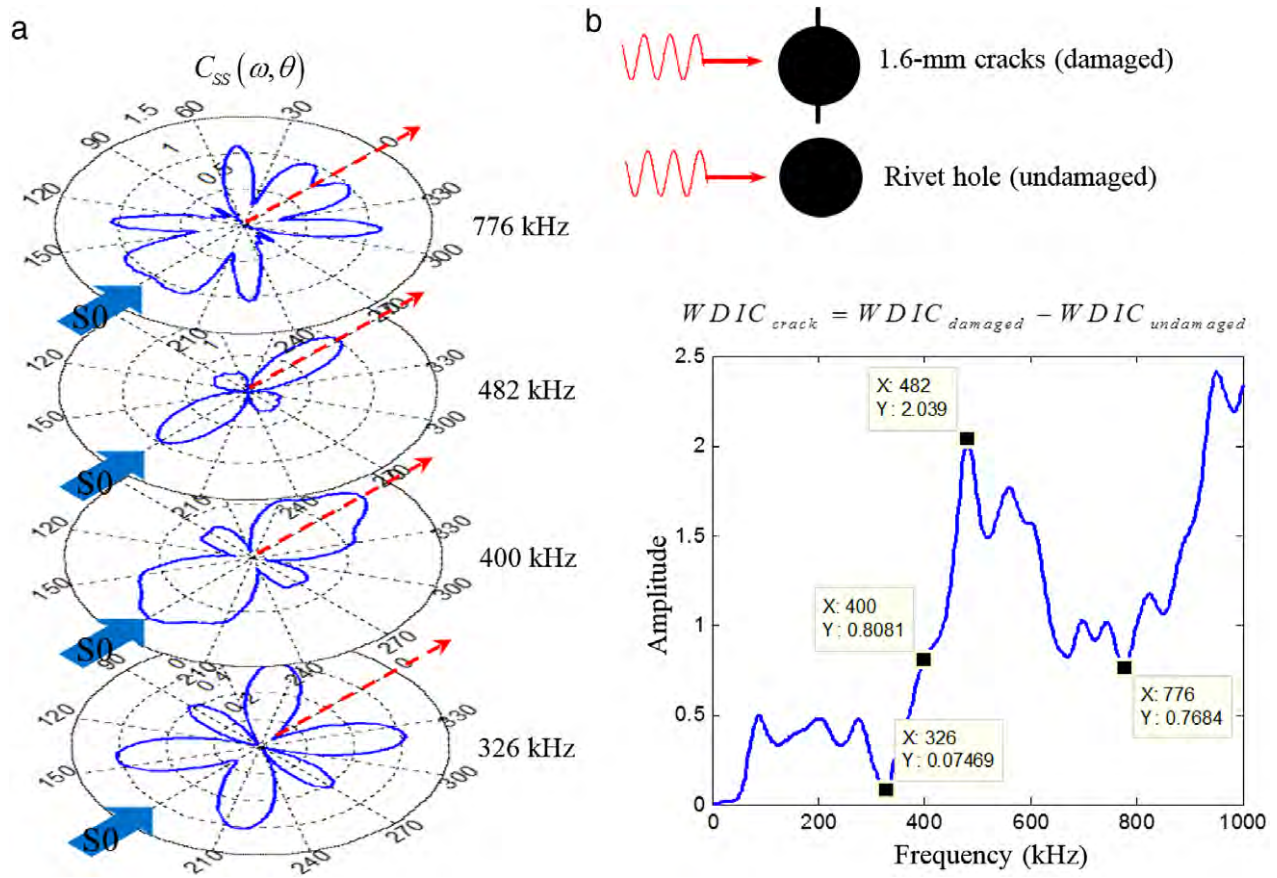

Fig. 25. (a) WDIC directivity plots under various frequencies; (b) WDIC in the forward direction as a function of frequency.

of this small-size local FEM model for the analysis of a rivet hole with butterfly cracks is shown in Fig. 24. The MLK NRB treatment was applied around this local FEM model such that the incident wave and the scattered waves will be fully absorbed at the model boundaries. The loading nodes were used to selectively generate the desired Lamb modes into the local FEM. A circular sensing boundary was used to pick up the scattered waves propagating in all the directions. Harmonic analysis was carried out to get the frequency domain response of the structure. It should be noted that the harmonic wave field will not support standing waves between the scatterer and the boundaries because the boundaries are fully absorbent. Instead, a propagating harmonic wave field will be created since the MLK NRB treatment simulates an infinite region outside the small FEM model. Due to its small size, the local FEM with MLK NRB treatment is very fast and efficient. The benefit of a harmonic analysis lies in the fact that it can provide the structural response under all the frequencies of interest with only one run of the simulation, i.e., in commercial FE software packages, one only needs to define the specific frequency range and step size, and the software will calculate the results for all the specified frequencies. This is an important benefit and advantage compared with time-domain transient analysis in which one has to conduct the simulation separately again and again to cover all the frequencies of interest. Of course, Fourier transform based post-processing of the transient analysis results may be applied to cover a wider frequency band, but this would require additional effort.

The scatter field was described in terms of wave-damage interaction coefficients (WDICs), as discussed in Ref. [27,28]. In our study, two situations were computed: (1) a plate with undamaged rivet hole generating the $WDIC_{undamaged}$ scatter field; and (2) a plate with a damaged rivet hole containing butterfly cracks generating the $WDIC_{damaged}$ scatter field. The scatter field of the butterfly crack $WDIC_{crack}$ was extracted from the total scatter field $WDIC_{damaged}$ by subtraction of the undamaged scatter field $WDIC_{undamaged}$, i.e.,

$$WDIC_{crack} = WDIC_{damaged} - WDIC_{undamaged} \tag{16}$$

For illustration, Fig. 25 present a few results from our analysis for the case of an S0 Lamb wave incident.

Fig. 25(a) shows the scattered S0 wave amplitude $C_{SS}(\omega,\theta)$ from an incident S0 mode impinging upon the damage. It can be observed that the scattered wave amplitude is a function of frequency ω and the azimuthal angle θ. Directivity plots are presented at various frequencies; one notices that the azimuthal scatter pattern of the directivity plots changes dramatically with frequency. It can be noticed that, when the butterfly cracks are directly facing the transmitter direction, the best sensing location seems to be along the wave propagation direction as indicated by the red arrows in Fig. 25. Similar results can be

obtained for the A0 incidence [27,28], but they will not be presented here for sake of brevity. For the same reason, mode conversion effects are not presented here either.

Since, the additional scatter field due to the butterfly crack damage is frequency dependent, the possibility of an optimal interrogation frequency arises. Fig. 25(b) presents a frequency plot of scatter field amplitude measured along the wave propagation direction. This frequency plot indicates that the best interrogation frequency seems to be around 482 kHz when the damage scatter field amplitude reaches a peak. Also noticed in Fig. 25(b) is the fact that certain frequencies might be bad choices because the scatter field would be very small, e.g., the 326 kHz frequency when the scatter amplitude is very small. It should be noted that the result and discussion was specific for this example. For different damage types, crack orientations, and interrogating wave modes, the results and best detection strategy may vary from case to case.

7. Summary and conclusions

This article presented a new method for constructing non-reflective boundaries (NRB) when using finite element method (FEM) analysis to simulate Lamb wave interaction with structural defects and damage. Our method is an extension of the LK ABC method that was developed for absorbing P and S waves at the edge of a semi-infinite half space. Our new contribution consists in extending the LK concept to the case of a plate. In our modification of the LK concept, we wrapped the LK absorbing interface to the top and bottom surfaces of the plate. (In the LK model, the absorbing interface was only applied to the vertical end of the semi-infinite half space.) We call our approach the modified Lysmer–Kuhlemeyer non-reflective boundaries (MLK NRB).

The main idea of our MLK NRB method is to take into account the fact that Lamb waves, by their nature, are the superpositions of P and S bulk waves that undergo multiple reflections at the top and bottom surfaces of the plate. Hence, we extended the LK absorbing interface over the top and bottom surfaces of the plate in order to attenuate these multiple bulk wave reflections in addition to attenuating their reflections at the vertical edge of the plate.

The paper started with a review of the existing non-reflective boundary literature and identified three major directions (i) infinite element methods; (ii) non-reflective boundary conditions, e.g., the conventional LK ABC method; and (iii) absorbing layer methods, e.g., the ALID family of methods. Current Lamb wave absorption techniques were found to stem mainly from the ALID family. The paper continued to discuss why the LK ABC approach is inadequate for Lamb waves and how it could be modified to compensate for this inadequacy. Subsequently, the paper presented details of our MLK NRB method. Several parametric studies were conducted to develop guidelines for the proper choice of MLK NRB parameters. Details of the implementation method and strategy of MLK NRB was provided in a systematic manner.

Comparative studies between our MLK NRB method and the existing ALID NRB and LK ABC methods were conducted. The studies showed that our MLK NRB method has better performance for all Lamb modes. The case of long wavelength Lamb waves that may appear at low frequencies for the fundamental S0, A0 modes and near the cut-off frequencies for the higher modes was also studied. It was again found that MLK NRB gives better performance.

Parametric study on the coverage length and plate thickness were also conducted. It was found that our MLK NRB method is better than the ALID method when applied to thin plate structures. However, in thicker plates, the ALID method seems to work better than our MLK NRB method.

Two application examples of our MLK NRB method were given. One example was performed in the time-domain and showed how a Lamb wave package scatters from a structural feature such as a rivet hole. The other example was performed in the frequency domain and illustrated how additional scatter due to butterfly crack damage in a rivet hole can be extracted from the scatter field of the pristine hole. Interesting effects related to the variation of the damage scatter with frequency were noticed and desirable interrogation frequencies (as well as undesirable ones) were identified. The application of our MLK NRB method to reflection suppression in a semi-infinite half space was also studied. It was found that our MLK NRB method can effectively suppress Rayleigh wave reflections, but is not very effective in suppressing S-wave reflections.

Since our MLK NRB method is based on a totally different mechanism than the ALID family of methods, the question arises as to whether these two methods could be combined to get an even better performance for suppressing Lamb wave reflections at the plate boundaries. We believe that the mechanisms behind MLK NRB and ALID methods are complimentary to each other; hence, the investigation of a hybrid technique combining these two mechanisms is fully justified and should be pursued in future work.

Acknowledgments

Support from Office of Naval Research # N00014-11-1-0271, Dr. Ignacio Perez, Technical Representative; Air Force Office of Scientific Research # FA9550-11-1-0133, Dr. David Stargel, Program Manager; is gratefully acknowledged. The authors also want to express their acknowledgment to the reviewers for their valuable comments and suggestions.

References

[1] D. Alleyne, P. Cawley, The interaction of Lamb waves with defects, IEEE Trans. Ultrason. Ferroelectr. Freq. Control 39 (1992) 381–397.
[2] F. Moser, L. Jocobs, J. Qu, Modeling elastic wave propagation in waveguides with the finite element method, NDT & E Int. 32 (1999) 225–234.

[3] M. Gresil, Y. Shen, V. Giurgiutiu, Benchmark problems for preditive FEM simulation of 1-D and 2-D guided waves for structural health monitoring, Rev. Prog. Quant. Nondestruct. Eval. 31 (2012) 1835–1842.
[4] J. Lysmer, R. Kuhlemeyer, Finite dynamic model for infinite media, J. Eng. Mech. Div. Proc. Am. Soc. Civ. Eng. EM4 (1969) 859–877.
[5] F. Hastings, J. Schneider, S. Broschat, Application of the perfectly matched layer (PML) absorbing boundary conditions to elastic wave propagation, J. Acoust. Soc. Am. 100 (1996) 3061–3096.
[6] G. Liu, S. Jerry, A non-reflecting boundary for analysing wave propagation using the finite element method, Finite Elem. Anal. Des. 39 (2003) 403–417.
[7] P. Rajagopal, M. Drozdz, E. Skelton, M. Lowe, R. Craster, On the use of absorbing layers to simulate the propgation of elastic waves in unbounded isotropic media using commercially available finite element packages, NDT & E Int. 51 (2012) 30–40.
[8] D. Givoli, J. Keller, Non-reflecting boundary conditions for elastic waves, Wave Motion 12 (1990) 261–279.
[9] D. Givoli, High-order local non-reflecting boundary condtions: a review, Wave Motion 39 (2004) 319–326.
[10] L. Moreau, A. Velichko, P. Wilcox, Accurate fintie element modelling of guided wave scattering from irregular defects, NDT & E Int. 45 (2012) 46–54.
[11] J. Berernger, A perfectly matched layer for the absorption of electromegnetic waves, J. Comput. Phys. 114 (1994) 185–200.
[12] E. Skelton, S. Adams, R. Craster, Guided elastic waves and perfectly matched layers, Wave Motion 44 (2007) 573–592.
[13] M. Israeli, S. Orszag, Apporximation of radiation boundary conditions, J. Comput. Phys. 41 (1981) 115–135.
[14] M. Castaings, C. Bacon, B. Hosten, M. Predoi, Finite element predictions for the dynamic response of thermo-viscoelastic material structures, J. Acoust. Soc. Am. 115 (2004) 1125–1133.
[15] M. Castaings, C. Bacon, B. Hosten, M. Predoi, Fintie element modeling of torsional wave modes along pipes with absorbing materials, J. Acoust. Soc. Am. 119 (2006) 3741–3751.
[16] W. Ke, M. Castaings, C. Bacon, 3D fintie element simulations of an air-coupled ultrasonic NDT system, NDT & E Int. 42 (2009) 524–533.
[17] J. Semblat, L. Lenti, A. Gandomzadeh, A simple multi-directional absorbing layer method to simulate elastic wave propagation in unbounded domains, Internat. J. Numer. Methods Engrg. 85 (2011) 1543–1563.
[18] J. Pettit, A. Walker, P. Cawley, M. Lowe, A stiffness reduction method for efficient absorption of waves at boundaries for use in commercial finite element codes, Ultrasonics 54 (2014) 1868–1879.
[19] M. Drozdz, L. Morreau, M. Castaings, M. Lowe, P. Cawley, Efficient numerical modelling of absorbing regions for boundaries of guided waves problems, AIP Conf. Proc. 820 (2006) 126–133.
[20] Z. Fan, M. Lowe, Interaction of weld-guided waves with defects, NDT & E Int. 47 (2012) 124–133.
[21] S. Hosseini, S. Duczek, U. Gabbert, Non-reflecting boundary condition for Lamb wave propagation problems in honeycomb and CFRP plates using dashpot elements, Composites B 54 (2013) 1–10.
[22] J. Rose, Ultrasonic Waves in Solid Media, Cambridge University Press, 2004.
[23] K. Graff, Wave Motion in Elastic Solids, Dover Publications, Inc., New York, 1975.
[24] V. Giurgiutiu, Structural Health Monitoring with Piezoelectric Wafer Active Sensors, second ed., Elsevier Academic Press, ISBN: 978-0-12-418691-0, 2014.
[25] J. Liu, Y. Du, X. Du, Z. Wang, J. Wu, 3D viscous-spring artificial boundary in time domain, Earthq. Eng. Eng. Vib. 5 (1) (2006) 93–102.
[26] ANSYS 14.0 Help Manual.
[27] Y. Shen, V. Giurgiutiu, WFR-2D: an analytical model for PWAS-generated 2D ultrasonic guided wave propagation, in: SPIE Smart Materials and Structures/NDE, San Diego, 2014.
[28] Y. Shen, Structural health monitorin using linear and nonlinear ultrasonic guided waves (Doctoral dissertation), University of South Carolina, Columbia, SC, 2014, http://scholarcommons.sc.edu/etd/2883/.

IOPscience iopscience.iop.org

Home Search Collections Journals About Contact us My IOPscience

Shear horizontal wave excitation and reception with shear horizontal piezoelectric wafer active sensor (SH-PWAS)

This content has been downloaded from IOPscience. Please scroll down to see the full text.

2014 Smart Mater. Struct. 23 085019

(http://iopscience.iop.org/0964-1726/23/8/085019)

View the table of contents for this issue, or go to the journal homepage for more

Download details:

IP Address: 129.252.23.119
This content was downloaded on 05/09/2014 at 16:34

Please note that terms and conditions apply.

IOP Publishing Smart Materials and Structures
Smart Mater. Struct. **23** (2014) 085019 (17pp) doi:10.1088/0964-1726/23/8/085019

Shear horizontal wave excitation and reception with shear horizontal piezoelectric wafer active sensor (SH-PWAS)

A Kamal and V Giurgiutiu

Mechanical Engineering Department, University of South Carolina, Columbia, SC, USA

E-mail: kamal@email.sc.edu and victorg@sc.edu

Received 20 November 2013, revised 6 April 2014
Accepted for publication 15 May 2014
Published 2 July 2014

Abstract

This article discusses shear horizontal (SH) guided-waves that can be excited with shear type piezoelectric wafer active sensor (SH-PWAS). The paper starts with a review of state of the art SH waves modelling and their importance in non-destructive evaluation (NDE) and structural health monitoring (SHM). The basic piezoelectric sensing and actuation equations for the case of shear horizontal piezoelectric wafer active sensor (SH-PWAS) with electro-mechanical coupling coefficient d_{35} are reviewed. Multiphysics finite element modelling (MP-FEM) was performed on a free SH-PWAS to show its resonance modeshapes. The actuation mechanism of the SH-PWAS is predicted by MP-FEM, and modeshapes of excited structure are presented. The structural resonances are compared with experimental measurements and showed good agreement. Analytical prediction of SH waves was performed. SH wave propagation experimental study was conducted between different combinations of SH-PWAS and regular in-plane PWAS transducers. Experimental results were compared with analytical predictions for aluminium plates and showed good agreement. 2D wave propagation effects were studied by MP-FEM. An analytical model was developed for SH wave power and energy. The normal mode expansion (NME) method was used to account for superpositioning multimodal SH waves. Modal participation factors were presented to show the contribution of every mode. Power and energy transfer between SH-PWAS and the structure was analyzed. Finally, we present simulations of our developed wave power and energy analytical models.

Keywords: shear horizontal (SH), piezoelectric wafer active sensor (PWAS), structural health monitoring (SHM), wave power and energy, dispersion wave speeds

(Some figures may appear in colour only in the online journal)

1. Introduction

A conventional piezoelectric wafer active sensor (PWAS) is a thin and rectangular or circular wafer that is poled in thickness direction with electrodes on the top and bottom surfaces. Those types of PWAS transducers are either used in in-plane or thickness mode. In the in-plane mode, applying an electric field in thickness direction causes the sensor lateral dimensions to increase or decrease, and a longitudinal strain will occur $\varepsilon_1 = d_{13}E_3$, where d_{13} is the piezoelectric coupling coefficient measured in [nm kV^{-2}]. Thickness mode is a mode that occurs simultaneously with extension mode, but dominates at higher frequencies in MHz. In the thickness mode, strain in the thickness direction will occur $\varepsilon_3 = d_{33}E_3$, where d_{33} is the piezoelectric coupling coefficient in thickness direction. A different mode of oscillation can be achieved when the applied electric field direction is perpendicular to the poling direction, and it is referred to as shear mode. The common piezoelectric coupling coefficient known for this mode is defined as d_{15}; however, this coupling coefficient occurs only when the electric current is applied in E_1 direction and the poling is along thickness direction. The shear coupled

 © 2014 IOP Publishing Ltd Printed in the UK

PWAS presented in this study is associated with the d_{35} coupling coefficient, in which electric current is applied across thickness (i.e., in x_3 direction), and the poling is in x_1 direction. A few studies considered this (d_{35}-mode) [1]. For most piezoelectric materials, the coupling coefficients associated with shear mode have the largest value of all coefficients [2–4]. The higher values of shear coupling coefficients make SH-PWAS superior in actuation and sensing [5]. SH waves are also preferable because the first symmetric mode is non-dispersive in isotropic materials, i.e., wave speed is constant at different frequencies. On the other hand, one of the important disadvantages of SH-PWAS is that thicker transducers are needed to sustain and generate the shear actuation. Due to the high density of piezoceramic materials ($\approx 7600\,\mathrm{kg\,m^{-3}}$ for APC850 piezoceramic Navy II type), using shear mode piezoelectric elements increases the mass of the system.

Shear mode piezoelectric transducers were used as an actuator element in a cantilever adaptive sandwich beam setup [6]. The stress distribution under mechanical and electrical loading was investigated across thickness and length. A similar study on using shear-type piezoelectric as a shear bender was studied by [7]. A piezoelectric device was also used for designing torsional actuators generating angular displacement [2], where the torsional element consists of different segments, and the neighbouring segments are of opposite poling. The application of a torsional actuator was applied in a later study by [8] to control rotor blade trailing edge flaps.

For SHM and NDE applications, shear horizontal (SH) guided waves showed high potential for quantitative detection of structure defects [9–11]. In [11], it was shown that SH wave mode conversion occurs at the damage from fundamental incident S0, and it was shown that SH0 could be used for quantitative identification of delamination in composite beams. In another application, SH polarized waves were used for evaluating the quality of bonding between the transducer and the structure [12]. This can be compared to the method of using an imaginary component of PWAS impedance analysis to test the bonding between the transducer and the structure [13]. Shear horizontal waves are usually associated with electromagnetic acoustic transducers, or EMAT [14], where SH waves were used for detection of weld defects. SH waves excited by EMAT have shown superiority over conventional shear vertical (SV) and longitudinal waves for detection of weld defects [15]; however, it was suggested that piezoelectric-based transducers generating SH would show better acoustic generation than EMAT [15]. Also, one point to consider is that EMAT needs conductive structures, while PWAS can be used for conductive metallic structures and non-conductive composites (e.g., glass fibre reinforced polymers), not including the fact that SH-PWAS is inexpensive. In terms of effectiveness, EMAT always showed reliability for detecting damages, especially magnetostrictive MsS®, which have been developed by Southwest Research institute (http://www.swri.org). Nevertheless, fibre optics were also used for detecting SH waves, [16] used fibre optic sensors for detection of SH0 wave type generated from mode conversion from excited Lamb waves, and this was used for detecting delamination in CFRP composites.

SH-PWAS can be used as an alternative for spiral wave ultrasonic conventional transducers in applications such as detecting weep holes in wing spars [17, 18]. This application is not necessarily used for weep holes, but it is used for holes with fasteners. SH-PWAS can be used as a torsional wave exciter and/or recipient for pipe crack damage detection. SH-PWAS can also be used in applications that require the detection of shear waves for finding adhesive shear stiffness [12].

This study focuses on generation of SH waves by piezoelectric wafer-type shear transducer; we call it SH-PWAS. The objectives are: (i) predictive modelling of SH-PWAS response and (ii) performing extensive experimental studies to support the predictive models. The study is structured into three main parts. In the first part, basic piezoelectric sensing and actuation equations for the case of SH-PWAS are discussed. A finite element model was performed to show how the transducer resonates. FEM is also used to show the excitability of SH waves and the axial-flexural waves. The second part presents generation and reception of SH waves and compares dispersion wave speeds with analytical predictions. Experimental studies investigate (1) different possible pitch–catch configurations between SH-PWAS and regular in-plane PWAS and (2) directivity of SH-PWAS and its effect on wave amplitudes. Moreover, FEM was performed to show the 2D effects associated with excitation and reception of SH waves. Finally, in the third part, predictive models for power and energy of SH waves were analytically developed based on the normal modes theory. In this study, it is shown how to superimpose SH wave power when multi-modes exist (typically at high excitation frequencies and in thick structures). Power is the time rate of change of wave energy. We developed energy models to verify our analytical models by showing that potential energy and kinetic energy are equal. Modelling the total wave power is important to better understand the power consumption of the electric source for practical SHM and NDT systems. Also, the developed power model shows how different modes contribute to the total power.

2. SH-PWAS constitutive relations and actuation mechanism

2.1. Constitutive relations

Most literature mentioned earlier dealt with shear dielectric coupling coefficient d_{15}; however, this is only applicable if the electric field (E_1) is applied in the in-plane direction and the piezoelectric poling is in the thickness direction. In such a case, the transducer electrodes are installed on two of the vertical sides. In our model and in FEM simulations, we use

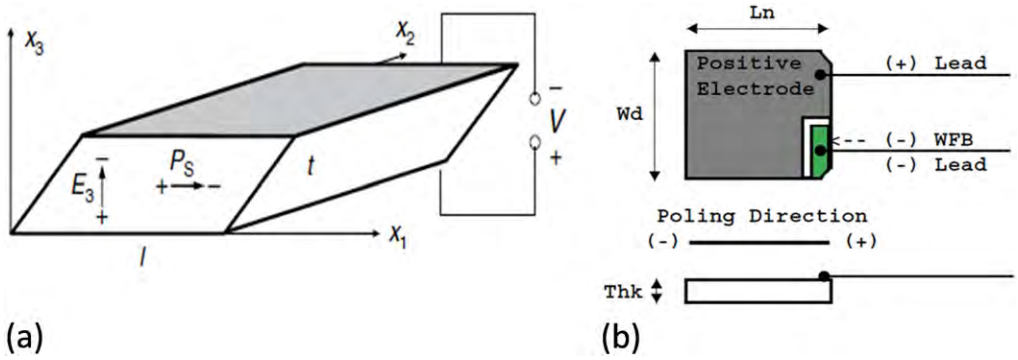

Figure 1. (a) Schematic diagram for SH-PWAS; shaded areas are the electrodes. Reproduced with permission from [13]. Copyright 2008 Elsevier. (b) provided transducer schematic from manufacturer, (source: APC Piezoceramic Int., Ltd [3]).

d_{35} as the SH-PWAS we used [3] is having its electrodes on top and bottom and hence electric field is applied along x_3 direction, and the poling is applied longitudinally (refer to figure 1(a)). From main constitutive equations of piezoelectricity, we have

$$S_{ij} = s^E_{ijkl} T_{kl} + d_{kij} E_k \tag{1}$$

$$D_i = d_{ikl} T_{kl} + \varepsilon^T_{ik} E_k \tag{2}$$

where S_{ij} are the strain components, s^E_{ijkl} denotes compliance matrix under a constant electric field condition, T_{kl} are stress components, d_{kij} are piezoelectric coupling coefficients, E_k represents the electric field vector, D_i is the electric displacement vector, and ε^T_{ik} are electric permittivity constants of the PWAS material. Equation (1) is considered the piezoelectric converse effect, where an applied electric field will result in induced strains. Equation (2) is the direct piezoelectric mechanism, where applied stresses will result in output electrical displacements. In the contracted Voigt contraction form, equations (1), (2) can be written as

$$\begin{Bmatrix} S_1 \\ S_2 \\ S_3 \\ 2S_4 \\ 2S_5 \\ 2S_6 \end{Bmatrix} = \begin{bmatrix} s^E_{11} & s^E_{12} & s^E_{13} & & & \\ s^E_{21} & s^E_{22} & s^E_{23} & & & \\ s^E_{31} & s^E_{32} & s^E_{33} & & & \\ & & & s^E_{44} & & \\ & & & & s^E_{55} & \\ & & & & & s^E_{66} \end{bmatrix} \begin{Bmatrix} T_1 \\ T_2 \\ T_3 \\ T_4 \\ T_5 \\ T_6 \end{Bmatrix} + \begin{bmatrix} & & d_{31} \\ & & d_{32} \\ & & d_{33} \\ & d_{24} & \\ d_{15} & & \\ & & d_{35} \end{bmatrix} \begin{Bmatrix} E_1 \\ E_2 \\ E_3 \end{Bmatrix} \tag{3}$$

$$\begin{Bmatrix} D_1 \\ D_2 \\ D_3 \end{Bmatrix} = \begin{bmatrix} & & & & d_{15} & \\ & & & d_{24} & & \\ d_{31} & d_{32} & d_{33} & & d_{35} & \end{bmatrix} \begin{Bmatrix} T_1 \\ T_2 \\ T_3 \\ T_4 \\ T_5 \\ T_6 \end{Bmatrix} + \begin{bmatrix} \varepsilon^T_{11} & & \\ & \varepsilon^T_{22} & \\ & & \varepsilon^T_{33} \end{bmatrix} \begin{Bmatrix} E_1 \\ E_2 \\ E_3 \end{Bmatrix}. \tag{4}$$

The mechanical compliance matrix of the piezoelectric material takes an orthotropic form. The electrical permittivity matrix is a diagonal matrix, corresponding to the three possible directions of the applied electric field. The piezoelectric coupling matrix contains coefficient d_{33} corresponding to the thickness strain, i.e., $\varepsilon_3 = d_{33} E_3$ and coefficients corresponding to the lateral strain, i.e., d_{13} and d_{23}. Also, the d_{24} coefficient relates the electric field in lateral direction E_2 with shear motion (in 2–3 direction, i.e., T_4,$2S_4$), while d_{15} relates the electric field in lateral direction E_1 with shear motion (in 1–3 direction, i.e., T_5,$2S_5$). In our SH-PWAS, provided by APC piezoceramic Int., Ltd. (figure 1(b)), the electric field is applied in E_3 direction, resulting in shear motion (in 1–3 direction, i.e., T_5, $2S_5$). So, the d_{35} term appears. For the SH-PWAS transducer in this study, we have an electric field in 3-direction, and the poling is in longitudinal direction, as shown in figure 1(a); the two equations (3), (4) reduce to

$$(2S_5) = u_1' = s^E_{55} T_5 + d_{35} E_3 \tag{5}$$

$$D_3 = d_{35} T_5 + \varepsilon_{33} E_3. \tag{6}$$

2.2. Free SH-PWAS response

A multiphysics finite element model was constructed for the free SH-PWAS using COMSOL Multiphysics. The coupled physics incorporates the induced mechanical strain due to an applied electrical field across the thickness in x_3 direction.

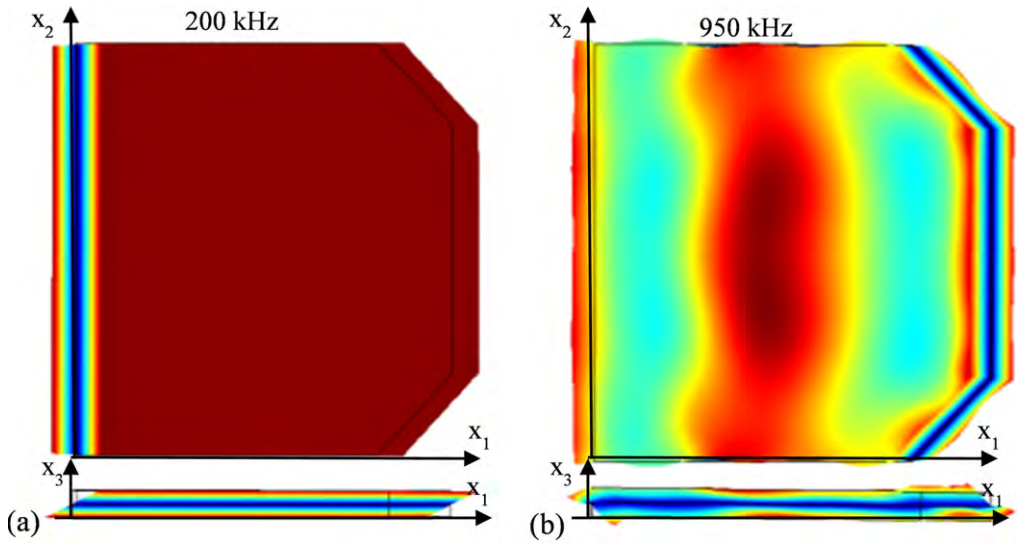

Figure 2. Mode shapes of vibrations for SH-PWAS using finite element analysis, (a) mode shape at 200 kHz, (b) mode shape at resonance frequency 950 kHz.

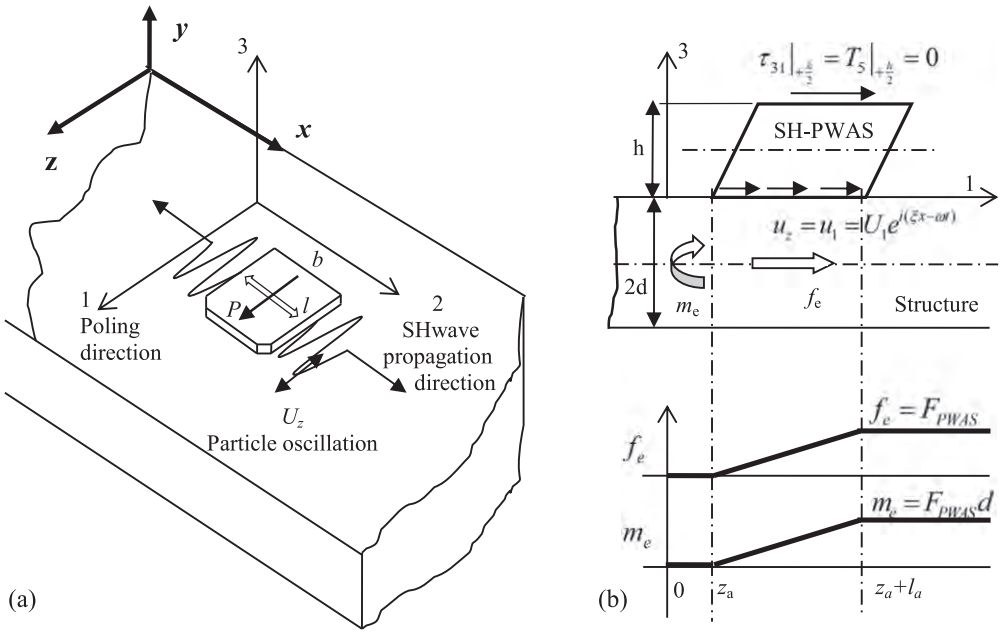

Figure 3. (a) Schematic of SH-PWAS bonded on the structure, (b) Axial–flexural response excited by SH-PWAS parallel to poling direction.

The SH-PWAS dimensions are 15 mm × 15 mm × 1 mm. One square side of the SH-PWAS was grounded, and a 10 volt was applied to the other side. A sweep of frequencies was performed from 100 kHz to 4 MHz, and the resulting displacement response was reported in figure 2 for two example frequencies: a) at 200 kHz and b) at 950 kHz, where the transducer's first resonance occurs. PWAS material is APC850; detailed properties can be found on the APC website (http://www.americanpiezo.com). Figure 2 shows a finite element analysis of the vibrations' modeshapes of SH-PWAS. It can be observed that at low frequency (figure 2(a)), the vibration has a linear shape across the thickness. Whereas at higher frequencies, e.g., ≈1 MHz, (figure 2(b)), the modeshape shows nonlinearities and a more complicated shape. The modeshape of vibration of the shear horizontal coupled PWAS is important, as it controls the excitation of guided waves in the structure, which is discussed in the next section.

2.3. Bonded SH-PWAS to beam structures

When SH-PWAS is bonded to the structure (figure 3(a)), SH waves are excited in the direction perpendicular to poling direction. Poling direction is the direction where the transducer vibrates when excited by electrical voltage. Because of this actuation mechanism, axial-flexural response can be obtained in the direction of poling *P*. Figure 3(b) shows the shear actuation of the transducer. Normal load transfer as well as bending moment transfer lead to an axial and flexural response in 1-direction.

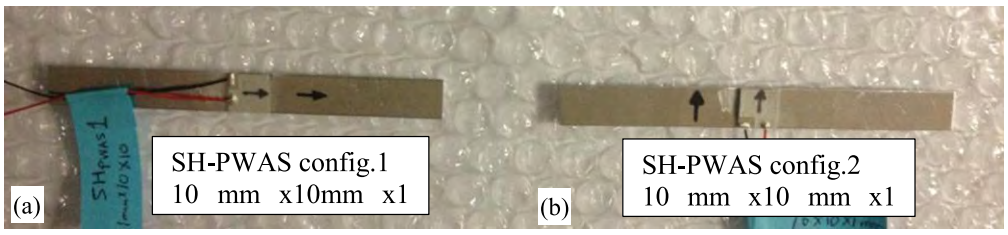

Figure 4. Experimental setup for SH-PWAS bonded on 1 mm aluminium beams (a) configuration-1, (b) configuration-2, (the black arrow indicates poling direction).

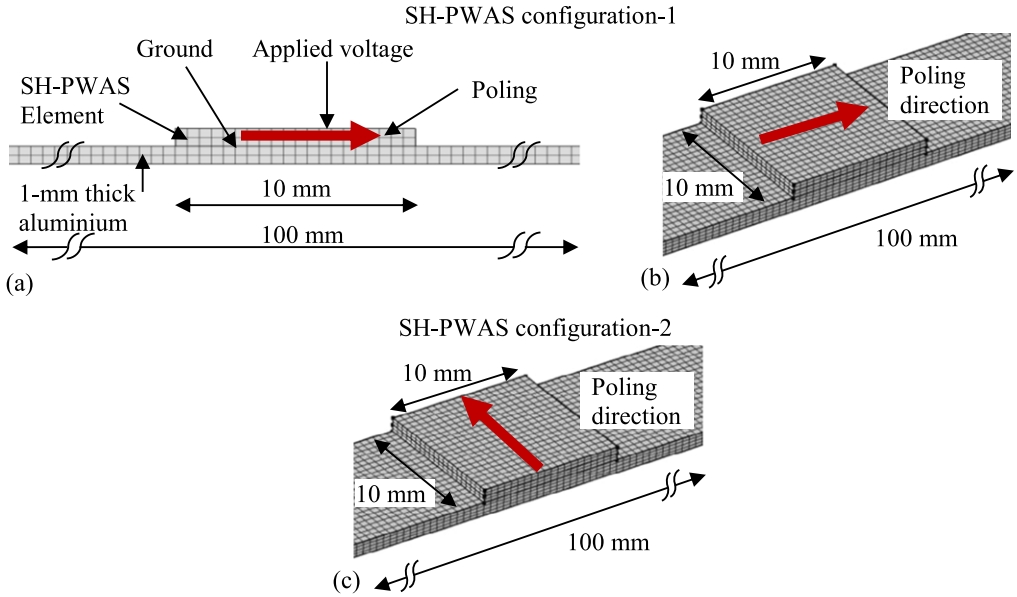

Figure 5. FEM for bonded SH-PWAS on 1 mm thick aluminium beams: SH-PWAS configuration-1: (a) 2D model, (b) 3D model, (c) SH-PWAS configuration-2, 3D model.

Electromechanical (E/M) impedance is measured for bonded SH-PWAS on 1 mm thick aluminium beams. A frequency sweep is performed up to 160 kHz to capture structure resonances. The objective is to study structure response when SH-PWAS is bonded in either one of two configurations: (a) transducer poling is parallel to the beam length or (b) transducer poling is perpendicular to the beam length (figure 4).

Finite element models are constructed for bonded SH-PWAS on 1 mm thick aluminium beams. Three models are constructed: (a) 2D model for the case where poling of the SH-PWAS is along the beam length, (b) 3D model for the same case of having poling direction parallel to the beam length, and (c) 3D model for the case of transducer poling perpendicular to the beam length. Figure 5 shows detailed finite element setups. The transducer top electrode is excited by electric voltage of 1 V. A sweep of frequency is performed up to 160 kHz. E/M impedance is calculated for different models and compared with bonded SH-PWAS experimental results.

2.4. Discussion of bonded SH-PWAS electromechanical response results

The elecromechanical impedance of bonded SH-PWAS in configuration-1 shows peaks at 42 kHz, 90 kHz, and 136 kHz (figure 6). Structure modeshapes at these frequencies indicate

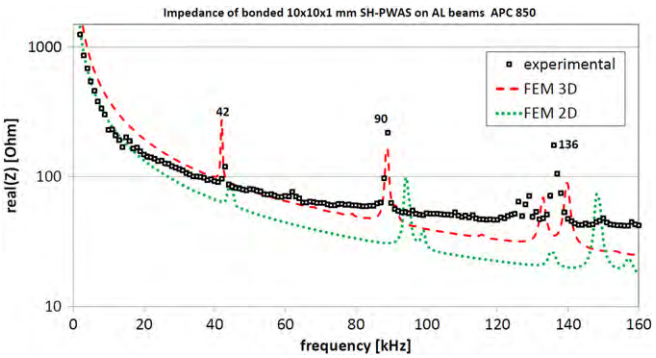

Figure 6. Comparison between experimental results and finite element simulations for E/M impedance of SH-PWAS bonded on 1 mm thick aluminium beam (configuration-1).

that these frequencies correspond to the axial-flexural response (figure 7). The modeshapes at 42 kHz and 136 kHz are width independent (z-invariant). However, the captured modeshape at 90 kHz has some width coupled vibration.

These results agree with the suggested mechanism of actuation of SH-PWAS for the response in the same direction of poling direction (figure 3(b)).

The SH-PWAS installed in configuration-2 showed SH response, where the beam length is perpendicular to the

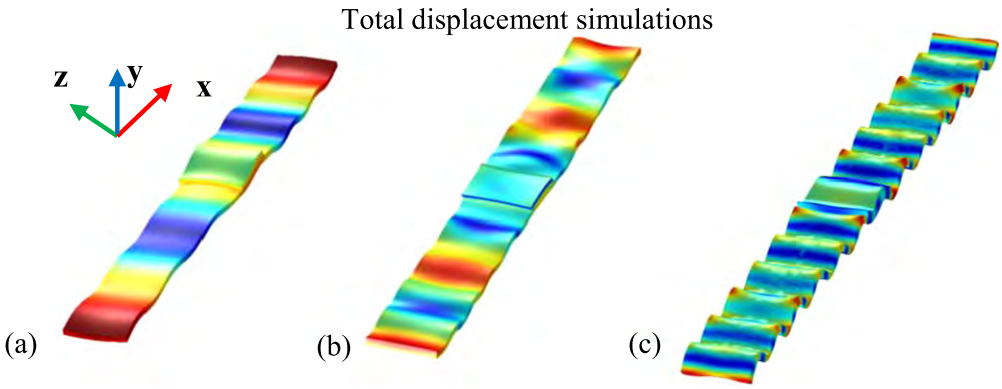

Figure 7. Modeshapes of vibrations of 1 mm thick aluminium beam with bonded SH-PWAS in configuration-1 (axial-flexural orientation) at excitation frequency: (a) 42 kHz, (b) 90 kHz, (c) 136 kHz. Plotted FEM variable is the total displacement.

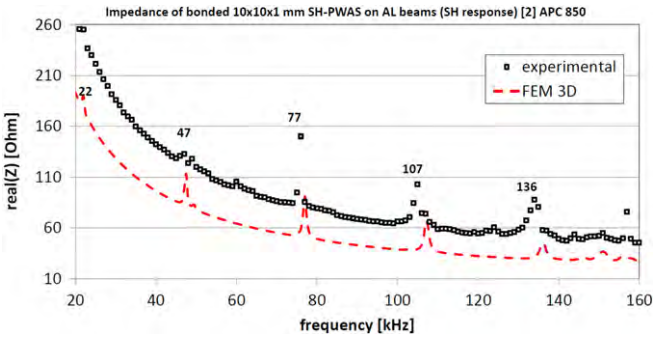

Figure 8. Comparison between experimental results and finite element simulations for E/M impedance of SH-PWAS bonded on 1 mm thick aluminium beam (configuration-2).

poling direction. The electromechanical impedance of the bonded transducer to the structure (figure 8) shows peaks at 22 kHz, 47 kHz, 77 kHz, 107 kHz, and 136 kHz. Figure 9 shows the finite element simulation of displacement in the z-direction, which is a shear horizontal response.

3. Guided wave excitation by SH-PWAS

3.1. Analytical review

Consider SH-PWAS bonded to the structure shown in figure 3(a). The structure half thickness is d, and μ is the shear modulus of the structure. SH PWAS dimensions are: length l, width b, and thickness h. Shear horizontal waves have a shear–type particle motion contained in the horizontal plane. Cartesian coordinates are defined such that the x-axis is placed along the wave propagation direction, whereas the z-axis is the direction of particle motion, and y is along the plate thickness. The poling direction of the piezoelectric transducer is in x_1 direction (coincides with global z-axis coordinate of the structure). An approximated 1D analytical model with a z-invariant assumption is well-developed in many previous studies [19–21]. The analytical model only predicts SH wave motion of particle oscillation along z direction and propagating in x direction. We use the analytical model to predict dispersion wave speeds of SH waves. The displacement is assumed to be harmonic

$$u_z(x, y, t) = U_z(y)e^{-i(\xi x-\omega t)} \tag{7}$$

where ξ is the wave number in x direction. Guided SH waves in plates (similar to guided Lamb waves) are multimodal in nature; as the frequency of excitation increases, new modes are excited in the plate. The frequencies at which new modes appear are called cut-off frequencies. The cut-off frequency can be determined by solving the characteristic equation $\sin(\eta^S d)\cos(\eta^A d) = 0$ for ηd values and by substituting in

$$f_{\text{cut-off}} = \frac{1}{2\pi}\frac{c_s}{d}(\eta d) \tag{8}$$

where η is defined from $\eta^2 = \omega^2/c_s^2 - \xi^2$, and c_s is the shear wave speed. We define cut-off frequency in units of Hz or normalized frequency (fd/c_s). The nth symmetric mode displacement is

$$u_z^n(x, y, t) = B_n \cos\left(\eta_n^S y\right) e^{-i\xi_n^S x} e^{i\omega t} \tag{9}$$

and the nth antisymmetric mode displacement is

$$u_z^n(x, y, t) = A_n \sin\left(\eta_n^A y\right) e^{-i\xi_n^A x} e^{i\omega t}. \tag{10}$$

The total displacement is

$$u_z(x, y, t) = \left[A_n \sin\left(\eta_n^A y\right) e^{-i\xi_n^A x} + B_n \cos\left(\eta_n^S y\right) e^{-i\xi_n^S x}\right] e^{i\omega t}. \tag{11}$$

The amplitudes A_n, B_n are normalized with respect to power flow and found to be [22]

$$B_n = \sqrt{\frac{1}{\omega\mu\xi_n^S d}}, \quad A_n = \sqrt{\frac{1}{\omega\mu\xi_n^A d}}. \tag{12}$$

Solving the characteristic equation $\sin(\eta^S d)\cos(\eta^A d) = 0$ results in finding wave speeds and group velocities.

Analytical evaluation for shear horizontal wave speeds and group velocities is presented in figure 10 for a 1 mm thick aluminium plate. Wave speeds are normalized with respect to shear (transverse) wave speed, which equals 3129 m s^{-1} for our case study aluminium 2024-T3 alloy. The

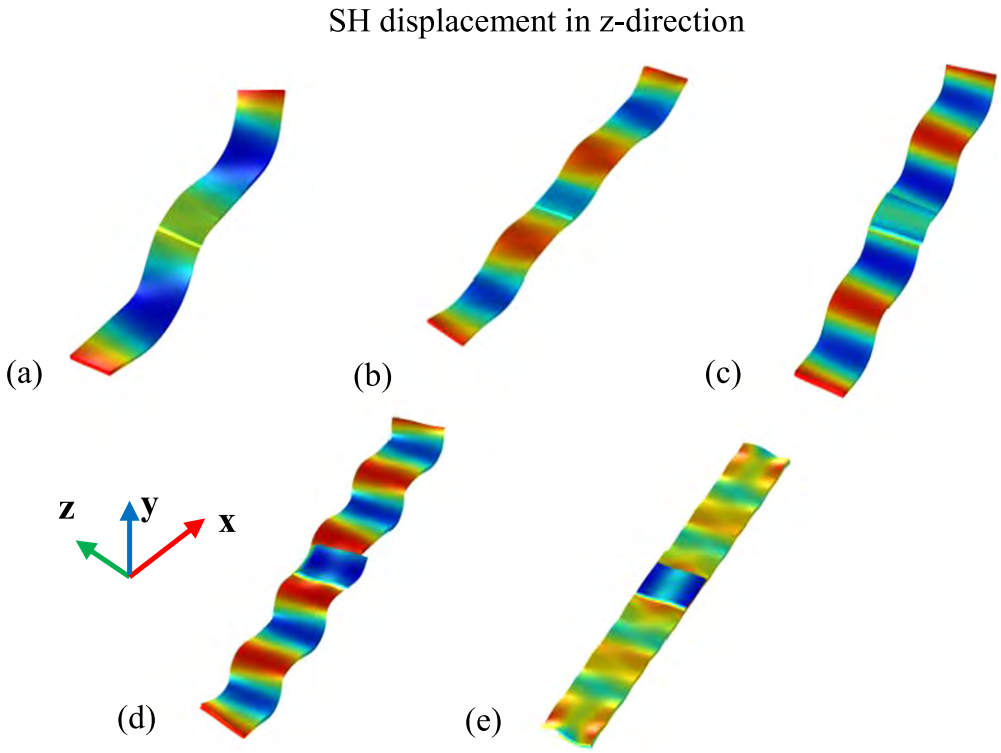

Figure 9. Modeshapes of vibrations of 1 mm thick aluminium beam with bonded SH-PWAS in configuration-2 (SH orientation) at excitation frequency: (a) 22 kHz, (b) 47 kHz, (c) 77 kHz, (d) 107 kHz, (e) 136 kHz. Plotted FEM variable is the Z-displacement field.

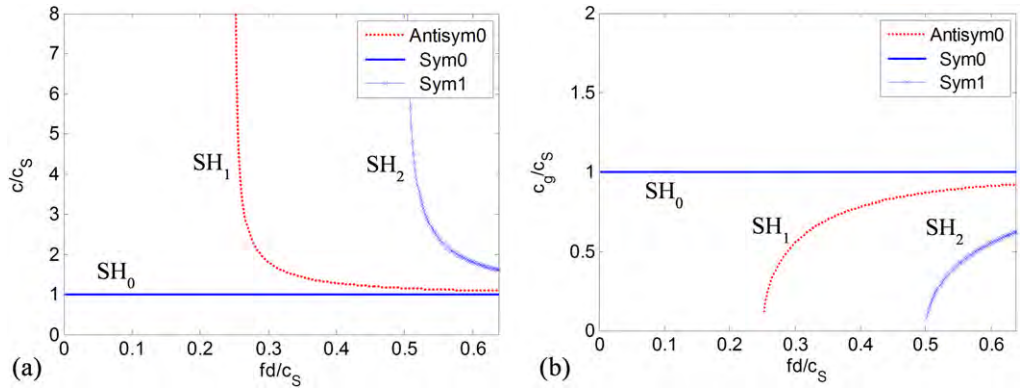

Figure 10. Shear horizontal wave velocities in aluminium: (a) phase velocities, (b) group velocities.

predicted SH wave modes were three modes in the 4000 kHz frequency window (corresponds to $fd/c_s = 0.64$). The first SH mode is SH0; it is a symmetric mode of vibration and has a constant propagation speed at any excitation frequency. The second SH mode is SH1; it is an antisymmetric mode with a cut-off frequency ≈0.25(=1565 kHz). The third mode in our simulation results is SH3; it is symmetric like SH0. However, it is dispersive, i.e., does not have a constant propagation speed. The cut-off frequency of SH3 is ≈0.5(=3130 kHz).

3.2. Experimental studies

3.2.1. Proof of concept. Three sets of experiments are performed. The first set of experiments was a proof of concept that was performed on 3.4 mm thick aluminium 7075 T6 alloy plate (figure 11). The SH-PWAS was 15 mm × 15 mm × 1 mm, and its material was APC850. SH-PWAS poling direction was along the z-direction (figure 11(c)). The distance between the two SH-PWAS was 150 mm, and the excitation was a 3-count tone burst signal with 10 V amplitude. The excitation frequencies used were 30, 45, 60, 75, and 90 kHz, as shown in the waveforms (figure 12). It was noticed that the received signals in figure 12 waveforms were non-dispersive, (i.e., they had shown the same shape as the excitation signal, ≈3 count tone burst), especially at frequencies 60, 75, and 90 kHz; this implies that the wave packet speed does not change with frequency, and that this is the intrinsic property of SH0 (the first shear horizontal guided wave in isotropic materials).

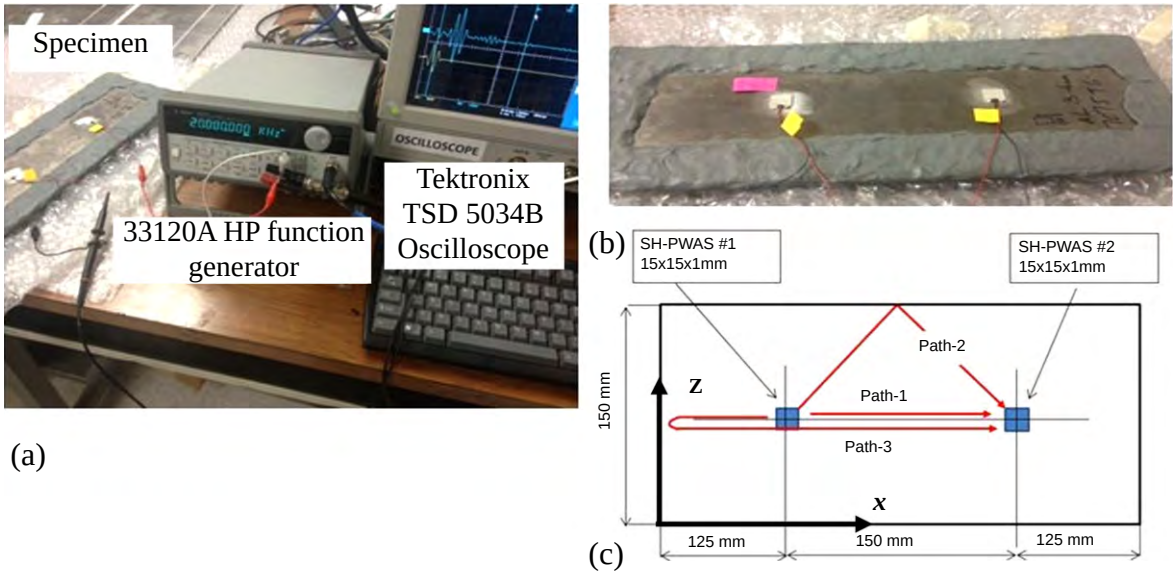

Figure 11. Pitch–catch experiment to excite SH waves and catch with another SH-PWAS.

In addition, it was observed that no waves propagate along (path 2) in figure 11(c). The actuation mechanism of SH-PWAS that is shown from free transducer mode shapes (figure 2) implies that the SH-PWAS resonates in the *z*-direction, and the generated waves propagate along the *x*-direction. Comparison between analytical and experimental results is shown in figure 13.

3.2.2. Pitch–catch experiments between combinations of SH-PWAS and in-plane PWAS transducers. The second set of experiments were a rigorous combination of pitch–catch experiments between (a) SH-PWAS transducers with different orientations (to study effect of poling direction) and (b) pitch–catch experiments between SH-PWAS transducers and regular PWAS. SH-PWAS materials was APC850, and the dimensions were 15 mm × 15 mm × 1 mm. The regular PWAS material was APC850, and a circular PWAS of diameter 15 mm and 0.2 mm thickness was used. A detailed set up is shown in figure 14(b). The aim behind those combinations of experiments was to have a better understanding of the following cases:

1. Does the SH-PWAS transmit only SH waves to another SH-PWAS?
2. Can regular PWAS receive SH waves transmitted by SH-PWAS?
3. How does SH-PWAS behave when excited by waves coming from regular PWAS? (The opposite situation of question 2.)
4. How does SH-PWAS behave if oriented 90 degrees; does it transmit SH waves in this case? Does it receive SH waves?

Seven experiments were performed on a 1 mm thick aluminium 2024-T3 square plate 1220 × 1220 mm with a frequency sweep up to 300 kHz. Table 1 summarizes the experiments and captured waves in each case.

The experiment between two SH-PWAS transducers showed the generation of shear horizontal waves, providing that both transducers are installed such that their polarization vectors are parallel to each other (experiment #1), (figure 15(a)).

However, for two SH-PWAS transducers installed such that their polarization directions are perpendicular to each other, the signals that SH-PWAS4 received from SH-PWAS6 had the speeds of S0 for the first symmetric Lamb wave modes, (experiment #4) (figure 15(c)).

Experiment #6 (the reverse situation of experiment #4) showed identical results to experiment #4. This was done to verify reciprocity and lack of nonlinear effects. The exciter SH-PWAS6 was oriented in the correct direction to send SH waves towards the receiver SH-PWAS4. SH-PWAS4 was the one oriented with 90°. In such a situation, we expected that transmitter SH-PWAS6 was sending out SH waves; however, receiver SH-PWAS4 neither responded nor picked SH waves, but rather picked S0 waves (figure 15(c)). This suggests that the transmitter excites the S0 wave in the measured direction. This observation is further explained in the discussion section of guided wave propagation results.

Another feature was observed: when SH-PWAS5 excites SH waves, the regular extensional mode PWAS2 picked up two types of guided waves: a Lamb wave antisymmetric A0 mode as well as a SH0 wave (experiment #2) (figure 15(b)). It was not expected that extensional type PWAS transducers resonate in shear mode and convert shear-mode waves to output voltage. This observation is further discussed in the discussion of guided wave propagation results section.

Finally, regular PWAS2 was excited, and the signal was caught by SH-PWAS5 (experiment #3). Similarly, PWAS2 was excited, and the signal was caught by SH-PWAS4 (experiment #7).

Experiment #3 was identical to experiment #2, where the SH-PWAS5 picked up SH waves (exactly like figure 15(b)). In experiment #7, where PWAS2 was excited, and the signal

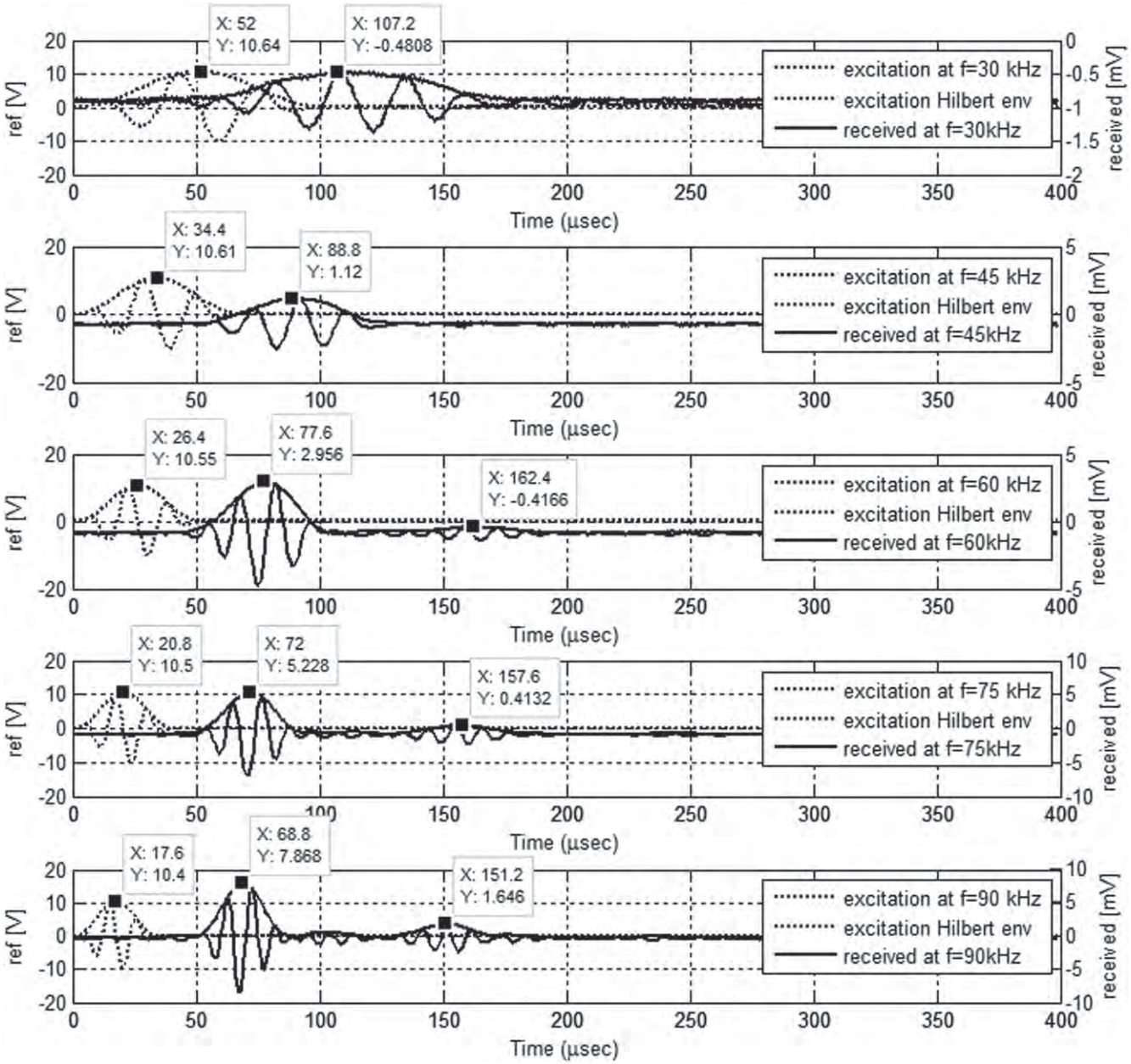

Figure 12. Waveforms associated with pitch–catch SH waves experiment on 3.4 mm thick aluminium.

was caught by SH-PWAS4, the received waveforms corresponded to guided Lamb waves only (figure 15(d)).

3.2.3. Directivity of SH-PWAS. The third set of experiments involves a similar setup to that of set #2, but with added transducers at 30° and 60° degree angles. The complete setup is shown in figure 14(a). Experiment #1 (SH-PWAS5 → SH-PWAS6) indicates the zero angle direction pitch–catch, experiment #1(30) indicates the 30° pitch–catch, and experiment #1(60) indicates the 60° pitch–catch.

Receiver SH-PWAS6 transducers in experiment #1(30) and (60) are no longer having parallel poling direction to transmitter SH-PWAS5.

Similarly, experiments #2 and #4 are performed at different angles: 0°, 30°, and 60°. Figure 16 shows the

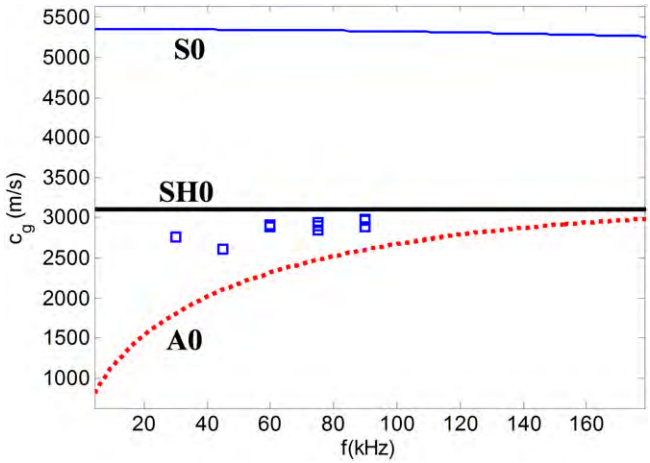

Figure 13. Experimental versus analytical wave group velocity curves (SH-PWAS experiment on 3.4 mm thick aluminium plate).

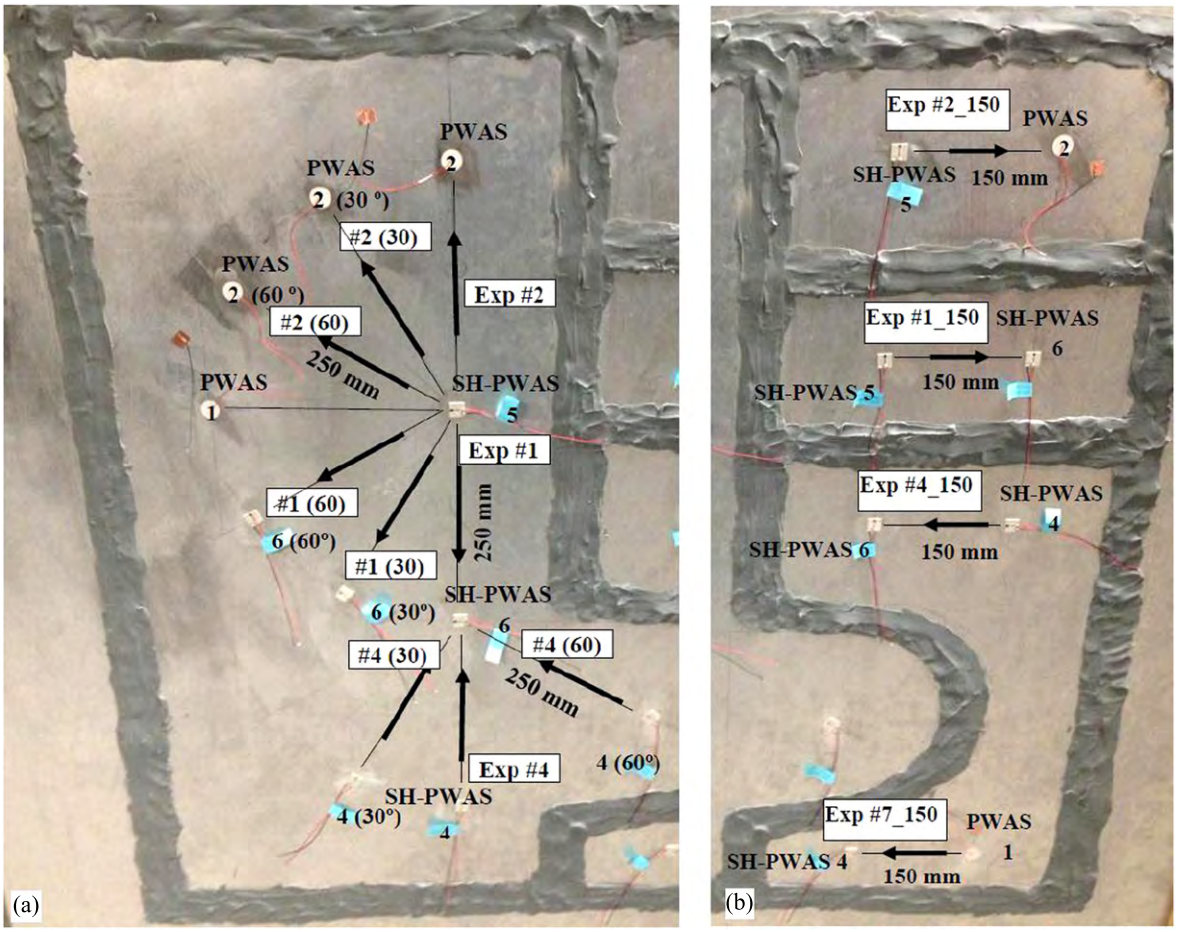

Figure 14. Numbering and directions of pitch–catch experiments on aluminium plate: (a) directivity experiment, (b) separated experiments for combination of SH-PWAS–regular PWAS pitch–catch configurations.

directivity patterns for received wave amplitudes at different experiments.

Figure 16(a) shows SH wave amplitudes for a pitch–catch experiment between two SH-PWAS transducers. Starting from parallel poling directions (at 0°), the SH wave amplitude is the maximum (e.g., at 60 kHz). At 30°, the SH wave amplitude decreases and then it further decreases at 60°. This is not observed with all the frequencies. On the other hand, A0 wave amplitudes received at SH-PWAS for the same experiment show an increase in amplitude as the angle increases from 0° to 30° to 60°. This agrees with the previous results of exciting an axial-flexural response along the poling direction. As the angle of the pitch–catch experiment changes towards 60°, a stronger A0 mode is obtained.

Experiment #2 (SH-PWAS5 → regular PWAS2) showed similar patterns to experiment #1. However, the received signals at 60° were noisy. Figure 16(c) shows amplitudes of SH waves received by PWAS2 and generated by SH-PWAS5 for experiment #2, 2(30), and 2(60). Figure 16(d) shows amplitudes of received A0 waves. Experiments #3 are the opposites of experiments #2. Those are not performed in this study.

Experiment #4 (SH-PWAS4 → SH-PWAS6) involves the pitch–catch experiments between two SH-PWAS transducers having poling directions perpendicular to each other (for 0° case). Figure 16(e), f are for the same received S0 wave amplitudes but at different frequencies. They are plotted on two polar plots because of considerable change in amplitude values in [mV] between 45 kHz, 75 kHz, and 255, 300 kHz. It is observed that the S0 amplitudes are much less at lower frequencies. Also, it is observed that the perpendicular poling directions—experiment #4(0)—cause the least S0 wave amplitudes. S0 wave amplitudes are much higher at 30° and 60° angles between poling directions of the two transducers.

Table 1. Description of experiments showing excitation and receiver PWAS transducers for each experiment and the possible paths of wave propagation.

Experiment No. and description of pitch–catch configuration	Captured waves
Experiment (#1) SH5 → SH6	SH0, A0
Experiment (#2) SH5 → PWAS2	SH0, A0
Experiment (#3) PWAS2 → SH5	SH0, A0
Experiment (#4) SH4 → SH6	S0
Experiment (#6) SH6 → SH4	S0
Experiment (#7) PWAS1 → SH4	A0, S0

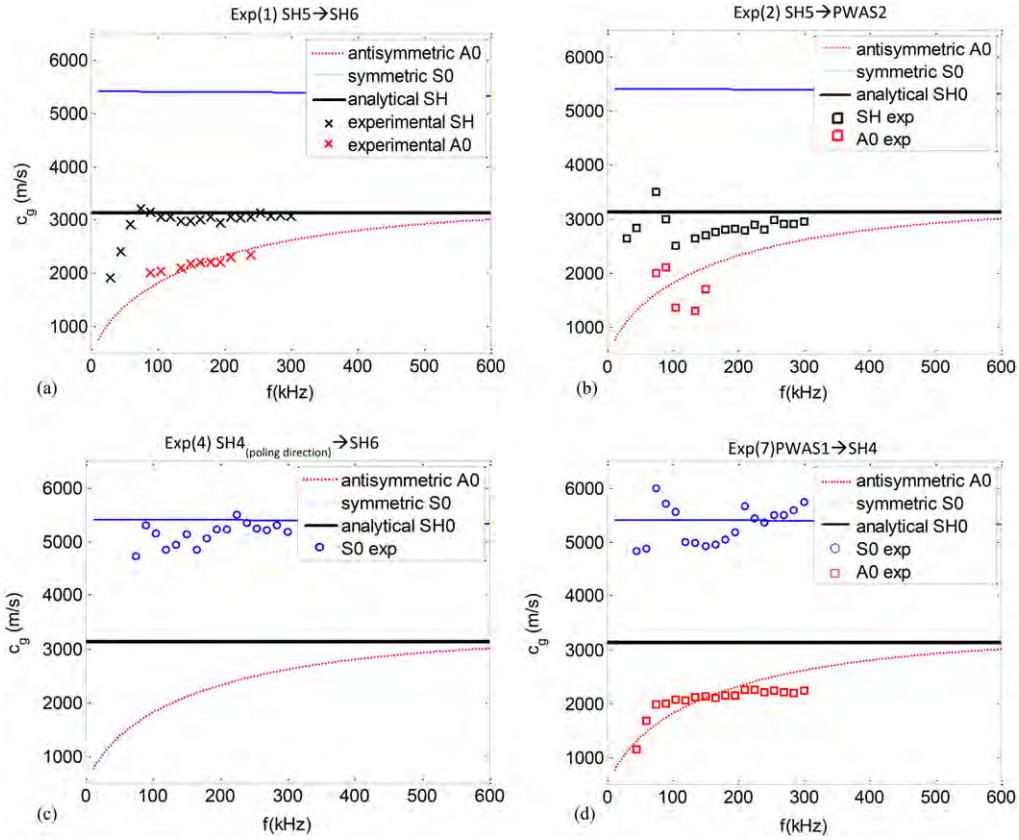

Figure 15. Dispersion group velocity curves for received wave signals (SH-PWAS experiment on aluminium).

3.3. Finite element simulations

The models in section 2.3 predict SH-PWAS effects at 0° and 90°, separately. Also, it is hard to combine (axial-flexural) and (shear horizontal) separate responses of figure 3(b) into a 2D analytical model. Hence, 2D multiphysics FEM simulations are constructed to better understand the possible excited waves by SH-PWAS and to verify directivity experiments. Shear horizontal SH0, symmetric S0 and antisymmetric A0 Lamb waves were picked by FEM simulations.

The finite element model was constructed for the bonded SH-PWAS to the structure. The SH-PWAS dimensions were 15 mm × 15 mm × 1 mm, while in-plane PWAS dimensions were 7 mm × 7 mm × 0.2 mm. The mesh size of SH-PWAS elements was 0.5 mm and 4 elements, per the 1 mm thickness. A 1 mm aluminium 2024 alloy plate was used in our simulations. The plate was a 450 mm square plate. The structure maximum element size was set to 4 mm and 2 elements through the 1 mm thick aluminium plate. The plate was modelled with free BC, and the SH-PWAS was perfectly bonded from the bottom surface and free from the upper surface.

Excitation signal was 3-count tone burst with canter frequency 60 kHz and voltage amplitude of 10 V. The time step selected was 0.5 μs, and simulation time was 200 μs. Figure 17 shows the results of the simulations. Figure 17(a) shows the displacement field in the z-direction, i.e., the direction of shear horizontal particle oscillation. SH0 waves had a strong oscillation in the z-direction and propagated in the x-direction between the transmitter and receiver SH PWAS transducers. Antisymmetric A0 and symmetric S0 modes were observed propagating in the z-direction. For comparison, the waves excited by in-plane PWAS (figure 17(b)) are reported; only A0 and S0 existed. The simulations in figure 17 are both captured at a simulation time that equals 77 μs. The displayed parameter in figure 17(b) is eZ the out of plane strain; it was selected rather than the displacement fields to be able to show S0 and A0 modes together.

When FEM simulation was repeated between the two SH-PWAS transducers, but with the transmitter SH-PWAS oriented by 90 degrees (figure 18), the waves that propagated toward the receiver SH-PWAS were S0 and a noisy A0. This was in good agreement with the observed results from experiment #4 (figures 14(b) and 15(c)). Figure 18 shows the displacement fields in the x-direction at 40 μs. Particle motion in the x-direction was selected because, for such a configuration, SH waves had a particle oscillation in the x-direction and propagated in the z-direction. Besides, the S0 Lamb wave was propagating in the x-direction–with dominant particle motion in the x-direction.

3.4. Discussion of guided wave propagation results

The FEM simulations of SH wave propagation between two SH-PWAS transducers (figure 17(a)) validate the transducer

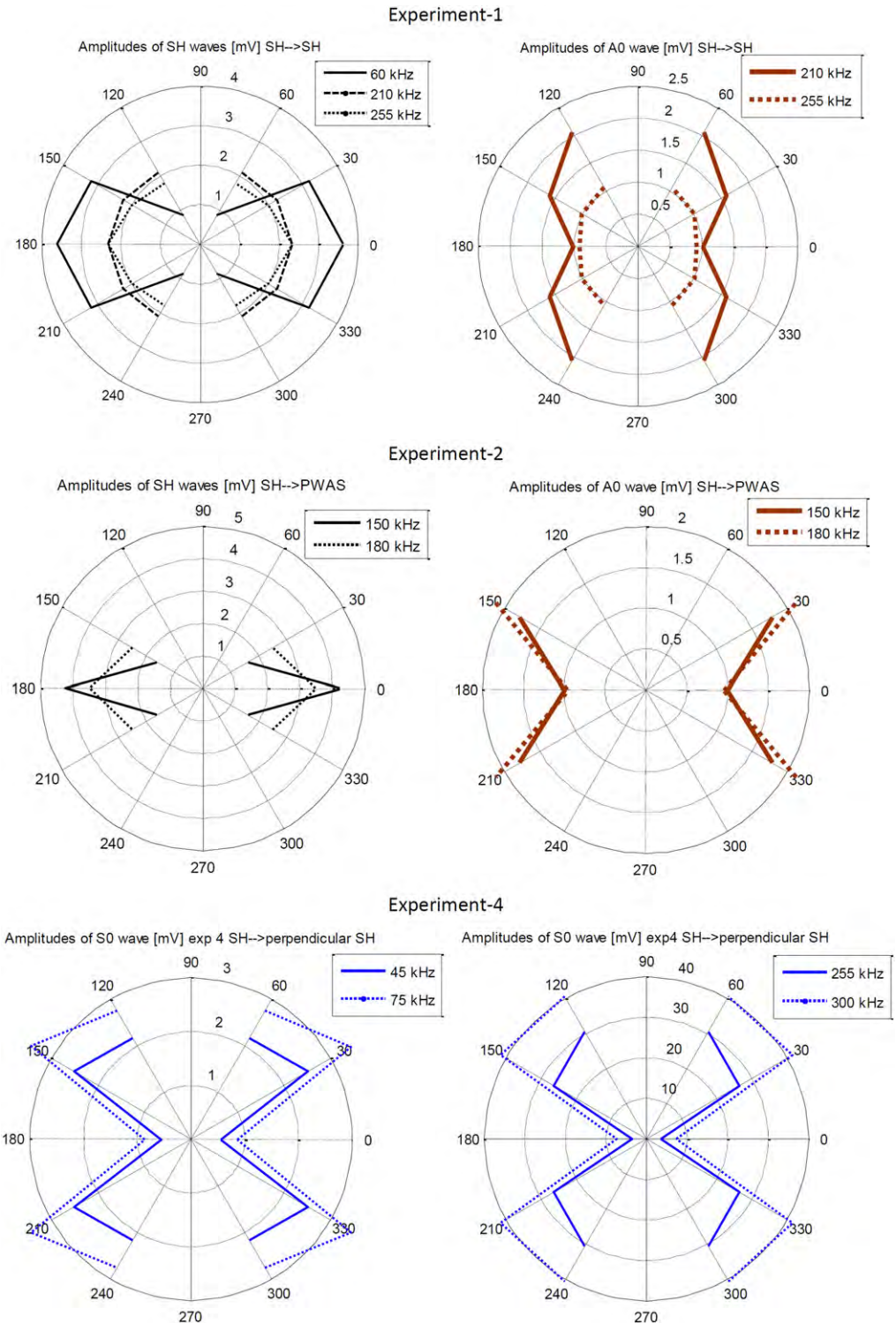

Figure 16. Amplitudes of different waves at different angles of pitch–catch experiments, associated with directivity experiment.

actuation mechanism of exciting SH waves in the direction perpendicular to the poling direction. SH wave amplitude decreases as the direction of the measured response changes from 0° towards 90°; this agrees with figure 16(a) at excitation frequency 60 kHz. Recalling experiment #6 in the pitch–catch experiments, i.e., the opposite of experiment #4 (figure 14(b)), the receiving of the S0 waves seem to contradict with the results of figure 15(a), where SH0 and A0 were only captured along the direction perpendicular to the poling direction of transmitter SH-PWAS. Referring to figure 17(a), a very weak S0 mode appears along 45 degrees from the x-direction (and almost vanishes along the x-direction). Hence, one can conclude that the SH-PWAS actually excites S0 waves in the same direction of exciting the SH

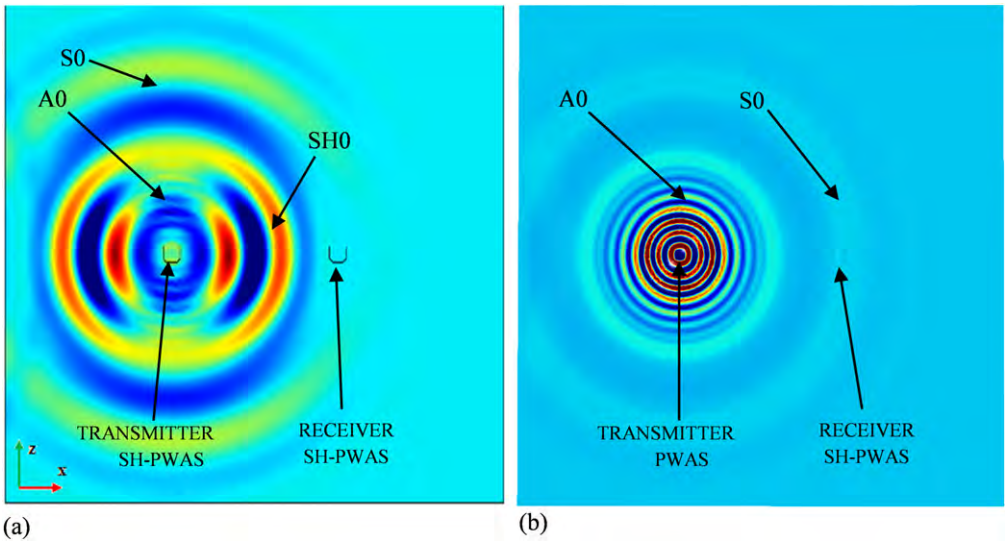

Figure 17. FEM simulations for waves excited at 60 kHz by (a) SH-PWAS, (b) in-plane PWAS.

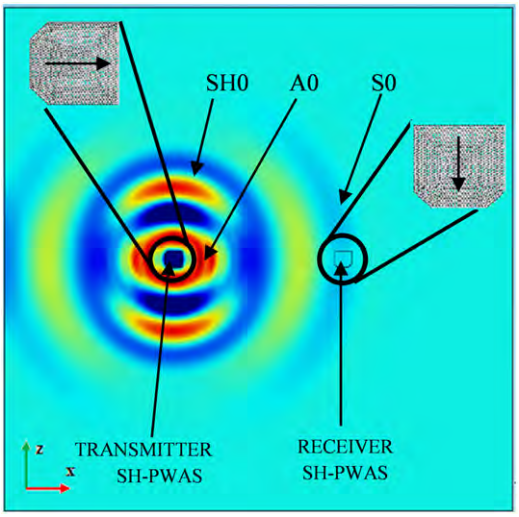

Figure 18. FEM simulation for the case of a 90° orientation difference between two SH-PWAS.

waves; and this is due to 2D effects and to the fact that structure particle vibrations at one side of the transducer definitely affect vibrating particles at the other sides. The considerably reduced S0 wave amplitudes are proven from figure 16(e), f along the 0° direction.

The feature observed in experiment #2 in section 3.2.2 was that the regular in-plane PWAS was able to pick up SH waves. This means that it resonates in its extensional-contraction mechanism when the shear wave front hits the transducer. Two dimensional effects can be the reason; that is, SH waves excited by SH-PWAS (with structure particles vibrations in the z-direction) arrive at regular PWAS with the z-direction vibrations; and, due to 2D effects, z-direction oscillations are actually considered extension-contraction oscillations (if viewed from another diameter of the receiver PWAS). In addition to the 2D effects, SH waves can be mode converted at the receiver PWAS because the transducer itself is considered an inhomogeneity in the wave field. A similar observation in [11] suggested that the S0 wave mode converts to SH0. SH0 can be mode converted (at the time of flight of receiving SH0) to a mode that regular PWAS interacts with.

4. Power and energy transduction with SH-PWAS

The study of power and energy transduction between PWAS and a bonded structure has been presented in [23], where exact guided Lamb waves' power and energy are studied. Energy transfers from electrical to mechanical in the transducer; then, the mechanical energy causes the wave to propagate. This paper presents an analytical model for the SH waves' power and energy based on the normal mode expansion (NME) technique. The solution assumes straight crested harmonic waves and that no evanescent (i.e., non propagating) waves exist. Mode amplitudes are normalized with respect to power flow; and the actual amplitudes can be determined from equation (12).

Considering that only SH waves are propagating; the surviving strains are

$$2S_{yz} = \frac{\partial u_z}{\partial y}, \quad 2S_{xz} = \frac{\partial u_z}{\partial x}. \tag{13}$$

Strains and stresses can be evaluated given the total displacement, equation (11); however, as we will show later, the symmetric and the antisymmetric displacements can be in separate solutions because the orthogonality condition cancels the terms involving multiplications between cosine and sine terms from symmetric and antisymmetric modes. Hence, we can proceed with a separate analysis. This can be useful to separate wave energy and power and to quantify the partition of symmetric modes as well as antisymmetric ones. Following the method presented in [22], modal participation factors are

found to be

$$a_n^+(x)=\begin{cases}\dfrac{\tilde{v}_z^n(d)}{4P_{nn}}e^{-i\xi_n x}\displaystyle\int_{-b/2}^{b/2}e^{i\xi_n\bar{x}}t_z(\bar{x})d\bar{x} & \text{for } \dfrac{b}{2}<x\\ \dfrac{\tilde{v}_z^n(d)}{4P_{nn}}e^{-i\xi_n x}\displaystyle\int_{-b/2}^{x}e^{i\xi_n\bar{x}}t_z(\bar{x})d\bar{x} & \text{for } -\dfrac{b}{2}\leqslant x\leqslant\dfrac{b}{2}\\ 0 & \text{for } x<-\dfrac{b}{2}.\end{cases} \quad (14)$$

Noting that equation (13) is valid for the forward propagating mode only, b is the width of SH-PWAS, and it is the transducer dimension along x direction in our study. d is half the plate thickness, P_{nn} is power flow factor, $\tilde{v}_z^n(.)$ is the conjugate of velocity field in z direction for the mode n, and t_z is the PWAS traction or shear stress. We denote $a_n^+(x)$ by a + sign to show that it is for the forward propagating mode. Modal participation factor is an extra term to be multiplied by the wave amplitudes. It is a function of the distance x and also accounts for the transducer dimension b. We define a_n^S as the modal participation factor for nth symmetric mode, and similarly a_n^A for the nth antisymmetric mode. Equations (11), (14) yield the strains and stresses as

$$\begin{cases}2S_{yz}=\left[A_n\eta_n^A\cos\eta_n^A y e^{-i\xi_n^A x}-B_n\eta_n^S\sin\eta_n^S y e^{-i\xi_n^S x}\right]e^{i\omega t}\\ 2S_{xz}=-i\left[A_n\xi_n^A\sin\eta_n^A y e^{-i\xi_n^A x}+B_n\xi_n^S\cos\eta_n^S y e^{-i\xi_n^S x}\right]e^{i\omega t}\\ T_{yz}=\mu\left[A_n\eta_n^A\cos\eta_n^A y e^{-i\xi_n^A x}-B_n\eta_n^S\sin\eta_n^S y e^{-i\xi_n^S x}\right]e^{i\omega t}\\ T_{xz}=-i\mu\left[A_n\xi_n^A\sin\eta_n^A y e^{-i\xi_n^A x}+B_n\xi_n^S\cos\eta_n^S y e^{-i\xi_n^S x}\right]e^{i\omega t}.\end{cases} \quad (15)$$

The total strain response (due to symmetric and antisymmetric waves) and the conjugate values of the strain are

$$\begin{aligned}2S_{xz}&=a_n^A(-i)A_n\left(\xi_n^A\sin\eta_n^A y\right)e^{-i\left(\xi_n^A x-\omega t\right)}\\&\quad+a_n^S(-i)B_n\left(\xi_n^S\cos\eta_n^S y\right)e^{-i\left(\xi_n^S x-\omega t\right)}\\2\tilde{S}_{xz}&=a_n^A(i)A_n\left(\xi_n^A\sin\eta_n^A y\right)e^{i\left(\xi_n^A x-\omega t\right)}\\&\quad+a_n^S(i)B_n\left(\xi_n^S\cos\eta_n^S y\right)e^{i\left(\xi_n^S x-\omega t\right)}\\2S_{yz}&=a_n^A A_n\left(\eta_n^A\cos\eta_n^A y\right)e^{-i\left(\xi_n^A x-\omega t\right)}\\&\quad-a_n^S B_n\left(\eta_n^S\sin\eta_n^S y\right)e^{-i\left(\xi_n^S x-\omega t\right)}\\2\tilde{S}_{yz}&=a_n^A A_n\left(\eta_n^A\cos\eta_n^A y\right)e^{i\left(\xi_n^A x-\omega t\right)}\\&\quad-a_n^S B_n\left(\eta_n^S\sin\eta_n^S y\right)e^{i\left(\xi_n^S x-\omega t\right)}.\end{aligned} \quad (16)$$

It needs to be mentioned that strain quantities in equation (16) are a summation for one single symmetric mode and one single antisymmetric mode, taking into account the modal participation factors.

From the displacement equation (11), we obtain the velocity and the conjugate velocity as

$$\begin{aligned}v_z&=a_n^A(i\omega)A_n\left(\sin\eta_n^A y\right)e^{-i\left(\xi_n^A x-\omega t\right)}\\&\quad+a_n^S(i\omega)B_n\left(\cos\eta_n^S y\right)e^{-i\left(\xi_n^S x-\omega t\right)}\\\tilde{v}_z&=a_n^A(-i\omega)A_n\left(\sin\eta_n^A y\right)e^{i\left(\xi_n^A x-\omega t\right)}\\&\quad+a_n^S(-i\omega)B_n\left(\cos\eta_n^S y\right)e^{i\left(\xi_n^S x-\omega t\right)}.\end{aligned} \quad (17)$$

The time averaged power is defined as

$$\langle p\rangle=-\frac{1}{2}\int_A\left(\tilde{T}_{xz}v_z\right)dA=-\frac{b}{2}\int_{-d}^{d}\mu\left\{2\tilde{S}_{xz}.\,v_z\right\}dy. \quad (18)$$

Substituting equations (16), (17) in equation (18) and simplifying yields the time averaged power as

$$\begin{aligned}\langle p\rangle&=-\frac{b}{2}\int_{-d}^{d}\mu\left\{2S_{xz}.v_z\right\}dy\\&=-\frac{b}{2}\begin{bmatrix}[a_n^S B_n]^2(-\mu\omega\xi_n^S)\displaystyle\int_{-d}^{d}\left\{\cos^2\eta_n^S y\right\}dy\\ [a_n^A A_n]^2(-\mu\omega\xi_n^A)\displaystyle\int_{-d}^{d}\left\{\sin^2\eta_n^A y\right\}dy\end{bmatrix}\\&=-\frac{b}{2}\begin{bmatrix}[a_n^S B_n]^2(-\mu\omega\xi_n^S)\left\{\left(\dfrac{\sin 2\eta_n^S d}{2\eta_{Sn}}+d\right)\right\}\\ [a_n^A A_n]^2(-\mu\omega\xi_n^A)\left\{\left(d-\dfrac{\sin 2\eta_n^A d}{2\eta_{An}}\right)\right\}\end{bmatrix}.\end{aligned} \quad (19)$$

First, terms with multiplied sine and cosine functions from the symmetric mode and the antisymmetric mode are cancelled; for the characteristic equations of the symmetric and the antisymmetric modes, either *sine* or *cosine* terms will be zero at a time. Hence, there is no dependency between symmetric and antisymmetric modes. Second, terms with $\sin(2\eta_n d)$ appearing with the analysis of single types of waves are also crossed out because $\sin(2\eta_n d)=2\sin(\eta_n d)\cos(\eta_n d)$, and for our characteristic equations for symmetric and antisymmetric, either *sine* or *cosine* terms will be zero at a time. The final result for wave power takes the form

$$\langle p\rangle=\frac{\mu\omega}{2}bd\left[\sum_n\left[a_n^S B_n\right]^2\xi_n^S+\sum_n\left[a_n^A A_n\right]^2\xi_n^A\right]. \quad (20)$$

The time-averaged power varies at different x values, as the x dependency comes from the modal participation factors.

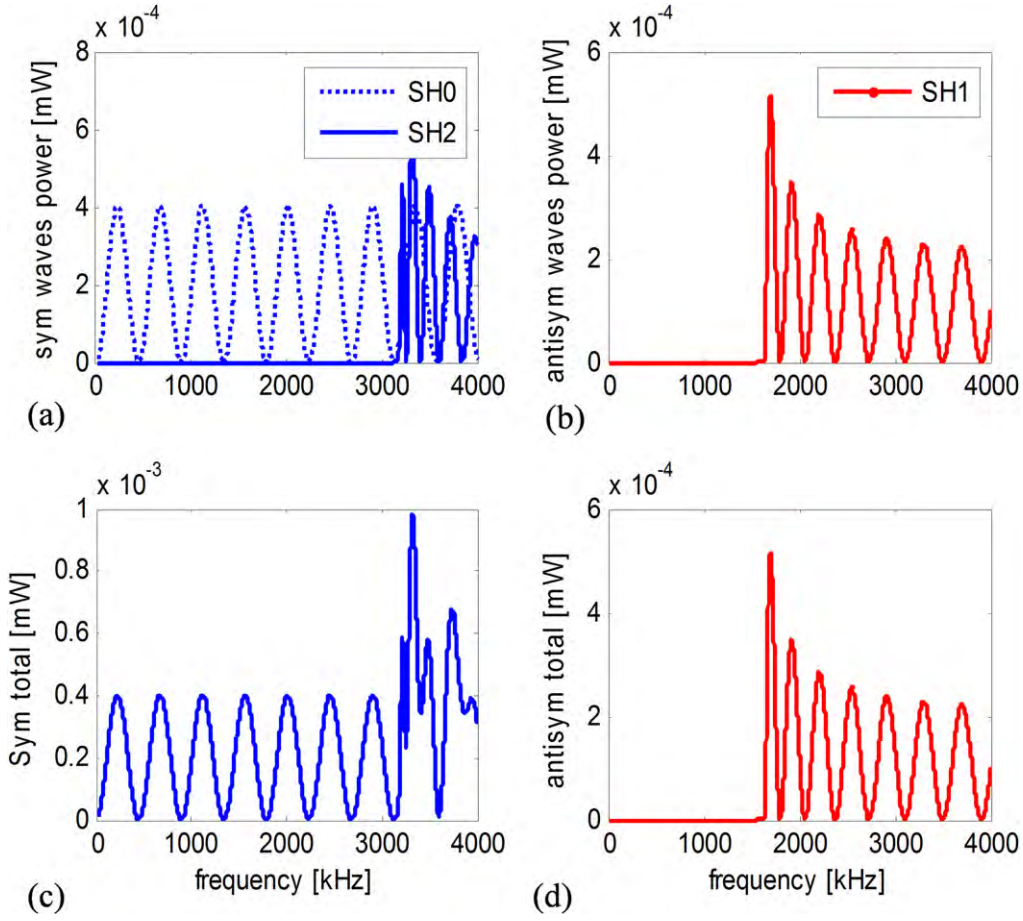

Figure 19. Guided SH wave power for three SH modes: two symmetric SH0, SH2, and one antisymmetric SH1: (a) individual wave power for SH0, SH2, (b) SH1 wave power, (c) total symmetric wave power, (d) total antisymmetric wave power.

All the following numerical illustrations are shown at the top surface of the structure ($y = d$) and at the edge of the transducer, where ($x = b/2$).

With similar analysis, we define time-averaged kinetic energy

$$\langle k_e \rangle = \frac{1}{2}\rho \int_A \frac{1}{2} v_z .\ \bar{v}_z dA \tag{21}$$

and the final analytical form will be

$$\langle k_e \rangle = \frac{b}{4}\int_{-d}^{d} \{\rho v_z .\ \bar{v}_z\}\, dy = \frac{\rho\omega^2}{4} bd \left[\sum_n \left[a_n^S B_n\right]^2 + \sum_n \left[a_n^A A_n\right]^2 \right]. \tag{22}$$

Time averaged potential energy is defined as

$$\langle v_e \rangle = \frac{1}{4}\int_A \left\{ (\mu)\, 2S_{xz} 2\bar{S}_{xz} + (\mu)\, 2S_{yz} 2\bar{S}_{yz} \right\} dA. \tag{23}$$

Using similar analysis to the one we followed in power and kinetic energy, then cancelling $\sin 2\eta_n d$ terms, results in

$$\langle v_e \rangle = \frac{b}{4}\int_{-d}^{d} \begin{Bmatrix} (\mu)\, 2S_{xz} 2\bar{S}_{xz} \\ + (\mu)\, 2S_{yz} 2\bar{S}_{yz} \end{Bmatrix} dy = \frac{b}{4}\left\{ \sum_n \mu d \left[a_n^S B_n\right]^2 \left[\left(\xi_n^S\right)^2 + \left(\eta_n^S\right)^2 \right] + \sum_n \mu d \left[a_n^A A_n\right]^2 \left[\left(\xi_n^A\right)^2 + \left(\eta_n^A\right)^2 \right] \right\}. \tag{24}$$

Using the relation $\eta^2 = \omega^2/c_s^2 - \xi^2$, we can then prove that time - averaged potential energy equals time averaged kinetic energy

$$\begin{aligned} \langle v_e \rangle &= \frac{b}{4}\left\{ \sum_n \mu d [a_n^S B_n]^2 \left[\frac{\omega^2}{c_s^2}\right] + \sum_n \mu d [a_n^A A_n]^2 \left[\frac{\omega^2}{c_s^2}\right] \right\} \\ &= \frac{b}{4}\left\{ \sum_n \cancel{\mu} d [a_n^S B_n]^2 \left[\frac{\rho\omega^2}{\cancel{\mu}}\right] + \sum_n \cancel{\mu} d [a_n^A A_n]^2 \left[\frac{\rho\omega^2}{\cancel{\mu}}\right] \right\} \\ &= \frac{\rho\omega^2}{4} bd \left[\sum_n [a_n^S B_n]^2 + \sum_n [a_n^A A_n]^2 \right] = \langle k_e \rangle. \end{aligned} \tag{25}$$

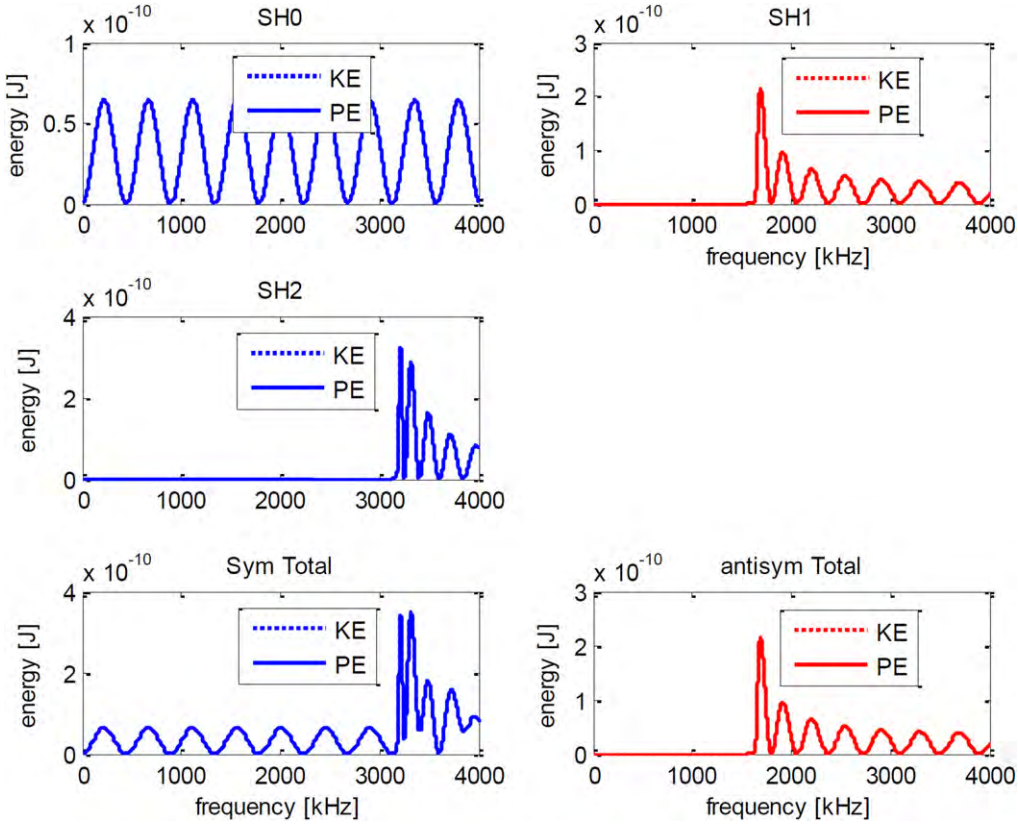

Figure 20. Guided SH wave energy (kinetic and potential energies) in [J].

4.1. Discussion of power and energy model results

Numerical simulations for developed analytical models were shown in figures 19 and 20. Figure 19 shows simulation results of our analytical model for wave power. The SH0 power flow oscillates as a function of frequency with constant amplitude (because of having constant dispersion wave speed). However, the peaks and valley response are due to SH-PWAS finite dimension effect (what is commonly referred to as tuning of the transducer). SH1 (antisymmetric shear horizontal mode) kicked off at 1560 kHz (figures 19(b), (d)). SH2 (symmetric mode) started at 3150 kHz (figures 19(a), (c)). Both SH1 and SH2 are dispersive modes with variable power consumption at different frequencies (because their wave speeds are not constant along the frequency spectrum). Similar conclusions are drawn from simulated results of wave energies (figure 20).

5. Summary and conclusions

The paper discussed the excitation and reception of SH waves using SH-PWAS; that is, piezoelectric wafer active sensor poled in shear direction. The paper also presented predictive models for power and energy of multimodal SH waves.

Excitation of SH waves was analyzed by finite element simulations and experiments. SH0 non-dispersive waves were captured in aluminium plates. Multiple experiments were performed to show the SH waves excitation and receiving capabilities of both SH-PWAS and regular in-plane PWAS transducers. It was shown that positioning and orientation of SH-PWAS affects the generation of SH waves: (1) SH-PWAS excites SH waves in the direction perpendicular to poling direction, and (2) Regular in-plane PWAS can sense SH waves. Additionally, (3) SH-PWAS transducers can sense A0 and S0 Lamb waves. Directivity analysis showed that excited SH wave amplitude gradually decreases as the measuring direction deviates from the maximum received amplitude direction.

A predictive model for a guided SH wave's power and energy was analytically developed based on a normal mode expansion technique. The model assumed that (a) waves are of straight crested harmonic type, (b) evanescent non-propagating waves are ignored, and (c) the modes are of orthogonal functions. The amplitudes of each mode were normalized with respect to the power flow, and modal participation factors were determined. Modal participation factors are a function of transducer dimension. The wave power, kinetic energy, and potential energy were modelled, and numerical results were presented. As expected, the kinetic energy equals the potential energy in total and for separate modes as well, due to the fact that modes are orthogonal. SH0 mode wave power and wave energy oscillate with frequency but have a constant amplitude due to the constant wave propagation

speed of SH0 in isotropic materials. SH1 and SH2 modes are dispersive shear horizontal modes.

Future work will include investigation of SH waves excitation in composite materials, a predictive analytical model for SH-PWAS electromechanical impedance for the free transducer and when bonded onto the structure, and further studies on modelling SH wave excitability by the SH-PWAS.

Acknowledgment

This work was supported by the Office of Naval Research grant #N00014-11-0271, program manager Dr Ignacio Perez, and by Air Force Office of Scientific Research grant #FA9550-11-1-0133, program manager Dr David Stargel.

References

[1] Zhou W, Li H and Yuan F 2014 Guided wave generation, sensing, and damage detection using in-plane shear piezoelectric wafer *Smart Mater. Struct.* **23** 015014
[2] Glazounov A and Zhang Q 1998 Piezoelectric actuator generating torsional displacement from piezoelectric d15 shear response *Appl. Phys. Lett.* **72** 2526–8
[3] APC International Ltd Physical and Piezoelectric Properties of APC Materials http://americanpiezo.com last accessed 11 June 2014
[4] Ferroperm Piezoceramics www.ferroperm-piezo.com last accessed 11 June 2014
[5] Baillargeon B P 2003 Active vibration suppression of smart structures using piezoelectric shear actuators *Theses and Dissertations* University of Maine Electronic
[6] Sun C and Zhang X 1995 Use of thickness-shear mode in adaptive sandwich structures *Smart Mater. Struct.* **4** 202–6
[7] Benjeddou A, Trindade M A and Ohayon R 1997 A unified beam finite element model for extension and shear piezoelectric actuation mechanisms *J. Intell. Mater. Syst. Struct.* **8** 1012–25
[8] Centolanza L R, Smith E C and Munsky B 2002 Induced-shear piezoelectric actuators for rotor blade trailing edge flaps *Smart Mater. Struct.* **11** 24–35
[9] Fortunko C M, King R B and Tan M 1982 Nondestructive evaluation of planar defects in plates using low-frequency shear horizontal waves *J. Appl. Phys.* **53** 3450–8
[10] Rose J L, Pelts S P and Li J 2000 Quantitative guided wave NDE *15th World Conf. NDT (Rome)*
[11] Su Z, Yang C, Pan N, Ye L and Zhou L M 2007 Assessment of delamination in composite beams using shear horizontal (SH) wave mode *J. Compos. Sci. Technol.* **67** 244–51
[12] Le Crom B and Castaings M 2010 Shear horizontal guided wave modes to infer the shear stiffness of adhesive bond layers *J. Acoust. Soc. Am.* **127** 2220–30
[13] Giurgiutiu V 2008 *Structural Health Monitoring with Piezoelectric Wafer Active Sensors* (New York: Elsevier Academic)
[14] Lee J, Kim Y and Cho S H 2009 Beam-focused shear-horizontal wave generation in a plate by a circular magnetostrictive patch transducer employing a planar solenoid array *Smart Mater. Struct.* **18** 015009
[15] Gao H, Ali S and Lopez B 2010 Inspection of austenitic weld with EMAT *AIP Conf. Proc.* **1211** 1175–81
[16] Li F, Murayama H and Kageyama K 2009 Guided wave and damage detection in composite laminates using different fiber optic sensors *Sensors* **9** 4005–21
[17] Aldrin J, Knopp J, Judd D, Mandeville J and Lindgren E 2006 Spiral creeping waves in ultrasonic angled-beam shear wave inspection of fastener holes in multilayer structures *AIP Conf. Proc.* **820** 187–94
[18] Aldrin J, Kropas-Hughes C, Knopp J, Mandeville J, Judd D and Lindgren E 2006 Advanced echo-dynamic measures for the characterisation of multiple ultrasonic signals in aircraft structures *Insight: Non-Destructive Testing & Condition Monitoring* **48** 144–8
[19] Auld B 1990 *Acoustic Fields and Waves in Solids* (New York: Wiley)
[20] Graff K 1991 *Wave Motion in Elastic Solids* (New York: Dover)
[21] Rose J 1999 *Ultrasonic Waves in Solid Media* (New York: Cambridge University Press)
[22] Santoni G 2010 Fundamental studies in the Lamb-wave interaction between piezoelectric wafer active sensor and host structure during structural health monitoring *Dissertation* University of South Carolina
[23] Kamal A, Lin B and Giurgiutiu V 2013 Exact analytical modeling of power and energy for multimode Lamb waves excited by piezoelectric wafer active sensors *J. Intell. Mater. Syst. Struct.* **25** 452–71

Original Article

Journal of Intelligent Material Systems and Structures

Journal of Intelligent Material Systems and Structures
2014, Vol. 25(4) 452–471
© The Author(s) 2013
Reprints and permissions:
sagepub.co.uk/journalsPermissions.nav
DOI: 10.1177/1045389X13498310
jim.sagepub.com
SAGE

Exact analytical modeling of power and energy for multimode lamb waves excited by piezoelectric wafer active sensors

Ayman M Kamal, Bin Lin and Victor Giurgiutiu

Abstract

This article presents an analytical model for power and energy transfer between excited piezoelectric wafer active sensors and host structure. This model is based on exact multimodal Lamb waves, *normal mode expansion* technique, and *orthogonality* of Lamb waves. Modal participation factors are presented to show the contribution of every mode to the total energy transfer. The model assumptions include the following: (1) straight-crested multimodal ultrasonic guided wave propagation, (2) propagating waves only, (3) ideal bonding (pin-force) connection between piezoelectric wafer active sensors and structure, and (4) ideal excitation source at the transmitter piezoelectric wafer active sensors. Constrained piezoelectric wafer active sensor admittance is reviewed. Electrical active power, mechanical converted power, and Lamb wave kinetic and potential energies are derived in closed-form formulae. Numerical simulations are performed for the case of symmetric and antisymmetric excitation of thin aluminum structure. The simulation results are compared with axial and flexural approximation for the case of low-frequency Lamb waves. In addition, a thick steel structure example is considered to illustrate the case of multimodal guided waves. A parametric study for different excitation frequencies and different transducer sizes is performed to show the best match of frequency and piezoelectric wafer active sensor size to achieve maximum energy transfer into the excited structure.

Keywords

Structural health monitoring, piezoelectric wafer active sensors, multimode guided Lamb waves, wave power, wave energy, nondestructive evaluation, ultrasonic power, impedance, admittance, lead zirconate titanate, normal mode expansion

Introduction

Structural health monitoring (SHM) is crucial for monitoring structure performance and detecting the initiation of flaws and damages in order to predict structural life. SHM uses permanently attached sensors to the structure. Using piezoelectric wafer active sensors (PWAS) has the following advantages: (1) low cost and (2) they serve as passive sensors, that is, without interacting with the structure, and/or (3) active sensors, where they interact with the structure to detect the presence and intensity of damage (Giurgiutiu, 2010). Guided waves are commonly used in nondestructive evaluation (NDE) techniques, such as pitch–catch, pulse–echo, and phased array (Figure 1).

Ultrasonic Lamb waves are used for finding damages and flaws in plates, pipes, rails, thin-walled structures, multilayered structures, and composite materials. The advantage of Lamb waves over other common ultrasonic techniques is that they travel at large distance along the structure. Lamb waves can be "tuned" to excite certain modes; some modes are more sensitive for certain types of defects.

Chinthalapudi and Hassan (2005) showed that energy loss of guided waves may be due to multiple reasons, among them is existing flaws in the structure. Impedance mismatch is considered as "energy-stealing" agent, and flaws such as delamination, split, and cavities cause this. In practice, the sensitivity to most simple defects such as notches and cracks is adequate and of similar magnitude due to the fairly uniform

Department of Mechanical Engineering, University of South Carolina, Columbia, SC, USA

Corresponding author:
Ayman M Kamal, Department of Mechanical Engineering, University of South Carolina, Columbia, SC 29208, USA.
Email: kamal@email.sc.edu

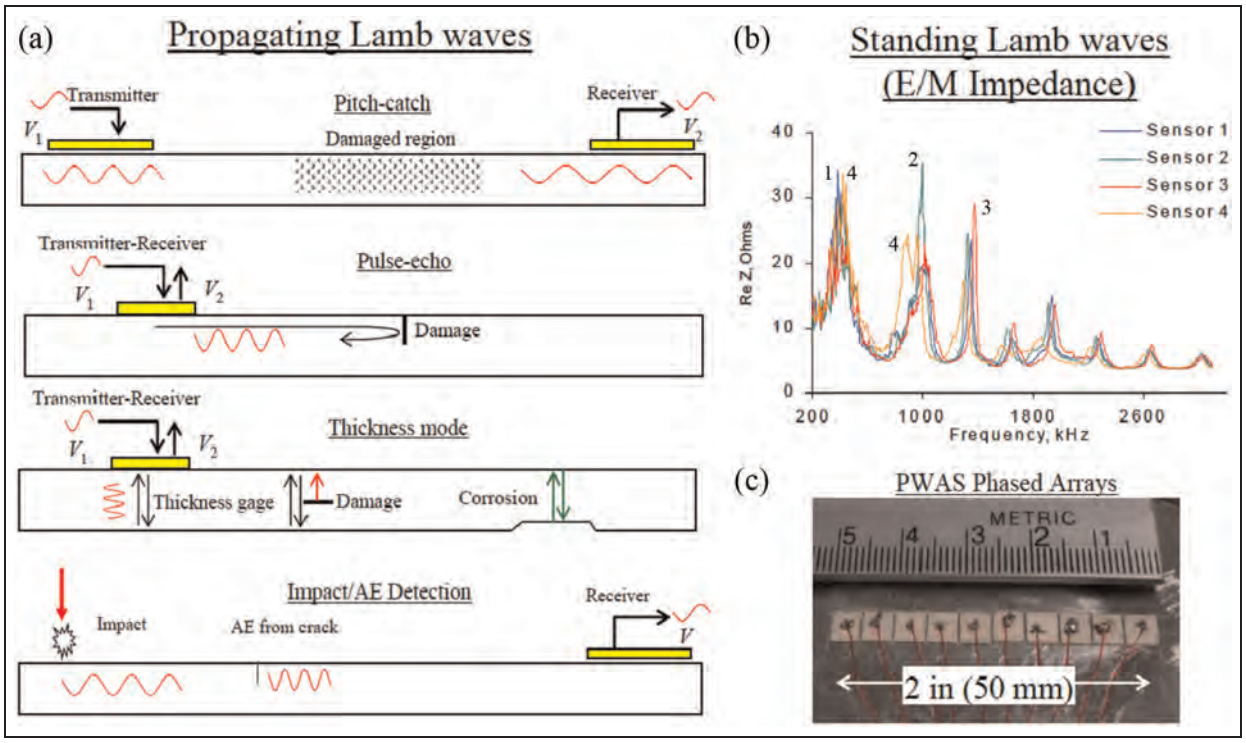

Figure 1. The various ways in which PWAS are used for structural sensing includes (a) propagating Lamb waves, (b) standing Lamb waves and (c) phased arrays. The propagating waves methods include: pitch-catch; pulse-echo; thickness mode; and passive detection of impacts and acoustic emission (Giurgiutiu, 2008).
PWAS: piezoelectric wafer active sensors; AE: acoustic emission.

distribution of energy through the thickness of the plate; the sensitivity considerations become much more important in anisotropic materials. Wilcox et al. (2001) showed an example of delamination detection in composites where certain modes were found to be blind to delamination at certain depths. Other studies (Alleyne and Cawley, 1992; Koh et al., 2002) gave more insights on how different defects interact with Lamb waves and how severity of impact damages can be predicted from the transmitted power. Generally, failure theories based on energy methods are more robust in predicting failure. Hence, it is very important to model Lamb wave power and energy transduction between PWAS and host structures. Another application that attracts more interests recently is energy harvesting applications. The need of optimizing energy transfer (Kural et al., 2011; Park et al., 2007) requires accurate models for Lamb wave energy, rather than simplified axial and flexural approximation valid only at low frequencies.

Excitation at frequencies beyond the cutoff frequency of A_1 and S_1 modes will generate multimodal Lamb waves. This phenomenon appears also for relatively thick structures. In these cases, every mode shares parts of the supplied power and energy. Our analytical model is developed based on "normal modes." Normal modes represent the possible vibration characteristics of the structure and are independent on loading scheme (Rose, 1999). The method of *normal mode expansion* (NME) is described in this study. It is worth mentioning that there are other methods that can be used to solve forced loading of a structure, for example, the *integral transform techniques* (ITT). Some of the most popular transforms are Laplace, Fourier, Hankel, and Mellin. Various integral transforms are used to transform a given function into another; this transformation is done via integration (over some domain) of the original function multiplied by a known kernel function. This is followed by either solving for the exact solution, for example, with residue theorem, or by numerically evaluating the integral in the case of complicated problems.

The solution of Lamb wave propagation in a plate that is excited with surface PWAS was obtained by Giurgiutiu (2008) with integral transform technique of the exact solution. NME method determines the expanded amplitudes. NME can be used for isotropic or generally anisotropic layers. The difference between isotropic and anisotropic cases is in evaluating the quantities appearing in the solution. Therefore, the NME method can be considered more general because the physical nature of the excitation process is clear and independent on the material. ITT method does have extensive algebra, and Viktorov (1967) discussed the method of ITT in detail and how the solution is different between isotropic and generally anisotropic layers.

Lamb wave NME

NME method is used to (1) find directly the amplitudes of given mode in terms of loading parameters and (2) evaluate the contribution factor of every mode to the total wave power and energy. Normal modes of the guided waves in the structure serve like the eigenfunctions. The method assumes that the desired solution can be written in the form of series of known functions, each with unknown amplitudes. Then, those amplitudes are to be determined either numerically or by finding a general expression that is valid for all modes.

Normal modes (eigenfunctions) of the analyzed structure are assumed "complete," meaning that any function can be represented exactly in terms of a finite or infinite number of functions in the set of "normal modes." Second condition for NME method is the orthogonality of the base functions (Rose, 1999). NME of the displacement can be written as summation of mode functions

$$u(x,y,t) = \sum_{j=1}^{\infty} C_j U_j(x,y) e^{i\omega t} \tag{1}$$

where C_j is the contribution factor for each mode and U_j is the mode shape. This solution is assumed for the particular case of time harmonics with angular frequency ω.

Lamb waves (guided plate waves) are fully analyzed in a number of textbooks (Graff, 1991; Rose, 1999). Here, we reproduce the essentials for power and energy models. The wave equations are

$$\begin{aligned} \frac{\partial^2 \phi}{\partial x^2} + \frac{\partial^2 \phi}{\partial y^2} + \frac{\omega^2}{c_P^2}\phi = 0 \\ \frac{\partial^2 \psi}{\partial x^2} + \frac{\partial^2 \psi}{\partial y^2} + \frac{\omega^2}{c_S^2}\psi = 0 \end{aligned} \tag{2}$$

where ϕ and ψ are two potential functions; $c_p = \sqrt{(\lambda + 2\mu)/\rho}$ and $c_s = \sqrt{\mu/\rho}$ are the pressure (longitudinal) and shear (transverse) wave speeds, respectively; λ and μ are the Lame constants; and ρ is the mass density. The time dependence is assumed harmonic, the displacement solution for symmetric and antisymmetric wave propagation (Figure 2), and can be obtained as

$$\begin{cases} u_x(x,y,t) = -B_n(\xi_{Sn}\cos\alpha_{Sn}y - R_{Sn}\beta_{Sn}\cos\beta_{Sn}y)e^{-i(\xi_{Sn}x-\omega t)} \\ u_y(x,y,t) = iB_n(\alpha_{Sn}\sin\alpha_{Sn}y + R_{Sn}\xi_{Sn}\sin\beta_{Sn}y)e^{-i(\xi_{Sn}x-\omega t)} \end{cases} \text{(symmetric)} \tag{3}$$

$$\begin{cases} u_x(x,y,t) = -A_n(\xi_{An}\sin\alpha_{An}y - R_{An}\beta_{An}\sin\beta_{An}y)e^{-i(\xi_{An}x-\omega t)} \\ u_y(x,y,t) = -iA_n(\alpha_{An}\cos\alpha_{An}y + R_{An}\xi_{An}\cos\beta_{An}y)e^{-i(\xi_{An}x-\omega t)} \end{cases} \text{(antisymmetric)} \tag{4}$$

where subscript n denotes the values for each mode; B_n and A_n are the amplitudes to be determined using *NME method*; ξ_{Sn} and ξ_{An} are wave numbers evaluated

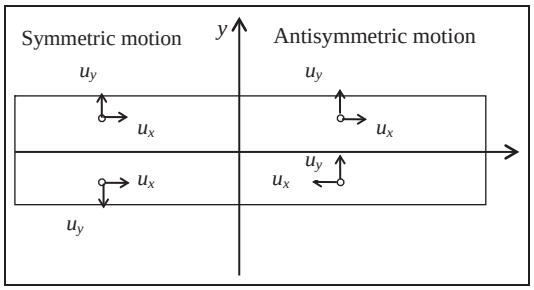

Figure 2. Symmetric and antisymmetric particle motion across the plate thickness.

using the relation $\xi = \omega/c$,where c is the wave speed; α and β are functions given by $\alpha^2 = (\omega^2/c_p^2) - \xi^2$ and $\beta^2 = (\omega^2/c_s^2) - \xi^2$; and R_{Sn} and R_{An} are the symmetric and antisymmetric eigen coefficients calculated from the solution of the Rayleigh–Lamb equation for symmetric and antisymmetric modes

$$\frac{\tan\alpha d}{\tan\beta d} = -\left[\frac{\left(\xi^2 - \beta^2\right)^2}{4\xi^2\alpha\beta}\right]^{\pm 1} \tag{5}$$

For free wave motion, the homogeneous solution is derived by applying the stress-free boundary conditions at the upper and lower surfaces ($y = \pm d$, where d is the plate half thickness)

$$R_S = \frac{\left(\xi_S{}^2 - \beta_S{}^2\right)\cos\alpha_S d}{2\xi_S\beta_S\cos\beta_S d},\ R_A = \frac{\left(\xi_A{}^2 - \beta_A{}^2\right)\sin\alpha_A d}{2\xi_A\beta_A\sin\beta_A d} \tag{6}$$

Power flow normalization is used to determine a closed form for expanded amplitudes B_n and A_n. This method is based on the complex reciprocity relation and orthogonal modes (Auld, 1990; Santoni, 2010).

Reciprocity relation for Lamb waves

Reciprocity relation is more or less an extension of Newton's third law of motion, where action and reaction are equivalent. Assume that $\mathbf{u}_{12}$ is the displacement of point P_1 due to force $\mathbf{F}_2$ and $\mathbf{u}_{21}$ is the displacement of point P_2 due to force $\mathbf{F}_1$. In its most elementary form, the *mechanics reciprocity principle* states that (Santoni, 2010) the work done at point P_1 by force $\mathbf{F}_1$ upon the displacement induced by force $\mathbf{F}_2$ is the same as the work done at point P_2 by force $\mathbf{F}_2$ upon the displacement induced by force $\mathbf{F}_1$, that is

$$\mathbf{F}_1 \cdot \mathbf{u}_{12} = \mathbf{F}_2 \cdot \mathbf{u}_{21}$$

For Lamb waves, one has real reciprocity and complex reciprocity; we focus on complex reciprocity following Auld (1990).

Considering a generic body Ω and two sources $\mathbf{F}_1$ and $\mathbf{F}_2$ applied at points P_1 and P_2 (Figure 3), the two

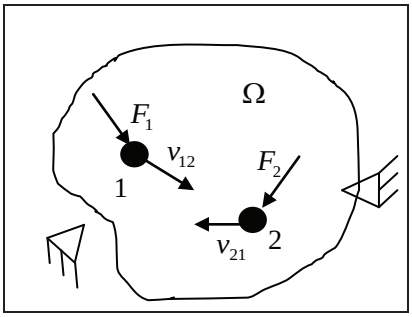

Figure 3. Reciprocity relation.

force sources produce two wave fields with velocity and stress $\mathbf{v}_1, \mathbf{T}_1$ and $\mathbf{v}_2, \mathbf{T}_2$. Using equation of motion and applying the two different sources (1) and (2) and adding the two field equations together, we can prove the complex reciprocity form that relates the velocity responses, tractions, and applied sources for harmonic excitation, that is

$$\nabla\left(\tilde{\mathbf{v}}_2 \cdot \mathbf{T}_1 + \mathbf{v}_1 \cdot \tilde{\mathbf{T}}_2\right) = -\left(\tilde{\mathbf{v}}_2 \cdot \mathbf{F}_1 + \mathbf{v}_1 \cdot \tilde{\mathbf{F}}_2\right) \quad (7)$$

For Lamb waves, a similar relation has been derived in Santoni (2010), with the assumption of time harmonic solution. One important assumption considered throughout the analysis is that Lamb wave fields are *z-invariant*. Hence, the only surviving stresses are normal stresses T_{xx} and T_{yy} and shear stress T_{xy}, v_x and v_y are the velocity fields, and superscripts 1 and 2 indicate fields due to sources 1 and 2.

The complex reciprocity relation for Lamb waves takes the form

$$\begin{aligned}&\frac{\partial}{\partial x}\left(\tilde{v}_x^2 T_{xx}^1 + \tilde{v}_y^2 T_{xy}^1 + v_x^1 \tilde{T}_{xx}^2 + v_y^1 \tilde{T}_{xy}^2\right)\\ &+ \frac{\partial}{\partial y}\left(\tilde{v}_x^2 T_{xy}^1 + \tilde{v}_y^2 T_{yy}^1 + v_x^1 \tilde{T}_{xy}^2 + v_y^1 \tilde{T}_{yy}^2\right)\\ &= -\tilde{v}_x^2 F_x^1 - v_x^1 \tilde{F}_x^2 - \tilde{v}_y^2 F_y^1 - v_y^1 \tilde{F}_y^2\end{aligned} \quad (8)$$

This reciprocity relation is the basic formula used to derive orthogonality condition; in addition, the source influence (PWAS excitation) determines modal contribution factors for each mode.

Orthogonality of Lamb waves

The definition of orthogonal functions U over given domain $[a, b]$ can be defined as

$$\int_a^b U_m U_n dy = 0 \quad \text{for } m \neq n \quad (9)$$

Recalling the complex reciprocity relation of equation (7) with the source forces F_x and $F_y = 0$ and assuming 1 and 2 are two solutions for time-harmonic-propagating Lamb waves, we get

$$\begin{aligned}\mathbf{v}_1(x,y,z,t) &= \left(v_x^n(y)\hat{\mathbf{x}} + v_y^n(y)\hat{\mathbf{y}}\right)e^{-i\xi_n x}e^{i\omega t}\\ \tilde{\mathbf{v}}_2(x,y,z,t) &= \left(\tilde{v}_x^m(y)\hat{\mathbf{x}} + \tilde{v}_y^m(y)\hat{\mathbf{y}}\right)e^{i\tilde{\xi}_m x}e^{-i\omega t}\end{aligned} \quad (10)$$

$$\mathbf{T}_1(x,y,z,t) = \begin{bmatrix} T_{xx}^n(y) & T_{yx}^n(y) & 0\\ T_{yx}^n(y) & T_{yy}^n(y) & 0\\ 0 & 0 & T_{zz}^n(y)\end{bmatrix} e^{-i\xi_n x}e^{i\omega t} \quad (11)$$

$$\tilde{\mathbf{T}}_2(x,y,z,t) = \begin{bmatrix} \tilde{T}_{xx}^m(y) & \tilde{T}_{yx}^m(y) & 0\\ \tilde{T}_{yx}^m(y) & \tilde{T}_{yy}^m(y) & 0\\ 0 & 0 & \tilde{T}_{zz}^m(y)\end{bmatrix} e^{i\tilde{\xi}_m x}e^{-i\omega t}$$

Substituting equations (10) and (11) in the reciprocity equation (7) with F_x and $F_y = 0$ and integrating over plate thickness, we get

$$\begin{aligned}&-i\left(\xi_n - \tilde{\xi}_m\right)\int_{-d}^{d}\left(v_y^n(y)\tilde{T}_{xy}^m(y) + \tilde{v}_y^m(y)T_{xy}^n(y)\right.\\ &\left.+ v_x^n(y)\tilde{T}_{xx}^m(y) + \tilde{v}_x^m(y)T_{xx}^n(y)\right)\\ &dy = -\left(v_y^n(y)\tilde{T}_{yy}^m(y) + \tilde{v}_y^m(y)T_{yy}^n(y)\right.\\ &\left.+ v_x^n(y)\tilde{T}_{xy}^m(y) + \tilde{v}_x^m(y)T_{xy}^n(y)\right)|_{-d}^{d}\end{aligned} \quad (12)$$

Using the assumption of traction-free boundary condition, $T_{xy} = T_{yy} = 0$, at the top and bottom surfaces, equation (12) yields

$$\begin{aligned}&-i\left(\xi_n - \tilde{\xi}_m\right)\int_{-d}^{d}\left(v_y^n(y)\tilde{T}_{xy}^m(y) + \tilde{v}_y^m(y)T_{xy}^n(y)\right.\\ &\left.+ v_x^n(y)\tilde{T}_{xx}^m(y) + \tilde{v}_x^m(y)T_{xx}^n(y)\right)dy = 0\end{aligned} \quad (13)$$

Alternatively, in short form

$$i\left(\xi_n - \tilde{\xi}_m\right)4P_{mn} = 0 \quad (14)$$

where

$$\begin{aligned}P_{nm} = &-\frac{1}{4}\int_{-d}^{d}\left(v_y^n(y)\tilde{T}_{xy}^m(y) + \tilde{v}_y^m(y)T_{xy}^n(y)\right.\\ &\left.+ v_x^n(y)\tilde{T}_{xx}^m(y) + \tilde{v}_x^m(y)T_{xx}^n(y)\right)dy\end{aligned} \quad (15)$$

Recall our assumption of considering only propagating waves (evanescent waves, which die out away from the source, are ignored); consequently, ξ_m and ξ_n are real and $\tilde{\xi}_m = \xi_m$. Since $\mathrm{Re}(\tilde{a} \cdot b) = \mathrm{Re}\left(a \cdot \tilde{b}\right)$, the orthogonality condition can be further simplified to

$$P_{mn} = \begin{cases} 0 & \text{if } m \neq n\\ \mathrm{Re}\left[-\frac{1}{2}\int_{-d}^{d}\left(\tilde{v}_x^n(y)T_{xx}^n(y) + \tilde{v}_y^n(y)T_{xy}^n(y)\right)dy\right] & \text{if } m = n\end{cases} \quad (16)$$

P_{mn} is a measure of average power flow through the plate and is used to determine Lamb wave amplitudes through normalization.

Normalization of wave amplitudes

To apply orthogonality of Lamb waves of equation (16), velocity fields v_x^n and v_y^n and stresses T_{xx}^n and T_{xy}^n are required. In addition, stresses are needed to evaluate potential energy and wave power. From elasticity equations, stresses are related to strains by Lame constants as

$$\begin{aligned} T_{xx} &= (\lambda + 2\mu)S_{xx} + \lambda S_{yy} \\ T_{yy} &= \lambda S_{xx} + (\lambda + 2\mu)S_{yy} \\ T_{xy} &= 2\mu S_{xy} \end{aligned} \tag{17}$$

where S_{xx}, S_{yy}, and S_{xy} are normal and shear strains; they can be derived by differentiating equations (3) and (4).

For symmetric waves (superscript S)

$$\begin{cases} S_{xx}^S = iB_n\xi_{Sn}(\xi_{Sn}\cos\alpha_{Sn}y - R_{Sn}\beta_{Sn}\cos\beta_{Sn}y)e^{-i(\xi_{Sn}x-\omega t)} \\ S_{yy}^S = iB_n\left(\alpha_{Sn}^2\cos\alpha_{Sn}y + R_{Sn}\xi_{Sn}\beta_{Sn}\cos\beta_{Sn}y\right)e^{-i(\xi_{Sn}x-\omega t)} \\ 2S_{xy}^S = B_n\left(2\xi_{Sn}\alpha_{Sn}\sin\alpha_{Sn}y + R_{Sn}\left(\xi_{Sn}^2 - \beta_{Sn}^2\right)\sin\beta_{Sn}y\right)e^{-i(\xi_{Sn}x-\omega t)} \end{cases} \tag{18}$$

Substituting the strains in Hooke's law, equation (17) becomes

$$\begin{cases} T_{xx}^S = iB_n\left[\left((\lambda + 2\mu)\xi_{Sn}^2 + \lambda\alpha_{Sn}^2\right)\cos\alpha_{Sn}y - 2\mu R_{Sn}\xi_{Sn}\beta_{Sn}\cos\beta_{Sn}y\right]e^{-i(\xi_{Sn}x-\omega t)} \\ T_{yy}^S = iB_n\left[\left(\lambda\xi_{Sn}^2 + (\lambda + 2\mu)\alpha_{Sn}^2\right)\cos\alpha_{Sn}y + 2\mu R_{Sn}\xi_{Sn}\beta_{Sn}\cos\beta_{Sn}y\right]e^{-i(\xi_{Sn}x-\omega t)} \\ T_{xy}^S = \mu B_n\left[2\xi_{Sn}\alpha_{Sn}\sin\alpha_{Sn}y + R_{Sn}\left(\xi_{Sn}^2 - \beta_{Sn}^2\right)\sin\beta_{Sn}y\right]e^{-i(\xi_{Sn}x-\omega t)} \end{cases} \tag{19}$$

Equations (19) can be rearranged using the relations

$$\begin{aligned} (\lambda + 2\mu)\xi^2 + \lambda\alpha^2 &= \mu\left(\xi^2 + \beta^2 - 2\alpha^2\right) \\ \lambda\xi^2 + (\lambda + 2\mu)\alpha^2 &= -\mu\left(\xi^2 - \beta^2\right) \end{aligned} \tag{20}$$

The stresses for symmetric case become

$$\begin{cases} T_{xx}^S = i\mu B_n\left[\left(\xi_{Sn}^2 + \beta_{Sn}^2 - 2\alpha_{Sn}^2\right)\cos\alpha_{Sn}y - 2R_{Sn}\xi_{Sn}\beta_{Sn}\cos\beta_{Sn}y\right]e^{-i(\xi_{Sn}x-\omega t)} \\ T_{yy}^S = i\mu B_n\left[-\left(\xi_{Sn}^2 - \beta_{Sn}^2\right)\cos\alpha_{Sn}y + 2R_{Sn}\xi_{Sn}\beta_{Sn}\cos\beta_{Sn}y\right]e^{-i(\xi_{Sn}x-\omega t)} \\ T_{xy}^S = \mu B_n\left[2\xi_{Sn}\alpha_{Sn}\sin\alpha_{Sn}y + R_{Sn}\left(\xi_{Sn}^2 - \beta_{Sn}^2\right)\sin\beta_{Sn}y\right]e^{-i(\xi_{Sn}x-\omega t)} \end{cases} \tag{21}$$

Similarly for antisymmetric waves, (*superscript A*) for the sake of completeness

$$\begin{cases} S_{xx}^A = iA_n\left(\xi_{An}^2\sin\alpha_{An}y - R_{An}\xi_{An}\beta_{An}\sin\beta_{An}y\right)e^{-i(\xi_{An}x-\omega t)} \\ S_{yy}^A = iA_n\left(\alpha_{An}^2\sin\alpha_{An}y + R_{An}\xi_{An}\beta_{An}\sin\beta_{An}y\right)e^{-i(\xi_{An}x-\omega t)} \\ 2S_{xy}^A = -A_n\left(2\xi_{An}\alpha_{An}\cos\alpha_{An}y + R_{An}\left(\xi_{An}^2 - \beta_{An}^2\right)\cos\beta_{An}y\right)e^{-i(\xi_{An}x-\omega t)} \end{cases} \tag{22}$$

The stresses for antisymmetric case are

$$\begin{cases} T_{xx}^A = i\mu A_n\left[\left(\xi_{An}^2 + \beta_{An}^2 - 2\alpha_{An}^2\right)\sin\alpha_{An}y - 2R_{An}\xi_{An}\beta_{An}\sin\beta_{An}y\right]e^{-i(\xi_{An}x-\omega t)} \\ T_{yy}^A = i\mu A_n\left[-\left(\xi_{An}^2 - \beta_{An}^2\right)\sin\alpha_{An}y + 2R_{An}\xi_{An}\beta_{An}\sin\beta_{An}y\right]e^{-i(\xi_{An}x-\omega t)} \\ T_{xy}^A = -\mu A_n\left[2\xi_{An}\alpha_{An}\cos\alpha_{An}y + R_{An}\left(\xi_{An}^2 - \beta_{An}^2\right)\cos\beta_{An}y\right]e^{-i(\xi_{An}x-\omega t)} \end{cases} \tag{23}$$

Velocity fields are evaluated by taking time derivative of displacements in equations (3) and (4)

$$\begin{cases} v_x^S = \dfrac{\partial u_x^S}{\partial t} = -i\omega B(\xi_S\cos\alpha_S y - R_S\beta_S\cos\beta_S y)e^{-i(\xi_S x-\omega t)} \\ v_y^S = \dfrac{\partial u_y^S}{\partial t} = -\omega B(\alpha_S\sin\alpha_S y + R_S\xi_S\sin\beta_S y)e^{-i(\xi_S x-\omega t)} \end{cases} \tag{24}$$

$$\begin{cases} v_x^A = \dfrac{\partial u_x^A}{\partial t} = -i\omega A(\xi_A\sin\alpha_A y - \beta_A R_A\sin\beta_A y)e^{-i(\xi_A x-\omega t)} \\ v_y^A = \dfrac{\partial u_y^A}{\partial t} = \omega A(\alpha_A\cos\alpha_A y + \xi_A R_A\cos\beta_A y)e^{-i(\xi_A x-\omega t)} \end{cases} \tag{25}$$

Substituting equations (21) and (23) to (25) in equation (16) and performing the integration yields

$$P_{nn} = \frac{\omega\mu {B_n}^2}{2} W_S \quad \text{(symmetric)},$$
$$P_{nn} = \frac{\omega\mu {A_n}^2}{2} W_A \quad \text{(antisymmetric)} \tag{26}$$

where

$$W_S = \left[\begin{array}{l} \xi_S d\left(R_S^2+1\right)\left(\xi_S^2+\beta_S^2\right) - R_S^2\xi_S\left(\xi_S^2-3\beta_S^2\right)\dfrac{\sin\beta_S d\cos\beta_S d}{\beta_S} \\ + \xi_S\left(\xi_S^2+\beta_S^2-4\alpha_S^2\right)\dfrac{\sin\alpha_S d\cos\alpha_S d}{\alpha_S} \\ + 4R_S\alpha_S\beta_S\sin\alpha_S d\cos\beta_S d - 2R_S\left(3\xi_S^2+{\beta_S}^2\right)\cos\alpha_S d\sin\beta_S d \end{array} \right] \tag{27}$$

$$W_A = -\left[\begin{array}{l} -\xi_A d\left(R_A^2+1\right)\left(\xi_A^2+\beta_A^2\right) - R_A^2\xi_A\left(\xi_A^2-3\beta_A^2\right)\dfrac{\sin\beta_A d\cos\beta_A d}{\beta_A} \\ + \xi_A\left(\xi_A^2+\beta_A^2-4\alpha_A^2\right)\dfrac{\sin\alpha_A d\cos\alpha_A d}{\alpha_A} \\ + 4R_A\alpha_A\beta_A\cos\alpha_A d\sin\beta_A d - 2R_A\left(3\xi_A^2+\beta_A^2\right)\sin\alpha_A d\cos\beta_A d \end{array} \right] \tag{28}$$

The symmetric mode coefficient B_n and the antisymmetric mode coefficient A_n can be resolved as

$$B_n = \sqrt{\frac{2P_{nn}}{\omega\mu W_{Sn}}}\,(\text{symmetric}),\ A_n = \sqrt{\frac{2P_{nn}}{\omega\mu W_{An}}}\,(\text{antisymmetric}) \tag{29}$$

For normal modes, we may assume $P_{nn} = 1$; hence

$$B_n = \sqrt{\frac{2}{\omega\mu W_{Sn}}}\ \text{(symmetric)},$$
$$A_n = \sqrt{\frac{2}{\omega\mu W_{An}}}\ \text{(antisymmetric)} \tag{30}$$

Modal contribution factors and PWAS excitation

Basic assumptions used in this study are (1) straight-crested Lamb waves, that is, z-invariant and (2) ideal bonding (pin-force) connection between PWAS and structure (Figure 4). After consideration of the orthogonality of Lamb wave modes and after the normalization of mode amplitudes with respect to the power, modal participation factor for each mode need to be evaluated (i.e. how much a particular mode contributes to the total wave power and energy). This uses the reciprocity relation with consideration of excitation forces from the source (e.g. a PWAS on the excited structure).

Recalling the complex reciprocity equation (7), multiplying by -1, and upon expansion of the del operator, we get

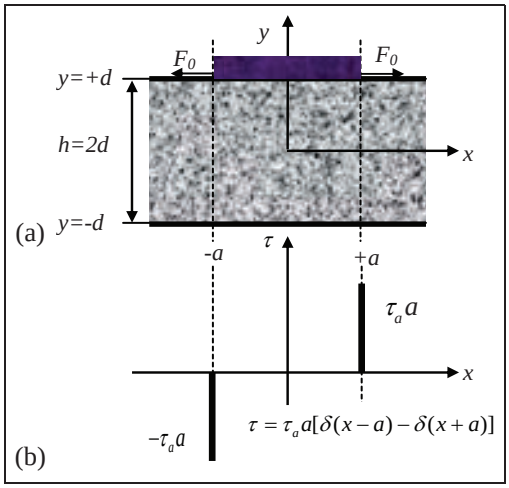

Figure 4. Pin-force model for structurally bonded PWAS: (a) PWAS pin forces at the ends on the upper surface and (b) shear stresses developed.
Source: Reproduced from Giurgiutiu (2008).
PWAS: piezoelectric wafer active sensors.

$$\frac{\partial}{\partial y}\left(-\tilde{\mathbf{v}}_2\cdot\mathbf{T}_1 - \mathbf{v}_1\cdot\tilde{\mathbf{T}}_2\right)\cdot\hat{\mathbf{y}} + \frac{\partial}{\partial x}\left(-\tilde{\mathbf{v}}_2\cdot\mathbf{T}_1 - \mathbf{v}_1\cdot\tilde{\mathbf{T}}_2\right)\cdot\hat{\mathbf{x}} = \tilde{\mathbf{v}}_2\mathbf{F}_1 + \mathbf{v}_1\tilde{\mathbf{F}}_2 \tag{31}$$

where $\mathbf{F}$ is a volume source, $\mathbf{T}\cdot\hat{\mathbf{y}}$ are the traction forces, and $\mathbf{v}$ are the velocity sources. Solution denoted by "1" like $\mathbf{T}_1$ indicates traction due to source excitation (e.g. by PWAS), while solution denoted by "2" is representing normal modes, that is, homogeneous solution of eigenfunctions of the free mode shapes of the structure—without considering excitation from the source. Fields due to excitation source can be represented as normal mode summation over all possible modes (Rose, 1999; Santoni, 2010), that is

$$\mathbf{v}_1 = \mathbf{v}_1(x,y) = \sum_m a_m(x)\mathbf{v}_m(y)$$
$$\mathbf{T}_1 = \mathbf{T}_1(x,y) = \sum_m a_m(x)\mathbf{T}_m(y) \tag{32}$$

where $a_m(x)$ are the modal participation factors that must be determined.

Homogeneous solution "2" can be represented as

$$\mathbf{v}_2(x,y) = \mathbf{v}_n(y)e^{-i\xi_n x}$$
$$\mathbf{T}_2(x,y) = \mathbf{T}_n(y)e^{-i\xi_n x} \tag{33}$$

Integrate equation (31) with respect to the plate thickness y from $y = -d$ to $y = +d$ to get

$$\left(-\tilde{\mathbf{v}}_2\cdot\mathbf{T}_1 - \mathbf{v}_1\cdot\tilde{\mathbf{T}}_2\right)\cdot\hat{\mathbf{y}}\Big|_{-d}^{d} + \int_{-d}^{d}\frac{\partial}{\partial x}\left(-\tilde{\mathbf{v}}_2\cdot\mathbf{T}_1 - \mathbf{v}_1\cdot\tilde{\mathbf{T}}_2\right)\cdot\hat{\mathbf{x}}\,dy = \int_{-d}^{d}\tilde{\mathbf{v}}_2\mathbf{F}_1\,dy \tag{34}$$

Substitution of equations (32) and (33) and rearrangement yields

$$\begin{aligned}&\left(-\tilde{\mathbf{v}}_n(y)\cdot\mathbf{T}_1-\mathbf{v}_1\cdot\tilde{\mathbf{T}}_n(y)\right)\cdot\hat{\mathbf{y}}\Big|_{-d}^{d}e^{i\tilde{\xi}_n x}\\&+\frac{\partial}{\partial x}\left[e^{i\tilde{\xi}_n x}\sum_m a_m(x)\int_{-d}^{d}\left(-\tilde{\mathbf{v}}_n(y)\cdot\mathbf{T}_m(y)-\mathbf{v}_m(y)\cdot\tilde{\mathbf{T}}_n(y)\right)\cdot\hat{\mathbf{x}}dy\right]\\&=e^{i\tilde{\xi}_n x}\int_{-d}^{d}\tilde{\mathbf{v}}_n(y)\,\mathbf{F}_1\,dy\end{aligned}\tag{35}$$

Recall the orthogonality relation in its general form

$$P_{mn}=-\frac{1}{4}\int_{-d}^{d}\left(\tilde{\mathbf{v}}_m(y)\cdot\mathbf{T}_n(y)+\mathbf{v}_n(y)\cdot\tilde{\mathbf{T}}_m(y)\right)\cdot\hat{\mathbf{x}}\,dy\tag{36}$$

In the absence of a volume force source term $\mathbf{F}_1$, equation (35) yields

$$\left(-\tilde{\mathbf{v}}_n\cdot\mathbf{T}_1-\mathbf{v}_1\cdot\tilde{\mathbf{T}}_n\right)\cdot\hat{\mathbf{y}}\Big|_{-d}^{d}e^{i\tilde{\xi}_n x}+\frac{\partial}{\partial x}e^{i\tilde{\xi}_n x}\sum_m 4a_m(x)P_{mn}=0\tag{37}$$

Since the modes are orthogonal, the summation in equation (37) has only one nonzero term corresponding to the propagating mode n (ξ_n real) for which $P_{nn}\neq 0$. Hence, equation (37) becomes

$$4P_{nn}\left(\frac{\partial}{\partial x}+i\tilde{\xi}_n\right)a_n(x)=\left(\tilde{\mathbf{v}}_n\cdot\mathbf{T}_1+\mathbf{v}_1\cdot\tilde{\mathbf{T}}_n\right)\cdot\hat{\mathbf{y}}\Big|_{-d}^{d}\tag{38}$$

This is a general ordinary differential equation (ODE), which needs to be solved to get the modal participation factor $a_n(x)$. $\tilde{\mathbf{T}}_n$ is the traction force; it must satisfy the traction-free boundary condition for Lamb waves, $T_{xy}^n\Big|_{\pm d}=0$ and $T_{yy}^n\Big|_{\pm d}=0$. $\mathbf{T}_1$ is the excitation shear. We have $T_{xy}\big|_d=t_x(x)$ at the upper surface and $T_{xy}\big|_{-d}=0$ on the lower surface since PWAS excitation is only on the upper surface (Figure 4).

For Lamb waves, equation (38) takes the form

$$4P_{nn}\left(\frac{\partial}{\partial x}+i\tilde{\xi}_n\right)a_n(x)=\begin{pmatrix}v_y^1(y)\tilde{T}_{yy}^n(y)+\tilde{v}_y^n(y)T_{yy}^1(y)\\+v_x^1(y)\tilde{T}_{xy}^n(y)+\tilde{v}_x^n(y)T_{xy}^1(y)\end{pmatrix}_{-d}^{d}\tag{39}$$

Applying traction-free conditions and PWAS excitation, and then solving the ODE, yields

$$a_n^{+}(x)=\left[\frac{\tilde{v}_x^n(d)}{4P_{nn}}\int_{-a}^{a}e^{i\xi_n\bar{x}}t_x(\bar{x})d\bar{x}\right]e^{-i\xi_n x}\quad\text{for } x>a\tag{40}$$

It should be noted that this formula is only for forward wave solution and outside the excitation region, that is, for $x>a$.

The total particle velocity using NME can be written as

$$\mathbf{v}(x,y)=\sum_n a_n(x)\mathbf{v}_n(y)\tag{41}$$

where $\mathbf{v}_n(y)$ is the velocity mode shape of the nth mode, that is, $\mathbf{v}_n(y)=\begin{Bmatrix}v_x^n(y)\\v_y^n(y)\end{Bmatrix}$. $\mathbf{v}_n(y)$ can be derived using the combination of the symmetric particle velocity in equation (24) with symmetric normalization coefficient of equation (30) and antisymmetric particle velocity in equation (25) with antisymmetric normalization coefficient of equation (30).

We exemplify the *NME* method for velocity fields with two examples: (1) 1-mm-thick aluminum plate, up to 2000 kHz where only S_0 and A_0 modes exist and (2) 2.6-mm-thick steel plate, with excitation up to 500 kHz. Figure 5 shows the particle velocity at plate's surface in x-axis and y-axis for the two plates. Note that the values of *NME* velocities are not multiplied yet by PWAS excitation. The displayed results are only for first symmetric S_0 and antisymmetric A_0 modes; the multimode demonstration will be shown in a later section.

Considering the ideal bonding assumption (pin-force model), the load transfer takes place over an infinitesimal region at the PWAS end. Assuming a PWAS with center at $x_0=0$ and length $l_a=2a$, the traction on the plate surface can be written as

$$\begin{aligned}t_x(x)&=a\tau_0[\delta(x-a)-\delta(x+a)]\\&=F_0(\omega)[\delta(x-a)-\delta(x+a)]\end{aligned}\tag{42}$$

Here, F_0 is the pin-force per unit width. Substitution of equation (42) into equation (40) gives the mode participation factor under PWAS excitation as

$$a_n^{PWAS}(x)=\frac{\tilde{v}_x^n(d)}{4P_{nn}}F_0(\omega)[e^{i\xi_n a}-e^{-i\xi_n a}]e^{-i\xi_n x}=g_nF_0(\omega)_0e^{-i\xi_n x}\tag{43}$$

where g_n is the coefficient $g_n=(\tilde{v}_x^n(d)/4P_{nn})[e^{i\xi_n a}-e^{-i\xi_n a}]$

The Lamb wave NME of the particle displacement under PWAS excitation is

$$u(x,y)=\frac{1}{i\omega}\sum_n g_nF_0(\omega)e^{-i\xi_n x}\mathbf{v}_n(y)\tag{44}$$

The displacement in x-direction at the PWAS end ($x=a, y=d$) is

$$u_x(a,d)=\frac{1}{i\omega}\sum_n\frac{\tilde{v}_x^n(d)}{4P_{nn}}v_x^n(d)[e^{i\xi_n a}-e^{-i\xi_n a}]F_0(\omega)e^{-i\xi_n a}\tag{45}$$

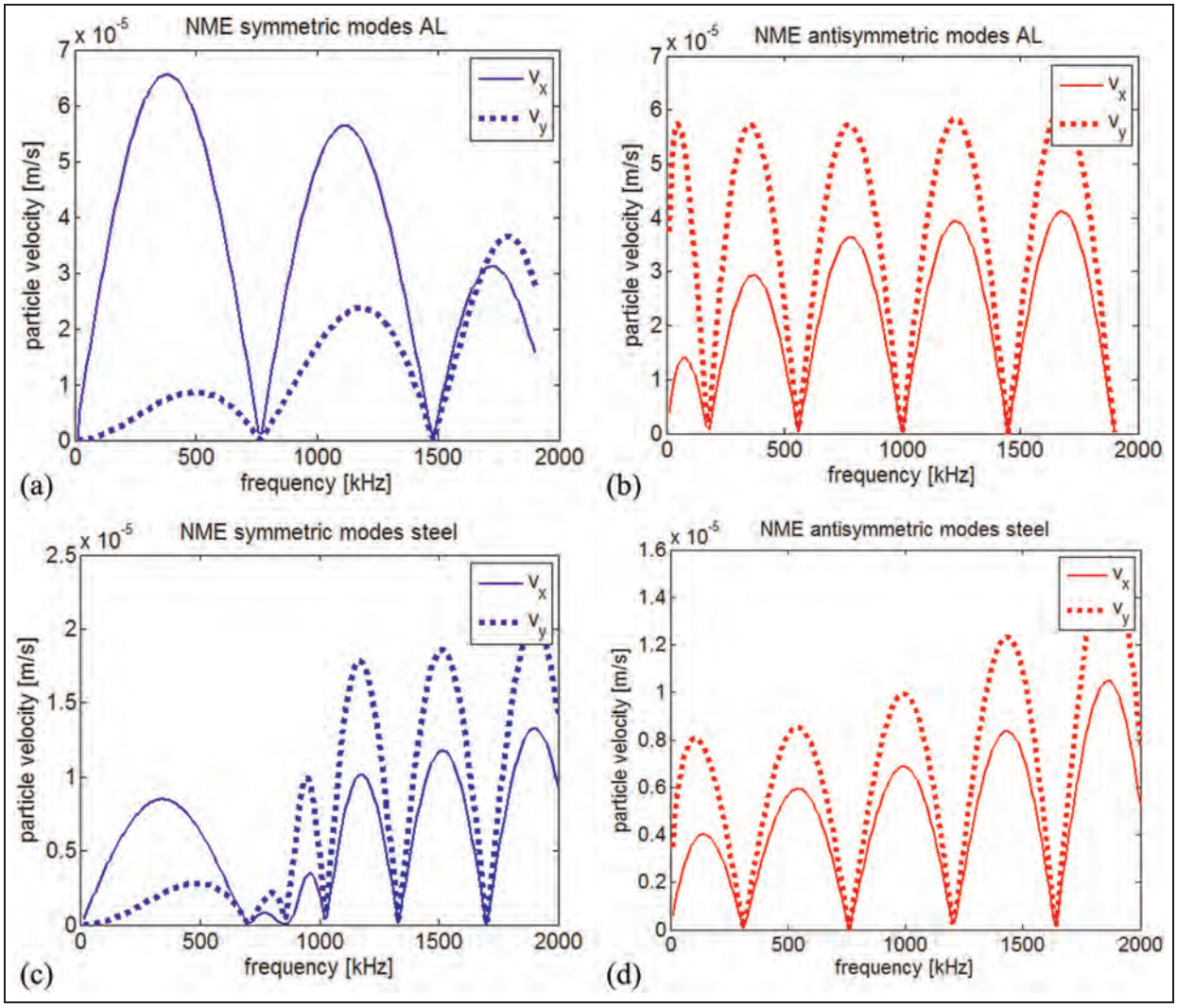

Figure 5. NME for particle velocity fields: (a) aluminum S_0, (b) aluminum A_0, (c) steel S_0, and (d) steel A_0 modes.
NME: normal mode expansion.

PWAS–structure interaction

Consider a PWAS of length $l = 2a$, width b, and thickness t_a; the relation between PWAS pin-force applied to the structure and the particle displacement is through the structural dynamic stiffness. The structures as well as the PWAS stiffness are now analyzed. When the PWAS transmitter is excited by an oscillatory voltage, its volume expands in phase with the voltage in accordance with the piezoelectric effect (Figure 6). Expansion of the PWAS mounted on the surface of the structure induces a surface reaction from the structure in the form of a force at the PWAS end. The PWAS end displacement is constrained by the plate and is equal to the plate displacement at $x = a$. The reaction force along the PWAS edge, $F_0(\omega)b$, depends on the PWAS displacement, u_{PWAS}, and on the frequency-dependent dynamic stiffness, $k_{str}(\omega)$, presented by the structure to the PWAS

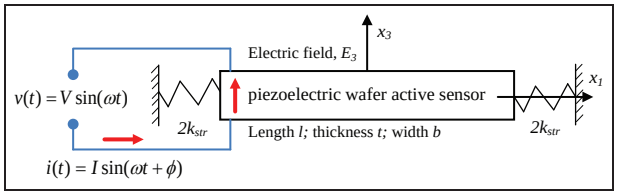

Figure 6. PWAS constrained by an overall structural stiffness k_{str}.
PWAS: piezoelectric wafer active sensors.

$$F_0(\omega)b = k_{str}(\omega)u_x(a,d) \tag{46}$$

The two stiffness elements on the right and the left of PWAS are selected to be $2k_{str}$; hence, the overall structure stiffness is k_{str} (Figure 6). Under harmonic excitation, the dynamic stiffness $k_{str}(\omega)$ is obtained by dividing the force by the displacement given by equation (44), that is

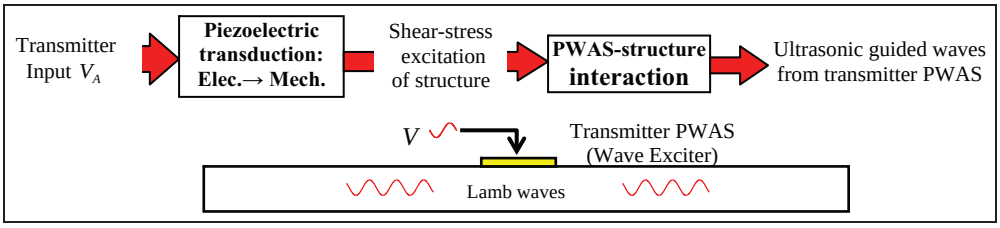

Figure 7. PWAS transmitter power flow.
PWAS: piezoelectric wafer active sensors.

$$k_{str}(\omega) = \frac{F_0(\omega)b}{\hat{u}_x(a,d)} = i\omega b\left[\sum_n g_n e^{-i\xi_n a}\mathbf{v}_n(d)\right]^{-1} \tag{47}$$

Define the static stiffness k_{PWAS} of a free PWAS as

$$k_{PWAS} = \frac{t_a b}{s_{11}^E a} \tag{48}$$

The dynamic stiffness ratio is defined as the ratio between $k_{str}(\omega)$ and k_{PWAS}, that is

$$r(\omega) = \frac{k_{str}(\omega)}{k_{PWAS}} \tag{49}$$

The relation between pin-force per unit width and the static stiffness of the PWAS is

$$F_0(\omega)b = k_{PWAS}\left(u_x(a,d) - \frac{1}{2}u_{ISA}\right) \tag{50}$$

where u_{ISA} is the "induced strain actuation" displacement (Giurgiutiu, 2008), which is defined as $u_{ISA} = ld_{31}\hat{V}/t_a$, and the quantity $u_x(a,d) - {}^1\!/_2 u_{ISA}$ represents the total x-direction displacement at the right tip of the PWAS (because of symmetry, only forward propagating wave needs to be considered.)

Substitute $u_x(a,d)$ from equation (45) into equation (50) and solve for F_0 using k_{str} from equation (47) to get

$$F_0(\omega) = \frac{1}{b}\left(\frac{r(\omega)}{1-r(\omega)}\right)\frac{k_{PWAS}u_{ISA}}{2} \tag{51}$$

The excitation pin-force $F_0(\omega)$ can now be used to determine the NME fields (displacements–strains–velocities), the modal participation factors $a_n^{PWAS}(x)$, and the coefficients g_n; then the power and energy can be analyzed.

Power transduction between PWAS and structure

The power and energy transduction flowchart for a PWAS transmitter on a structure is shown in Figure 7 (Lin et al., 2012). The electrical energy due to the input voltage applied at the PWAS terminals is converted through piezoelectric transduction into mechanical energy that activates the expansion–contraction motion of the PWAS transducer. This motion is transmitted to the underlying structure through the shear stress in the adhesive layer at the PWAS–structure interface. As a result, ultrasonic guided waves are excited into the underlying structure. The mechanical power at the interface becomes the acoustic wave power, and the generated Lamb waves propagate in the structure.

PWAS admittance and electrical active power

To calculate the transmitter electrical power and energy, we need to calculate the input electrical power by using input admittance of the PWAS when attached to the structure. Because of the electromechanical coupling, the impedance is strongly influenced by the dynamic behavior of the structure and is substantially different from the free-PWAS impedance.

Under harmonic excitation, the time-averaged power is the average amount of energy converted per unit time under continuous harmonic excitation. The time-averaged product of the two harmonic variables is one half the product of one variable times the conjugate of the other. When a harmonic voltage is applied to the transmitter PWAS, the current is

$$I = Y\hat{V} \tag{52}$$

The constrained PWAS admittance can be expressed (Giurgiutiu, 2008) using the frequency-dependent stiffness ratio of equation (49), that is

$$Y(\omega) = i\omega C_0\left[1 - k_{31}^2\left(1 - \frac{1}{r(\omega) + \phi(\omega)\cot\phi(\omega)}\right)\right] \tag{53}$$

where $\phi(\omega) = \xi(\omega)a$. A simplified form of equation (53) can be obtained under the quasi-static assumption in which the PWAS dynamics are assumed to happen at much higher frequencies than the Lamb wave propagation ($\phi(\omega) \to 0$, $\phi(\omega)\cot\phi(\omega) \to 1$), that is

$$Y(\omega) = i\omega C_0\left[1 - k_{31}^2\frac{r(\omega)}{1 + r(\omega)}\right] \tag{54}$$

This simplified model of admittance was used in Lin and Giurgiutiu (2012); it was used for axial and flexural wave propagation at low-frequency excitation. Here, we use a new definition of $r(\omega)$ in equation (49) and $k_{str}(\omega)$ in equation (47) based on NME for multimodal Lamb wave propagation.

The power rating, time-averaged active power, and reactive power are

$$P_{rating} = \frac{1}{2}|Y|\hat{V}^2 = \sqrt{P_{active}^2 + P_{reactive}^2}, \quad P_{active} = \frac{1}{2}Y_R\hat{V}^2,\ P_{reactive} = \frac{1}{2}Y_I\hat{V}^2 \tag{55}$$

where Y_R is the real part of admittance and Y_I is the imaginary part of admittance.

The active power is the power that is converted to the mechanical power at the interface. The reactive power is the imaginary part of the complex power that is not consumed and is recirculated to the power supply. The power rating is the power requirement of the power supply without distortion. In induced strain transmitter applications, the reactive power is the dominant factor since the transmitter impedance is dominated by its capacitive behavior (Lin et al., 2012). Managing high reactive power requirements is one of the challenges of using piezoelectric induced strain actuators.

Mechanical power

Due to electromechanical transduction in the PWAS, the electrical active power is converted into mechanical power, and through shear effects in the adhesive layer between PWAS and the structure, the mechanical power transfers into the structure and excites guided wave. Santoni (2010) studied shear lag solution for the case of multiple Lamb wave modes. This solution can be simplified by considering that the shear stress transfer is concentrated over some infinitesimal distances at the ends of the PWAS actuator (Figure 4). The concept of ideal bonding (also known as the pin-force model) assumed that all the load transfer takes place over an infinitesimal region at the PWAS ends; the generated mechanical power is the multiplication of this load times the structure particle velocity at the PWAS tip. The time-averaged power is defined as

$$\langle p \rangle = \frac{1}{T}\int_0^T p(t)dt \tag{56}$$

The time-averaged product of two harmonic variables is one half the product of one variable times the conjugate of the other. The time-averaged mechanical power at PWAS–structure interface is

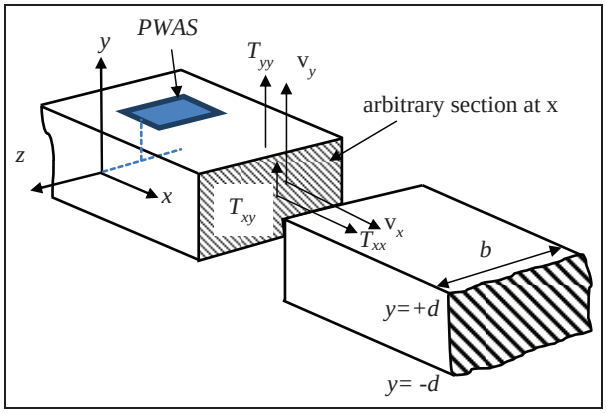

Figure 8. Representation of stresses and velocities at arbitrary section of the structure.
PWAS: piezoelectric wafer active sensors.

$$\langle p_0 \rangle = -\frac{1}{2}\tilde{F}_0(\omega)\hat{v}_0(\omega) \tag{57}$$

Mechanical power excites both forward and backward propagating waves initiating from the two end tips at $x = a$ and $x = -a$. Due to symmetry, we only need to consider the forward wave, which will contain only half of the mechanical power converted from the electrical active power.

Lamb wave power and energy

The mechanically converted power is in turn transferred into the power of the propagating forward wave. It is important to mention that evanescent (nonpropagating) waves are not considered in this study. The time-averaged wave power is

$$\langle p \rangle = -\frac{1}{2}\int_A \left(\tilde{T}_{xx}v_x + \tilde{T}_{xy}v_y\right)dA \tag{58}$$

where v denotes particle velocity either in x- or y-direction, T denotes stress, and $\tilde{T}$ is the conjugate, which are determined from equations (17), (24), and (25). Figure 8 shows all associated stresses and velocities.

The time-averaged wave power can be determined for a given section x by integration over the cross-sectional area. Under the *z-invariant* assumption, the width b is taken outside the integration; equation (58) can be further simplified as

$$\langle p \rangle = -\frac{b}{2}\int_{-d}^{d} \left\{\left((\lambda + 2\mu)\tilde{S}_{xx} + \lambda\tilde{S}_{yy}\right)v_x + \left(2\mu\tilde{S}_{xy}\right)v_y\right\}dy \tag{59}$$

Orthogonality of Lamb waves can be used during the expansion of equation (59) because all the quantities are defined as summation of symmetric solution plus

antisymmetric solution, for example, v_x is the summation of v_x parts of equations (24) and (25). The same is true for strains.

When evaluating the multiplication of $\tilde{S}_{xx}$ times v_x and integrating, the quantities generated from multiplying symmetric part times antisymmetric parts end up as integration of sine times cosine terms and vanish due to orthogonality of Lamb waves. However, "$\cos^2$" and "$\sin^2$" terms are retained. The time-averaged wave power takes the closed form

$$\langle p \rangle = \sum_n \langle p_n^S \rangle + \sum_n \langle p_n^A \rangle \tag{60}$$

where $\langle p_n^S \rangle$ and $\langle p_n^A \rangle$ are the time-averaged wave powers for symmetric mode S_n and antisymmetric mode A_n, respectively

$$\langle p_n^S \rangle = -\frac{b}{2}\left[g_n^S B_n F(\omega)\right]^2 \begin{pmatrix} -(\lambda+2\mu)\omega\xi_{Sn}\int_{-d}^{d}\left\{\begin{array}{l}\xi_{Sn}^2\cos^2\alpha_{Sn}y + R_{Sn}^2\beta_{Sn}^2\cos^2\beta_{Sn}y \\ -2R_{Sn}\beta_{Sn}\xi_{Sn}\cos\alpha_{Sn}y\cos\beta_{Sn}y\end{array}\right\}dy \\ -\lambda(\omega/\xi_{Sn})\int_{-d}^{d}\left\{\begin{array}{l}\xi_{Sn}^2\alpha_{Sn}^2\cos^2\alpha_{Sn}y - R_{Sn}^2\beta_{Sn}^2\xi_{Sn}^2\cos^2\beta_{Sn}y \\ +R_{Sn}\beta_{Sn}\xi_{Sn}(\xi_{Sn}^2-\alpha_{Sn}^2)\cos\alpha_{Sn}y\cos\beta_{Sn}y\end{array}\right\}dy \\ -\mu\omega\int_{-d}^{d}\left\{\begin{array}{l}2\xi_{Sn}\alpha_{Sn}^2\sin^2\alpha_{Sn}y + R_{Sn}^2\xi_{Sn}(\xi_{Sn}^2-\beta_{Sn}^2)\sin^2\beta_{Sn}y \\ +R_{Sn}\alpha_{Sn}(3\xi_{Sn}^2-\beta_{Sn}^2)\sin\alpha_{Sn}y\sin\beta_{Sn}y\end{array}\right\}dy \end{pmatrix} \tag{61}$$

$$\langle p_n^A \rangle = -\frac{b}{2}\left[g_n^A A_n F(\omega)\right]^2 \begin{pmatrix} -(\lambda+2\mu)\omega\xi_{An}\int_{-d}^{d}\left\{\begin{array}{l}\xi_{An}^2\sin^2\alpha_{An}y + R_{An}^2\beta_{An}^2\sin^2\beta_{An}y \\ -2R_{An}\beta_{An}\xi_{An}\sin\alpha_{An}y\sin\beta_{An}y\end{array}\right\}dy \\ -\lambda(\omega/\xi_{An})\int_{-d}^{d}\left\{\begin{array}{l}\xi_{An}^2\alpha_{An}^2\sin^2\alpha_{An}y - R_{An}^2\beta_{An}^2\xi_{An}^2\sin^2\beta_{Sn}y \\ +R_{An}\beta_{An}\xi_{An}(\xi_{An}^2-\alpha_{An}^2)\sin\alpha_{An}y\sin\beta_{An}y\end{array}\right\}dy \\ -\mu\omega\int_{-d}^{d}\left\{\begin{array}{l}2\xi_{An}\alpha_{An}^2\cos^2\alpha_{An}y + R_{An}^2\xi_{An}(\xi_{An}^2-\beta_{An}^2)cos^2\beta_{An}y \\ +R_{An}\alpha_{An}(3\xi_{An}^2-\beta_{An}^2)\cos\alpha_{An}y\cos\beta_{An}y\end{array}\right\}dy \end{pmatrix} \tag{62}$$

The terms $g_n^{S_n}$ and $g_n^{A_n}$ represent the coefficients in equation (43) for symmetric and antisymmetric modes.

Kinetic energy for Lamb waves is defined as

$$k_e(x,t) = \frac{1}{2}\rho\int_A \left(v_x^2 + v_y^2\right)dA \tag{63}$$

The time-averaged kinetic energy associated with velocity components can be calculated as half the velocity times the conjugate of itself

$$\langle k_e \rangle = \frac{1}{4}\rho\int_A \left(v_x.\tilde{v}_x + v_y.\tilde{v}_y\right)dA \tag{64}$$

The kinetic energy contains both symmetric and antisymmetric wave energies. Upon rearrangement, the time-averaged kinetic energy takes the form

$$\langle k_e \rangle = \sum_n \langle k_e^{S_n} \rangle + \sum_n \langle k_e^{A_n} \rangle \tag{65}$$

where $\langle k_e^{S_n} \rangle$ and $\langle k_e^{A_n} \rangle$ are the time-averaged kinetic energies for symmetric mode S_n and antisymmetric mode A_n. Upon multiplication and then integration over thickness, kinetic energy can be expressed in closed form as

$$\langle k_e^{S_n} \rangle = \frac{b}{4}\left[g_n^{S_n} B_n F(\omega)\right]^2 \left(\begin{array}{l}\rho\omega^2\int_{-d}^{d}\left\{\xi_{Sn}^2\cos^2\alpha_{Sn}y + R_{Sn}^2\beta_{Sn}^2\cos^2\beta_{Sn}y - 2R_{Sn}\beta_{Sn}\xi_{Sn}\cos\alpha_{Sn}y\cos\beta_{Sn}y\right\}dy \\ +\rho\omega^2\int_{-d}^{d}\left\{\alpha_{Sn}^2\sin^2\alpha_{Sn}y + R_{Sn}^2\xi_{Sn}^2\sin^2\beta_{Sn}y + 2R_{Sn}\xi_{Sn}\alpha_{Sn}\sin\alpha_{Sn}y\sin\beta_{Sn}y\right\}dy\end{array}\right) \tag{66}$$

$$\langle k_e^{A_n} \rangle = \frac{b}{4}\left[g_n^{A_n} A_n F(\omega)\right]^2 \left(\begin{array}{l}\rho\omega^2\int_{-d}^{d}\left\{\xi_{An}^2\sin^2\alpha_{An}y + R_{An}^2\beta_{An}^2\sin^2\beta_{An}y - 2R_{An}\beta_{An}\xi_{An}\sin\alpha_{An}y\sin\beta_{An}y\right\}dy \\ +\rho\omega^2\int_{-d}^{d}\left\{\alpha_{An}^2\cos^2\alpha_{An}y + R_{An}^2\xi_{An}^2\cos^2\beta_{An}y + 2R_{An}\xi_{An}\alpha_{An}\cos\alpha_{An}y\cos\beta_{An}y\right\}dy\end{array}\right) \tag{67}$$

Equations (66) and (67) can be further simplified as

$$\langle k_e^{S_n} \rangle = \frac{b}{4}\left[g_n^{S_n} B_n F(\omega)\right]^2 \rho\omega^2 \int_{-d}^{d}\left[(\xi_{Sn}\cos\alpha_{Sn}y - R_{Sn}\beta_{Sn}\cos\beta_{Sn}y)^2 + (\alpha_{Sn}\sin\alpha_{Sn}y + R_{Sn}\xi_{Sn}\sin\beta_{Sn}y)^2\right]dy \tag{68}$$

$$\langle k_e^{A_n} \rangle = \frac{b}{4}\left[g_n^{A_n} A_n F(\omega)\right]^2 \rho\omega^2 \int_{-d}^{d}\left[(\xi_{An}\sin\alpha_{An}y - R_{An}\beta_{An}\sin\beta_{An}y)^2 + (\alpha_{An}\cos\alpha_{An}y + R_{An}\xi_{An}\cos\beta_{An}y)^2\right]dy \tag{69}$$

Potential energy of the wave can be evaluated by the double inner (double dots) product between stress and strain

$$v_e(x,t) = \frac{1}{2}\int_A \mathbf{T} : \mathbf{S}\ dA \tag{70}$$

$$v_e(x,t) = \frac{1}{2}\int_A \begin{pmatrix} T_{xx} & T_{xy} & T_{xz} \\ T_{yx} & T_{yy} & T_{yz} \\ T_{zx} & T_{zy} & T_{zz} \end{pmatrix} : \begin{pmatrix} S_{xx} & S_{xy} & S_{xz} \\ S_{yx} & S_{yy} & S_{yz} \\ S_{zx} & S_{zy} & S_{zz} \end{pmatrix} dA \tag{71}$$

T_{zz} and S_{zz} are ignored due to the *z-invariant* assumption. Also, $T_{yx} = T_{xy}$, $T_{zx} = T_{xz}$, and $T_{zy} = T_{yz}$ due to symmetry of both stress and strain tensors; equation (71) yields

$$v_e(x,t) = \frac{1}{2}\int_A \left(T_{xx}S_{xx} + T_{yy}S_{yy} + 2T_{xy}S_{xy} + 2T_{xz}S_{xz} + 2T_{yz}S_{yz}\right)dA \tag{72}$$

Stresses and strains associated with Lamb waves are T_{xx}, T_{xy}, and T_{yy} and S_{xx}, S_{xy}, and S_{yy}, respectively, and then Lamb wave potential energy reduces to

$$v_e(x,t) = \frac{1}{2}\int_A \left(T_{xx}S_{xx} + T_{yy}S_{yy} + 2T_{xy}S_{xy}\right)dA \tag{73}$$

The time-averaged potential energy is

$$\langle v_e\rangle = \frac{1}{4}\int_A \left\{(\lambda + 2\mu)S_{xx}\tilde{S}_{xx} + 2\lambda S_{yy}\tilde{S}_{xx} + (\lambda + 2\mu)S_{yy}\tilde{S}_{yy} + 2\left(2\mu S_{xy}\right)\tilde{S}_{xy}\right\}dA \tag{74}$$

Similar to the kinetic energy, the time-averaged potential energy is the summation of the potential energy of all modes, that is

$$\langle v_e\rangle = \sum_n \left\langle v_e^{S_n}\right\rangle + \sum_n \left\langle v_e^{A_n}\right\rangle \tag{75}$$

where $\left\langle v_e^{S_n}\right\rangle$ and $\left\langle v_e^{A_n}\right\rangle$ are the time-averaged potential energies for symmetric mode S_n and antisymmetric mode A_n, respectively, that is

$$\left\langle v_e^{S_n}\right\rangle = \frac{b}{4}\left[g_n^{S_n}B_nF_0(\omega)\right]^2 \left(\begin{array}{l} (\lambda + 2\mu)\xi_{Sn}^2\int_{-d}^{d}(\xi_{Sn}\cos\alpha_{Sn}y - R_{Sn}\beta_{Sn}\cos\beta_{Sn}y)^2dy + \\ (2\lambda)\int_{-d}^{d}\left\{\begin{array}{l}\xi_{Sn}^2\alpha_{Sn}^2\cos^2\alpha_{Sn}y - R_{Sn}^2\beta_{Sn}^2\xi_{Sn}^2\cos^2\beta_{Sn}y + \\ R_{Sn}\beta_{Sn}\xi_{Sn}(\xi_{Sn}^2 - \alpha_{Sn}^2)\cos\alpha_{Sn}y\cos\beta_{Sn}y\end{array}\right\}dy + \\ (\lambda + 2\mu)\int_{-d}^{d}\left(\alpha_{Sn}^2\cos\alpha_{Sn}y + R_{Sn}\beta_{Sn}\xi_{Sn}\cos\beta_{Sn}y\right)^2dy + \\ \mu\int_{-d}^{d}\left(2\xi_{Sn}\alpha_{Sn}\sin\alpha_{Sn}y + R_{Sn}\left(\xi_{Sn}^2 - \beta_{Sn}^2\right)\sin\beta_{Sn}y\right)^2dy \end{array}\right) \tag{76}$$

$$\left\langle v_e^{A_n}\right\rangle = \frac{b}{4}\left[g_n^{A_n}A_nF_0(\omega)\right]^2 \left(\begin{array}{l} (\lambda + 2\mu)\xi_{An}^2\int_{-d}^{d}(\xi_{An}\sin\alpha_{An}y - R_{An}\beta_{An}\sin\beta_{An}y)^2dy + \\ (2\lambda)\int_{-d}^{d}\left\{\begin{array}{l}\xi_{An}^2\alpha_{An}^2\sin^2\alpha_{An}y - R_{An}^2\beta_{An}^2\xi_{An}^2\sin^2\beta_{An}y + \\ R_{An}\beta_{An}\xi_{An}(\xi_{An}^2 - \alpha_{An}^2)\sin\alpha_{An}y\sin\beta_{An}y\end{array}\right\}dy + \\ (\lambda + 2\mu)\int_{-d}^{d}\left(\alpha_{An}^2\sin\alpha_{An}y + R_{An}\beta_{An}\xi_{An}\sin\beta_{An}y\right)^2dy + \\ \mu\int_{-d}^{d}\left(2\xi_{An}\alpha_{An}\cos\alpha_{An}y + R_{An}\left(\xi_{An}^2 - \beta_{An}^2\right)\cos\beta_{An}y\right)^2dy \end{array}\right) \tag{77}$$

The total energy for Lamb waves per unit length is summation of the kinetic and potential energies. The total time-averaged Lamb wave energy at the plate cross-section corresponding to the PWAS end is

$$\langle e_e\rangle = \langle k_e\rangle + \langle v_e\rangle \tag{78}$$

Simulation results

This section gives results of the simulation of power and energy transduction between PWAS and structure using the exact Lamb wave model. Comparison is performed between the exact Lamb wave model results presented here and the simplified axial and flexural wave model results of Lin and Giurgiutiu (2012). This is followed by a parametric study to show how wave power and energy change with different PWAS size and excitation frequency. The last part of this section will show the applicability of our model for the case of multimodal Lamb waves, which happen either at higher frequency or in thicker structures. We exemplify with simulation of two plates: (1) 1-mm-thick aluminum plate up to 2000 kHz and (2) 12.7-mm-thick steel plate (½ in) up to 500 kHz frequency. Figure 9(a) and (b) shows dispersion curves for the two plates. Figure 9(a) also shows how the simplified axial and flexural waves are compared with S_0 and A_0 Lamb waves at low frequencies.

For 1-mm-thick aluminum plate, harmonic excitation of 10 V is applied on a 7 mm PWAS with frequency sweep from 1 to 2000 kHz such that only S_0 and A_0 Lamb waves exist. However, the 12.7-mm-thick steel plate (Figure 9(b)) is excited up to 500 kHz, such that three symmetric modes (S_0, S_1, S_2) and three antisymmetric modes (A_0, A_1, A_2) exist. Complete simulation parameters are given in Tables 1 and 2.

Thin plate structure (one symmetric and one antisymmetric mode)

The simulation results for the 1-mm-thick aluminum structure are given in Figure 10. As expected, the reactive electrical power required for PWAS excitation is orders of magnitude larger than the active electrical power. Hence, the power rating of the PWAS transmitter is dominated by the reactive power, that is, by the capacitive behavior of the PWAS. We note that the transmitter reactive power is directly proportional to the transmitter admittance ($Y = i\omega C$), whereas the transmitter active power is the power converted into the ultrasonic acoustic waves generated into the structure from the transmitter. A remarkable variation of active power with frequency is shown in Figure 10(a): we notice that the active power (i.e. the power converted into the ultrasonic waves) is not monotonic with frequency but manifests peaks and valleys. As a result, the ratio between the reactive and active powers is not constant but presents the peaks and valleys. The increase and decrease of active power with frequency correspond

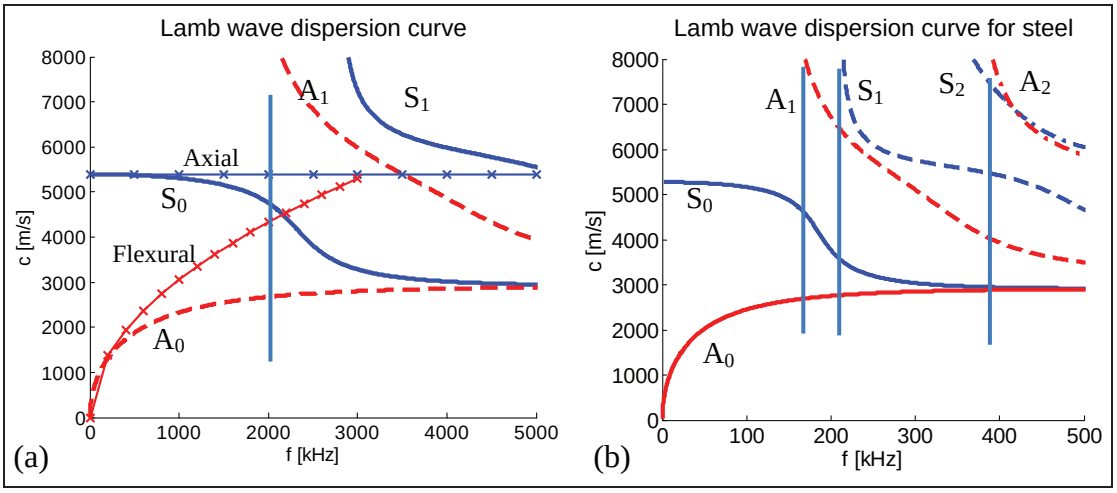

Figure 9. Dispersion curves: (a) 1-mm-thick aluminum plate and (b) 12.7-mm-thick steel plate (½ in).

Table 1. Structure simulation parameters.

	Symbol	2024 Al alloy	AISI 4340 steel
Length	L	∞	∞
Thickness	h	1 mm	12.7 mm (½ in)
Width	b	7 mm	7 mm
Young's modulus	E	72.4 GPa	200 GPa
Poisson ratio	ν	0.33	0.29
Density	ρ	2780	7850
Harmonic input voltage amplitude	$\hat{V}$	10 V	10 V
Frequency	F	Sweep: 1–2000 kHz	1–500 kHz

Table 2. Transmitter PWAS (PZT850) properties (as from the company website www.americanpiezo.com).

	Symbol	PZT850
Length	l	5–25 mm
Thickness	t_a	0.2 mm
Width	b	7 mm
Young's modulus	E	63 GPa
Elastic compliance	s_{11}^E	15.8e–12 m^2/N
Relative dielectric constant	$\varepsilon_{33}^T/\varepsilon_0$	1750
Coupling coefficient	k_{31}	0.353
Piezoelectric coefficient	d_{31}	−175e–12 m/V

PWAS: piezoelectric wafer active sensor.

to the PWAS tuning in and out of various ultrasonic waves traveling into the structure. The maximum active power seems to be ~8 mW at 340 kHz. At ~1460 kHz, PWAS is not transmitting any power; hence, no power was delivered into wave power at this frequency. This is because of tuned rejection Lamb waves at this particular frequency for both S_0 and A_0. Figure 5(a) and (b) shows that v_x and v_y vanish for both S_0 and A_0 at ~1460 kHz. Since the electrical active power is equally divided into forward and backward waves, the Lamb wave power plot of Figure 10(c) is the half of the electrical active power plot of Figure 10(a). Figure 10(d) shows the simulation results for Lamb wave kinetic energies (equations (68) and (69)) and potential energies (equations (76) and (77)).

Comparison with low-frequency (axial and flexural) approximation

Figure 9(a) shows that axial wave can be approximated to S_0 mode up to ~700 kHz for this particular case of excited 1-mm-thick aluminum plate. Flexural wave can approximate to A_0 for up to ~100 kHz. The axial and flexural models of Lin and Giurgiutiu (2012) compared with our exact Lamb wave model show good agreement at relatively low-frequency excitation (Figure 11). At higher frequencies, that is, beyond 700 kHz for S_0 and 100 kHz for A_0, the differences between exact and approximate models are very significant.

Parametric study

Figure 12 presents the results of a parametric study for various PWAS sizes (5–25 mm) and frequencies (1–1000 kHz). The resulting parametric plots are presented

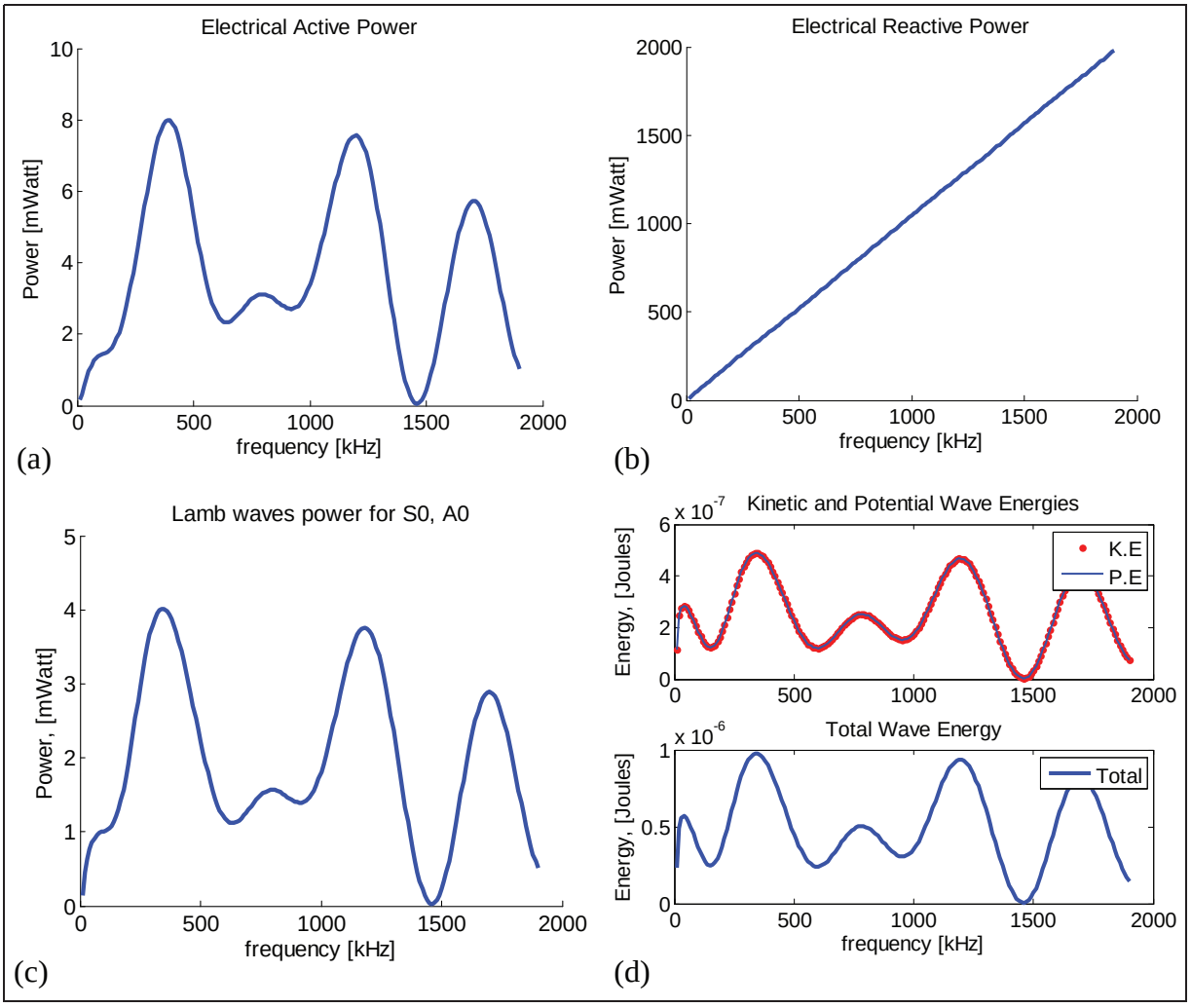

Figure 10. Simulation results for 1-mm-thick aluminum plate: (a) electrical active power, (b) electrical reactive power, (c) Lamb wave power, and (d) Lamb wave kinetic and potential energies.

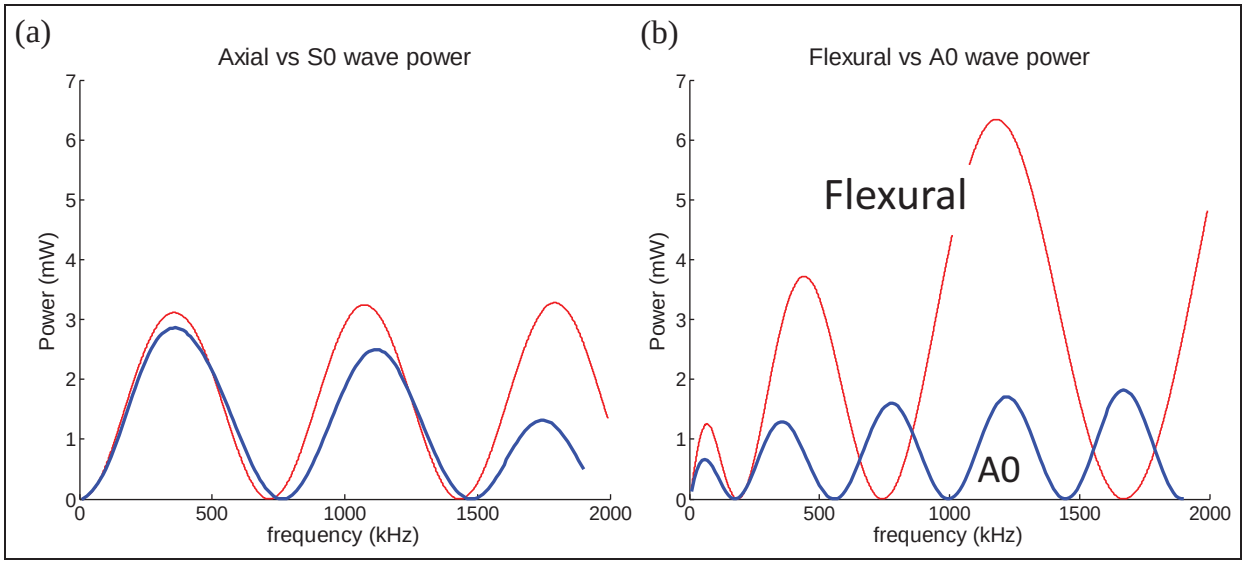

Figure 11. Comparison between (a) axial and S0 wave powers, (b) flexural and A0 wave powers.

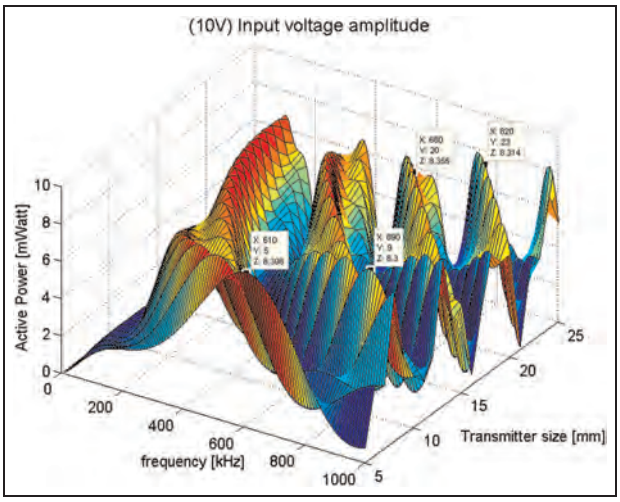

Figure 12. Parametric study for active power for 1 mm aluminum simulation.

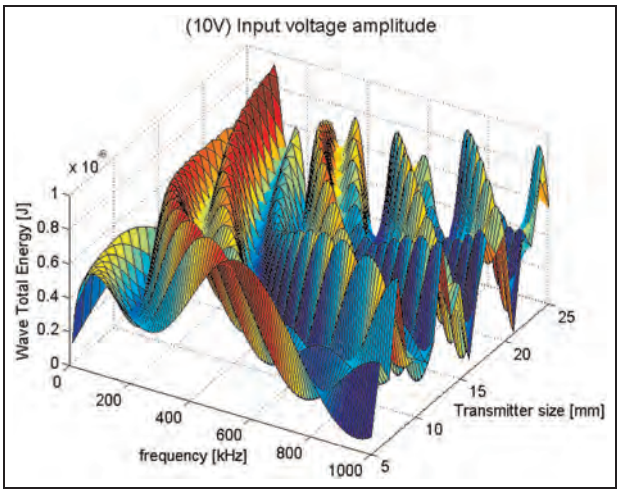

Figure 13. Parametric study for total Lamb wave energy for 1 mm aluminum simulation.

as three-dimensional (3D) mesh plots. It indicates that active power generated from the PWAS to the structure contains the tuning effect of transmitter size and excitation frequency. A larger PWAS does not necessarily produce more wave power at a given frequency. The maximum active power in the simulation is ~8.3 mW. This can be achieved by different combinations of PWAS and excitation frequencies (e.g. 5 mm PWAS size and 610 kHz, 9 mm PWAS and 890 kHz, 20 mm PWAS and 680 kHz, or 23 mm PWAS and 820 kHz). These combinations provide guidelines for the design of transmitter size and excitation frequency in order to obtain maximum wave power into the SHM structure. Similarly, the total Lamb wave energy shows the same tuning trend in relation of PWAS sizes and excitation frequency as shown in Figure 13.

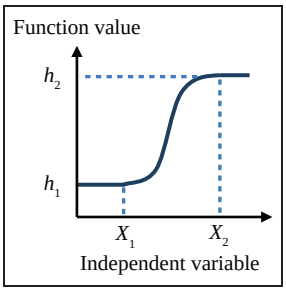

Figure 14. ADAMS step function.

Thick plate structure (multimode Lamb waves)

Multimodal Lamb wave simulation was performed on a 12.7-mm-thick steel plate for up to 500 kHz excitation frequency and 10 V harmonic voltage applied to PWAS. All structural simulation parameters are listed in Table 1 and PWAS parameters are listed in Table 2.

The objective is to evaluate electrical active power and reactive power and show how the active power part is converted to Lamb wave power in the presence of multimodal Lamb waves. Dispersion curve plots in Figure 9(b) show that S_1 mode starts at ~215 kHz and S_2 starts at ~370 kHz, while A_1 starts at ~170 kHz and A_2 starts at 390 kHz. Due to sudden appearance of Lamb wave modes at *cutoff frequencies*, the NME solution encounters sudden jumps due to sudden appearance of new components due to the new modes. For that reason, a smoothing function is applied as described in the next section.

Smoothing function. The smoothing function is a smoothed step function (Sohoni, 1995) as shown in Figure 14. Mathematical formula is

$$f(x) = \begin{cases} h_1 & x < X_1 \\ f(x, X_1, h_1, X_2, h_2) & X_1 \leqslant x \leqslant X_2 \\ h_2 & x > X_2 \end{cases} \quad (79)$$

$$f(x) = h_1 + \left[\frac{\Delta h}{\Delta x}\right](x - X_1) - \left[\frac{\Delta h}{2\pi}\right] \sin\left\{\left(\frac{2\pi}{\Delta x}\right)(x - X_1)\right\} \quad (80)$$

This is implemented in our *NME* solution by setting X_1 to the cutoff frequency of selected mode and h_1 to 0; hence, the mode is forced to start from 0, and consequently, its contribution to the NME summation is smoothed $\Delta h = 1$; Δx is arbitrary; we selected $\Delta x = 150$ kHz for symmetric modes and $\Delta x = 120$ kHz for antisymmetric modes. NME for velocity fields after applying smoothing are shown in Figure 15.

For the sake of clarity, it needs to be mentioned that the plots in Figure 15 are the absolute values of *NME* velocities after applying normalized amplitudes as well as modal participation factors. Note that the summation value in some areas is less than the individual

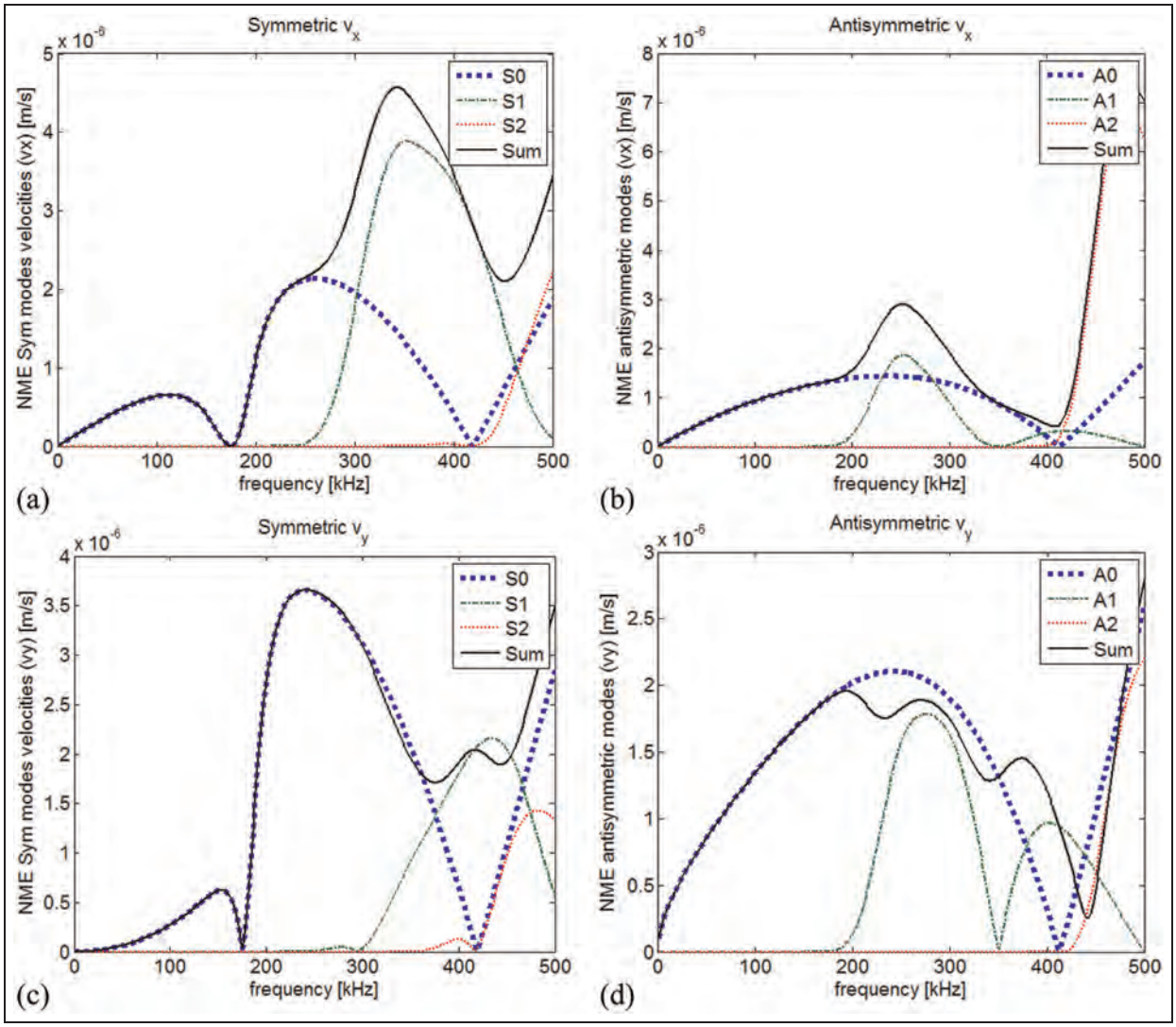

Figure 15. NME for particle velocity fields for 12.7-mm-thick steel plate with three symmetric modes and three antisymmetric modes (smoothed): (a) particle velocities in x-direction of symmetric modes, (b) x-direction of antisymmetric modes, (c) y-direction of symmetric modes, and (d) y-direction of symmetric modes.
NME: normal mode expansion.

values because the individual values are plotted as absolute values, whereas the summation is done algebraically, which allows for some cancelations. Complex values of *NME* velocities are due to phase differences. Figure 16 shows the summary of the velocity fields; it displays the summation for the three symmetric modes as well as antisymmetric modes.

Figure 17 shows the reactive and active electrical power the PWAS utilizes to excite desired Lamb wave modes. It can be seen from Figure 17 that the reactive power is three orders of magnitude larger than the active power (active power is the power that is further converted to propagating wave power). The maximum active power attained in this simulation is ~0.9 mW at 500 kHz; however, if the simulation is evaluated for larger frequency sweep, active power experiences higher maximum, but careful consideration is needed as the fourth symmetric and antisymmetric modes will come into account.

Multimodal Lamb wave simulations for power are shown in Figure 18. It can be seen that maximum value for Lamb wave power is ~0.45 mW at 500 kHz, and the plot in Figure 18(a) is identical to the half of active electrical power of Figure 17(a).

Summary and conclusion

The ability to excite certain Lamb wave modes is important in SHM as different defects respond differently to various Lamb wave modes. Detection of through-thickness cracks with pulse–echo method is much better with S_0 mode than A_0 mode. While antisymmetric modes are better for detection delaminations, it disbonds with pitch–catch techniques. Different

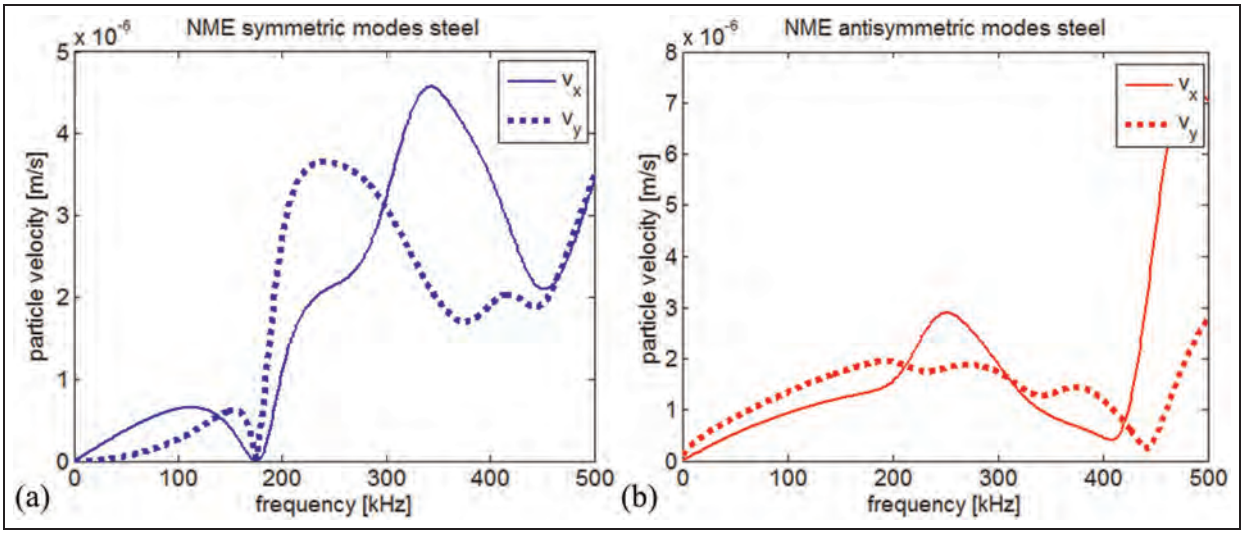

Figure 16. Summation of normal mode expanded velocities in *x*- and *y*-directions with applied modal participation factors for (a) symmetric and (b) antisymmetric modes.
NME: normal mode expansion.

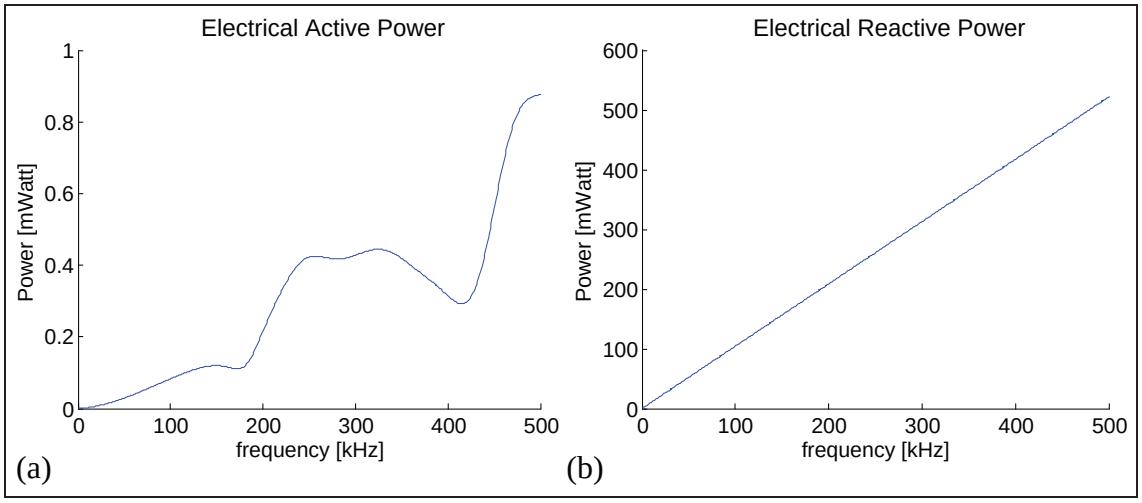

Figure 17. Simulation results for 12.7-mm-thick steel plate: (a) electrical active power and (b) electrical reactive power.

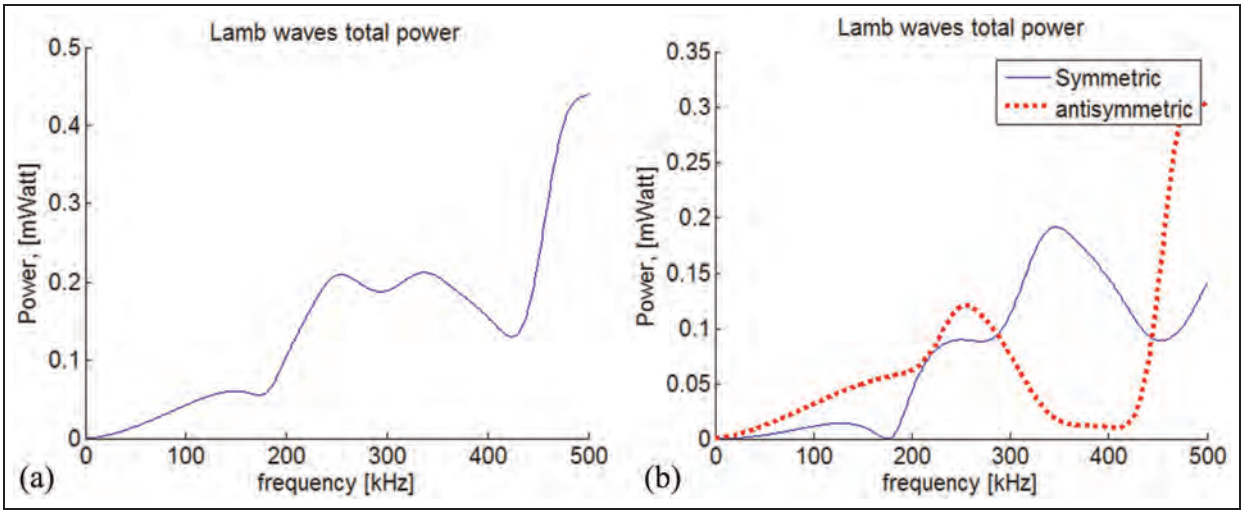

Figure 18. (a) Lamb wave power and (b) Lamb wave power separated as symmetric modes and antisymmetric modes.

researches studied scattering of wave energy at defects, for example, cracks; hence, it became important to develop an analytical model for multimodal Lamb wave power and wave energy. This study has analyzed the power and energy transformation from electrical to mechanical for PWAS bonded to host structures. The analysis started by reviewing of literature to show the motivation of modeling power and energy for Lamb waves for SHM applications. This was followed by the basics of Rayleigh–Lamb equation and the solution of Lamb wave symmetric and antisymmetric fields, that is, displacement strains and velocities. Power flow analysis is based on complex reciprocity and orthogonality of Lamb wave modes, and through normalization of power flow, Lamb wave displacement amplitudes were determined. The analysis for multimodal waves was based on *NME* technique, which was used to determine modal participation factors, that is, how much each mode contributes to the final power.

In order to calculate the transmitter electrical power and energy, we calculated the input electrical power by using input admittance of the PWAS when attached to the structure. Because of the electromechanical coupling, the impedance is strongly influenced by the dynamic behavior of the substructure and is substantially different from the free-PWAS impedance. The active power is the power that is converted to the mechanical power at the interface. The reactive power is the imaginary part of complex power that is not consumed and is recirculated to the power supply. It was shown that the reactive electrical power required for PWAS excitation is two orders of magnitude larger than the active electrical power. Hence, the power rating of the PWAS transmitter is dominated by the reactive power, that is, by the capacitive behavior of the PWAS. A remarkable variation of active power with frequency was noticed. The active power (i.e. the power converted into the ultrasonic waves) is not monotonic with frequency but manifests peaks and valleys. As a result, the increase and decrease of active power with frequency correspond to the PWAS tuning in and out of various ultrasonic waves traveling into the structure. For instance, for single symmetric and single antisymmetric excitation simulation example, there was a particular frequency at which almost there was no energy transfer for waves to propagate. Electrical active power is further divided and converted to forward propagating wave power and backward one, and our simulations were performed for only forward wave and showed that wave power was the half of electrical active power.

The developed model for Lamb wave case was compared with axial and flexural waves, which approximate Lamb waves at relatively low frequencies, and the two simulations showed good agreement. This was followed by a parametric study to optimize the transducer size with excitation frequency to guarantee maximum energy transfer between source and examined structure. In this study, it was showed that the maximum wave power can be achieved with different combinations of PWAS size and excitation frequencies. Multimodal wave simulations were presented, and this is a practical case for most on-site thick structures at which not only S_0 and A_0 modes exist when excited by PWAS. Simulations have been done for thick steel plate. The results for electrical active/reactive power and Lamb wave power are presented. This study provided a closed-form analytical model for Lamb wave power as well as kinetic and potential energies.

Future work is to validate this model through experimental study and to use the power flow normalization in finding the normalized amplitudes that best fit experimental data.

Declaration of conflicting interests

Any opinions, findings, and conclusions or recommendations expressed in this material are those of the authors and do not necessarily reflect the views of the National Science Foundation, Office of Naval Research, and Air Force Office of Scientific Research.

Funding

This material is based upon the work supported by the National Science Foundation under grant no. CMS-0925466, Office of Naval Research under grant no. # N00014-11-1-0271 (Dr Ignacio Perez, Program Manager), and Air Force Office of Scientific Research under grant no. #FA9550-11-1-0133 (Dr David Stargel, Program Manager).

References

Alleyne D and Cawley P (1992) The interaction of Lamb waves with defects. *IEEE Transactions on Ultrasonics Ferroelectrics and Frequency Control* 39(3): 381–396.

Auld B (1990) *Acoustic Fields and Waves in Solids*. John Wiley & Sons, New York, USA.

Chinthalapudi A and Hassan H (2005) *Investigation of methods to detect defects in thin layered materials*. Master's Thesis, Blekinge Institute of Technology, Karlskrona, Sweden.

Giurgiutiu V (2008) *Structural Health Monitoring with Piezoelectric Wafer Active Sensors*. Elsevier Academic Press, Amsterdam.

Giurgiutiu V (2010) Predictive simulation of piezoelectric wafer active sensors for structural health monitoring. In: *APWSHM 2010: 3rd Asia Pacific workshop on structural health monitoring*, Tokyo, Japan, 30 November–2 December 2010.

Graff K (1991) *Wave Motion in Elastic Solids*. Dover Publications Inc. New York, USA.

Koh Y, Chiu W and Rajic N (2002) Effects of local stiffness changes and delamination on Lamb wave transmission using surface-mounted piezoelectric transducers. *Composite Structures* 57: 437–443.

Kural A, Pullin R, Featherston C, et al. (2011) Wireless power transmission using ultrasonic guided waves. *Journal of Physics: Conference Series* 305: 012088 (1–11).

Lin B and Giurgiutiu V (2012) Power and energy transduction analysis of y active sensors for structural health monitoring. *Structural Health Monitoring: An International Journal* 11(1): 109–121.

Lin B, Giurgiutiu V and Kamal A (2012) The use of exact Lamb waves modes for modeling the power and energy transduction of structurally bonded piezoelectric wafer active sensors. In: Proceedings of SPIE: non destructive evaluation, San Diego, CA, 11–15 March 2012, vol. 8345, paper no. 8345-0A (1-12).

Park G, Rosing T, Todd M, et al. (2007) Energy harvesting for structural health monitoring sensor networks, Los Alamos National Laboratory Report LA 14314-MS, February 2007, Los Alamos National Laboratory.

Rose J (1999) *Ultrasonic Waves in Solid Media*. New York: Cambridge University Press.

Santoni G (2010) Fundamental studies in the Lamb-wave interaction between piezoelectric wafer active sensor and host structure during structural health monitoring. Campus access Dissertation, paper #256, University of South Carolina, Columbia, SC.

Sohoni VN (1995) A new smooth step function for ADAMS. Available at: http://webcache.googleusercontent.com/search?q=cache:fZ-a–O62ksJ:web.mscsoftware.com/support/library/conf/adams/na/1995/UC950030.PDF+&cd=1&hl=en&ct=clnk&gl=us

Viktorov I (1967) *Rayleigh and Lamb Waves—Physical Theory and Applications*. New York: Plenum Press.

Wilcox P, Lowe M and Cawley P (2001) Mode and transducer selection for long range Lamb wave inspection. *Journal of Intelligent Material Systems and Structures* 12: 553–565.

Appendix I

Notation

a	half-length of the piezoelectric wafer transducer, m
$a_n(x)$	modal participation factor
A_n	amplitude of nth antisymmetric mode
A_0, A_1, A_2	antisymmetric Lamb wave modes
b	width, m
B_n	amplitude of nth symmetric mode
c	wave speed, m/s
c_p	pressure (longitudinal) wave speed, m/s
c_s	shear (transverse) wave speed, m/s
C	mode contribution factor
C_0	capacitance, F
d	plate half thickness, m
d_{31}	piezoelectric coupling coefficient in 31, m/V
$\langle e_e \rangle$	time-averaged total Lamb wave energy
E	Young's modulus, GPa
f	frequency, Hz
$\mathbf{F}$	force vector
$F_0(\omega)$	pin-force at PWAS ends
g_n	coefficient to simplify modal participation factor
h	plate thickness $= 2d$, m
i	$\sqrt{-1}$
I	electric current, A
Im	imaginary part of a complex quantity
k_e	kinetic energy
$\langle k_e \rangle$	time-averaged kinetic energy
k_{PWAS}	PWAS stiffness, N/m
k_{str}	dynamic stiffness, N/m
k_{31}	electromechanical cross-coupling coefficient
l, l_a	PWAS length $= 2a$
p	power, W
$\langle p \rangle$	time-averaged power
P_{mn}	power factor (measure of average power flow)
$r(\omega)$	dynamic stiffness ratio
R	eigen coefficients
Re	real part of a complex quantity
s_{11}^E	mechanical compliance under constant electric field, m^2/N
S_{ij}	mechanical strains
S_0, S_1, S_2	symmetric Lamb wave modes
t	time, s
t_a	PWAS thickness, m
$t_x(x)$	traction in x-direction
T_{ij}	stress in tensor notation
T	period time, s
$\mathbf{T_n}$	stress tensor for nth guided wave mode, Pa
u	displacement, m
u_{ISA}	induced strain actuation PWAS displacement
U	displacement amplitudes (also orthogonal modes), m
v	velocity
$\mathbf{v}$	velocity vector
v_e	potential energy
$\langle v_e \rangle$	time-averaged potential energy
V	voltage
W	parameter to simplify normalized mode formula, m^{-2}
x, y, z	global coordinates, m
x_1, x_2, x_3	material polarization directions
Y	admittance, S
$\lvert Y \rvert$	absolute of admittance
Y_I	imaginary part of admittance
Y_R	real part of admittance
α, β	wave numbers, m^{-1}
δ	Kronecker delta
ε_{jk}^T	dielectric permittivity measured at zero mechanical stress, $T = 0$
λ	Lame constant, Pa
μ	shear modulus of the material (equivalent to the engineering constant G), Pa
ν	Poisson ratio

ξ	wave numbers, m^{-1}
ρ	material density, kg/m^3
τ, τ_a	shear stress at PWAS tip $x = a$
ϕ	Lamb wave longitudinal potential function
$\phi(\omega)$	dynamic
ψ	Lamb wave shear potential function
ω	angular frequency, rad/s
Ω	domain

Subscripts

A	antisymmetric modes
i, j	indices = 1, 2, 3
m, n	different normal modes
n	nth guided wave mode
S	symmetric modes
x, y, z	global coordinates, m
1	solution due to source excitation
2	solution due to homogeneous solution (free mode shapes)

Superscripts

$\tilde{a}$	conjugate of a
$\hat{a}$	amplitude of a
A	antisymmetric modes
m, n	different normal modes
S	symmetric modes
1	solution due to source excitation
2	solution due to homogeneous solution (free mode shapes)

Key Engineering Materials Vol. 558 (2013) pp 116-127
© (2013) Trans Tech Publications, Switzerland
doi:10.4028/www.scientific.net/KEM.558.116

Time-Domain Hybrid Global-Local Prediction of Guided Waves Interaction with Damage

Matthieu Gresil[1, a] and Victor Giurgiutiu[1, b]

[1]University of South Carolina, 300 Main Street, Columbia, SC 29208, USA

[a]matthieu@engr.sc.edu (corresponding author)

[b]victorg@.sc.edu

Keywords: Guided wave, finite element method, structural health monitoring, piezoelectric wafer active sensor, hybrid global-local.

Abstract. This paper presents a hybrid finite element and analytical method to predict the 1-D guided wave propagation interaction with damage for nondestructive evaluation (NDE) and structural health monitoring (SHM) application. The finite element mesh is used to describe the region around the damage (defects or flaws). In contrast to other hybrid models developed elsewhere, the interaction between Lamb waves and defects is computed in the time domain using the explicit solver of the commercial finite element method (FEM) software ABAQUS. Analytical methods can perform efficient modeling of wave propagation but are limited to simple geometries. Realistic structures with complicated geometries are usually modeled with the FEM. However, to obtain an accurate wave propagation solution at ultrasonic frequencies is computationally intensive and may become prohibitive for realistic structures. In response to today's complex cases not covered by the simulation tools available, we aim to develop an efficient and accessible tool for SHM applications. This tool will be based on a hybrid coupling between analytical solutions and time domain numerical codes. Lamb wave interaction with a notch is investigated by using this method, and the results obtained are with respect to transmission, reflection and mode conversion. Because of the symmetric mode shape, S0 is more sensitive to the shallow notch than A0. By making use of the fact that the reflection increases with increase in notch depth and mode conversion are maximized when the notch is around half through the thickness of the plate, the reflection and conversion coefficients can be used to characterize the depth of the notch.

Introduction

Many authors have already investigated the interaction of Lamb waves with a single defect like crack, notch, or circular cavity. Some of them used analytical [1] or semi-analytical [2] solutions, whereas others chose a finite element, a boundary element, or spectral element method [3-10]. Analytical or semi-analytical solutions can be used when the geometry of the defect is regular and when the problem presents symmetries. Finite or boundary element modeling (FEM/BEM) allows studying the interaction of Lamb modes with irregular defects but require respecting spatial and temporal discretization norms which can cause computational problems at high frequency-thickness product values. In addition, to obtain accurate wave propagation FEM/BEM solution at ultrasonic frequencies is computationally intensive and may become prohibitive for realistic structures.

A hybrid formulation can be used wherein the finite element method is employed to model small regions near the defect whereas regions away from the defect are modeled using a suitable set of analytical wave functions. Goetschel et al. [11] developed a global-local finite element formulation for modeling axisymmetric scattering of a steady, compressive, incident elastic wave in a homogeneous, isotropic host medium with an axisymmetric inclusion. The method was later applied to model wave interaction with defected lap-shear joints [12], as well as notches in plates [13].

Many structural components are complex in either their geometry or their material properties. In this case, theoretical wave solutions for the global portion are either nonexistent or hard to determine. The Semi Analytical Finite Element (SAFE) method can help handle these cases because of its ability to extract modal solutions of complex structures in a computationally efficient manner

All rights reserved. No part of contents of this paper may be reproduced or transmitted in any form or by any means without the written permission of TTP, www.ttp.net. (ID: 129.252.23.155-22/05/13,15:09:14)

[14-17]. Sabra et al. [18] demonstrated the application of the SAFE-aided hybrid formulation to the detection of holes in aluminum plates. Srivastava [19] extends the global-local approach to model notches in aluminum plates and delamination-like defects in composite panels.
In contrast to the above hybrid formulations, this paper calculates the interaction between Lamb waves and defects in the time domain. This approach is implemented in three steps using propriatary analytical software (WaveFormRevealer) and commercial FEM software. The first step of this method uses the WaveFormRevealer software developed for this application. The second step uses the output from the WaveFormRevealer software as inputs into the FEM model. The third step of our method uses again the WaveFormRevealer software to transfer the output from the FEM local damage to the receiver transducer placed in the global region away from damage. The FEM output serves as input into the Global region. This hybrid global-local-global approach is compared with the analytical solution and experimental results.

Fundamental of Lamb waves

Guided waves (Lamb waves) travel at long distances in thin wall structures. Guided waves are typically transmitted and received using piezoelectric wafer active sensors (PWAS) [25], and are used to detect defects and damage in thin wall structures. Two types of guided waves propagate: symmetric waves and antisymmetric waves. Each of these wave types propagates with multiple modes.
By solving a boundary value problem for a free plate or by considering the reflection of waves at plate boundaries, the Rayleigh-Lamb frequency equations (dispersion equations) can be found [20-23]. For a uniform traction-free isotropic plate, the equation for symmetric modes is

$$\frac{\tan(qh)}{\tan(ph)} = -\frac{4k^2pq}{(q^2-k^2)^2} \tag{1}$$

For antisymmetric modes, we have

$$\frac{\tan(qh)}{\tan(ph)} = -\frac{(q^2-k^2)^2}{4k^2pq} \tag{2}$$

where

$$p^2 = \frac{\omega^2}{c_L^2} - k^2, \quad q^2 = \frac{\omega^2}{c_T^2} - k^2, \quad k = \frac{\omega}{c_p} \tag{3}$$

The notations $h, k, c_L, c_T, c_p, \omega$ signify the half plate thickness, wave number, velocities of longitudinal and transverse modes, phase velocity, wave circular frequency, respectively.
The phase velocity is found numerically by solving the roots of the dispersion equation as a function of material properties, frequency, and material thickness. Group velocity dispersion curves are found from the phase velocity [23].
Phase and group velocity dispersion curves for a 3.2 mm-thick aluminum plate are shown in Figure 1, where longitudinal and transverse velocities of the plate are equal to $c_L = 6211\text{m/s}$, and $c_T = 3129\text{m/s}$, respectively. These curves were generated and plotted using our propriatary software "Wavescope" [24]. Figure 1 shows the dispersion curves of the first two symmetric and antisymmetric modes. At low frequencies, the wave velocity of the first symmetric mode (S0) is nearly non-dispersive, while the wave velocity of the first antisymmetric mode (A0) is highly dispersive. At higher frequencies, group velocity of both A0 and S0 approaches the Rayleigh wave velocity, $c_R \approx 2900\text{m/s}$.

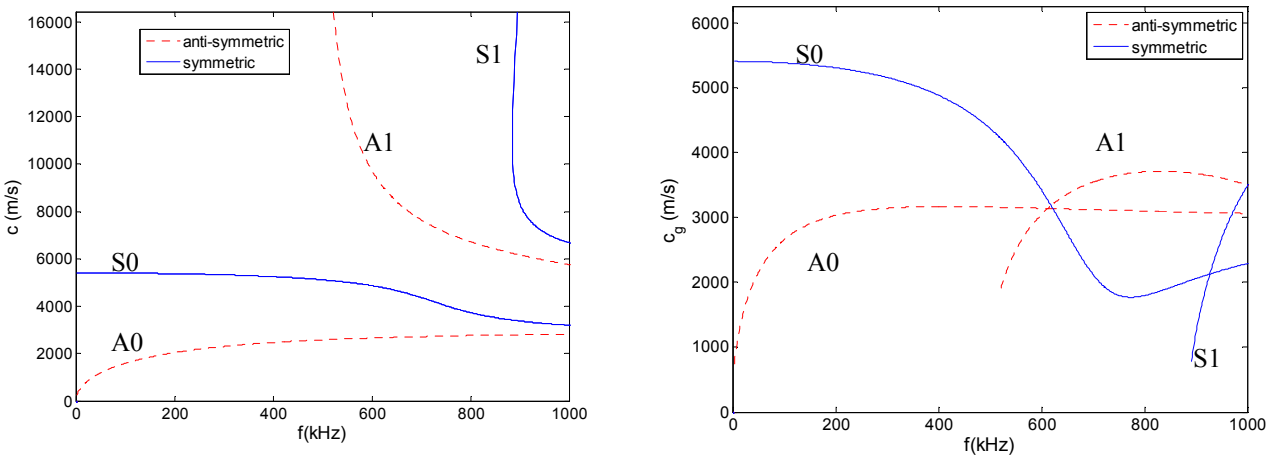

Figure 1: Dispersion curves for 3.2-mm thick aluminum plate: (a) phase velocity dispersion curves; (b) group velocity dispersion curves.

Analytical model for the global domain

PWAS transducers are the enabling technology for active and passive SHM systems [25]. PWAS couples the electrical and mechanical effects through the tensorial piezoelectric constitutive equations

$$S_{ij} = s^{E}_{ijkl} T_{kl} + d_{kij} E_k, \qquad D_j = d_{jkl} T_{kl} + \varepsilon^{T}_{jk} E_k \tag{4}$$

where, S_{ij} is the mechanical strain; T_{kl} is the mechanical stress; E_k is the electrical field; D_j is the electrical displacement; s^{E}_{ijkl} is the mechanical compliance of the material measured at zero electric field $E = 0$, ε^{T}_{jk} is the dielectric permittivity measures at zero mechanical stress $T = 0$, and d_{kij} represents the piezoelectric coupling effect. PWAS utilize the d_{31} coupling between in-plane strain and transverse electric field. A 7-mm diameter, 0.2mm thick, PWAS weights around 78 mg and costs around $1. PWAS transducers are lightweight and inexpensive and hence can be deployed in large numbers on the monitored structure.

PWAS transducers can serve several purposes [25]: (a) high-bandwidth strain sensors; (b) high-bandwidth wave exciters and receivers; (c) resonators; (d) embedded modal sensors with the electromechanical impedance spectroscopy method. By application types, PWAS transducers can be used for (i) active sensing of far field damage using pulse-echo, pitch-catch, and phased-array methods, (ii) active sensing of near field damage using the high frequency electro-mechanical impedance spectroscopy (EMIS) and thickness gage mode, and (iii) passive sensing of damage-generating events through detection of low-velocity impacts and acoustic emission at the tip of advancing cracks.

The analytical modeling of the pitch-catch process between two PWAS transducers separated by a distance x is carried out in frequency domain in four steps [26-28]:

- Fourier transform the time-domain excitation signal $V_e(t)$ into the frequency domain spectrum, $\tilde{V}_e(\omega)$;
- Calculate the frequency-domain structural transfer function at the receiver location, $G(x,\omega)$;
- Multiply the structural transfer function by frequency-domain excitation signal to obtain the frequency domain signal at the receiver, i.e., $\tilde{V}_r(x,\omega) = G(x,\omega) \cdot \tilde{V}_e(\omega)$;
- Perform inverse Fourier transform to obtain the time-domain receiver signal, $V_r(x,t) = IFFT\{\tilde{V}_r(x,\omega)\} = IFFT\{G(x,\omega) \cdot \tilde{V}_e(\omega)\}$.

In this paper, the main interest is in symmetric fundamental mode (S_0) and anti-symmetric fundamental mode (A_0). For Lamb waves with only two modes (A_0 and S_0) excited, the structure transfer function $G(\omega)$ is given by Eq. (99) of ref. [25], page 327, which gives the in-plane strain at the plate surface as

$$\begin{aligned}\varepsilon_x(x,t)\Big|_{y=d} = &-i\frac{a\tau_0}{\mu}(\sin k^S a)\frac{N_S(k^S)}{D_S'(k^S)}e^{-i(k^S x-\omega t)}\\ &-i\frac{a\tau_0}{\mu}(\sin k^A a)\frac{N_A(k^A)}{D_A'(k^A)}e^{-i(k^A x-\omega t)}\end{aligned} \tag{5}$$

$$G(\omega) = S(\omega)e^{-ik^S x} + A(\omega)e^{-ik^A x} \tag{6}$$

$$S(\omega) = -i\frac{a\tau_0}{\mu}(\sin k^S a)\frac{N_S(k^S)}{D_S'(k^S)}, \quad A(\omega) = -i\frac{a\tau_0}{\mu}(\sin k^A a)\frac{N_A(k^A)}{D_A'(k^A)} \tag{7}$$

$$\begin{aligned}D_S(\omega,d) &= \left(k^2-\beta^2\right)^2 \cos\alpha d\ \sin\beta d + 4k^2\alpha\beta\ \sin\alpha d\ \cos\beta d\\ D_A(\omega,d) &= \left(k^2-\beta^2\right)^2 \sin\alpha d\ \cos\beta d + 4k^2\alpha\beta\ \cos\alpha d\ \sin\beta d\end{aligned} \tag{8}$$

$$N_S = k\beta\left(k^2-\beta^2\right)\cos(\alpha d)\sin(\beta d), \quad N_A = k\beta\left(k^2-\beta^2\right)\sin(\alpha d)\cos(\beta d) \tag{9}$$

$$\alpha^2 = \frac{\omega^2}{c_p^2} - k^2, \quad \beta^2 = \frac{\omega^2}{c_s^2} - k^2 \tag{10}$$

where a is the half length of the PWAS, d is the half thickness of the plate, τ_0 is the shear stress between PWAS and the plate, μ is Lame's constant, k^S and k^A are the wavenumbers for S_0 and A_0 respectively, x denotes the distance between the two PWAS transducers, k represents the wavenumber for S_0 or A_0 accordingly, c_p and c_s are the wave speed for pressure wave and shear wave respectively. In the transfer function, it could be observed that $S(\omega)$ and $A(\omega)$ will determine the amplitude of S_0 and A_0 mode. In both $S(\omega)$ and $A(\omega)$ terms, there is $\sin(k^S a)$ and $\sin(k^A a)$, which represent the tuning effect.

The wave speed dispersion curve is obtained by solving Rayleigh-Lamb equations (1) and (2), which are transcendental equations that require numerical solution. The usual form of Rayleigh-Lamb equations (1) and (2) expressed as

$$D_S(\omega,d) = 0 \qquad \text{and} \qquad D_A(\omega,d) = 0 \tag{11}$$

After getting the wave speed dispersion curve, the wavenumber for each frequency component i.e. $\xi = \omega/c$ is known. Thus, all the terms involved in the plate transfer function could be solved, and the plate transfer function $G(\omega)$ is obtained. After the plate transfer function $G(\omega)$ is obtained, the excitation signal is Fourier transformed.

Software development for the global domain

The analytical model presented in the previous section was used to develop the software program 'WaveFormRevealer' utilizing the Matlab graphical user interface (GUI) environment to predict the waveform for the analytical modeling part of the HGL approach [26, 27]. The GUI of the software is shown in Figure 2.

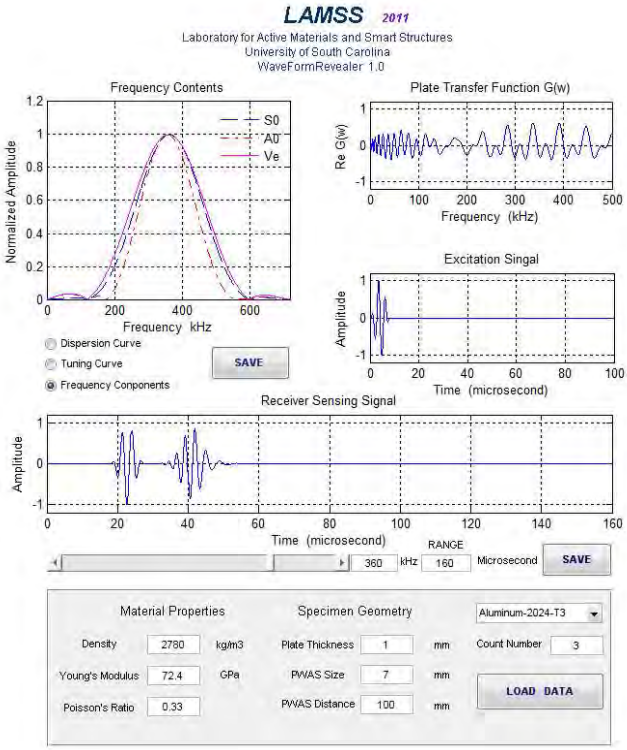

Figure 2: Interface of the analytical software „WaveFormRevealer 1.0" [27-29].

This software allows users to get the desired analytical signal prediction by inputting material properties, specimen geometry, excitation signal count number, excitation signal frequency, and time range. It can also show a continuous waveform change by clicking on the frequency control slider, which is just like the waveform shown on an oscilloscope when adjusting the excitation signal frequency. The signal range in time domain can be set by entering the 'Range' information.

Finite element model in the local region

The effectiveness of conventional finite element modeling of elastic waves propagating in structural components has been shown for the case of Lamb waves in free plates in [30, 31]. The FEM package used in the present study, ABAQUS/Explicit, uses an explicit time integration based on a central difference scheme [32]. The stability of the numerical solution is dependent upon the temporal and the spatial resolution of the analysis. The maximum frequency of the dynamic problem, $f_{\max}$, limits both the integration time step and the element size. To avoid numerical instability, ABAQUS/Explicit [32] recommends a stability limit for the integration time step of [31]

$$\Delta t = \frac{1}{20 f_{\max}} \tag{12}$$

The size of the finite element mesh, L_e, is typically derived from the smallest wavelength to be analyzed, $\lambda_{\min}$. For a good spatial resolution, 20 nodes per wavelength are advisable [31]. This condition can be written as

$$L_e = \frac{\lambda_{\min}}{20} \tag{13}$$

To generate the appropriate Lamb mode (S0 or A0), boundary conditions are imposed on the plate. To simulate the time profile of the excitation, a 3-cycle tone burst enclosed in a Hanning window centered on the excitation frequency is used. The plate length is defined to prevent reflections from the edges and is minimized to reduce the computing time.

Experimental set-up

A test specimen was designed to develop and calibrate the damage-detection methodology using a simple geometry specimen, and also to validate the analytical, and the hybrid global-local results. The aluminum plate specimen was constructed from 3.2-mm-thick 2024-alloy stock in the form of a square plate $(1118\,\text{mm}\times1118\,\text{mm}\times3.2\,\text{mm})$. The specimen was instrumented with arrays of 7-mm square and 7-mm circular PWAS (Figure 3). The (x, y) sensor locations are given in Table 1. An HP33120A arbitrary signal generator was used to generate a 150 kHz windowed harmonic-burst excitation to active sensors with a 10 Hz repetition rate. Under harmonic burst excitation, the transmitter PWAS generates a packet of elastic waves that spread out into the entire plate according to a circular wave front pattern. A Tektronix TDS210 four-channel digital oscilloscope, synchronized with the signal generator, was used to collect the response signals from the receiver PWAS transducers.

The results of the rectangular plate tests were remarkably clear and easy to interpret. Reflections wave packets could be easily separated because the edges of the rectangular plate were far away from the source.

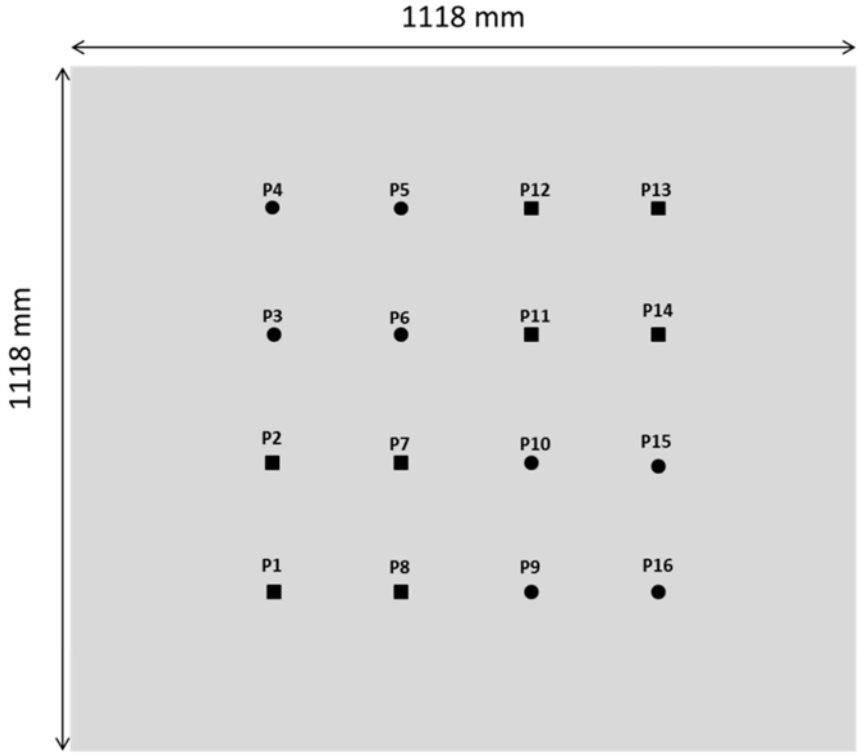

Figure 3: Arrangment of piezoelectric wafer active sensor (PWAS) transducers bonded on the plate specimen.

Table 1: Location of PWAS transducers on the square plate specimen.

PWAS#	1	2	3	4	5	6	7	8	9	10	11	12	13	14	15	16
x (mm)	31	31	31	31	51	51	51	51	71	71	71	71	91	91	91	91
y (mm)	31	51	71	91	91	71	51	31	31	51	71	91	91	71	51	31
Square	X	X					X	X			X	X	X	X		
Circular			X	X	X	X			X	X					X	X

Hybrid Global-Local Method

In response to today's most complex cases not covered by the simulation tools available, we aim to develop an efficient and accessible tool simulation for SHM application. This tool is based on a hybrid coupling between analytical solution and numerical codes. We couple global analytical calculation with local FEM analysis to utilize the advantages of both methods and obtain a rapid and accurate simulation method. Figure 4 illustrates this concept, whereby only the local material region close to the defect needs to be FEM modeled whereas the global waveguides to the left and right of the FEM region are modeled analytically with compatibility being ensured at the interface.

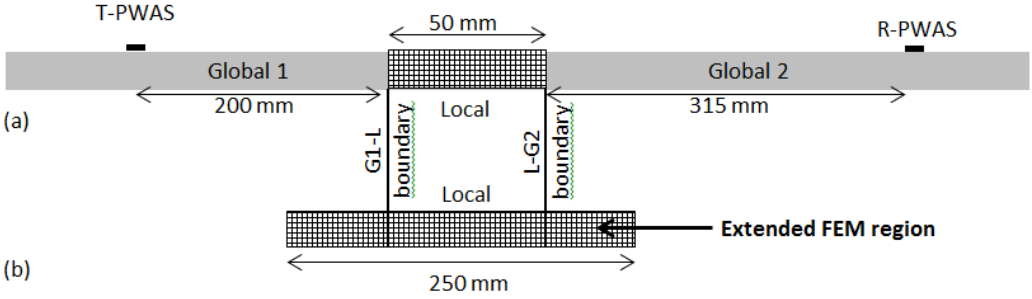

Figure 4: Waveguide problem in 1-D solved by the hybrid global-local (HGL) method in the time domain: (a) overall HGL set-up; (b) FEM discretization including extended regions for reflection a voidance.

The first step of this method consists in using the WaveFormRevealer software to predict analytically the wave propagation in the "Global" wave guide. The signal received after a path of 200 mm through global region corresponds to the output signal from the Global 1 region and serves as the input data for the local region modeled by FEM. This analysis takes place in the time domain. The second step consists in using the Global 1 output as two inputs (one for the S0 mode and the other for the A0 mode) in the FEM model. In order to avoid the reflections from the edges of the FEM domain, we extended the FEM domain outside the 100-mm local region to a total length of 250 mm (Figure 4). The received signal from the local FEM model is the new input data for the Global 2 analytical region.

The hybrid global-local-global signal is compared with the analytical model, and the experimental results, received at R-PWAS after a path length of 565 mm (Figure 5). A good agreement for the S0 wave packet is observed. For the A0 mode, a good agreement is also observed but a slight time shift exists at the end of the A0 wave packet. We can conclude that this time domain HGL approach is in good agreement with the experimental results and with the analytical model. The slight difference in the A0 packet can be explained by the fact that these models, analytical and HGL, are 1D guided waves which are not exactly representative of the experimental results, i.e. 2D guided waves.

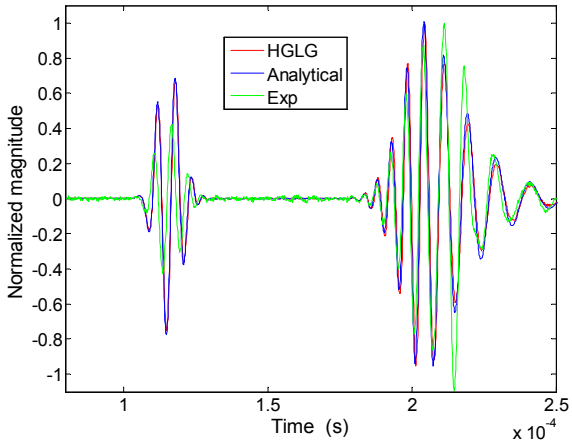

Figure 5: Comparison of the received signal after a distance travel of 565 mm for the analytical model, the experimental results and for the HGL three-step approach (global-local-global).

Hybrid Global-Local approach for damage detection

Metal structures exhibit a wide range of damage types including cracks and corrosion. The later may be uniform, pitting, galvanic, crevice, concentration cell, and graphite corrosion [33].When a waveguide structure has changes in geometry, materials properties, supports, or attachments, the guided waves that propagate through it will be modified accordingly. E.g., loss of material due to corrosion presents geometrical changes which will cause the guided waves scattering and can be used for corrosion inspection. In this study, corrosion is simulated by a uniform notch in an aluminum plate. The notch depth and the width were increased gradually in order to simulate corrosion progression. This thickness loss produced a change in the waveguide elasto-dynamic impedance and thus caused (i) scattering and reflection; (ii) modification of the wave speed of the Lamb waves crossing the corrosion area; and (iii) mode conversion. In the HGL model, simulated corrosion was made on 3.2-mm thick aluminum plate. The location of the corrosion was on the middle of the local FEM area. Transient analysis of Lamb wave interaction with a surface notch in a plate is conducted using our HGL approach as described in the previous section. In practice, corrosion defects are geometrically complex and require multiple parameters to describe them and their scattering behaviors. We used the simplified shape of a uniform notch to reduce the number of parameters in order to better understand the changes causes by material loss.

Incident wave from the T-PWAS will propagate and then interact with the notch, undergoing mode conversion. Hence, there will be reflected waves traveling toward the left edge to be captured by T-PWAS and transmitted waves traveling towards the right edge to be captured by the R-PWAS. If the incident wave is fixed, the reflection and transmission coefficients are affected by the severity of the structural discontinuity, which, in this case, is the notch geometry. These coefficients, when measured experimentally, can be used as a quantitative measure to characterize the discontinuity. To analyze the sensitivity of the Lamb waves to the size of the notch, the reflection coefficients of A0 and S0 from the notch are computed using our HGL approach.The rectangular notches have a constant width of 1 mm and depth varying from 1 to 3 mm. The results are shown in Figure 6 for A0 input and in Figure 7 for S0 input. The reflection coefficients of A0 and S0 from a notch have been studied by Lowe et al. [34] and by Lowe and Diligent [35] by using an in-house FEM software. The results in Figure 6a and Figure 7a agree with their results. A simpler interpretation of the reflection coefficient curves against notch depth can be made here based on Figure 6 and Figure 7 by considering mode shape and energy conservation with respect to transmission, reflection, and mode conversion.

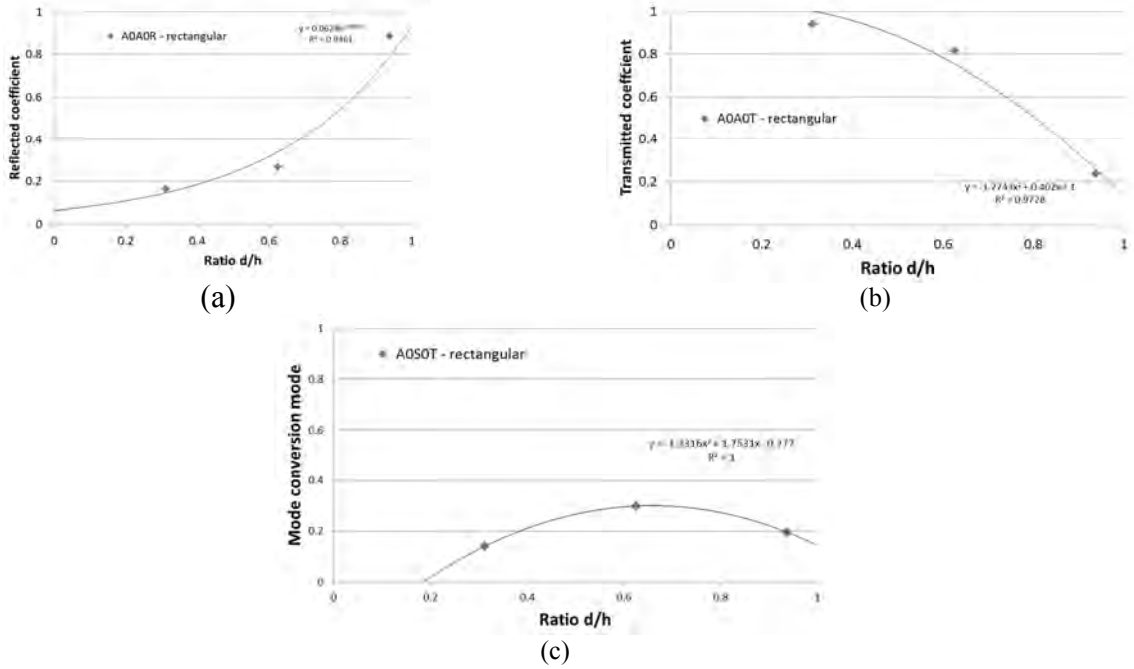

Figure 6: Coefficients versus normalized notch depth ratio for A0 incident wave packet; (a) reflected A0; (b) transmitted A0; (c) transmitted S0 mode conversion.

The case of A0 input is first discussed based on Figure 6. The notch depth is normalized by the plate thickness, d/h. As shown in Figure 6a, for $d/h < 0.6$, the notch depth is around 1/20 the wavelength of A0 (which is 12.4 mm). Hence, the wave will transmit through the notch almost completely with negligible reflection, which agrees well with the low coefficients obtained for the reflected A0 wave components. If the notch spans over the full depth, then the A0 wave is fully reflected with no conversion. The coefficient for the reflected A0 wave component approaches 1 and that for the trnasmitted S0 wave approaches 0. In between these two extremes, the incident A0 wave will undergo mode conversion, partially transmitted and partially reflected containing both A0 and S0 components. It is also not surprising that in Figure 6c, the transmitted S0 coefficient first increases and then decreases with depth, with the maximum value occurring when the notch depth is close to half the thickness of the plate.

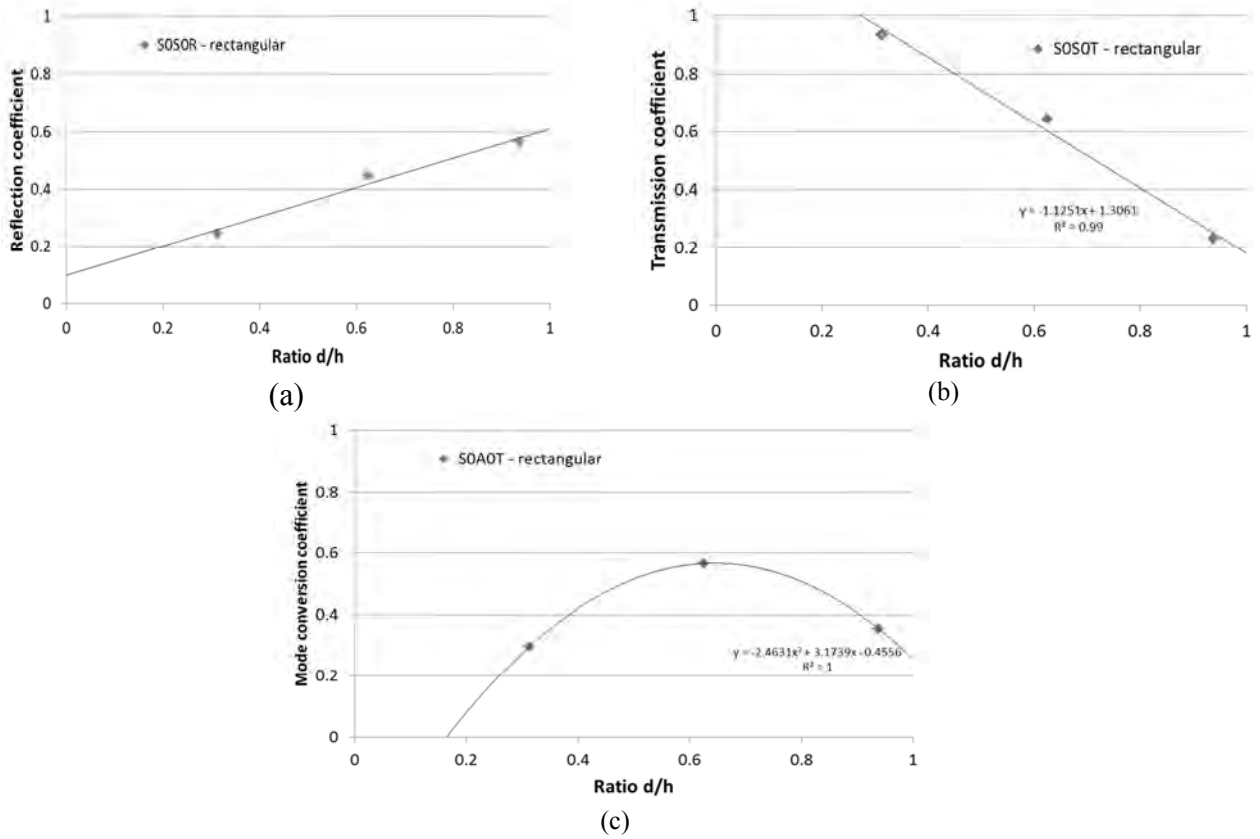

Figure 7: Coefficients versus normalized notch depth ratio for S0 incident wave packet. (a) reflectd S0; (b) tranmitted S0; (c) transmitted A0 mode conversion.

The reflection, transmission, and mode conversion coefficients for S0 input are plotted in Figure 7. A phenomenon similar to the A0 case can be observed where mode conversion is maximum when notch depth is about half plate thickness (Figure 7b). Unlike A0, the S0 exhibits good sensitivity even for a shallow notch. For $d/h > 0.4$, the notch depth is around 1/100 wavelength of S0 (which is 35.9 mm) and the reflection can be distinctly observed. This could be due to its small value at the surface meaning that any change becomes significant. The existence of surface crack destroys the symmetry of the wave, resulting in mode conversion. It is shown here that the mode shape also contributes significantly to the sensitivity of the detection. This is consistent with the observation by Ditri et al. [36] that energy distribution inside a plate for different Lamb modes could be used to predict their detectability due to the presence of cracks.

Similar analysis can be performed to evaluate the dependence of the coefficients on notch width, which for conciseness reasons will not be discussed in detail. They agree well with the results presented by Lowe et al. [34], and Lowe and Diligent [35]. The variation of the coefficients against notch width is somewhat periodic and relates to the wavenumber of the Lamb modes.

A damage index can be computed by taking the ratio of the amplitudesd of the original and mode-converted waves as received at the R-PWAS. Figure 8 shows the damage index for S0 and for A0 input. For $d/h \le 0.2$, the ratio based on the S0 input would be more sensitive than the A0 input mode. However, for $d/h > 0.6$, the damage index is bigger for A0 mode input. So using the S0 and the A0 mode, we could quantify the dimension of the notch.

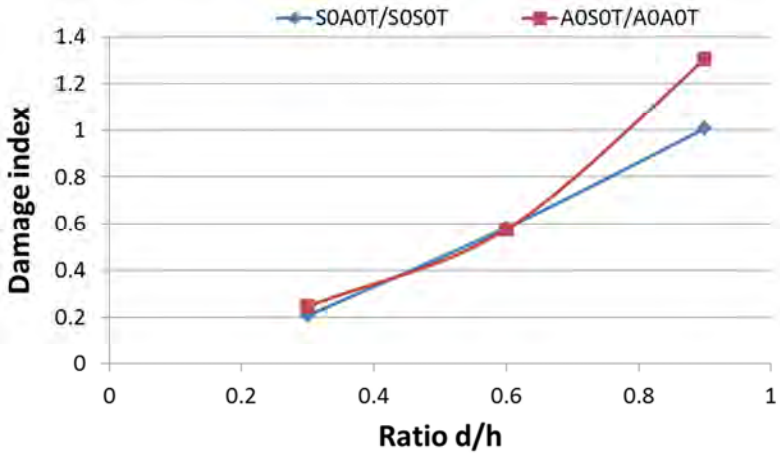

Figure 8: Damage index based on the ratio of the transmitted mode conversion and the undamaged transmitted for S0 and for A0 input.

Conclusion

This paper presents a hybrid finite element and analytical method to predict the 1-D guided wave propagation interaction with damage for nondestructive evaluation (NDE) and structural health monitoring (SHM) application. The finite element mesh is used to describe the region around the damage (defects or flaws). In contrast to other hybrid models developed elsewhere, the interaction between Lamb waves and defects is computed in the time domain using the explicit solver of the commercial finite element method (FEM) software ABAQUS. Compared to usual FEM model, the main advantage of the hybrid method is to reduce meaningfully the length of the mesh used to investigate the interaction of Lamb modes with defects and hence the computing time. Theory of guided wave propagation between two PWAS transducers was studied and an analytical model was built to give the theoretical waveforms of pitch-catch signals. Analytical modeling and finite element modeling have shown good match with experimental results, and can well describe guided wave propagation between two PWAS transducers. Lamb wave interaction with a notch is investigated by using this method, and the results obtained are consistent with respect to transmission, reflection and mode conversion. Because of the symmetric mode shape, S0 is more sensitive to the shallow notch than A0. By making use of the fact that the reflection increases with increase in notch depth and mode conversion are maximized when the notch is around half through the thickness of the plate, the reflection and conversion coefficients can be used to characterize the depth of the notch.

In future work, the analytical model will be extended to 3D circular PWAS analysis using Bessel function representation. Thus, we will realize the modeling of the guided wave propagation between two circular PWAS transducers in an arbitrary 2D geometry. The analytical modeling is expected to include damage/flaw in the plate structure, more complex structure (plate with double stiffener), and also include the second modes A1 and S1. The main complexity would be to develop a time domain hybrid global local model for 2-D wave propagation in structures.

Acknowledgements

This work was supported by the Office of Naval Research grant #N00014-11-0271, program manager Dr. Ignacio Perez and by Air Force Office of Scientific Reasearch grant #FA9550-11-1-0133, program manager Dr. David Stargel.

References

[1] Grahn, T (2003) "Lamb wave scattering from a circular partly through-thickness hole in a plate", *Wave Motion,* **37**(1), 63-80, 2003

[2] Castaings, M; Le Clezio, E; Hosten, B (2002) "Modal decomposition method for modeling the interaction of Lamb waves with cracks", *The Journal of the Acoustical Society of America,* **112**(6), 2567-2582, 2002

[3] Diligent, O; Lowe, M J S; Cawley, P (2001) "Reflection and scattering of the S0 Lamb mode from circular defects in plates", *AIP Conference Proceedings,* **557**(1), 134-141, 2001

[4] Alleyne, D N; Cawley, P (1992) "The interaction of Lamb waves with defects", *Ultrasonics, Ferroelectrics and Frequency Control, IEEE Transactions on,* **39**(3), 381-397, 1992, doi: 10.1109/58.143172

[5] Gresil, M; Lin, B; Shen, Y; Giurgiutiu, V (2011) "Predictive Modeling of Space Structures for SHM With PWAS Transducers," *Proceedings of the ASME 2011 Conference on Smart Materials, Adaptive Structures and Intelligent Systems*, Phoenix, Arizona, USA, 2011, pp. 525-534.

[6] Giurgiutiu, V; Gresil, M; Lin, B; Cuc, A; Shen, Y; Roman, C (2012) "Predictive modeling of piezoelectric wafer active sensors interaction with high-frequency structural waves and vibration", *Acta Mechanica*, 1-11, 2012, doi: 10.1007/s00707-012-0633-0

[7] Guo, N; Cawley, P (1993) "The interaction of Lamb waves with delaminations in composite laminates", *J. Acoust. Soc. Am.,* **94**(4), 2240-2246, 1993

[8] Galan, J M; Abascal, R (2005) "Boundary element solution for the bi-dimensional scattering of guided waves in laminate plates", *Computers and Structures,* **83**(10-11), 740-757, 2005

[9] Peng, H; Meng, G; Li, F (2009) "Modeling of wave propagation in plate structures using three-dimensional spectral element method for damage detection", *Journal of Sound and Vibration,* **320**(4-5), 942-954, 2009

[10] Gresil, M; Yu, L; Giurgiutiu, V (2011) "Fatigue crack detection in thick steel structures with piezoelectric wafer active sensors ", *Proc. SPIE 7983, Nondestructive Characterization for Composite Materials, Aerospace Engineering, Civil Infrastructure, and Homeland Security*, 7983 2Y, 2011, doi: doi:10.1117/12.882137.

[11] Goetschel, D B; Dong, S B; Muki, R (1982) "A Global Local Finite Element Analysis of Axisymmetric Scattering of Elastic Waves", *Journal of Applied Mechanics,* **49**(4), 816-820, 1982

[12] Chang, Z; Mal, A K (1995) "A global local method for wave propagation across a lap joint", *Numerical Methods in Structural Mechanics ASME,* **204**, 1-11, 1995

[13] Mal, A; Chang, Z (2000) "A semi-numerical method for elastic wave scattering calculations", *Geophysical Journal International,* **143**, 328-334, 2000

[14] Hayashi, T (2004) "Guided wave animation using semi-analytical finite element method", *16th World Conference on NDT,* **1328**, 2004

[15] Hayashi, T; Kawashima, K; Sun, Z; Rose, J L (2003) "Analysis of flexural mode focusing by a semi-analytical finite element method", *J. Acoust. Soc. Am.,* **113**(3), 2003

[16] Hayashi, T; Murase, M; Song, W J; Park, I K (2006) "Development of Calculation Software for Guided Wave Propagation In a Pipe", *AIP Conference Proceedings,* **820**(1), 173-180, 2006

[17] Bartoli, I; Lanza di Scalea, F; Fateh, M; Viola, E (2005) "Modeling guided wave propagation with application to the long-range defect detection in railroad tracks", *NDT & E International,* **38**(5), 325-334, 2005

[18] Sabra, K G; Srivastava, A; di Scalea, F L; Bartoli, I; Rizzo, P; Conti, S (2008) "Structural health monitoring by extraction of coherent guided waves from diffuse fields", *The Journal of the Acoustical Society of America,* **123**(1), EL8-EL13, 2008

[19] Srivastava, A, "Quantitative structural health monitoring using ultrasonic guided waves," Structural Engineering, University of California, San Diego, 2009.

[20] Viktorov, I A, *Rayleigh and Lamb waves - Physical theory and application*. New York Plenum Press, 1967.
[21] Auld, B A, *Acoustic fields and waves in solids* vol. I: Wiley Inter-sciences publication, 1973.
[22] Achenbach, J D; Xu, Y (1999) "Use of elasto-dynamic reciprocity to analyze point-load generated axisymmetric waves in plate", *Wave Motion,* **30**(1), 57-67, 1999
[23] Rose, J L, *Ultrasonic waves in solid media*. Cambridge University: Cambridge University Press, 1999.
[24] http://www.me.sc.edu/Research/lamss/NV/html/L_software.html.
[25] Giurgiutiu, V, *Structural Health Monitoring With Piezoelectric Wafer Active Sensor*: Elsevier Academic Press, 2008.
[26] Gresil, M; Shen, Y; Giurgiutiu, V (2011) "Predictive modeling of ultrasonics SHM with PWAS transducers," *8th International Workshop on Structural Health Monitoring*, Stanford, CA, USA, 2011.
[27] Gresil, M; Shen, Y; Giurgiutiu, V (2011) "Benchmark problems for predictive fem simulation of 1-D and 2-D guided waves for structural health monitoring with piezoelectric wafer active sensors", *Review of Progress in Quantitative Non-destructive Evaluation,* **1430**(1), 1835-1842, 2011, doi: 10.1063/1.4716434
[28] Shen, Y; Giurgiutiu, V (2012) "Predictive simulation of nonlinear ultrasonics," *Proc. SPIE*, San-Diego, 2012.
[29] Shen, Y; Giurgiutiu, V (Submitted 2013) "WaveForm Revealer - An analytical predictive tool for the simulation of multi-mode guided waves interaction with damage," *AIAA SDM*, Boston, USA, Submitted 2013.
[30] Alleyne, D N; Cawley, P (1990) "A 2-dimensional Fourier transform method for the quantitative measurement of Lamb modes", *IEEE Ultrasonics Symposium*, 1143-1146, 1990
[31] Moser, F; Jacobs, L J; Qu, J (1999) "Modeling elastic wave propagation in waveguides with the finite element method", *NDT & E International,* **32**(4), 225-234, 1999
[32] ABAQUS, "Analysis User's Manual," 6-9.2 ed., 2008.
[33] Roberge, P, *Corrosion inspection and monitoring*. New-York: McGraw-Hill John Wiley & Sons, 2007.
[34] Lowe, M J S; Cawley, P; Kao, J Y; Diligent, O (2002) "The low frequency reflection characteristics of the fundamental antisymmetric Lamb wave A0 from a rectangular notch in a plate", *Journal of the Acoustical Society of America,* **112**, 2612-2622, 2002
[35] Lowe, M J S; Diligent, O (2002) "Low-frequency reflection characteristics of the S0 Lamb wave from a rectangular notch in plate", *J. Acoust. Soc. Am.,* **111**(1), 64-74, 2002
[36] Ditri, J J; Rose, J L; Chen, G (1992) "Mode selection criteria for defect detection optimization using Lamb waves", *Review of Progress in Quantitative Non-destructive Evaluation,* **11**, 2109, 1992

1.

1. Report Type

Final Report

Primary Contact E-mail

Contact email if there is a problem with the report.

victorg@sc.edu

Primary Contact Phone Number

Contact phone number if there is a problem with the report

803-777-8018

Organization / Institution name

UNIVERSITY OF SOUTH CAROLINA

Grant/Contract Title

The full title of the funded effort.

PREDICTIVE MODELING OF STRUCTURAL SENSING FOR AEROSPACE APPLICATIONS

Grant/Contract Number

AFOSR assigned control number. It must begin with "FA9550" or "F49620" or "FA2386".

FA9550-11-1-0133

Principal Investigator Name

The full name of the principal investigator on the grant or contract.

VICTOR GIURGIUTIU

Program Manager

The AFOSR Program Manager currently assigned to the award

DAVID STARGEL

Reporting Period Start Date

07/01/2011

Reporting Period End Date

06/30/2015

Abstract

A methodology for multi-scale multi-domain predictive simulation of structural sensing in metallic aerospace structures was developed. The methodology is able to predict the signal response of structural sensors as a function of the structural state and/or the presence of structural flaws or damage, in linear and nonlinear regimes. The approach has been to combine analytical solutions with numerical analysis (e.g., finite element method, FEM) into a hybrid global-local (HGL) analysis. This novel approach allows one to keep the computational effort at a manageable level while preserving the fidelity needed to capture the local interaction between ultrasonic guided waves and structural damage.

The major achievements of this project are:

• One to two orders of magnitude increase in computational speed compared with conventional FEM modeling of wave propagation in interaction with damage

• Development of an unique analytical framework and predictive tool for simulation of multi-modal guided wave propagation and interaction with damage – WaveFormRevealer for both straight-crested (WFR-1D) and circular-crested (WFR-2D) guided Lamb waves

• Inclusion of multi-physics piezoelectric effects in both analytical and FEM models for both axial-active and shear-active piezoelectric wafer active sensors (PWAS)

• Novel combination of time-domain and frequency-domain approaches to the HGL implementation

• Development, for the first time, of nonreflective boundaries (NRB) for Lamb wave FEM modeling
• Efficient extraction of wave-damage interaction coefficients (WDIC) from small NRB FEM local models
• Modeling of nonlinear higher-harmonics wave-damage interactions in cracks and joints using nonlinear FEM

This fundamental research project has high relevance to USAF because it has produced a methodological framework for coupling global and local models to achieve the concurrent analysis of the structure in interaction with coupled-field phenomena and efficient treatment of nonlinearities.

The results of this project can be used to generate virtual data sets for testing data-driven models and filling data gaps will allow the autonomous model updating of the “digital-twins” models to predict future performance for new mission profiles.

Distribution Statement

This is block 12 on the SF298 form.

Distribution A - Approved for Public Release

Explanation for Distribution Statement

If this is not approved for public release, please provide a short explanation. E.g., contains proprietary information.

SF298 Form

Please attach your SF298 form. A blank SF298 can be found here. Please do not password protect or secure the PDF The maximum file size for an SF298 is 50MB.

SF 298 FA9550-11-1-0133.pdf

Upload the Report Document. File must be a PDF. Please do not password protect or secure the PDF . The maximum file size for the Report Document is 50MB.

FA9550-11-1-0133 final report.pdf

Upload a Report Document, if any. The maximum file size for the Report Document is 50MB.

Archival Publications (published) during reporting period:

1. J100 Shen, Y.; Giurgiutiu, V. (2015) “Effective non-reflective boundary for Lamb waves: theory, finite element implementation, and applications”, Wave Motion (in press)
2. J95 Kamal, A.; Giurgiutiu, V. (2014) “Shear horizontal wave excitation and reception with shear horizontal piezoelectric wafer active sensor (SH-PWAS)” Smart Materials and Structures, 23 085019 doi:10.1088/0964-1726/23/8/085019
3. J94 Shen, Y.; Giurgiutiu, V. (2014) “WaveFormRevealer: An analytical framework and predictive tool for the simulation of multi-modal guided wave propagation and interaction with damage”, Structural Health Monitoring – An International Journal, Vol. 13, No. 5, pp. 491-511, online May 2014, doi: 10.1177/1475921714532986
4. J93 Shen, Y.; Giurgiutiu, V. (2014) "Predictive Modeling of Nonlinear Wave Propagation for Structural Health Monitoring with Piezoelectric Wafer Active Sensors”, Journal of Intelligent Material Systems and Structures, Aug. 2013, DOI 10.1177/1045389X13500572, jim.sagepub.com, Jan 2014 in print Vol. 25, No. 4, pp. 506-520
5. J92 Kamal, A.; Lin, B.; Giurgiutiu, V. (2014) “Exact Analytical Modeling of Power and Energy for Multimode Lamb Waves Excited by Piezoelectric Wafer Active Sensors”, Journal of Intelligent Material Systems and Structures, first published on August 14, 2013 as doi:10.1177/1045389X13498310, Jan. 2014 in print Vol. 25, No. 4, pp. 452-471
6. J89 Gresil, M; Giurgiutiu, V (2013) “Time-Domain Global-Local Prediction of Guided Waves Interaction with Damage”, Key Engineering Materials, Vol. 558 (2013), pp. 116-127
7. J88 Gresil, M; Giurgiutiu, V (2013) “Time-Domain Hybrid Global-Local Concept for Guided-Wave Propagation with Piezoelectric Wafer Active Sensor”, Journal of Intelligent Material Systems and Structures, Vol. 24, No. 15, pp. 1897-1911, 2013, doi: 10.1177/1045389x13486712

Changes in research objectives (if any):

NONE

Change in AFOSR Program Manager, if any:

NONE

Extensions granted or milestones slipped, if any:

NONE

AFOSR LRIR Number

LRIR Title

Reporting Period

Laboratory Task Manager

Program Officer

Research Objectives

Technical Summary

Funding Summary by Cost Category (by FY, $K)

	Starting FY	FY+1	FY+2
Salary			
Equipment/Facilities			
Supplies			
Total			

Report Document

Report Document - Text Analysis

Report Document - Text Analysis

Appendix Documents

2. Thank You

E-mail user

Jul 30, 2015 09:39:42 Success: Email Sent to: victorg@sc.edu